THESIS

WASTE HEAT DRIVEN COOLING AT BEEF PROCESSING FACILITIES

Submitted by

Samuel Paul Colosimo

Department of Mechanical Engineering

In partial fulfillment of the requirements

For the Degree of Master of Science

Colorado State University

Fort Collins, Colorado

Summer 2021

Master's Committee:

Advisor: Todd M. Bandhauer

Shantanu Jathar
Jasmine Dillon

ABSTRACT

WASTE HEAT DRIVEN COOLING AT BEEF PROCESSING FACILITIES

Waste heat recovery technologies present an opportunity to utilize typically wasted energy to reduce overall energy consumption by producing mechanical work, electricity, heating, or cooling. In this study, the technoeconomic performance of a turbo-compression cooling system (TCCS) driven by waste heat from boiler exhaust gas produced at beef processing facilities is investigated. The cooling produced by the TCCS is integrated to the primary refrigeration system (PRS) of a beef processing facility to provide condenser subcooling, which enhances the performance of the PRS and produces refrigeration energy savings. Further savings are produced by rejecting condenser heat from the TCCS to feedwater entering the boiler, allowing for a reduction in boiler natural gas consumption. Process level natural gas and water data was collected at a beef processing plant and used to calculate waste heat availability and boiler water flow rate. TMY3 weather data for five cities was used to model a beef plant refrigeration system with a condenser cooling tower. To justify the installation of a TCCS, the performance and economics of the system are compared to three technologies: an electrically driven dedicated mechanical subcooler (DMS), an organic Rankine cycle (ORC), and a feedwater economizer (FWE). The results of this study show that a TCCS used to subcool the PRS yielded the highest annual savings of the four technologies. A coupled thermodynamic, heat transfer, and economic model was produced to determine the capital cost, payback period, and net present value of each technology. Then, an optimization study was carried out for the TCCS, DMS, and ORC to minimize payback period and maximize net present value by varying the effectiveness values of the heat exchangers.

The feedwater economizer was found to have the lowest average payback period of 0.92 years at an initial investment cost of $50,815. The average net present value of the FEW across the five cities was found to be $245,000. The ORC had the second lowest payback period of 1.82 years at an initial investment cost of $95,000. To achieve such a low payback period, the ORC produces almost no electricity, generating revenue solely through boiler feedwater heating. The net present value of the ORC was the second lowest at $175,000. The TCCS was found to have the third lowest average payback period of 2.22 years at a capital cost of $328,000, and the highest net present value of $429,000. The DMS was found to have the slowest payback period of 3.88 years at an investment cost of $465,000, and the lowest net present value of $84,000.

ACKNOWLEDGEMENTS

I would like to first thank Dr. Todd Bandhauer for advising me on this project and throughout my graduate career. There were many times in the last three years when I wasn't sure if I would finish, and Dr. Bandhauer was always there to encourage me that I could, and push me further than I thought possible. I am forever grateful for your mentorship!

I'd also like to thank all other members of the REACH CO-Lab who helped me greatly in finishing this work, specifically, Nickolas Roberts and Shane Garland, who both spent many hours reviewing my writing and answering my endless list of dumb questions. Beyond these two, I would like to thank the many other members of the lab for their support and encouragement including Alex Grauberger, John Simon, Derek Young, David Hobby, Caleb Anderson, Zach Gilvey, and Josh Richey.

Finally, I want to thank my family and friends for their constant love and support: Mom, Dad, Lucy, Joe, Taylor, Lawrence, Audrey, Kevin, Meagan, Riley, Hayley, Henry, Jack, Logan, Ben, and Ryan. Thank you all for the love that you have shown me. You make my life incredibly rich and inspire me in ways beyond which I can express in this short paragraph!

TABLE OF CONTENTS

LIST OF TABLES

LIST OF FIGURES

NOMENCLATURE

Variable	Name	Units
h	Enthalpy	kJ kg^{-1}
c_p	specific heat capacity	kJ kg^{-1} K^{-1}
T_c	critical temperature	°K
ε	heat exchanger effectiveness	
L	temperature lift	°C
η	efficiency	
ω	humidity ratio	kg kg^{-1}
Mbtu	British thermal unit	1000 btu
HHV	Higher heating value	MJ M^{-3}

Subscript	Name
cool	cooling
r	refrigerant
comp	compressor
s	isentropic
cond	condenser
ct	cooling tower
a	air-water mixture
sat	saturated

Subscript	**Name**
in	inlet
out	outlet
w	water
tp	two-phase
sh	superheat
br	boiler exhaust heat exchanger
min	minimum
turb	turbine
ext	external
hot	hot side
cold	cold side
mech	mechanical
pc	power cycle
cc	cooling cycle
gen	generator
elec	electricity
econ	economizer
recup	recuperator

CHAPTER 1. Introduction

1.1. Motivation

In 2019, the U.S. consumed 100.2 quads of energy [1]. Of this total, energy sourced from fossil fuels, including petroleum, natural gas, and coal accounted for about 80%. Figure 1.1 provides a breakdown of total U.S. energy use by source.

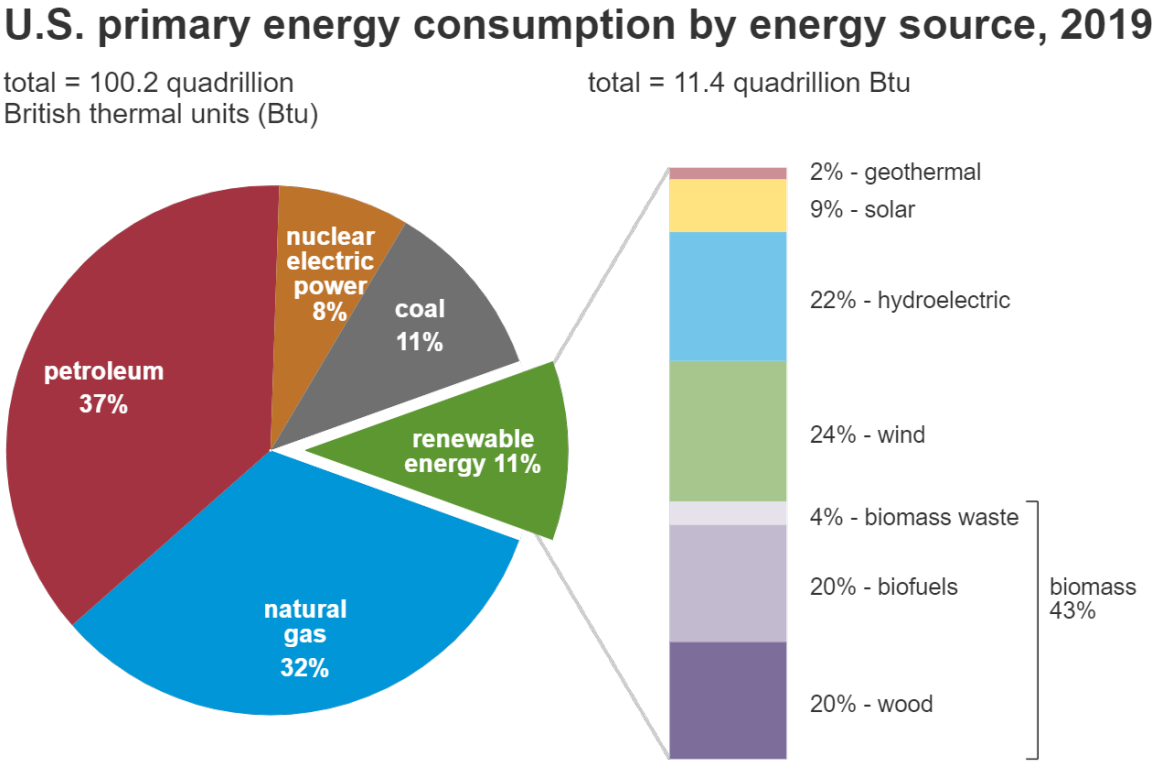

Figure 1.1 U.S. primary energy consumption by energy source, 2019 [1].

Energy in the U.S. has a variety of end uses, but end uses are generally broken down into four broad categories: commercial, residential, transportation, and industrial energy use. Of these four categories, the largest consumer is industrial, accounting for 33% of U.S. energy consumption [2]. The industrial sector includes a wide array of end uses, including facilities and equipment used for manufacturing, agriculture, mining, and construction. Of these four sub-categories, manufacturing consumed the largest portion of energy, accounting for 76% of total industrial

energy use. Within the manufacturing sector, the food processing industry is the fifth largest consumer of energy, ranking below bulk chemical, refining, metals, and paper. In total, the food processing industry accounts for 5% of all industrial energy use. Figure 1.2 breaks down all U.S. energy use, industrial energy use, and manufacturing energy use.

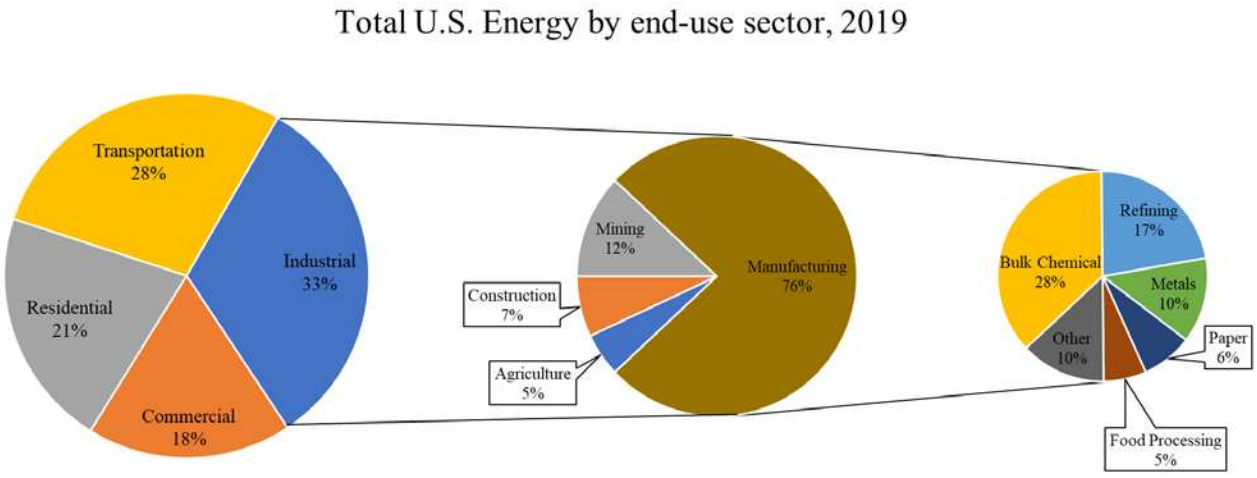

Figure 1.2 Share of total U.S. energy consumption by end-use sectors, 2019 [2].

Food processing ranks as one of the highest energy consumers in many other parts of the world as well. In Europe, the food industry is accountable for 26% of total energy consumption, and in the UK, the food processing industry is the fourth highest industrial energy user [3]. Although the food processing industry consumes the fifth most energy of any manufacturing industry (due to the vast size of the food industry), the energy consumption per dollar value of product is much lower than chemical manufacturing, refining, paper, or metals [4]. Table 1.1 describes the energy consumption and energy intensity of selected manufacturing industries according to a 2007 report conducted by the U.S. Environmental Protection Agency (EPA) [5].

Table 1.1 Energy consumption of five manufacturing sectors [5].

Manufacturing Sector	Energy Consumption (Tbtu)	Energy Consumption Per Dollar Value of Shipments (thousand Btu/$)
Chemical Manufacturing	3769	8.5
Petroleum Refining	3086	16.1
Pulp and Paper	2361	15.2
Iron and Steel	1455	27.8
Food Manufacturing	1116	2.6

Considering Table 1.1, energy consumption per dollar value of shipments in the food industry was found to be 2.6 kBtu per dollar of shipped product, which is significantly lower than other industries that consume similar quantities of energy. The comparatively non-energy intensive nature of the food industry has led to a trend of neglecting energy management, indicating a potential for significant energy savings [4].

Considering the types of energy most used in food processing, natural gas accounts for the largest of energy consumed at 570 trillion BTU/year, followed by electricity 247 trillion BTU/year [6]. Figure 1.3 and 1.4 breakdown electricity and natural gas use for the five most energy intensive sectors within the food processing industry. Considering these figures, animal slaughtering consumes the most electricity, and the second most natural gas of any sector within the food processing industry. Within animal slaughtering, the subsystems that consume the most electricity and natural gas are the refrigeration and boiler systems, respectively.

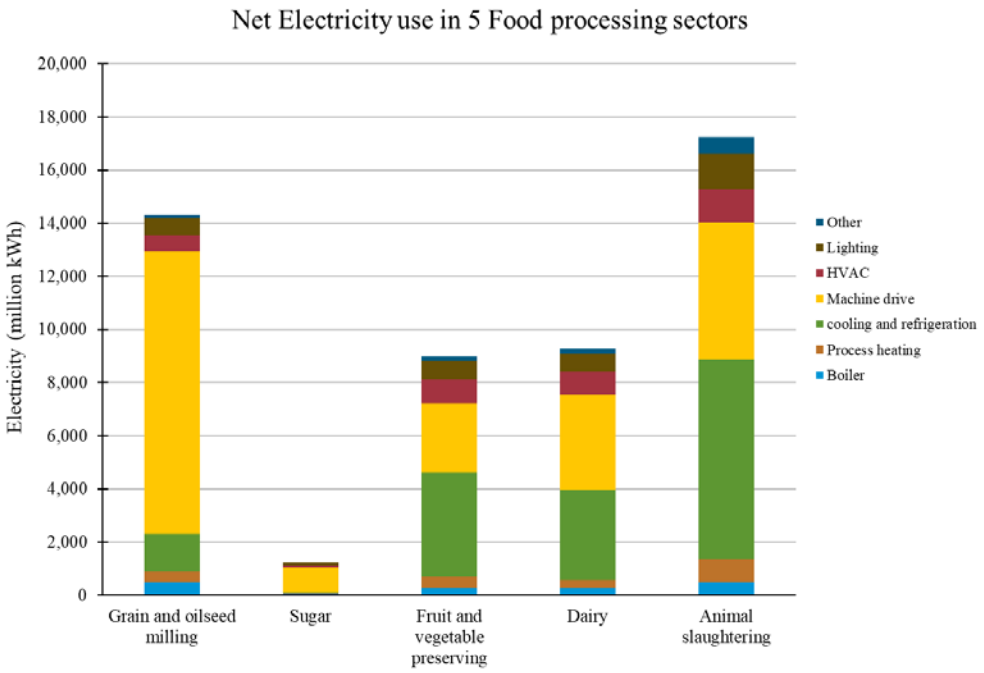

Figure 1.3 U.S. Electricity use in different sectors of the food processing industry [6].

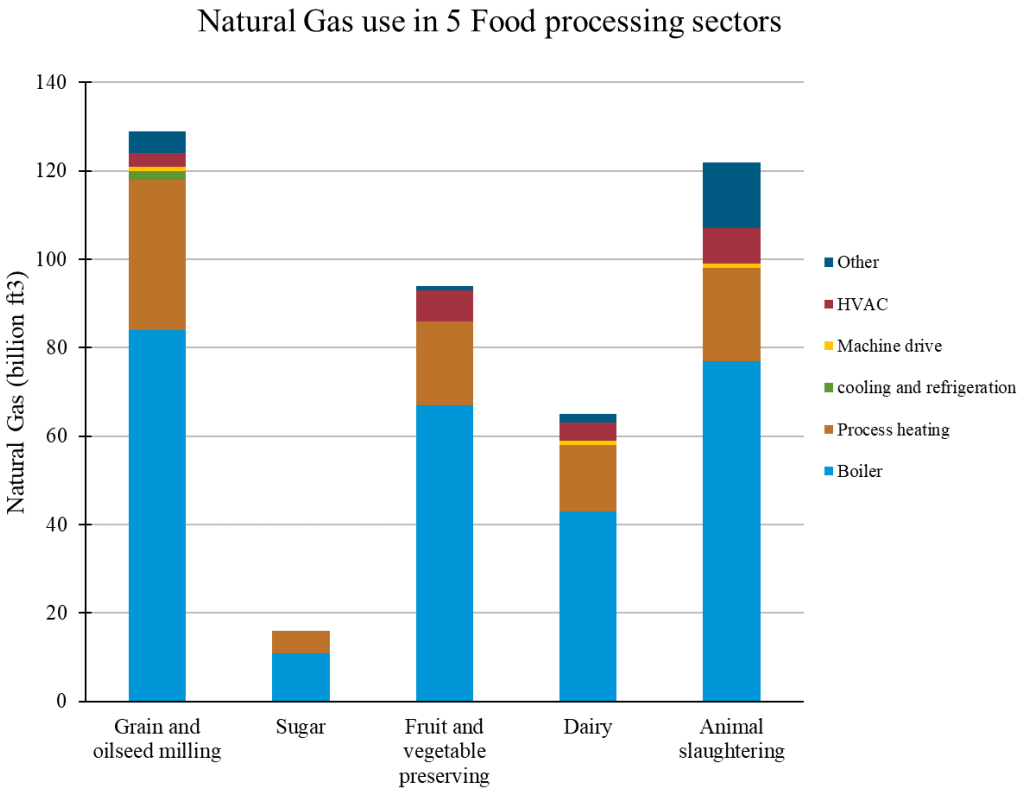

Figure 1.4 U.S. Natural gas use in different sectors of the food processing industry [6].

Not only is animal slaughtering highly energy consumptive, but it is also a large contributor to global greenhouse gas emissions. According to a collaborative report published by GRAIN and the Institute for Agriculture and Trade Policy (IATP), the combined emissions from the world's top five meat and dairy corporations are now greater than those produced by ExxonMobil, Shell, or BP. Figure 1.5 shows the total annual emissions produced by JBS, Tyson Foods, Cargill, Dairy Farmers of America, and Fonterra compared with total emissions of ExxonMobil, Shell, or BP.

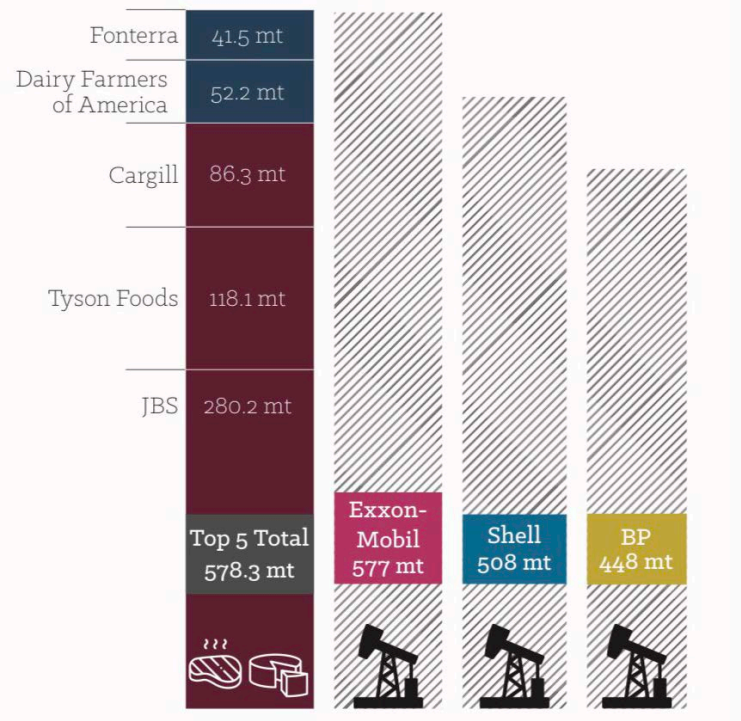

Figure 1.5 The top 5 meat and dairy companies combined emit more greenhouse gases than ExxonMobil, Shell, or BP [7].

In an effort to reduce global greenhouse gas emissions, the Paris Agreement was established in 2016 as an agreement between 195 nations to limit the global temperature rise to 1.5°C [8]. To meet this goal, the world will need to decarbonize most sectors of the economy including food production. According to the IATP study, the average per capita meat consumption must fall to 22 kg by 2030, and then to 16 kg by 2050. According to a study from the Center of

Sustainable Systems at the University of Michigan, reducing the intake of all animal-based foods by 50% in the US diet has the potential to reduce diet related greenhouse gas emissions by 35% [9]. Achieving such a goal by 2030 would result in an expected emission reduction of 224 million metric tons (MMT) per year from the current diet, bringing the US 24% closer (based on 2017 total emissions) to meeting its nationally determined contribution. Further reducing beef consumption by 90% of current levels, combined with 50% reductions in other animal-based foods, has the potential to bring down emissions in 2030 by 330 MMT below the current diet, or 36% closer to the US nationally determined contribution. In contrast to this, many large companies, including Brazilian based JBS, have plans to increase global meat consumption to 48 kg by 2030, up from 37 kg per person in 1999. Figure 1.6 shows global production of beef, pork, and chicken for selected years.

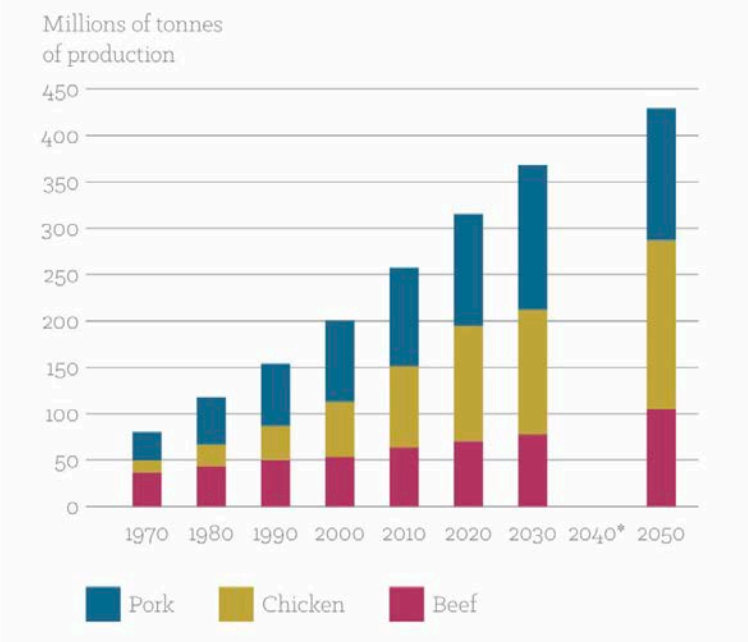

Figure 1.6 Global production of all beef, pork, and chicken, selected years [7].

The report also suggests that the livestock sector could contribute up to 80% of the GHG budget if meat consumption continues its expected growth [7]. Figure 1.7 shows the estimated

global greenhouse gas emission targets to keep within a 1.5°C rise in temperature compared to emissions from global meat and dairy production based on business-as-usual growth projections.

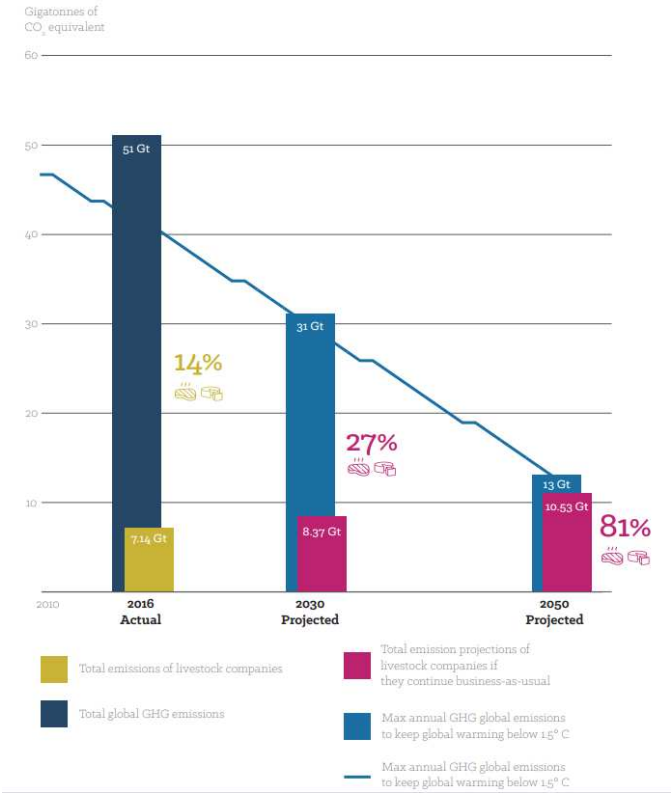

Figure 1.7 Estimated global GHG targets to keep within a 1.5°C rise in temperature compared to emissions from global meat and dairy production based on business-as-usual growth projections [7].

In summary, animal slaughtering consumes high levels of energy, and results in large quantities of greenhouse gas emissions. Ultimately, if GHG emissions are to be kept within the desired targets, a significant reduction is required in meat production and consumption in countries that overproduce and overconsume, such as the United States. However, there are many ways that the industry can increase efficiency and decrease energy consumption, specifically at processing facilities. The motivation for this paper is to investigate the thermodynamic and economic performance of technologies that beef processing facilities can adopt to reduce energy consumption. Considering that the most energy consumptive systems at processing plants are the

boiler and refrigeration systems, reducing the energy consumed by these systems will be of particular focus.

1.2. Waste Heat in Food Processing

One way that beef processing facilities could reduce their energy consumption is through waste heat recovery. Waste heat losses occur at beef processing plants as a byproduct of process heating, product refrigeration, steam boilers, and on-site generation of electricity. By capturing and using this energy, economic and energy savings would occur through reduced energy consumption and reduced capital cost by selecting equipment with less capacity. Table 1.2 outlines common process inlet temperatures for food processing operations that could take advantage of higher temperature sources of waste heat.

Table 1.2 Inlet temperatures of common low temperature processes [10].

Process	**Working Temperature (°C)**
Cleaning	60
Cooking	110-115
Pasteurization	65
	80-110
Whitening	85
Drying	30-120
Washing	40-85
Sterilization	80-90
	140-150
Boiling	95-105
Heat Treatment	40-60
Drainage	38-104

The topic of waste heat recovery from industrial processes has received increasing attention recently [11–16]. In beef processing, a variety of processes are responsible for the production of waste heat. Waste heat can be recovered from many sources including the refrigeration systems, meat processing, and by-product rendering [17]. Due to the many heating requirements that exist at a beef plant (water heating, cooking, space heating etc.), many plants have already developed

methods of using waste heat for lower temperature heating, however, waste heat could also be used to produce electricity or provide thermally activated cooling. Figure 1.8 shows a breakdown of different waste heat driven technologies, broken into three categories: waste heat to power, waste heat, and waste heat to heat.

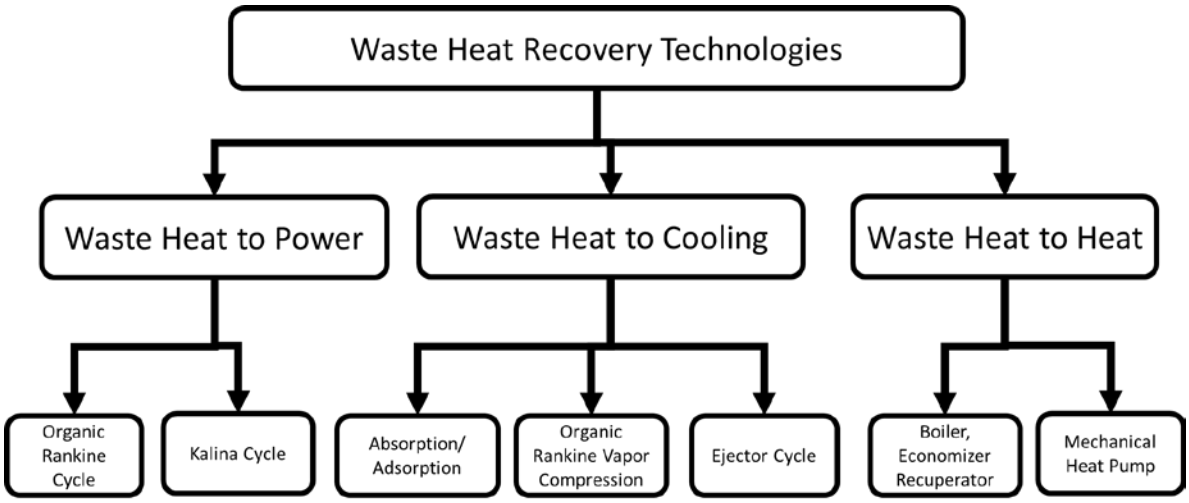

Figure 1.8 Outline of existing waste heat recovery technologies.

The first category of technologies is waste heat to power. Two of the most prominent technologies that are used to convert waste heat to power are with an organic Rankine Cycle or a Kalina cycle. Both the ORC and Kalina cycle are variants of a thermodynamic power cycle which convert waste heat into electricity at an efficiency of 10-20%. Though the Kalina cycle is slightly more efficient than the ORC, the ORC is more commonly found as it is less complex and more flexible in operation [14]. By generating power from waste heat, a plant could use an ORC or Kalina cycle to reduce its overall electric consumption and save energy.

The second category of technologies is waste heat to heat. Waste heat can be recovered and used for heating with technologies such as waste heat boilers, recuperators, economizers, and mechanical heat pumps. Economizers recover low-medium temperature heat from waste fuel gas for heating or pre-heating liquids entering a system. Recuperators recover waste heat of any grade

to preheat inlet air into a system. Waste heat boilers are used to recover medium or high-grade waste to generate steam as an output. Mechanical heat pumps use waste heat energy and external work input to transfer heat from its source to a thermal reservoir. By generating heat from waste heat, a plant could use any of these technologies to reduce overall natural gas consumption and save energy.

The final way that waste heat can be used is to produce cooling. Of the waste heat technology types, waste heat to cooling is the least researched and understood. There are several different thermally activated cooling technologies that exist such as absorption, adsorption, ejector systems, and organic Rankine vapor compression (ORVC) systems. Although an existing food processing facility is likely to already have a primary refrigeration system installed for its cooling needs, a plant could install a waste heat driven cooling technology to provide supplemental refrigeration in the form of condenser subcooling, which would increase the efficiency of the primary system, and reduce the overall energy required to produce cooling.

1.3. Research Objectives

The goal of this work is to simulate the use of four energy saving technologies at a beef processing facility to determine their thermodynamic performance and economic feasibility. The specific technologies which will be analyzed include a feedwater economizer (FWE), a dedicated mechanical subcooler (DMS), an ORC, and a thermally activated cooling system known as a turbo-compression cooling system (TCCS). The FWE is a waste heat driven technology that is configured to recover waste heat from a beef plant's boiler exhaust gas and use it to preheat boiler feedwater resulting in energy savings via a reduction in natural gas. A DMS is an auxiliary vapor compression cycle that is installed to provide condenser subcooling to a beef plant's primary refrigeration system (PRS), which results in a reduction in PRS compressor electricity

consumption. An ORC is a power generation device that is configured to recover waste heat from a beef plant's boiler exhaust gas and converts it into electricity, which is used by the plant resulting in a reduction in overall grid electricity consumption. The final energy saving technology considered in this study is the TCCS, which is a type of ORVC technology under development at Colorado State University that consumes waste heat and produces refrigeration. In the present study, the use of a TCCS will be modeled at a beef processing plant as a waste heat driven mechanical subcooler, providing subcooling to the condenser outlet of the PRS, resulting in a reduction in PRS electricity consumption. The source of waste heat driving the TCCS in the present study is waste heat recovered from boiler exhaust gas. In addition to reducing electricity consumption, the DMS, ORC, and TCCS will also be used to provide boiler feedwater heating, allowing the technologies to reduce beef plant natural gas consumption. The DMS, ORC, and TCCS will accomplish this by rejecting heat from the condenser of each cycle directly into the boiler feedwater. A beef plant of average size was considered in five different U.S. cities to determine how climate impacts cooling system performance. After annual savings are determined for each technology, heat transfer and economic models are used to estimate the capital cost of each system to determine simple payback period, simple cash flow, and net present value of each technology. This will allow for a more detailed assessment and comparison of the four technologies in terms of investment viability. Finally, a system optimization analysis will be performed to investigate the tradeoff between system size, performance and economics of each technology with the goal of minimizing payback period and maximizing net present value.

This study is unique because it is the first to analyze the use of a thermally driven cooling technology to provide subcooling to a primary refrigeration system, and the first study to qualitatively compare different energy saving technologies at meat processing facilities. In

addition, the model considers yearly weather variation, as well as yearly variation in water and natural gas use at a beef packing plant. Beyond a new application, this study builds upon prior TCCS research by considering more advanced configurations of the TCCS. In this study, two new heat exchangers are included in the TCCS: a power cycle recuperator, and a cross-cycle economizer, which both serve to improve the performance of the TCCS. Additionally, the TCCS in this study is configured to provide both cooling to the PRS, and heating to the boiler feedwater. Finally, this study considers the net present value (NPV) of the TCCS, while in past research, a minimum cost of cooling energy was calculated to yield a NPV of $0.

1.4. Thesis Organization

The following chapters detail a technoeconomic study of a turbo-compression cooling system driven by waste heat to provide subcooling for beef processing facilities. Chapter 2 will be dedicated to the literature that was reviewed in preparation for this research. Starting with an introduction of the vapor compression refrigeration cycle (VCRC), then going into a review of literature regarding recent advances in vapor compression cycle technology. The literature review will go into specific detail on three different VCRC technology advancements: expansion loss recovery, multi-stage cycles, and subcooling technologies. Next, the research needs for Ammonia VCRC retrofitting will be outlined. In doing so, a qualitative and quantitative comparison of the technology advancements will be made to determine which would be most viable for the application of retrofitting an ammonia refrigeration system typically used at beef processing facilities. Next, a review on different waste heat driven cooling technologies will be presented that discusses how these technologies could be used to provide subcooling to a refrigeration system at a beef processing plant. Finally, the focus of the current investigation will be outlined. Chapter 3 will outline the modeling approach used in this research, detailing the thermodynamic, heat

transfer, and economic models. In the last section of Chapter 3, the system optimization routine will be presented which aims to minimize the payback period and maximize the net present value of the ORC, DMS, and TCCS. Chapter 4 will begin with a presentation of the baseline results from the thermodynamic, heat transfer, and economic models, and finish by discussing the results of the optimization study. The final chapter will provide closing remarks and offer recommendations for future work. Appendix A will provide a representative calculations of the baseline plant thermodynamic model, TCCS thermodynamic model, TCCS heat transfer model, and TCCS economic model Appendix B presents the thermodynamic state points calculated by the TCCS, DMS, and ORC simulations at varying effectiveness values.

CHAPTER 2. Literature Review

In the sections below, background information and review are provided regarding the vapor compression cycle, as well as recent VCRC technology advances. Within the review, three different technology advances will be discussed: expansion loss recovery, multi-stage cycles, and subcooling cycles. Then, each technology will be qualitatively and quantitatively compared to determine which is the most viable when considering the application of retrofitting an existing ammonia refrigeration system at a food processing facility. Following this analysis, the primary gaps in the research will be identified to provide better context for the present work. Based on these gaps in the literature, the focus of the current investigation will be identified.

2.1. Vapor Compression Refrigeration Cycles

The vapor compression cycle was first theorized in the early 1800's by Oliver Evans [18], but it was not until 1854 that James Harrison built the first practical and commercially successful unit [19]. The technology has proven to be incredibly resilient, as the same basic process is still used today for most air conditioners, refrigerators, and freezers. To understand and analyze a vapor compression system, one must first understand the Carnot cycle. The Carnot cycle is an ideal thermodynamic cycle that provides an upper efficiency limit that a thermodynamic engine can achieve when converting heat into work. Figure 2.1 displays a schematic and P-V diagram of a Carnot vapor power cycle

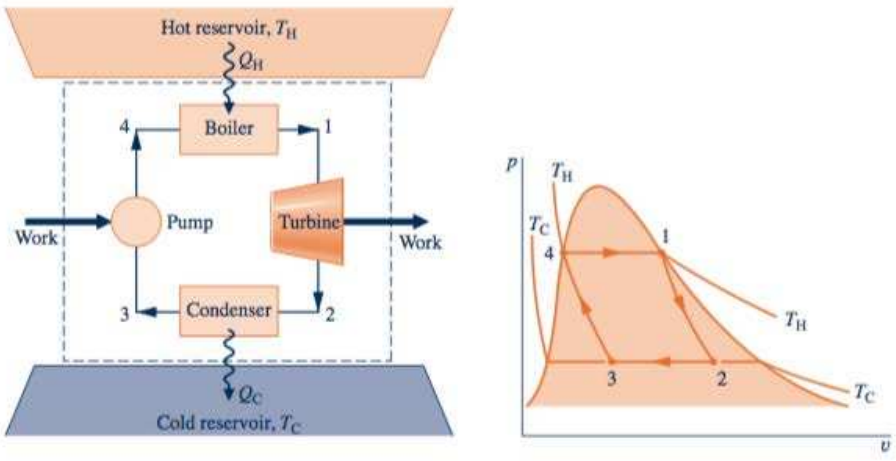

Figure 2.1 Schematic P-V diagram of a Carnot Vapor Power Cycle [20].

In a Carnot cycle, four individual, internally reversible processes occur: two adiabatic processes alternated with two isothermal processes. When a fluid undergoes this ideal cycle, thermal energy is converted into work at a maximum efficiency. This maximum efficiency is also referred to as the Carnot efficiency, shown in Equation (2.1) and can also be based solely on the temperatures of the hot and cold reservoirs

$$\eta_{\text{carnot}} = \frac{W}{Q_{\text{H}}} = 1 - \frac{T_{\text{c}}}{T_{\text{h}}} \tag{2.1}$$

where T_{c} is the temperature of the cold reservoir and T_{h} is the temperature of the hot reservoir. If a Carnot power cycle is operated in the opposite direction, the result would be a reversible refrigeration cycle. Like Carnot efficiency, the maximum theoretical coefficient of performance of a refrigeration cycle is decided by the temperatures it operates between.

$$\beta_{\text{max}} = \frac{Q_{\text{in}}}{W_{\text{c}} - W_{\text{t}}} = \frac{T_{\text{c}}}{T_{\text{h}} - T_{\text{c}}} \tag{2.2}$$

Where Q_{in} is the rate of heat rejected to the cold reservoir from the evaporator, W_{c} is the rate of work input of the compressor and W_{t} is the rate work produced in the turbine. An actual vapor compression system differs from the Carnot cycle in a few ways, resulting in lower

coefficients of performance than would be calculated in the equation above. The most significant departure from the Carnot refrigeration cycle is related to heat transfers between the refrigerant and the hot and cold regions. To achieve a rate of heat transfer sufficient to maintain a cold region temperature of T_c, the actual evaporator temperature must be several degrees below T_c. Similarly, on the warm side, to maintain enough heat transfer to the warm region T_h, the refrigerant in the condenser must maintain a slightly higher temperature. Maintaining temperatures that are slightly lower and higher than T_c and T_h respectively, will result in a reduction in overall coefficient of performance.

Another reduction in COP will occur when considering the impracticalities of wet compression. Wet compression is the term used when a liquid-vapor mixture is compressed and is normally avoided in real systems due to the damage that liquid droplets can inflict upon a compressor. In actual systems, compressors handle vapor only, operating as dry compressors. A final reduction in COP of the refrigeration system occurs because of the expansion device used. Although the expansion process typically produces some work that could be harvested with a turbine—it would be a relatively small amount of work harvested at very low isentropic efficiency. For this reason, most real-world systems replace the turbine with a simple, low cost throttling valve. What remains is the most typically found version of the vapor compression cycle, consisting of a compressor, condenser, evaporator, and throttling valve.

Aside from physical components, there are other differences between ideal vapor compression cycle and an actual vapor compression cycle. For instance, the performance drops due to adiabatic compression irreversibilities which are not present in the ideal cycle. When the working fluid is compressed, there is an increase in specific entropy from compressor inlet to exit. The magnitude of this increase in specific entropy is directly related to isentropic efficiency of the

compressor. Another factor that separates the ideal from the actual vapor compression cycle are pressure drops that occur as the refrigerant moves through the evaporator and condenser. These pressure drops decrease the effective working fluid temperature and degrade heat exchanger performance. One final distinction between the ideal and actual cycle are that typically, the working fluid leaves the condenser as a subcooled liquid, and the evaporator as a superheated vapor which required additional energy without positively benefiting the cycle. Figure 2.2 shows a schematic and T-S diagram of an actual vapor compression system, showing the irreversibilities that distinguish it from the ideal vapor compression cycle.

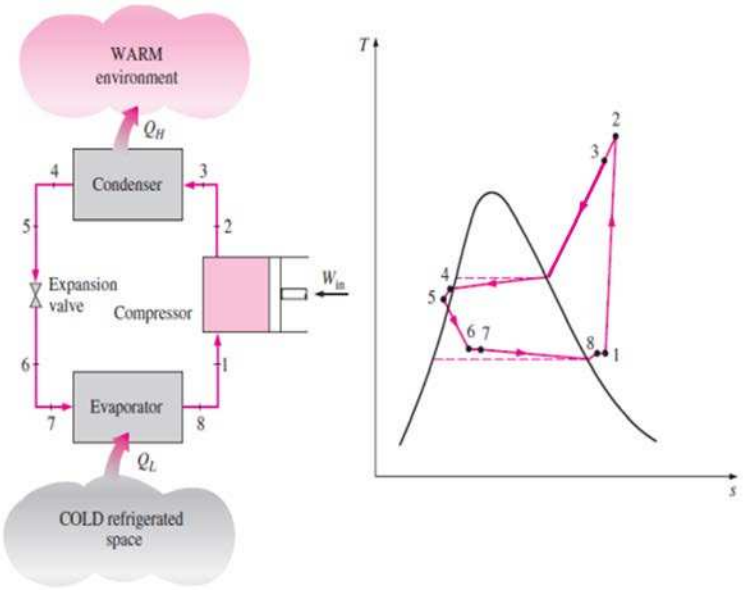

Figure 2.2 Schematic and T-S diagram of an actual VCRC with irreversibilities [21].

Thermodynamic analysis of a VCRC is most effectively performed by drawing system boundaries around the four components: the compressor, condenser, expansion device, and evaporator. To begin, the refrigerant is compressed to a high pressure and temperature by the compressor. To compress the refrigerant to a high pressure/temperature, work input is required. Using the thermodynamic state point listed in Figure 2.2, the mass and energy rate balances for a control volume enclosing a compressor give

$$\dot{W}_{\text{comp}} = \dot{M}_{\text{r}} * (h_2 - h_1) \tag{2.3}$$

Where $\dot{W}_{\text{comp}}$ is the rate of work input to the compressor, $\dot{M}_{\text{r}}$ is the mass flow rate of refrigerant through the compressor, h_2 and h_1 are the specific enthalpies at compressor outlet and inlet. Considering that an actual compression process will be adiabatic and irreversible, compressor efficiency must be considered. The effect of irreversible compression can be accounted for by using the isentropic compressor efficiency, which is given by

$$\eta_{\text{comp}} = \frac{h_{2\text{s}} - h_1}{h_2 - h_1} \tag{2.4}$$

Where $h_{2\text{s}}$ is the enthalpy of the refrigerant at the compressor outlet if constant entropy is assumed. Once the refrigerant is compressed, it passes through the condenser where heat is rejected from the refrigerant to the cooler surroundings. After being condensed, the refrigerant exists in a single-phase liquid state. For a control volume enclosing the refrigerant side of the condenser, the rate of heat transfer from the refrigerant to its surroundings is given by

$$\dot{Q}_{\text{out}} = \dot{Q}_{\text{cond}} = \dot{M}_{\text{r}} * (h_3 - h_4) \tag{2.5}$$

Where h_3 and h_4 are the enthalpies at the condenser inlet and outlet, respectively. After being condensed, the refrigerant enters the expansion device and expands to the lower, evaporator pressure. This process is generally referred to as the throttling process, and is isenthalpic, meaning that enthalpy remains constant. The energy balance for this process is described as

$$h_5 = h_6 \tag{2.6}$$

After being throttled, the refrigerant enters the evaporator as a two-phase liquid-vapor mixture. In the evaporator, heat is transferred from the refrigerated space to the vaporizing refrigerant. As heat is absorbed by the refrigerant, it is removed from the environment resulting in a cooled space. The mass and energy rate balance used to describe the refrigerant passing through the evaporator is given by

$$\dot{Q}_{in} = \dot{Q}_{\text{cool}} = \dot{M}_{\text{r}} * (h_8 - h_7) \tag{2.7}$$

Where h_7 and h_8 are the enthalpies at the evaporator inlet and outlet, respectively. As the refrigerant leaves the evaporator as a low pressure vapor, it repeats the cycle by entering the suction of the compressor. Using the quantities and expressions introduced above, the coefficient of performance can be evaluated, which is the metric most used to quantify the performance of a VCRC.

$$COP_{\text{vcrc}} = \frac{\dot{Q}_{\text{cool}}}{\dot{W}_{\text{comp}}} = \frac{h_8 - h_7}{h_2 - h_1} \tag{2.8}$$

2.2. Advances in Vapor Compression Technology

Since the invention of vapor compression refrigeration, many research efforts have been made to improve the performance of these systems. The purpose of this section is to provide a survey of available literature related to recent advancements in vapor compression technology. In Figure 2.3, advances are categorized by technology type.

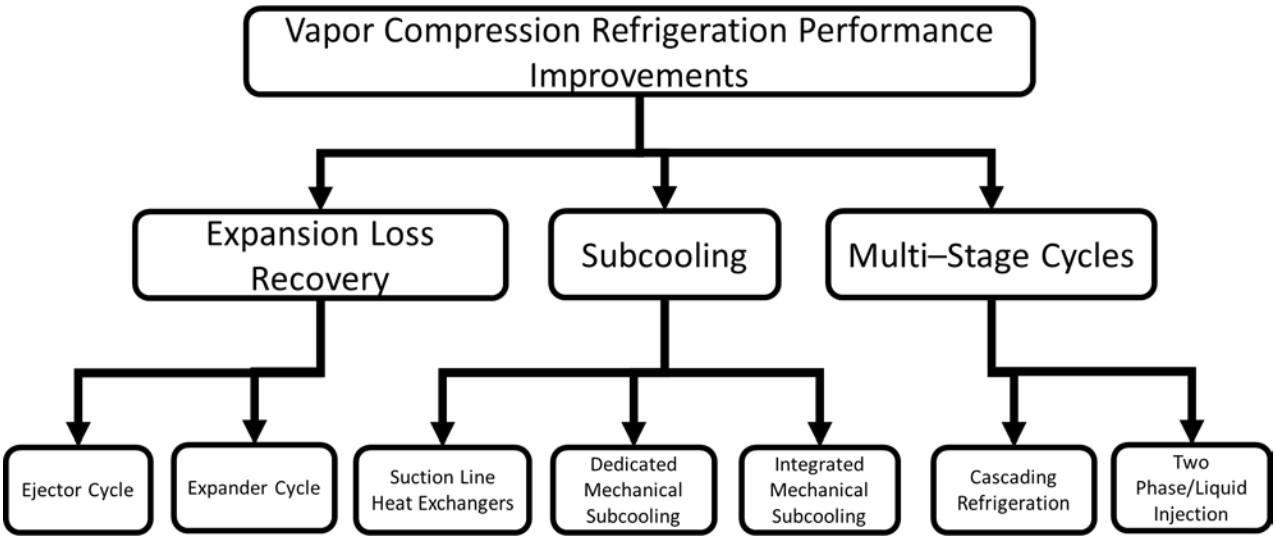

Figure 2.3 An overview of technology advancements to improve VCRC performance.

2.2.1. Expansion Loss Recovery

Expansion loss recovery is a technique used to improve the performance of a VCRC that is focused on replacing the throttling device from a typical system with either an expander or an ejector. When the refrigerant is throttled in a typical VCRC, it undergoes an isenthalpic process which results in thermodynamic losses [22]. Thermodynamic losses can be eliminated if the isenthalpic process is replaced by an isentropic process. An expander or ejector can be used as a replacement for a throttling valve to produce this isentropic condition.

2.2.1.1. Expander Cycles

An expander cycle is a vapor compression cycle where the isenthalpic throttling valve is replaced with an expansion device. Using an expander in place of an isenthalpic throttle will improve the COP of a vapor compression systems in two ways. First, the expander device extracts work from the refrigerant which can be used to supplement the compressor load. Second, replacing an isenthalpic process with an isentropic process results in an increase in cooling capacity, as the refrigerant leaves the expansion device with a lower vapor quality. Figure 2.4 shows a schematic and T-S diagram of a vapor compression cycle with an expander.

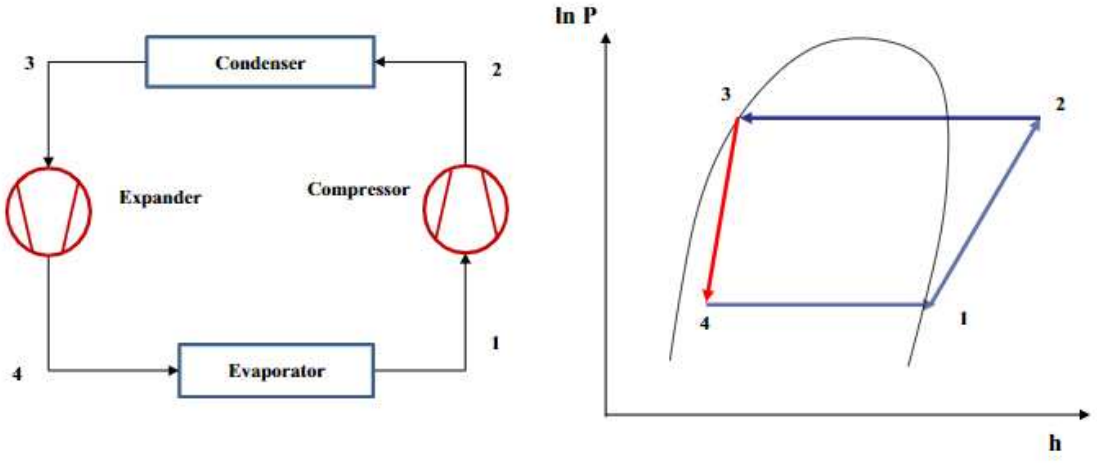

Figure 2.4 Schematic and T-S diagram of a vapor compression cycle with an expander [23].

Huff et al. investigated the use of positive displacement expanders for trans critical CO_2 cycles [24]. These cycles tend to have lower coefficients of performance than subcritical cycles due to high superheating and throttling losses. For this reason, the study considers the use of a work-extracting expander instead of an isenthalpic throttle to make COP comparable to that achieved with a subcritical cycle. First law modeling from this analysis showed that the use of an expander resulted in COP improvements between 40%-70% and capacity improvements between 5%-15%. In a follow-up report, Huff et al. assessed different integration strategies for selected types of expanders into CO_2 systems to provide a realistic evaluation of system performance [25].

Many other researchers have investigated the use different expander types to improve efficiency. Nicki et al. investigated the inclusion of a three-stage expander into a CO_2 refrigeration system to determine optimal system integration [26]. In the lab, a three-stage expander was developed and integrated into a normal refrigeration cycle. Testing results showed the optimal performance occurred after installing a vapor-liquid separator between the second and third stage of expansion. At the separator, vapor undergoes a third expansion process while liquid is supplied to the evaporator for cooling. Use of a three-stage expander instead of a throttling valve resulted in 40% increase in COP. Wang et al. also simulated the use of a novel vane-type expander with two internal expansion stages for a R-410A refrigeration system [27]. The study found that an expander with a volumetric ratio up to 7.6 and isentropic efficiency of 55% at 2000 rpm, improved the refrigeration COP from 4.0 to 4.56, a 14.2% increase under design operation conditions. Subiantoro et al. expanded on these thermodynamic studies by performing an economic analysis of expanders in medium scale air-conditioners with a variety of different conventional refrigerants, such as R134A and Ammonia, as well as more eco-friendly refrigerants such as R1234yf and CO_2 [28]. In this study, payback period was found to be less than 5 years for most conventional systems

when using an expander with 50% isentropic efficiency. Of all the refrigerants tested, ammonia benefited the least from an expander, with a maximum COP improvement of 7%, mainly due to the low operating mass flow rate. Also, it was found that expanders would be most attractive for applications in high temperature regions. In general, payback periods were the shortest for systems with highly efficient expanders, high cooling loads, high ambient temperatures, and low refrigerating temperature applications.

Overall, expanders have great potential to improve conventional vapor compression refrigeration systems. Expanders can be integrated by either generating electricity, which is sent to the compressor, or directly coupled to the compressor with a shaft. The biggest limiting factor for expanders is low expander efficiency, which can be improved by using multiple expanders to recover losses more efficiently. Other limiting factors for these devices include internal leakage, heat transfer and valve losses.

2.2.1.2. Ejector Cycles

Like expander cycles, ejector cycles improve the COP of a traditional vapor compression cycle by reducing compressor work and increasing cooling capacity. An ejector is a different type of expansion work recovery device that converts expansion losses into kinetic energy, and then to an increase in pressure which decreases the work input required from the compressor. When an ejector is used in place of a throttling valve, the system is often referred to as an ejector cycle, or a vapor jet refrigeration system. An ejector is composed of four components: a nozzle, mixing chamber, constant area mixing section (also called an ejector throat), and diffuser [29]. As the high-pressure fluid (also called the primary fluid) leaves the condenser, it enters the ejector nozzle. As the primary stream exits the nozzle, pressure is lowered and supersonic speeds are reached, where it mixes with the low-pressure stream (also called the secondary fluid) that comes from the

evaporator outlet. The entrainment ratio, ω, is the ratio between the secondary fluid mass flow rate and the primary fluid mass flow rate [30], and is calculated as

$$\omega = \frac{m_s}{m_p} \tag{2.9}$$

In the mixing chamber, both streams mix at constant pressure, and recover pressure in the diffuser section. Figure 2.8 shows a schematic and T-S diagram of an ejector cycle.

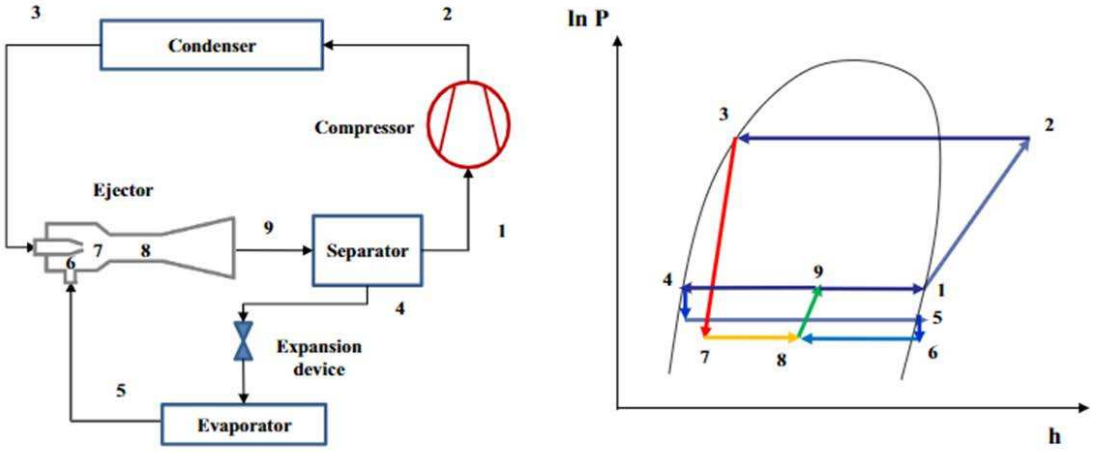

Figure 2.5 Schematic and T-S diagram of an ejector cycle.

Disawas and Wongwises experimentally investigated the performance of a two-phase ejector as an expansion device for a VCRC with R-12 and R-134a [31]. Specifically, external parameters such as heat sink and source temperatures were varied to determine how system performance was impacted. Heat sink temperatures were varied from 27°C to 37°C, while heat source temperatures were varied between 8°C and 16°C. The authors reported that as heat sink temperature increased, COP improvement decreased.

Li and Groll investigated using an ejector-expansion device for a trans critical CO_2 refrigeration cycle under typical AC operating conditions [32]. The study focused on the COP impact for varying operating conditions compared to a typical trans critical CO_2 refrigeration cycle. Some parameters that were studied included entrainment ratio, gas cooler pressure, gas cooler

outlet temperature, evaporation temperature, and evaporator superheat. As entrainment ratio decreases, pressure rise increases resulting in an improvement in COP. As gas cooler pressure increases, performance increases until an optimum is reached. As gas cooler outlet temperature increases, performance decreases because at higher gas cooler outlet temperatures, the system will experience an overall loss in evaporator capacity. The same relationship is found with performance versus evaporator temperature— as evaporator temperature increases, performance decreases. Finally, an increase in evaporator superheat was found to decrease performance as well. Overall, the ejector cycle increased the COP by 16% over a standard trans critical CO_2 refrigeration cycle for air conditioning applications.

Lawrence and Elbel compared the performance of a standard ejector refrigeration cycle with a liquid-vapor separator to an alternate ejector cycle with dual evaporators [33,34]. Unlike the standard ejector, the dual evaporator configuration does not require a separator and allows for evaporation at two different temperatures. A schematic and T-S diagram of this cycle are shown in Figure 2.6. As the refrigerant stream leaves the condenser, it is split into two separate streams: the first stream is sent to the ejector, while the second is isenthalpically throttled and sent to a low temperature evaporator. The two streams are then recombined in the ejector's nozzle region. In this study, the theoretical COP remained the same between the standard ejector cycle and two different versions of the dual evaporator configuration, however the dual evaporator configuration allows for some operating constraints to be relaxed between the ejector entrainment ratio and the quality of the ejector outlet stream. Boumaraf et al. conducted a simulation study comparing the performance of the standard ejector cycle to a dual evaporator ejector cycle and found that the COP increased by more than 17% for both R134a and R1234yf at a condensing temperature of 40^{o}C [35]. Similarly, Lawrence and Elbel conducted an experimental study of a dual evaporator

ejector cycle and found COP improvements of 6% with R1234yf and 5% with R134a over the standard ejector cycle [34].

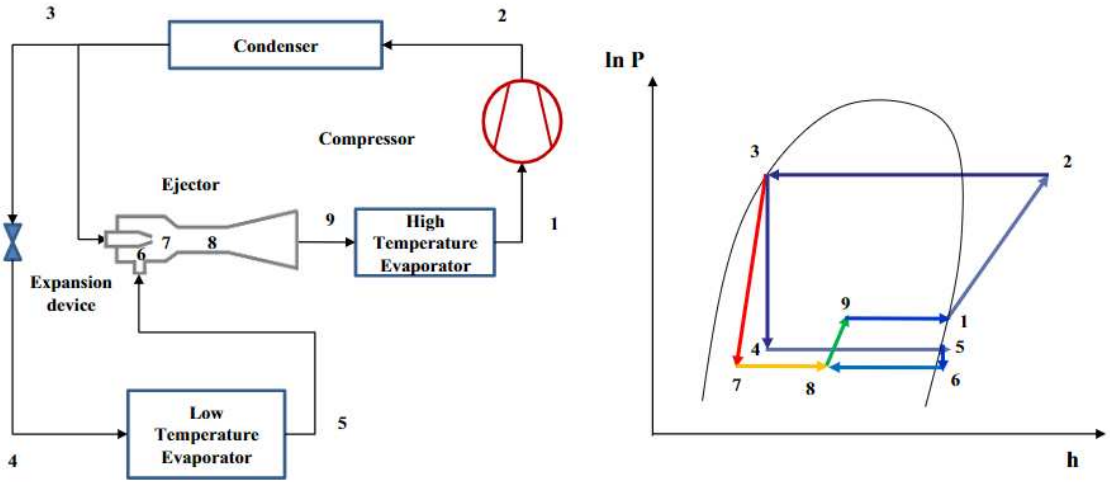

Figure 2.6 Schematic Diagram and T-S diagram of a dual evaporator ejector cycle.

Haffner et al. modelled a multi-ejector concept using R-744 for supermarket applications, and found a significant COP increase between the multi-ejector system and the reference system [36]. The multi-ejector system exhibited a COP increase between 5%-17% in cooling mode, and an increase of 20%-30% in heating mode, compared to the reference system.

There are limited studies that investigate the use of expansion loss recovery for ammonia refrigeration systems. Visentin et al. investigated the use of an expander for refrigeration systems operating with R134A, propane, and ammonia and found that COP improvement for the ammonia cycle was the lowest of the three refrigerants, ranging from 5-10% at varying condenser temperatures [37]. Kornhauser et al. conducted a first order analysis of a VCRC with an ejector for various refrigerants and found that COP improved by 12% for a VCRC with R717, which was the lowest improvement of any refrigerant tested. In both studies, it makes sense that COP improvement would be lowest for ammonia systems, because with ammonia, most losses occur

due to heat transfer from the superheated vapor, and not during expansion. For this reason, the potential increase in COP for ammonia systems through expansion loss recovery is limited.

In conclusion, expansion loss recovery cycles can dramatically improve the performance of the standard vapor compression cycle, although VCRCs with ammonia working fluids had the least beneficial impact. Most research in expansion loss recovery has focused on the use of either an expander or an ejector in place of an isenthalpic throttling valve to reduce losses that occur during this process. For expander cycles, throttling losses are recovered and converted into mechanical work that is used to supplement the compressor. For these cycles, the factor that most limits COP improvement is expander efficiency. For ejector cycles, compressor work is reduced by converting expansion losses into kinetic energy, and then into pressure increase which results in lower compressor load. For these cycles, performance can be limited by ejector efficiency, and the fixed geometry of the ejector that leads to limited operating conditions.

2.2.2. Multi-stage cycles

Refrigeration cycles that deal with high ambient temperatures or low evaporator temperatures often are limited due to irreversibilities in the compression process. To remedy these irreversibilities, many researchers have focused on multi-stage compression cycles to increase the cooling capacity and mitigate high compressor discharge temperatures. Multi-stage cycle research, as the name implies, focuses on breaking down the fundamental processes involved in vapor compression into multiple processes to enhance performance. Multi-stage cycle research is broken down into vapor or liquid refrigerant injection cycles, and saturation cycles.

2.2.2.1. Vapor or Liquid Refrigerant Injection Cycle

The first area of multi-stage cycle research is vapor or liquid refrigerant injection. Liquid injection is defined as injecting the liquid refrigerant that exits the condenser into the hot gas refrigerant at the discharge side of the compressor, or directly into the sealed compressor pocket.

Liquid refrigerant injection is commonly used for decreasing extremely high compressor discharge temperatures which improves performance and ensures reliable system operation. A schematic of a liquid injection refrigeration cycle is shown in Figure 2.7. By reducing the compressor discharge temperature, the cooling load required of the condenser is reduced, and COP increases. Dutta et al., and Cho et al. both conducted studies regarding the use of liquid injection in a scroll compressor driven refrigeration cycle with R22 as a working fluid and found that as injection ratio increased, discharge temperature decreased, improving the overall performance of the cycle [38,39]. Reported COP increases for the system in both studies ranged from 0-10%, based on injection ratio and compressor frequency.

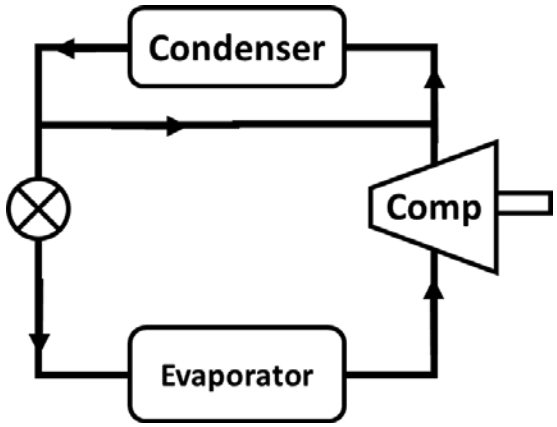

Figure 2.7 Schematic of Liquid refrigerant injection.

Vapor injection involves injecting vapor into the intermediate location of the compressor. According to a review on injection techniques by Pawale et al., vapor injection is more beneficial than liquid injection for two reasons [40]. Firstly, with vapor injection, system capacity can be varied by controlling the injected refrigerant mass flow rate, which permits some energy savings by avoiding intermittent operation of the compressor. Secondly, the compressor discharge temperature of a vapor injection cycle is lower than the liquid injection cycle, due to the injected vapor entering the compressor at a lower temperature than the injected liquid, reducing the

compressor work. The two basic cycles that are most used to provide vapor injection are flash tank vapor injection and subcooler vapor injection. For the flash tank cycle, refrigerant vapor is provided from phase separation that occurs after a high stage expansion device. A schematic and P-H diagram of a flash tank vapor injection cycle is shown in Figure 2.8.

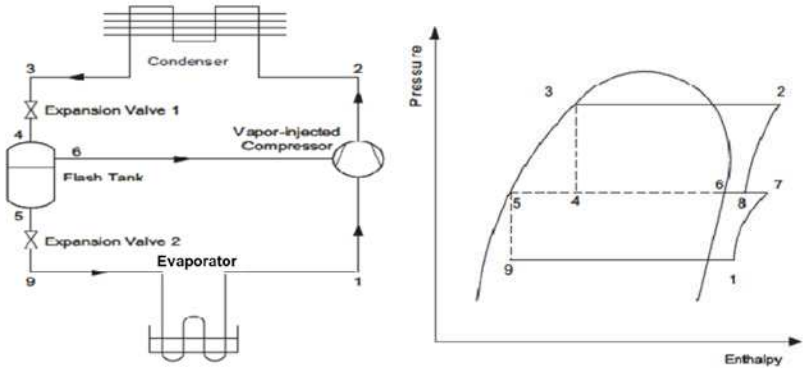

Figure 2.8 Schematic and P-H diagram of a flash tank vapor injection cycle [40].

For the subcooler cycle, vapor is provided to the compressor from a heat exchanger placed before and after the high-stage expansion device. A schematic and P-H diagram of a subcooler vapor injection cycle is shown in Figure 2.9. Each of these cycles has advantages and disadvantages. The flash tank cycle has better performance but is more difficult to control at high compressor speeds. The subcooler cycle has lower performance but allows for more accurate cycle control due to the ability to vary the amount of vapor injection.

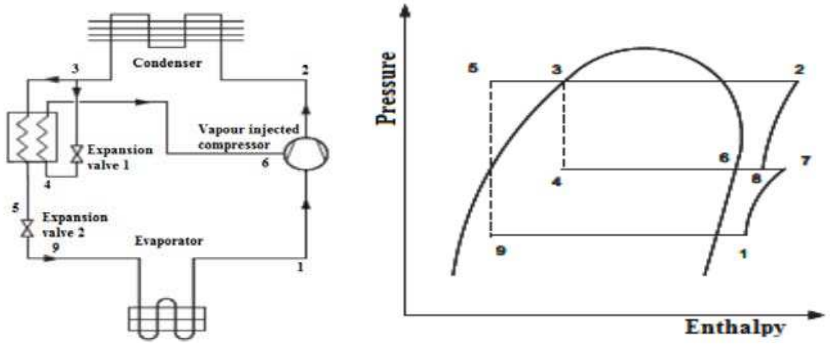

Figure 2.9 Schematics and P-H diagrams of a subcooler vapor injection cycle [40].

Winandy and Lebrun performed a theoretical and experimental investigation on the performance of an R-22 refrigeration system with liquid and vapor injection [41]. The study showed that vapor injection allowed for a slight increase in cooling capacity and constant COP, while liquid injection decreased compressor discharge temperature by 1.2^{o}C for each percent of injection ratio. Heo et al. researched the effects of flash tank vapor injection on the heating performance of a R410A heat pump for cold regions [42]. The results of this study were that COP and heating capacity of the injection cycle were enhanced by 10% and 25%, respectively, at an ambient temperature of -15^{o}C compared to non-injection cycles. Heo et al. also investigated the heating performance of a subcooler vapor injection cycle, as well as two novel cycles. The first novel cycle was a combination of the two cycles, referred to as the flash tank subcooler cycle (FTSC). The second novel cycle was a double expansion subcooler (DESC). The finding of this study was that heating capacity of the two novel cycles were higher than the original two vapor injection cycles, however the COP for all four cycles remained relatively the same. The author suggested that FTSC was superior, as it combines the performance of a flash tank cycle with the variability of a subcooler cycle.

2.2.2.2. Saturation Cycle

The saturation cycle is an ideal version of the vapor compression cycle that attempts to reduce thermodynamic losses associated with single phase gas compression and isenthalpic expansion. Lee et al. first suggested the possibility of a saturation cycle in 2013 [43]. To improve the compression and throttling processes, the saturation expansion and saturation compression processes are used simultaneously together with compression and condensing processes. While previous multi-stage cycle research suggests the efficacy of saturation compression through injection, the saturation cycle seeks to also improve cycle efficiency through reducing throttling losses. Figure 2.10 shows i-stage refrigerant injection vapor compression cycles, which approach

the ideal saturation vapor compression and expansion cycle. In theory, the refrigerant injection processes could be repeated as many times as the compressor design allows. As the number of stages increases, the cycle approaches the ideal saturation cycle.

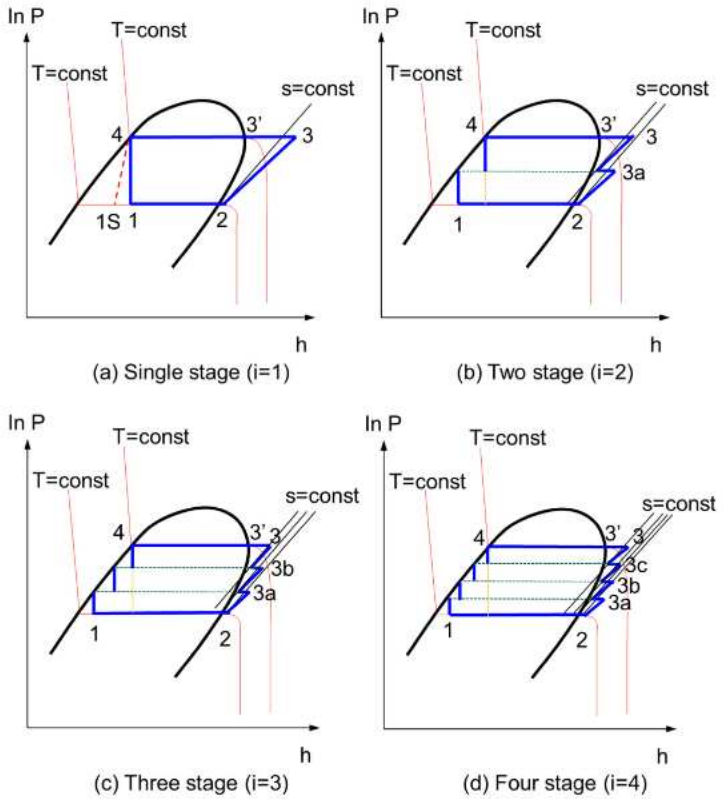

Figure 2.10 i-stage cycles in p-h diagrams (single stage (a) and three multi-stage cycles (b-d)).

As refrigerant leaves the condenser, it is expanded through the high stage expansion valve, entering a flash tank separator. In the flash tank separator, the cold vapor and some of the liquid are used for two phase refrigerant injection, while the low enthalpy liquid is further expanded to the next stage until reaching the bottoming stage. A schematic of an n-stage saturation cycle is shown in Figure 2.11.

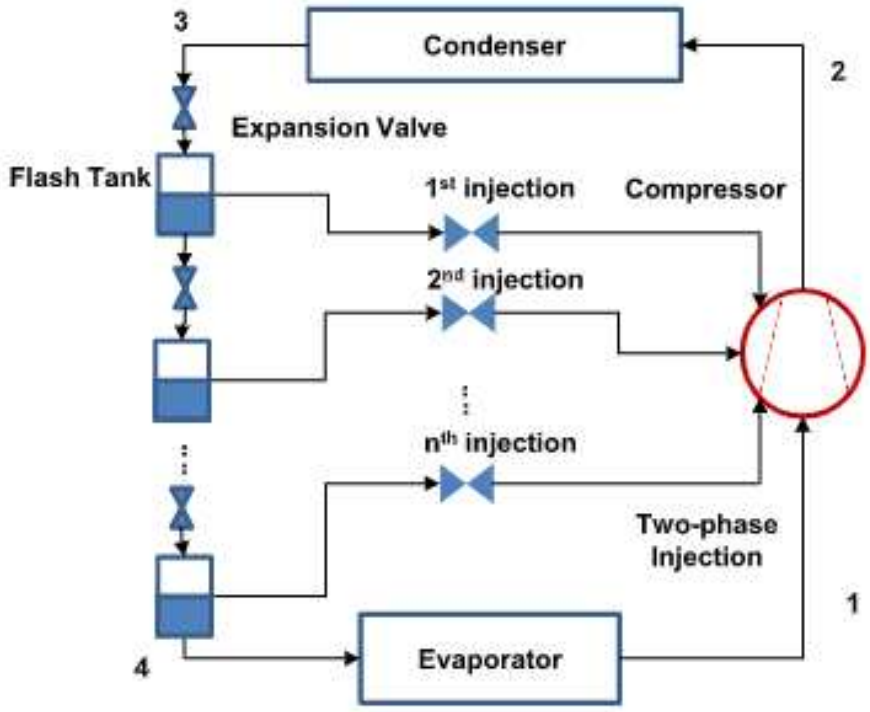

Figure 2.11 Schematic of a two-phase injected multi-stage vapor compression cycle [44].

Lee et al. performed a simulation study to determine how COP would be impacted by number of stages and working fluid selection [44]. In the study, performance was simulated with one through four stages running with either R410a or propane. The result of the simulation showed that under extreme heating conditions, the COP of the four-stage cycle increased by 42.4% for R410a and 38.2% for propane over their respective single stage cycle. In a follow up study, Lee et al. developed a transient thermal model of a passenger car's cabin and implementation of a saturation cycle with alternative working fluids [45]. In the model, it was found that the four-stage saturation cycle using R1234yf MAC (mobile air conditioning) improved cycle efficiency by 24% and reduced power consumption by 20% over a typical vapor compression cycle.

No studies were found that specifically analyzed the impact of multi-stage cycle technologies on ammonia refrigeration systems. Wang et al. investigated the potential benefits of compressor cooling for two different refrigeration systems, a low temperature system, and an air

conditioner [46]. The study did not explicitly consider any injection technique, but rather, focused on evaluating the theoretical performance of a system where the compression process approaches the isothermal condition. Four refrigerants were investigated in both systems: R22, R410A, R744, and R134a. The results found that compressor cooling resulted in the highest power reduction for the low temperature system with R744 as the working fluid. The low temperature application benefitted more from compressor cooling due to high pressure ratios and high discharge temperatures. Of the systems and refrigerant combinations studied, the low temperature R744 system experienced the greatest compressor power reduction of 16%, due to it having the highest discharge temperature. Because of ammonia's high latent heat and low gas density, ammonia refrigeration systems are typically operated at low evaporator temperatures and have high compressor discharge temperatures. For this reason, the findings of this study suggest that an ammonia refrigeration system would benefit greatly from compressor cooling.

In conclusion, multi-stage cycles show significantly higher COP values than the standard VCRC. Multi-stage cycle research focuses primarily on a variety of injection techniques, taking refrigerant from the condenser outlet, in vapor, two-phase, or liquid form, to provide cooling to the lower the temperature of the refrigerant that leaves the compressor. For refrigeration systems that use ammonia that experience high losses due to high compressor discharge temperatures, multi-stage cycle technologies have the potential to improve performance dramatically, as they increase performance by providing cooling to the compressor.

2.2.3. Subcooling

The final research area within vapor compression technology advancement is subcooling. Subcooling cycles improve the efficiency of a vapor compression refrigeration cycle by subcooling the exit of the condenser and increasing the amount of heat a refrigerant can absorb in the

evaporator. Any heat sink of appropriate temperature can be used to subcool a vapor compression refrigeration cycle, however three techniques in specific will be discussed: suction line heat exchangers, integrated mechanical subcooling, and dedicated mechanical subcooling.

2.2.3.1. Suction Line Heat Exchangers

Suction line heat exchangers have been widely applied to vapor compression refrigeration systems to improve performance and protect system components. A suction line heat exchanger is an internal heat exchanger that transfers heat from the high-pressure refrigerant at the condenser outlet to the low-pressure refrigerant at the condenser inlet. Using a SLHX ensures that the refrigerant enters the expansion device as a subcooled liquid and enters the compressor as a single-phase gas. Figure 2.12 provides a schematic and P-H diagram of a vapor compression system with a SLHX.

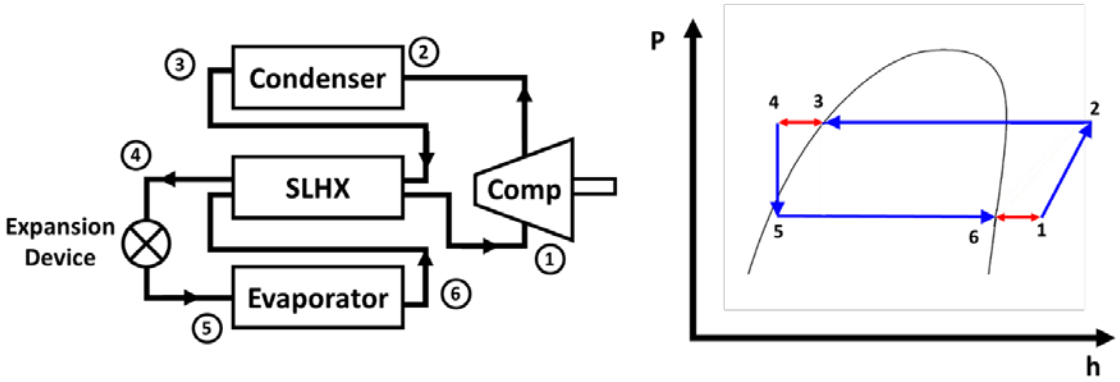

Figure 2.12 Schematic diagram and p-h diagram of a vapor compression system with SLHX.

Domanski et al suggested the benefit of the SLHX is dependent on both operating conditions and fluid properties [47]. In the study, theoretical performance was determined for 29 refrigerants at fixed reduced condensing and evaporating temperatures of 0.82 and 0.65, respectively. Reduced temperature is defined as the ratio of the absolute temperature to the critical temperature of a substance. As a result of using reduced temperatures, the simulation results for each refrigerant are at different evaporator and condenser temperatures and different temperature

lifts. Therefore, they were unable to obtain a satisfactory correlation between refrigerant properties and SLHX performance. Klein et al. investigated the influence of a SLHX on the performance of a vapor compression system using a new dimensionless group for various refrigerants [48]. Through a systematic evaluation of refrigeration properties, it was discovered that the relative capacity index (RCI) for a specified temperature lift correlates well with the dimensionless quantity

$$D = \frac{\Delta h_{\text{vap}}}{(C_{\text{p,L}} * T_{\text{c}})} \tag{2.10}$$

where Δh_{vap} is the enthalpy of vaporization at the evaporator pressure, $C_{\text{p,L}}$ is the specific heat of the saturated liquid refrigerant at the evaporator temperature and T_{c} is the critical temperature of the refrigerant. Once the dimensionless quantity is determined for a refrigerant at a certain evaporator temperature, the effect of a SLHX on refrigeration capacity can be quantified in terms of the RCI. RCI quantifies the increase or decrease in refrigeration capacity due to the addition of a SLHX as shown in Equation (2.11). The correlation to the dimensionless quantity, D, is determined with Equation (2.12) below:

$$RCI = \left(\frac{Capacity - Capacity_{\text{no SLHX}}}{Capacity_{\text{no SLHX}}}\right) * 100 \tag{2.11}$$

$$\begin{aligned} RCI/\epsilon = {} & -3.0468 + 19.3484D - 19.091D^2 + 1.2094L \\ & + 0.02101L^2 - 5.9980DL - 0.02797DL^2 \\ & + 5.52865D^2L) \end{aligned} \tag{2.12}$$

Where ϵ is the effectiveness, and L is the temperature lift between the condenser and evaporator saturation temperature. Using these equations, one can decide whether to implement a SLHX based on the refrigerant used, and the temperature lift of the VCRC. For refrigerants such as R717 that have very high enthalpies of vaporization, the use of a SLHX is detrimental to the performance of

a VCRC. The relationship between this dimensionless quantity and relative capacity found by Klein et al is shown in Figure 2.13, which shows that the SLHX would be best applied to systems with refrigerants having low dimensionless quantity values.

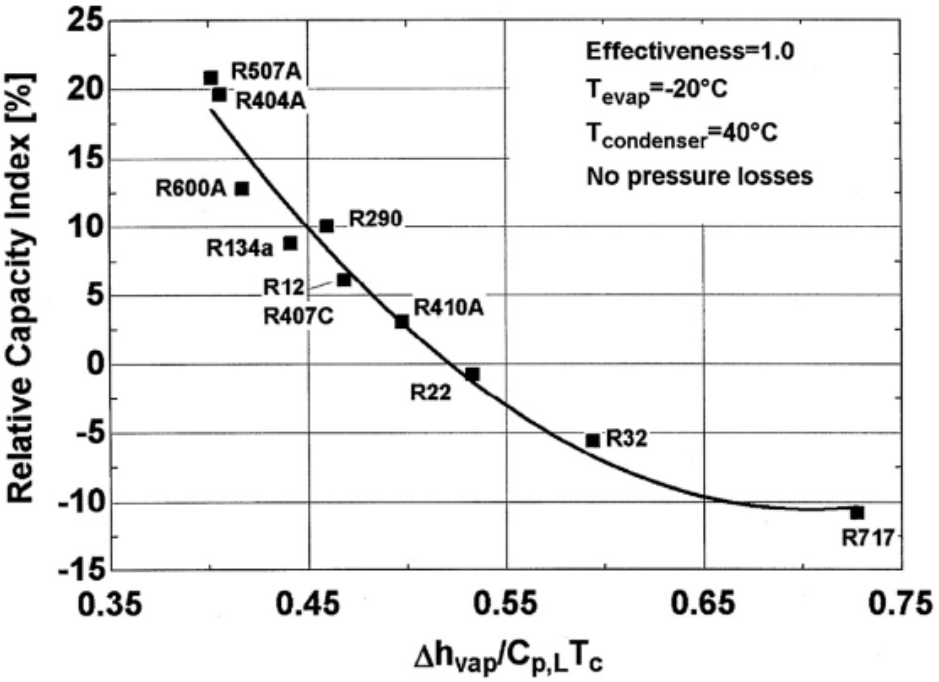

Figure 2.13 Relative Capacity Index versus $\Delta h_{vap}/(c_{p,L}*T_c)$ at saturated evaporating and condensing temperatures of -20°C and 40°C, respectively.

Mastrullo et al. conducted a numerical investigation to determine whether or not a vapor compression system would benefit from a SLHX for 19 different refrigerants [49]. In the study, a chart was introduced which evaluates whether a SLHX should be used based on refrigerant type, evaporator temperature, and condenser temperature as shown in Figure 2.14. For example, if an R-22 system has an evaporator temperature of -20°C and a condenser temperature of 45°C, the operation point lies above the curve, and thus system performance will improve by implementing a SLHX. These findings further validate the findings of Klein et al., demonstrating that VCRC's with some refrigerants, such as R717, never experience an increase in cooling capacity due to the implementing of a SLHX.

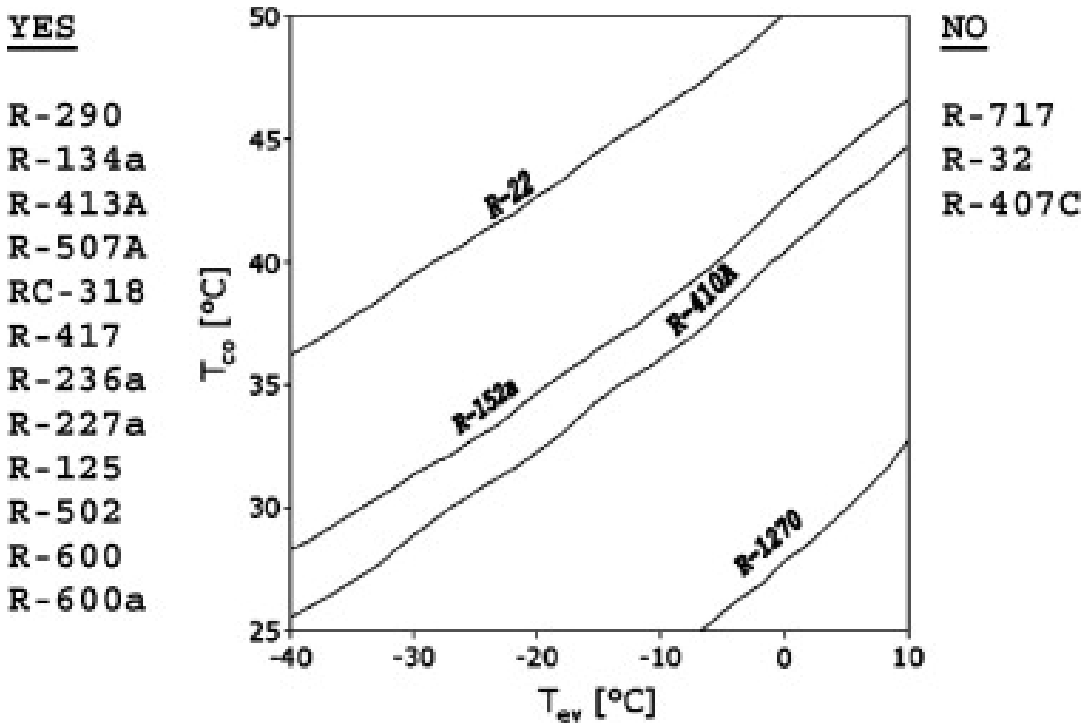

Figure 2.14 Map predicting the impact of a SLHX on vapor compression performance [49].

Many researchers have investigated the use of SLHX to improve the performance of vapor compression cycles that use CO_2 as a refrigerant. CO_2 cycles tend to be less efficient due to high superheating and throttling losses. Lorentzen and Pettersen showed COP improvement by using the SLHX to reduce throttling losses [50]. Other researchers have represented performance variation of a CO_2 cycle with the SLHX by comparing their characteristics with those of other conventional refrigeration systems [51,52]. Cho et al. reported that the cooling capacity and COP of the CO_2 cycle increased by 6.2%-11.9% and 7.1%-9.1% respectively, at the tested compressor frequencies from 40 to 60 hz [53].

Other researchers have suggested the use of the SLHX for automotive air conditioning systems that use R1234yf as a working fluid [54–56]. R1234yf is a low GWP refrigerant that has been implemented in many automotive systems as a replacement for R134a due to their similar thermophysical properties. However, because it has a smaller latent heat of evaporation than

R134a, research has suggested the use of a SLHX to improve performance. Navarro-Esbri et al. experimentally analyzed the influence of a SLHX on the performance of a R1234yf refrigeration system [57]. For a system that used R1234yf as a drop-in replacement for R134a, COP reductions of 6-13% occurred, however the SLHX reduced these COP reductions by 2-6%. Similarly, Cho et al. researched a SLHX for a R1234yf system, and also found that the SLHX reduced decreases in performance [58]. The results of the study showed that, without the SLHX, the replacement of refrigerants resulted in a decrease in cooling capacity and COP of up to 7% and 4.5%, respectively. However, with the SLHX, cooling capacity and COP only decreased by 1.8% and 2.9%. Pottker and Hrnjak experimentally investigated the effect of AC systems using R1234yf and R134a, with and without a SLHX [59]. For a given operating condition, the system COP increased up to 18% for R1234YF and 9% for R134a. Qualitatively, the study found that as condenser subcooling increases, COP undergoes a maximum. Also, results indicated that the system with R1234yf benefitted more than the R134a system when a SLHX was used.

2.2.3.2. Integrated Mechanical Subcooling

While a SLHX can generally be applied to vapor compression systems of all sizes, mechanical subcoolers are generally applied to medium to large size systems. Mechanical subcooling utilizes a small cooling system which supplements the main refrigeration system, improving overall capacity and increasing COP. There are two main techniques of mechanical subcooling that are discussed in the literature: integrated mechanical subcooling and dedicated mechanical subcooling.

The first type of mechanical subcooling is known as integrated mechanical subcooling. After the refrigerant leaves the condenser, it is split into two streams. The subcooling stream is extracted from the primary liquid stream and is expanded to the subcooler pressure. This results in evaporation of an extracted liquid refrigerant and subcooling of the primary liquid in the subcooler.

Then, the refrigerant gas generated in the subcooler is re-compressed to the condenser pressure utilizing a small compressor. On leaving the subcooler, the sub-cooled liquid enters the expansion valve, where its pressure is decreased, and is then sent to the evaporator. Figure 2.15 shows a schematic of a VC system with integrated mechanical subcooling and a p-h diagram of the cycle.

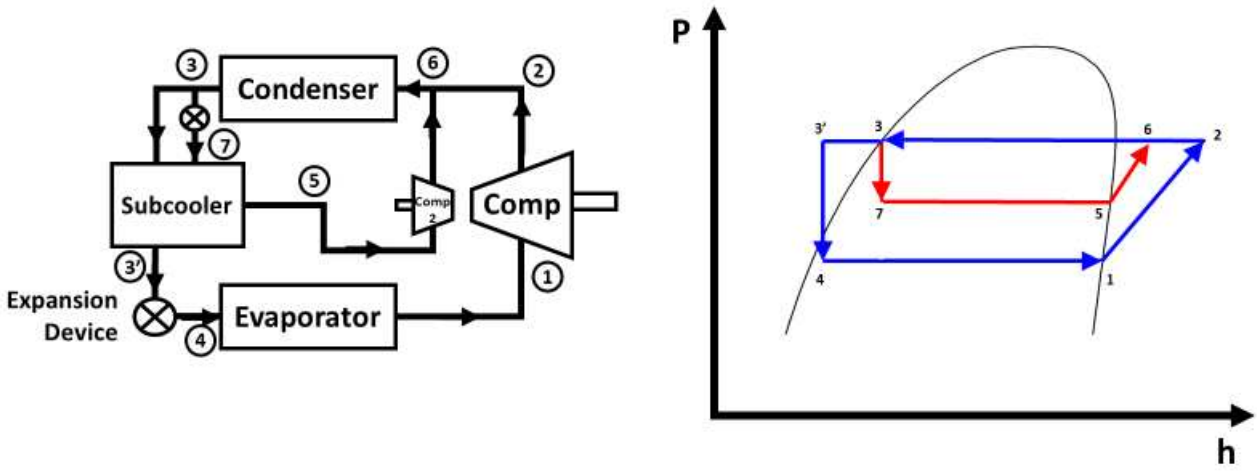

Figure 2.15 Integrated mechanical sub-cooling of a vapor compression refrigeration cycle.

Zubair et al. performed a second law based thermodynamic analysis of an R134a VCRC with an IMS, and evaluated COP improvement as a function of subcooler saturation temperature for evaporator and sub-cooling temperatures of -30°C and 3°C, respectively [60]. They found the COP improvement was greatest when the condenser temperature was highest, and subcooler saturation temperature was halfway in between the evaporator and condenser temperatures of the primary cycle. In a follow-up study, Khan and Zubair investigated another R134a VCRC with an IMS, developing a model to study system performance for various conditions, and predicting the optimum distribution of heat exchanger area [61]. From this numerical investigation, the maximum COP improvement of 7.5% was possible for the system. Qureshi and Zubair studied the impact of fouling on the performance of a VCRS with an IMS for a variety of refrigerants [62]. Of the

refrigerants considered, R134a and R717 showed the best performance unless when the evaporator was being fouled.

2.2.3.4. Dedicated Mechanical Subcooling

Dedicated mechanical subcooling utilizes a small mechanical vapor compression cycle, coupled to the primary cycle at the exit of the condenser. Figure 2.16 shows a schematic of a vapor compression system (PRS) with dedicated mechanical subcooling (DMS), as well as a p-h diagram illustrating the impact of subcooling.

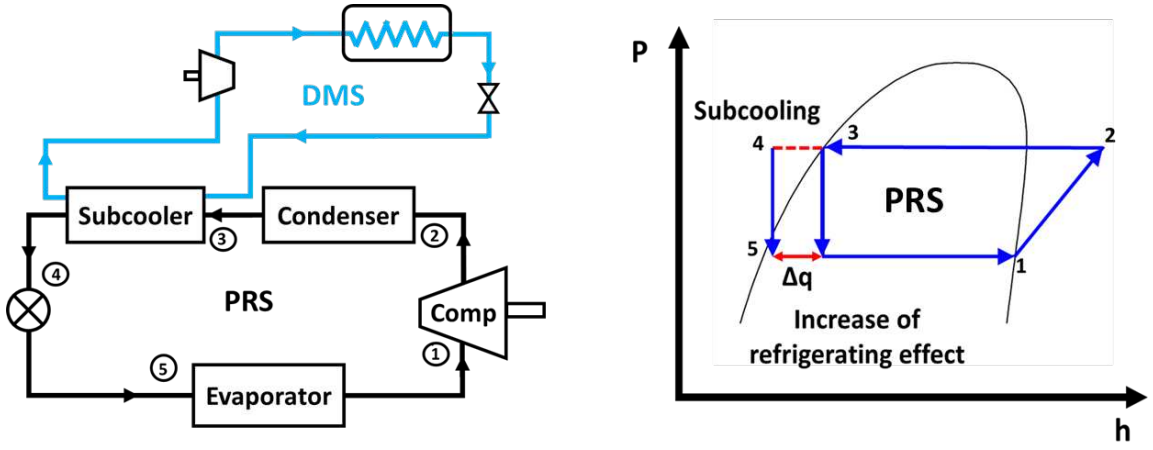

Figure 2.16 Schematic diagram of dedicated mechanical subcooling and p-h diagram illustrating the impact of dedicated mechanical subcooling.

Couvillion et al. first developed a mathematical model of a dedicated mechanical subcooling system that showed an improvement of 6-80% in COP and 20-170% increase in capacity over a conventional vapor compression cycle [63]. The amount of subcooling, the thermal lift of the subcooling cycle, and the resulting performance of the overall cycle, can be directly related to the temperature of the subcooling cycle evaporator. Thornton et al. determined the optimum value of the subcooling evaporator temperature using an ideal dedicated subcooling cycle [64]. The improvement of the overall COP with subcooling was found to be 10% over a range of conditions for supermarket applications. Khan and Zubair created a thermodynamic model of a dedicated mechanical subcooler to simulate actual system performance [65]. The study found that

the performance of the main cycle was directly related to refrigerant saturation temperature. Hrnjak et al. researched the effect of condenser subcooling on the performance of a VC system, and found that the COP reaches a maximum as a result of a trade-off between increasing refrigerating effect and specific compression work [66]. The study also showed that refrigerants with large latent heats of vaporization tended to benefit less from condenser subcooling. Figure 2.17 shows the normalized COP as a function of the condenser subcooling for R1234yf, R410A, R134a and R717.

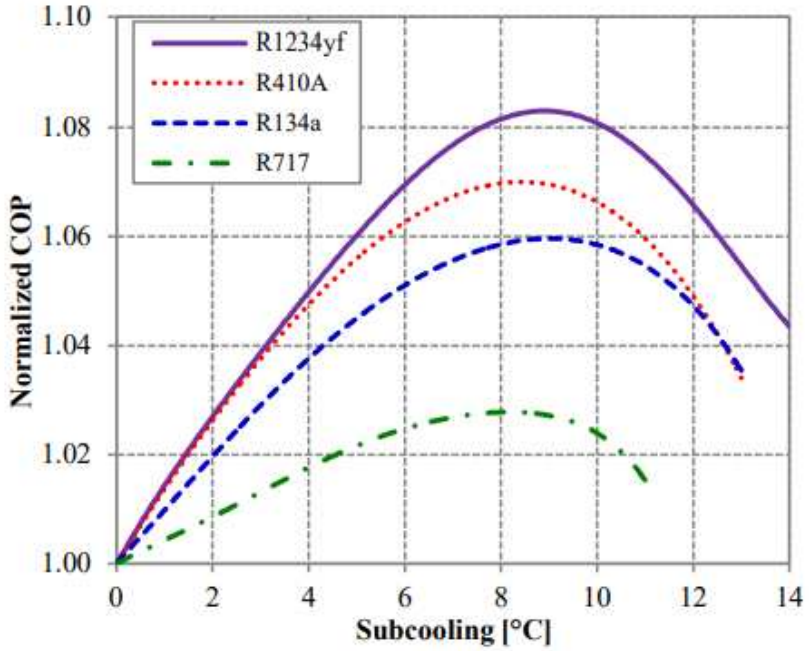

Figure 2.17 Effect of condenser subcooling on normalized COP for R717, R134a, R410A, and R1234yf at outdoor and indoor temperatures of 35°C and 27°C [66].

Qureshi and Zubair studied the effect of different refrigerant combinations on vapor compression cycles with dedicated mechanical subcooling [67]. Main cycle refrigerants that were investigated included R134a and R717, and subcooling cycle refrigerants that were investigated included R134a, R310a, R407c, R717, and R404. At equal distribution of heat exchanger area between the DMS condenser and evaporator, system performance improved most when R134a was used in both cycles, with a COP increase of 41%. When using R717 in the main cycle, and R134a in the subcooler cycle, system performance improved by a maximum of 13%. For both

R134a and R717 as main cycle fluids, R134a was the optimal subcooler cycle fluid. However, the subcooler cycle fluid had less impact on COP improvement than the distribution of heat exchanger inventory.

2.3. Research Needs for Ammonia VCRC Retrofitting

The above literature review provides a summary of the current state of research into three different technologies that are being investigated to improve the performance of the vapor compression cycle: expansion loss recovery, multi-stage cycles, and subcooling. Each technology type presented has its own advantages and drawbacks. For this study, the focus is to determine the technology that can be used for retrofitting an existing ammonia VCRC. The first technology type discussed is expansion loss recovery. Within expansion loss recovery, most research is focused on expander and ejector cycles. Expander cycle research focuses on the replacing the isenthalpic throttling valve from a standard vapor compression cycle with an isentropic expansion device. Ejector cycles improve the performance of the vapor compression cycle in the same way as expander cycles: by reducing compressor work and increasing cooling capacity. The second technology type discussed is multi-stage cycles. Within multi-stage cycle research, most efforts have focused on refrigerant injection cycles and saturation cycles. For both cycles, performance is improved by using refrigerant at the condenser outlet to provide cooling to the refrigerant stream at the compressor discharge. The third technology type discussed is subcooling cycles. Subcooling cycles improve the performance of the traditional VCRC by providing supplemental cooling to the VCRC at the condenser outlet, causing the VCRC refrigerant to enter the evaporator at a lower quality, increasing overall refrigeration capacity. Subcooling research is primarily focused on the use of a SLHX, or an auxiliary cooling system in the form of either an integrated or dedicated mechanical subcooled.

Although the advanced VCRC technologies listed above have distinct advantages, many of them have fundamental weaknesses which limit their implementation in ammonia VCRCs including:

- Several technologies present challenging retrofit scenarios including ejector cycles, multi-stage cycles, and integrated mechanical subcooling. Installing these systems with existing PRS systems would likely be too invasive to be practical.
- Ejectors, multi-stage, and dedicated mechanical subcooling suffer from high capital costs which limit their implementation.
- Minimal COP improvement is shown for expander and suction line heat exchangers. Although these two technologies have simple retrofit capacity and low capital costs, they provide little performance incentive for successful installation on ammonia refrigeration systems.
- Additional electrical input for integrated and dedicated mechanical subcooling limits their performance and can decrease performance in certain scenarios.

Table 2.1 compares these technologies over a range of categories like the bulleted list above. Based on the analysis of all ammonia VCRC improvement options, three solutions provide significantly higher performance as compared with the others: ejector cycles, saturation cycles, and dedicated mechanical subcooling. The primary drawback associated with ejector and saturation cycles is retrofit complexity. For both technologies, major alterations would be required to retrofit an existing VCRC with these technologies. Comparatively, the complexity of retrofitting an existing VCRC with a dedicated mechanical subcooler would be relatively low, while still providing similar levels of COP improvement. The primary limitation of mechanical subcooling

systems is that additional compressor work is required to provide subcooling. For this reason, COP improvement is limited, and can worsen if too much subcooling is provided.

Table 2.1 Comparison of vapor compression technologies used to retrofit an ammonia refrigeration system.

Technology Type		Additional Electricity Input	Technological Status	Retrofit Complexity	Capital Cost	Ammonia Cycle COP improvement
Expansion Loss Recovery Cycles	Expander cycle	None	Research Stage	Low	Medium	0-10% [37]
	Ejector Cycle	None	Research Stage	High	High	12% [22]
Multi-Stage Cycles	Vapor/Liquid Injection Cycle	None	Research Stage	High	High	10% (R410a) [46]
	Saturation Cycle	None	Research Stage	High	High	42.4% (R410a) [44]
Subcooling Cycles	Suction Line Heat Exchanger	None	Commercialized	Medium	Low	0% [48,49]
	Integrated Mechanical Subcooling	High	Research Stage	High	Medium	7.5% (R134a) [61]
	Dedicated Mechanical Subcooling	High	Research Stage	Low	High	13% [67]

2.3.1. Waste Heat Driven Subcooling

One idea, which has received little attention within the field of subcooling research, is the use of a thermally driven cooling technology to provide mechanical subcooling. Thermally driven cooling systems are a type of waste heat recovery technology that uses waste heat to produce cooling and requires little to no electrical work input. While the COP improvement of the traditional mechanical subcooling techniques comes as a tradeoff with additional compressor work, a thermally driven subcooler is bound only by waste heat availability.

There are four primary types of heat driven cooling systems: absorption, adsorption, ejector, and organic Rankine-vapor compression (ORVC). Although absorption and adsorption

systems are mature and commercially available technologies, they tend to suffer from operation challenges including crystallization and also have high initial costs and large footprints [68,69]. ORVC and ejector systems both have advantages over absorption and adsorption because they are smaller and less complex, however both technologies are less technologically mature. Ejector systems also suffer from low COPs (between 0.2 and 0.4) due to ejector irreversibility's, and typically do not perform well at off-design conditions due to ejector geometric constraints [70]. ORVC systems can have higher COPs comparable to absorption while having easier operation and the capability to be smaller.

The thermally activated cooling technology that will be considered in this work is a turbo-compression cooling system. A basic process flow diagram of a TCCS providing subcooling to a primary refrigeration system is shown in Figure 2.18. The TCCS is a type of ORVC, where a highly efficient centrifugal turbo-compressor directly couples the organic Rankine power cycle and vapor compression refrigeration cycle. The turbo-compression cooling system is a relatively new technology but shows much promise [71–75]. Garland et al. established that the primary benefits of the TCCS compared to other thermally driven cooling technologies are as follows [76]:

- The TCCS has minimal complexity, moderate to low working pressures, and no corrosive working fluids. The selection of working fluids also allows the system to avoid crystallization issues that can affect absorption systems.
- The temperature range of the TCCS is better than absorption, allowing the system to operate over high temperature waste heat streams without additional components.
- The TCCS has simpler operation during start-up and transient conditions which is a distinct advantage over other heat activated cooling technologies that suffer from long startup times and require operation at a constant load.

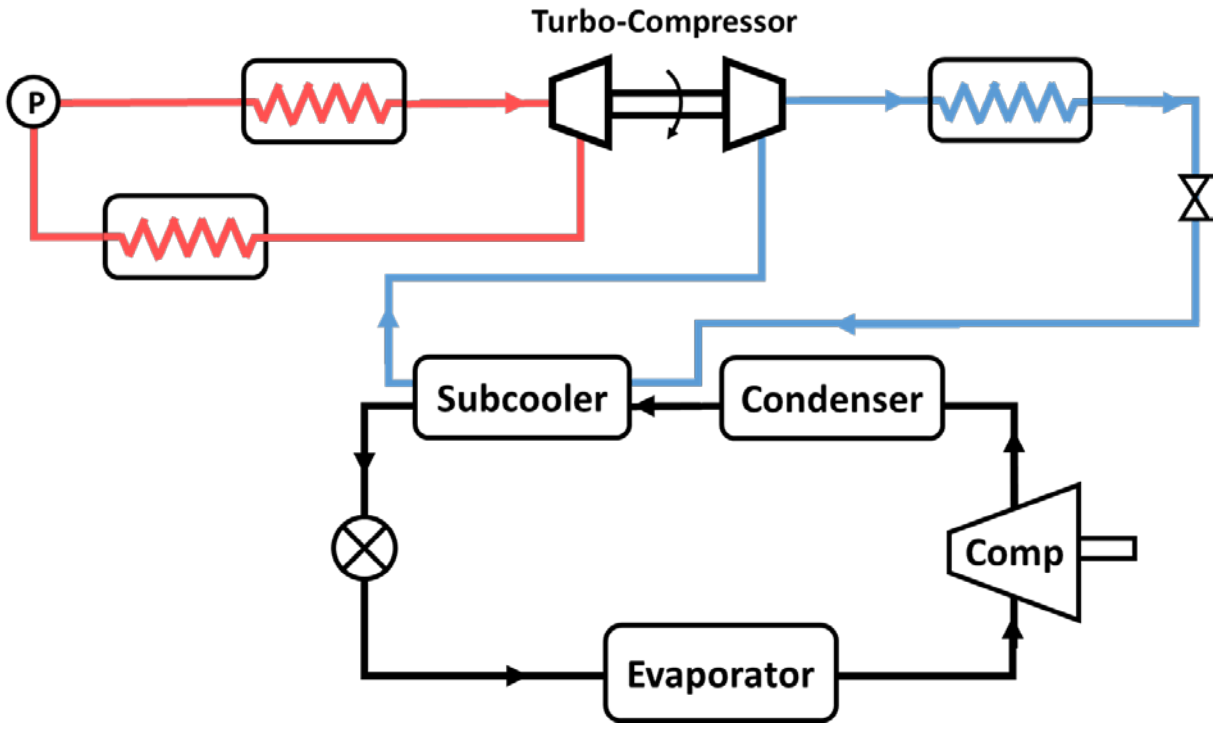

Figure 2.18 Process flow diagram of a TCCS providing mechanical subcooling to a primary refrigeration system.

2.4. Focus of Current Investigation

The current research seeks to model the integration of a waste heat driven TCCS used to provide condenser subcooling to a PRS at a beef processing facility. The TCCS is advantageous over other waste heat driven cooling technologies due to minimal complexity, and high flexibility, as noted in section 2.3.1. The TCCS is advantageous over the traditional, dedicated mechanical subcooling technique because very little electrical work input is required for the system, which is the primary limitation of the DMS. In this study, several key components of a beef processing facility, as well as the TCCS, are modeled to evaluate the thermodynamic performance and economics of the TCCS. To validate the use of a thermally driven cooling technology as a subcooler, TCCS savings are compared to the savings produced by a similarly sized, electrically powered DMS. To further validate the use of the TCCS, two other waste heat driven technologies

that would produce energy savings at a plant are modeled: a feedwater economizer, and an ORC. A feedwater economizer would provide savings by recovering heat from the boiler exhaust gas to preheat the water that enters the boiler, resulting in a reduction in boiler natural gas consumption. An ORC would produce savings by recovering heat from the boiler exhaust gas to generate power, reducing plant electricity consumption. The TCCS, ORC, and DMS are configured to provide further energy savings by rejecting heat from the cycle condensers directly to the feedwater entering a beef plants water boiler, resulting in a reduction in boiler natural gas consumption.

The following chapter will fully describe the modeling process used to determine the technoeconomic performance of the TCCS, ORC, DMS, and FWE implemented at a beef processing facility. Starting with the baseline plant model, the plant refrigeration and boiler system will be evaluated to estimate baseline refrigeration energy requirements and boiler performance. Then, the thermodynamic models of the four technology options will be outlined, which determine the energy savings that each technology produces. Then, the heat transfer model will be presented, which determines the heat exchanger performance, size for the ORC, DMS and TCCS. Next, the economic model will be discussed, which determines the annual savings, capital cost, payback period, and net present value of each technology. Finally, the system optimization study will be presented, which investigates the tradeoff between system size, performance, and economics. The goal of the optimization study is to vary heat exchanger effectiveness until a maximum net present value and a minimum payback period is achieved.

CHAPTER 3. Modeling Approach

As discussed in the previous chapter, the TCCS could be used to provide subcooling to a PRS in the same way as the DMS. The TCCS is a system that has shown distinct benefits over other thermally driven cooling technologies – specifically regarding complexity and flexibility. For applications where waste heat is available, such as at a meat processing plants, the TCCS technology could provide performance benefits over a traditional DMS due to the lack of electricity input. In this chapter, the modeling approach is presented to determine the thermodynamic performance and economics of four different technologies used to reduce energy use at a beef processing facility. First, a model overview is presented describing the raw data used, as well as the flow of data inputs and outputs through each sub model. The distinct thermodynamic models of this study are as follows: a beef plant refrigeration model, a beef plant boiler model, as well as four models that evaluate the performance of a FWE, ORC, DMS, and TCCS. All thermodynamic modeling for this study is performed using Engineering Equation Solver (EES). A complete sample calculation for the plant refrigeration system, boiler system, TCCS thermodynamics, heat transfer, and capital cost is shown in Appendix A. Results from the thermodynamic and heat transfer models of each of the four technology models are fed into an economic model to evaluate annual savings, capital cost, payback period, and net present value of each technology. In the final section of this chapter, an optimization process is presented, which investigates optimal system size of the TCCS, DMS, and ORC to minimize payback period and maximize NPV.

3.1. Model Overview

There are several data inputs utilized in this study to model the use of energy at a beef processing facilitiy: Heat exchanger geometry, thermodynamic assumptions, TMY3 weather data, average daily cattle capacity, utility consumption, and utility prices. Figure 3.1 shows how these data inputs are propagated through the thermodynamic model to determine the annual savings of each of the four technologies considered in this research. Once annual savings of each technology is determined, these results are fed into the heat transfer and economic models, which are discussed in the latter sections of this chapter.

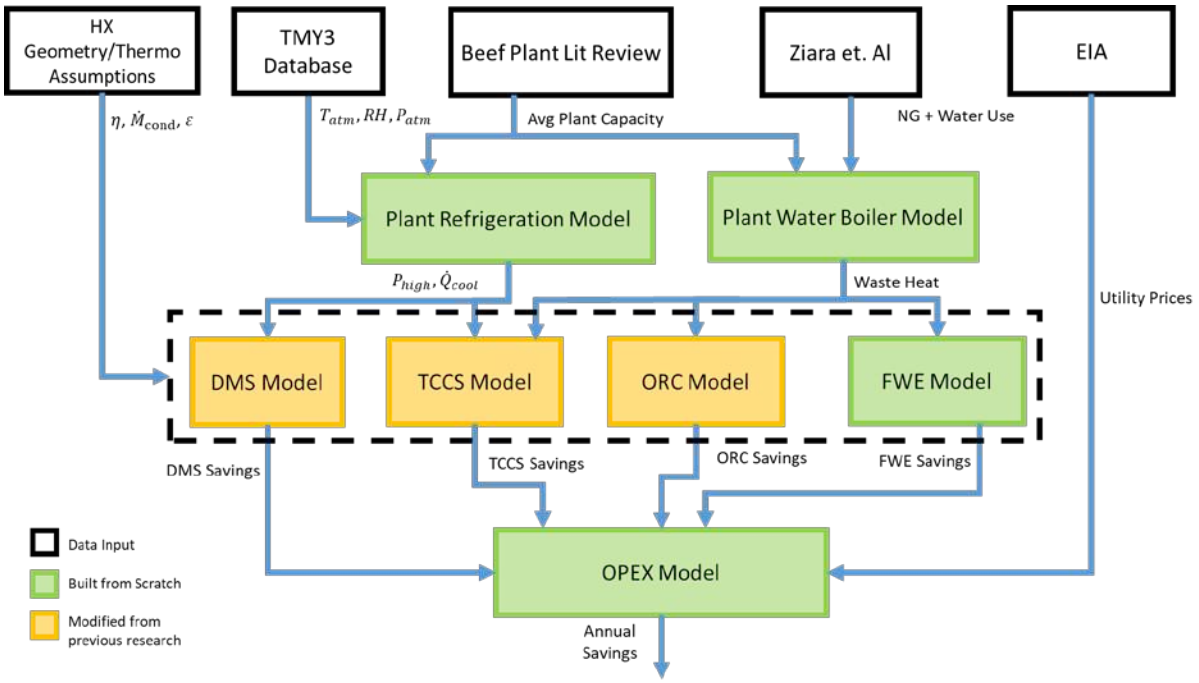

Figure 3.1 Illustration of the flow of data through the beef plant refrigeration subcooling model. Data inputs are shown in black boxes, models built from scratch are shown in green boxes, and models modified from previous research are shown in yellow boxes.

Heat exchanger geometry inputs and thermodynamic assumptions are the first model input, which are used to estimate the performance of each of the four technologies. Several assumptions are also made to model the plant refrigeration and boiler systems, which will be discussed in the Section 3.2.1 and Section 3.2.2. The next model input is hourly weather data which is used to

characterize the yearly variation in performance of a beef plant refrigeration system. Weather inputs include dry air temperature, ambient pressure, and relative humidity which are gathered from the TMY3 database for five different cities in the United States: Denver, Green Bay, Fresno, Atlanta, and Grand Island. These five cities were selected as locations for the plants in this study due to their varying ambient conditions, utility costs, and because they are in states that are top livestock producers. The average daily cattle capacity for the plants modeled in this study is assumed to be 3200 head/day [77–79]. This value is used to estimate the overall refrigeration load, waste heat availability, and condenser water flow rate. The next model input is utility consumption data collected by Ziara et al. which includes daily natural gas consumption at a beef plant, and hourly water use trends [80] which are used specifically as inputs to the plant boiler model. Finally, EIA monthly natural gas and electricity price data for 2019 is used to evaluate economic savings produced by each technology [81,82]. Economic savings results are described in terms of annual savings (or OPEX), which are determined by summing the hourly natural gas and electricity savings produced by each technology. OPEX is the primary result of the thermodynamic modeling and is one of the main inputs for the economic model. A flow diagram of the economic and heat transfer model is shown in Figure 3.2.

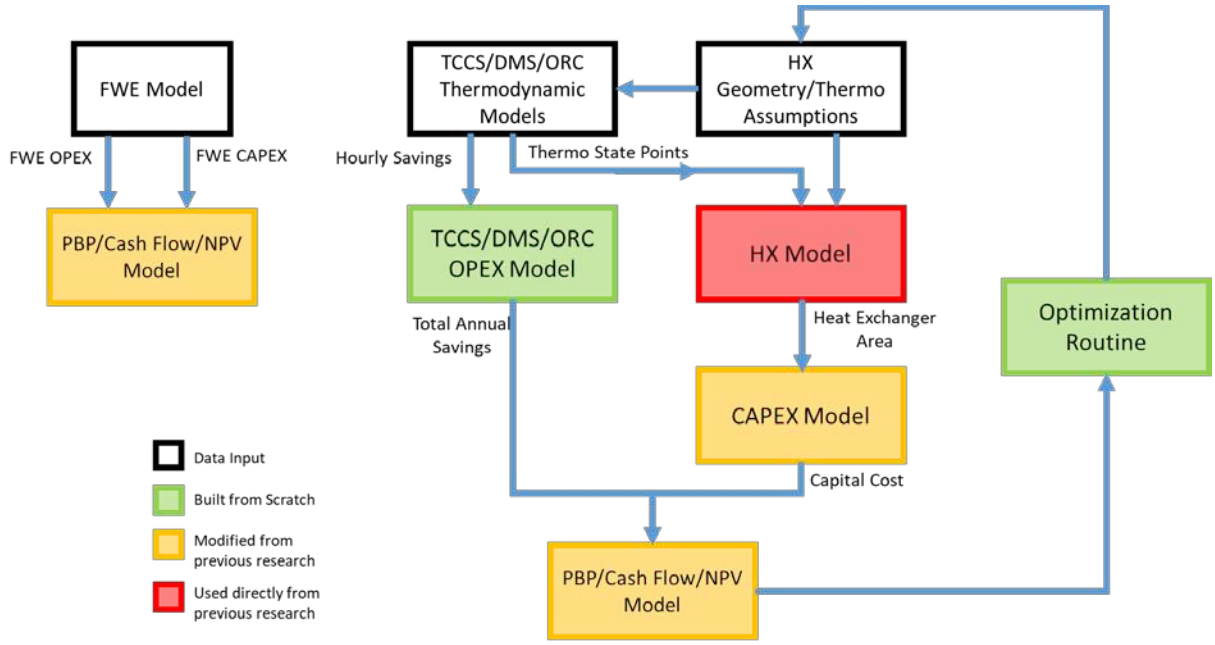

Figure 3.2 Illustration of the flow of data through the heat transfer and economic model, color coded to describe data inputs, models built from scratch, models that were modified from prior research, and models that were used directly from prior research.

The primary inputs for the heat transfer and economic models are the performance results from the thermodynamic models, as well as some additional assumptions that are made regarding the heat transfer properties and geometry of each system. For each technology, annual savings and total system cost are used to calculate payback period, cash flow, and net present value. Once these economic parameters were determined, heat exchanger effectiveness inputs were varied to assess optimal system size to minimize payback period and maximize net present value. The total cost of each system was determined by summing the costs of each individual component in the CAPEX model. Heat exchanger costs were determined based on the heat transfer model which uses empirical correlations to calculate heat transfer coefficients through each region of all the heat exchangers. Then, the overall heat transfer coefficient was used to calculate the total heat exchanger area of each heat exchanger in the system. The cost of all other components in the

system were calculated using high fidelity cost models. In the next section the thermodynamic model of this study will be discussed in detail.

3.2. Thermodynamic Modeling

In the following subsections, the thermodynamic models will be described for each of the systems considered in this study. The first two sections will be used describe the model of the primary refrigeration system (PRS) and the boiler system at a beef processing facility. The goal of these models is to assess baseline energy use as well as waste heat availability at a plant generic plant processing 3200 head of cattle per day, located in five different cities with varying ambient weather conditions. Then, the models of four distinct technologies will be described, which could be installed at a beef plant to reduce electricity and natural gas consumption, resulting in economic savings. These technologies include a feedwater economizer, an organic Rankine cycle, a dedicated mechanical subcooler, and a turbo-compression cooling system.

3.2.1. Beef Plant Refrigeration Model

The refrigerant system modeling effort is divided into two sections: determining the initial baseline performance of the PRS, then determining the performance of the PRS with TCCS or DMS subcooling options. The PRS is a standard ammonia VCRC with a reciprocating type compressor and a condenser which is coupled to a wet cooling tower. The inputs for the model are hourly ambient temperature, pressure, and relative humidity from the TMY3 database. TMY, which stands for typical meteorological year, is a collation of selected weather data for a specific location, listing hourly values for a one year period. TMY3, which is the third iteration of the TMY dataset, reflects weather in 1020 locations in the USA, and is derived from a weather dataset spanning 1976-2005. The hourly values in the one year period are specially selected to represent a range of weather phenomena for the location in question, while still giving annual averages that

are consistent with the long term averages. Average monthly dry air temperature, wet bulb temperature, relative humidity, and atmospheric pressure for each city is shown in Figure 3.3a-d.

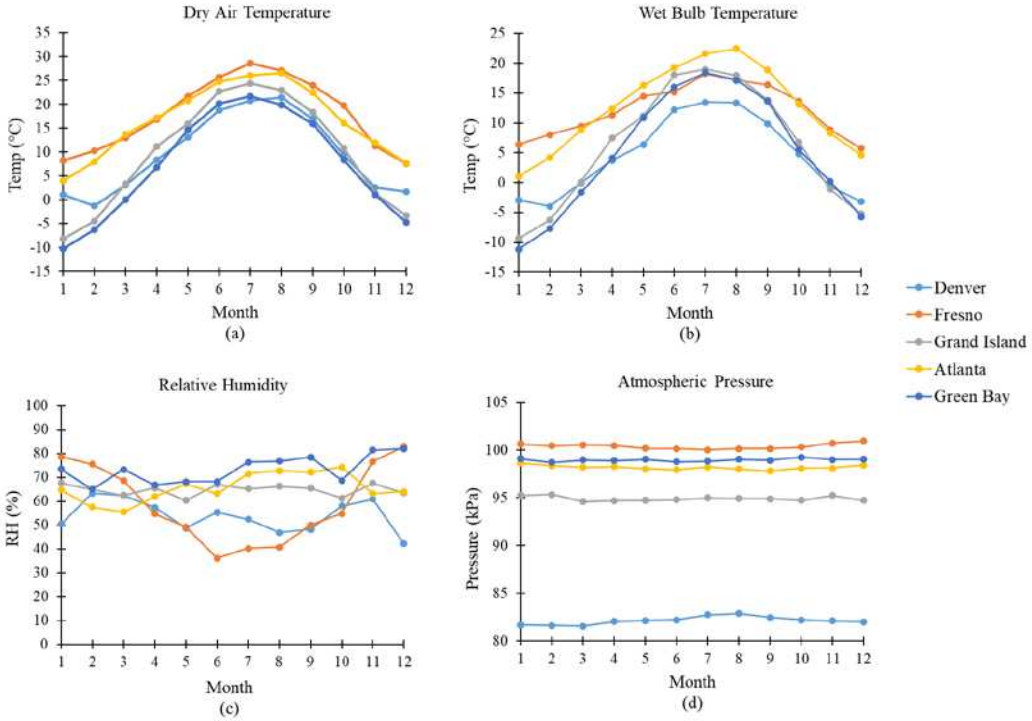

Figure 3.3 Monthly average weather for each city. Dry air temperature (a), wet bulb temperature (b), relative humidity (c), and atmospheric pressure (d) [83].

In all five cities, dry bulb temperature (Figure 3.3a) increases from January to June, peaks during July and August, then decreases steadily until December. Of the five cities, Fresno and Atlanta are the warmest, with average dry air temperatures of 17.9°C and 16.6°C, respectively. In comparison, Denver, Grand Island, and Green Bay are significantly colder with average dry air temperatures of 9.7°C, 9.6°C, and 7.3°C, respectively. Due to extreme cold temperatures achieved in the winter months, Green Bay and Grand Island have the greatest variation in dry bulb temperature, with average monthly temperatures ranging -10.2°C-21.7°C, and -8.1°C-24.4°C, respectively. Atmospheric pressure (Figure 3.3d) varied the least of any weather metric and varies between the cities as a function of city elevation. Relative humidity (Figure 3.3c) shows no

seasonal trend except for in Fresno, where humidity decreases significantly during the summer months. Fresno also experiences the greatest variation in humidity, with average monthly humidity ranging from 36.2% in June to 82.9% in December. The most humid city was found to be Green Bay, with an average annual relative humidity of 73.2%. The least humid city was found to be Denver, with an average relative humidity of 53.8%. Wet Bulb temperature (shown in Figure 3.3b) is a measure of the amount of water vapor that can be held in the air based on ambient air pressure, relative humidity, and temperature. Looking at the five cities, Denver was found to have the lowest average annual wet bulb temperature of 4.5°C. Atlanta was found to have the highest average annual wet bulb temperature of 12.7°C. In a cooling tower application, the wet bulb temperature is the lowest temperature that water can be cooled to via evaporation, making it a useful metric to predict the performance of a cooling system. The beef plant refrigeration model is described by the schematic and T-S diagram shown in Figure 3.4.

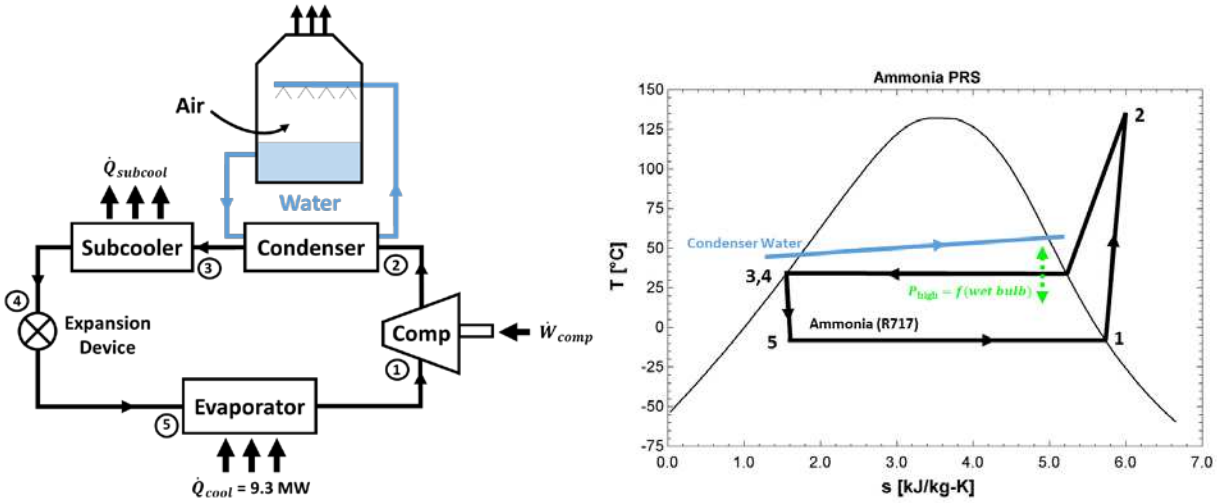

Figure 3.4 Schematic and T-S diagram of a beef plant refrigeration system with condenser cooling tower.

At lower wet bulb temperatures, cooling systems are able to perform more efficiently because cooling tower water can be cooled to a lower temperature, allowing for a lower ammonia

condenser temperatures which reduce the required compressor power of the PRS and increases the COP of the ammonia system [84]. The assumptions made for the beef plant refrigeration model are shown in Table 3.1.

Table 3.1 Assumptions made for baseline cooling tower and refrigeration model.

MODEL		Assumption	Value
Working Fluids		Refrigerant	R717
		Condensing/Evaporating Fluid	Water
		Cooling Tower Fluid	Air-H2O
		Evaporator Fluid	Water
VCRC	Evaporator	Low Side Pressure	322 kPa
		$T_{\mathrm{w,in}}$	10.4 °C
		$T_{\mathrm{w,out}}$	6.7 °C
		$\varepsilon_{\mathrm{tp}}$	0.21
		$\dot{Q}_{\mathrm{cool}}$	9.3 MW
	Compressor	η_{comp}	65%
	Condenser	$\Delta \mathrm{T}_{\mathrm{cond,w}}$	5.56 °C
		$\varepsilon_{\mathrm{tp}}$	0.31
Cooling Tower		$\varepsilon_{\mathrm{ct}}$	0.65 [84]
		Air Flow	650,000 CFM

The working fluid for the refrigeration model is ammonia, which rejects heat to water in the condenser, and provides refrigeration with the evaporator. The evaporator pressure is set constant at 322 kPa (approximately 32 PSIG). In the model, the plant cooling load is represented by a stream of water which is cooled by ammonia in the evaporator from 10.6°C to 6.7°C. Water in the condenser is cooled by wet air in the condenser cooling tower. The inlet and outlet temperature of water are not set, but rather, determined based on ambient weather conditions. The range of the cooling tower, which is the temperature difference between water entering the tower and leaving the tower is set to 5.56°C, or 10°F, which is based on standard design conditions developed by the Cooling Tower Institute (CTI) [85]. The air flow rate through the tower is set to 650,000 CFM [86], and the cooling tower effectiveness is set to 65%. The overall cooling load of

the ammonia system is set to 9.3 MW, which is constant for all hours of the year. The overall cooling load was calculated from compressor electricity data collected at a beef processing plant and an assumed COP of an ammonia refrigeration system found in the literature [87]. Compressor electricity data from a real beef plant, collected by Ziara et al., is plotted in Figure 3.5 [80].

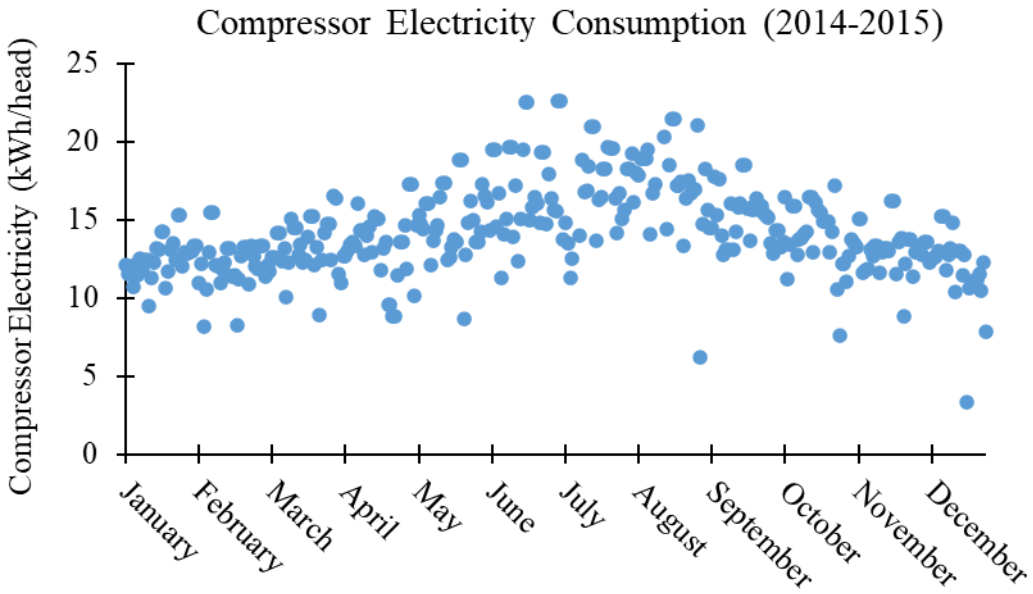

Figure 3.5 PRS compressor electricity throughout the year at a beef processing facility [80].

From Figure 3.5, the average compressor electricity requirement is 14.5 kWh/head. Assuming an ammonia PRS COP of 4.8, and 3200 head of cattle processed per day, the constant overall cooling load of 9300 kW is calculated. Although the cooling load likely fluctuates depending on plant activity, it was set constant in the model to more clearly illustrate the impact that ambient weather has on refrigeration performance. Furthermore, it is assumed that there is no subcooling in the condenser and no superheating in the evaporator to understand the impact of subcooling more clearly. Ambient weather impacts the cycle performance because, as temperature and humidity increase, the condenser saturation pressure must increase which also increase cycle pressure ratio, and thus more compressor power is required.

The thermodynamic state points, heat duties, and work inputs, for the refrigeration system are determined from energy balance calculations based on the fixed inputs and ambient weather conditions. The performance of the PRS was simulated for every hour of the year in each city using Engineering Equation Solver (EES). To describe the baseline PRS with no condenser subcooling, the heat duty of the evaporator is calculated as shown in Equation (3.1) through Equation (3.3), where $\dot{Q}_{\mathrm{cool}}$ is the fixed cooling load of 9.3 MW.

$$\dot{Q}_{\mathrm{cool}} = \dot{m}_{\mathrm{r}} * (h_1 - h_5) \tag{3.1}$$

$$\dot{Q}_{\mathrm{cool}} = \dot{m}_{\mathrm{w}} * C_{\mathrm{p}} * (T_{\mathrm{w,in}} - T_{\mathrm{w,out}}) \tag{3.2}$$

$$\dot{Q}_{\mathrm{cool}} = \varepsilon_{\mathrm{tp}} * \ C_{\mathrm{min}} * (T_{\mathrm{w,in}} - T_5) \tag{3.3}$$

Equation (3.1) describes heat transfer on the refrigerant side of the evaporator, where $\dot{m}_{\mathrm{r}}$ is mass flow rate of ammonia through the PRS, $h_1$is the enthalpy of ammonia leaving the evaporator as a saturated vapor, and h_5 is the enthalpy of the two-phase ammonia exiting the isenthalpic expansion valve and entering the evaporator. Equation (3.2) describes heat transfer on the external stream side of the evaporator, where $\dot{m}_{\mathrm{w}}$ is the mass flow rate of water being chilled, C_{p} is the specific heat of water, and $(T_{\mathrm{w,in}} - T_{\mathrm{w,out}})$ is the change in chilled water temperature as it goes through the evaporator. Equation (3.3) describes the heat transfer efficiency of the PRS evaporator, where $\varepsilon_{\mathrm{tp}}$ is the assumed effectiveness of the two-phase region of the evaporator, and C_{min} is the minimum heat capacity rate, which is the product of mass flow rate and specific heat of chilled water. Once ammonia has been vaporized in the evaporator, it enters the compressor of the PRS. PRS compressor work is evaluated as shown in Equation (3.4)-(3.5).

$$\dot{W}_{\text{comp}} = \dot{M}_{\text{r}} * (h_2 - h_1) \tag{3.4}$$

$$\eta_{\text{comp}} = \frac{h_{2\text{s}} - h_1}{h_2 - h_1} \tag{3.5}$$

In Equation (3.4), $\dot{W}_{\text{comp}}$ is the PRS compressor work input, and h_2 is the enthalpy of the superheated ammonia at the compressor outlet. In Equation (3.5), η_{comp} is the assumed isentropic efficiency of the compressor, and $h_{2\text{s}}$ is the enthalpy of ammonia at the compressor outlet assuming constant entropy. Ammonia leaves the compressor as a superheated vapor and then enters the condenser where it is cooled to a saturated liquid. In the thermodynamic model, the condenser is split into two distinct regions: superheated and two-phase, where heat transfer in each region is described using Equation (3.6)-(3.8).

$$\dot{Q} = \dot{m}_{\text{r}} * (h_{\text{r,in}} - h_{\text{r,out}}) \tag{3.6}$$

$$\dot{Q} = \dot{m}_{\text{ext}} * C_{\text{p}} * (T_{\text{ext,in}} - T_{\text{ext,out}}) \tag{3.7}$$

$$\dot{Q} = \varepsilon * C_{\text{min}} * (T_{\text{hot,in}} - T_{\text{cold,in}}) \tag{3.8}$$

Once heat duty has been evaluated in both the superheated and two-phase region of the PRS condenser, total condenser heat duty is calculated as shown in Equation (3.9).

$$\dot{Q}_{\text{cond}} = \dot{Q}_{\text{cond,sh}} + \dot{Q}_{\text{cond,tp}} \tag{3.9}$$

In the baseline model, it is assumed that no condenser subcooling occurs and the ammonia refrigerant enters the expansion device as a saturated liquid. Using Equation (3.1)-(3.9), the thermodynamic performance of the VCRC portion of the PRS is fully defined. However, to account for the impact of ambient weather conditions, several additional thermodynamic equations are required to describe the performance of the condenser cooling tower. The ammonia stream of the PRS is condensed by rejecting heat to water circulating through the cooling tower. To describe the cooling tower, hot water from the condenser enters at the top of the cooling tower as a spray

and flows downward. Fans draw ambient air into the tower, and the air flows in counterflow with the water. As water and air come into contact, a small amount of water is evaporated, transferring heat from the downward moving water to the upward moving air. Cooled water then exits at the bottom of the tower where it is sent back to the condenser to repeat the loop. To model the cooling tower, the maximum energy transfer is defined, which occurs when the air leaving the tower is saturated at the water inlet temperature as shown in Equation (3.10):

$$\dot{Q}_{\mathrm{ct,max}} = \dot{M}_{\mathrm{a}} * (h_{\mathrm{a,sat,in}} - h_{\mathrm{a,in}}) \tag{3.10}$$

Where $\dot{Q}_{\mathrm{ct,max}}$ is the maximum energy transfer, $\dot{M}_{\mathrm{a}}$ is the mass flow rate of air through the tower, $h_{\mathrm{a,sat,in}}$ is the enthalpy of air at the tower water inlet temperature, and $h_{\mathrm{a,in}}$ is the actual inlet enthalpy of the air [84]. Then, using the assumed cooling tower effectiveness in Table 3.1, the energy transfer rate of the cooling tower is calculated as shown in Equation (3.11):

$$\dot{Q}_{\mathrm{ct}} = \varepsilon * \dot{M}_{\mathrm{a}} * (h_{\mathrm{a,sat,in}} - h_{\mathrm{a,in}}) \tag{3.11}$$

With Equation (3.10) and (3.11), as well as the assumption of no heat loss between the condenser and cooling tower ($\dot{Q}_{\mathrm{ct}} = \dot{Q}_{\mathrm{cond}}$), the model is able to determine an appropriate condenser refrigerant pressure based on ambient weather conditions for each hour of the year. After determining cooling tower performance, the state points in the system are solved for and the COP is calculated as shown in Equation (3.12).

$$COP_{\mathrm{prs}} = \frac{\dot{Q}_{\mathrm{cool}}}{\dot{W}_{\mathrm{comp}}} \tag{3.12}$$

Figure 3.6a-d shows the results from the baseline model for each city, averaged monthly. The baseline refrigeration model results are expected, considering the correlation between wet bulb temperature (Figure 3.3b) and system performance. Considering the evaporative cooling model, the wet bulb temperature is the lowest temperature that water can be cooled to as it

circulates through the tower. Therefore, as wet bulb temperature increases, water temperature through the tower (Figure 3.6c) increases, so the refrigerant saturation temperature and pressure (Figure 3.6a) must increase which drives an increase in compressor work, resulting in a reduction in system performance (Figure 3.6d).

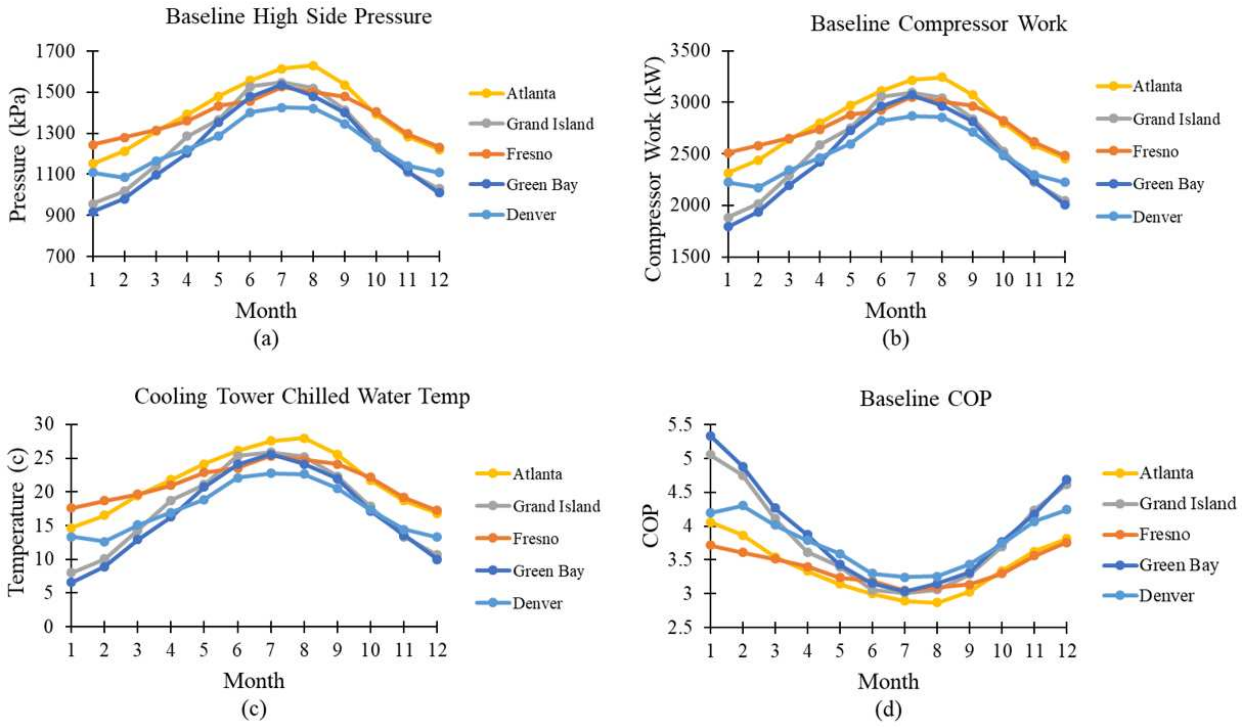

Figure 3.6 Baseline refrigeration model results for each city averaged by month. High side pressure (a), compressor work (b), cooling tower chilled water temperature (c), and COP (d).

To give a few examples of performance variation, the PRS was found to perform the worst in Atlanta in the month of August. The average wet bulb temperature for the month of August in the city of Atlanta is 22.5°C, which is the greatest wet bulb temperature of any month in any city. At this wet bulb temperature, cooling tower water is provided to the PRS condenser at an average temperature of 30°C. To provide adequate condensing when water is delivered at 30°C, the PRS must operate at a condenser saturation temperature of 41.7°C, and saturation pressure of 1630 kPa. To compress the refrigerant to the condenser saturation pressure, 3250 kW of work input are required, so the COP of the PRS is 2.86. The highest monthly average performance occurred in

Green bay in the month of January. The average wet bulb temperature for the month of January in Green bay is -11.1°C, which is the lowest wet bulb temperature of any month in any city. At this wet bulb temperature, cooling tower water is provided to the PRS at an average temperature of 6.57°C, allowing for a condenser saturation temperature and pressure of 22°C, and 919 kPa, respectively. At such a low condenser pressure, only 1790 kW of work input are required to power the compressor, resulting in a high COP of 5.34. This range of COP values is consistent with the literature, which document the COP of an ammonia VCRC to be 4.84 at standard operating conditions [87].

After determining baseline performance of the ammonia refrigeration system, the impact of mechanical subcooling can be evaluated. For a refrigeration system with a fixed overall cooling load, mechanical subcooling decreases the PRS mass flow rate, resulting in a decrease in compressor work. Using the state points shown in Figure 3.4, the mass flow of ammonia refrigerant in the PRS is determined using an energy balance of the evaporator as

$$\dot{M}_{\mathrm{r}} = \frac{\dot{Q}_{\mathrm{cool}}}{(h_1 - h_5)} = \frac{\dot{Q}_{\mathrm{cool}}}{(h_1 - h_4)} \tag{3.13}$$

where $\dot{Q}_{\mathrm{cool}}$ is the fixed refrigeration load, h_4 and h_5 are unknown because they are a function of the amount of subcooling, but h_4 is solved for as a function of subcooling as

$$h_4 = h_3 - \frac{\dot{Q}_{\mathrm{subcool}}}{\dot{M}_{\mathrm{r}}} \tag{3.14}$$

where $\dot{Q}_{\mathrm{subcool}}$ is the amount of heat removed by the subcooler device. Substituting Equation (3.14) into Equation (3.13) and rearranging to solve for $\dot{M}_r$, an expression is made that solves for mass flow rate of ammonia through the PRS as a function of subcooling provided:

$$\dot{M}_{\mathrm{r}} = \frac{\dot{Q}_{\mathrm{cool}} - \dot{Q}_{\mathrm{subcool}}}{(h_1 - h_3)} \tag{3.15}$$

Then, the overall work required to operate the PRS with subcooling is determined as

$$\dot{W}_{\mathrm{overall}} = \dot{M}_{\mathrm{r}}(h_2 - h_1) + \dot{W}_{\mathrm{subcooler}} \tag{3.16}$$

where $\dot{W}_{\mathrm{subcooler}}$ is the work required to operate the subcooling device, and $\dot{M}_{\mathrm{r}}$ is determined using Equation (3.16). If no subcooling is provided, then $\dot{Q}_{\mathrm{subcool}}$ and $\dot{W}_{\mathrm{subcooler}}$ are both zero. Power savings is determined by taking the difference between overall work with and without subcooling as shown in Equation (3.17).

$$Power\ Savings = \dot{W}_{\mathrm{overall,no\ subcool}} - \dot{W}_{\mathrm{overall,subcool}} \tag{3.17}$$

Depending on the subcooling device, $\dot{W}_{\mathrm{subcooler}}$ will vary. If an electrically driven DMS (shown in Figure 2.16) is used, $\dot{W}_{\mathrm{subcooler}}$ of Equation (3.16) is equivalent to the compressor work that is required to drive the subcooler cycle. If a turbo-compression cooling system is used as a subcooler (shown in Figure 2.18), $\dot{W}_{\mathrm{subcooler}}$ of Equation (3.16) is equivalent to the pump work required to drive the power cycle of the TCCS. The amount of subcooling provided by the DMS and TCCS are discussed in Section 3.2.5-3.2.6 and is based on several factors including waste heat availability, condenser water temperature and flow rate, and the high-side pressure of the ammonia PRS. In the next section the beef plant boiler model will be described in detail, which is used to calculated boiler waste heat availability and boiler feedwater flow rate.

3.2.2. Beef Plant Boiler Model

To determine the performance of a thermally driven cooling technology, it is critical to accurately estimate waste heat availability. Waste heat in the form of exhaust gas is rejected from several systems at a beef plant including natural gas boilers and furnaces. For this study, the waste heat source that will be considered is the exhaust gas rejected from the stacks of the plant boiler

system. Natural gas boilers are used at a beef plant for process water heating and steam production for the rendering process, while furnaces are primarily used for space heating. Before creating the boiler thermodynamic model, an hourly boiler natural gas dataset was created. This was done using data collected at a beef processing plant by research collaborators at the university of Nebraska Lincoln. The data collected by collaborators included total plant natural gas use for the year 2016, and the breakdown of natural gas use at the process level [80]. Figure 3.7 plots total natural gas use at a beef plant, normalized to reflect a plant processing 3200 head per day.

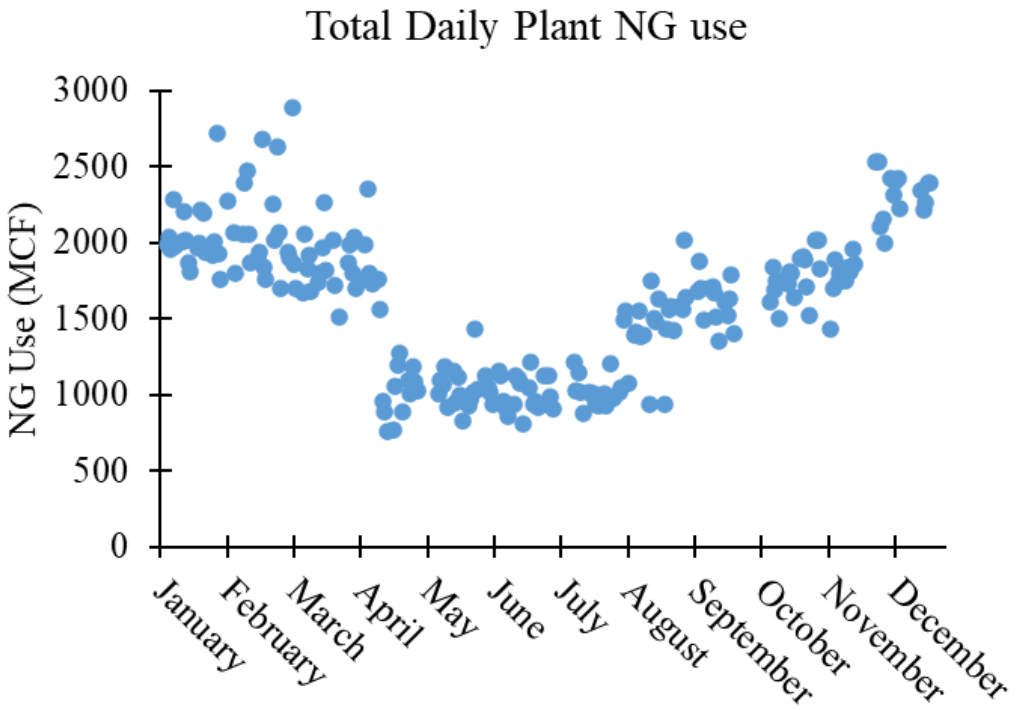

Figure 3.7 Daily natural gas consumption at a beef processing facility (3200 head/day) [80].

Along with total natural gas consumption, the end use of natural gas was also quantified. Natural gas usage at a beef plant is described in Table 3.2. As mentioned earlier, natural gas is used at a beef plant for the creation of hot water and steam (which are produced by the plant's central boiler), and to power furnaces responsible located throughout the plant for space heating.

Gas use at a plant varies throughout the year and is broken up into a summer and winter period. The highlighted rows of Table 3.2 reflect the gas usage of the central plant boiler specifically.

Table 3.2 Natural gas usage at a beef processing facility, with boiler natural gas highlighted [80].

Functions of natural gas use	Process description	Summer		Winter	
		Mbtu/head	% of total	Mbtu/head	% of total
Natural gas for heating water	Cold water	0	0.00%	0	0.00%
	90 F water	26.9	5.90%	31.4	3.80%
	110 F water	12.5	2.80%	13.8	1.70%
	140 F water	231.1	50.70%	245.5	29.40%
	Hot water	99.4	21.80%	103.7	12.40%
	Subtotal	**369.9**	**81.20%**	**394.4**	**47.30%**
Natural gas for furnaces	Fabrication	6.2	1.40%	44.7	5.40%
	Rendering	5.3	1.20%	101.3	12.20%
	Kill floor	15	3.30%	89.8	10.80%
	Maintenance area	12.5	2.70%	71.1	8.50%
	Subtotal	**39**	**8.60%**	**306.9**	**36.80%**
Natural gas for steam in rendering process	Steam for processing blood	21.7	4.80%	21.7	2.60%
Unaccounted	heat loss etc.	25.1	5.50%	110.7	13.30%

Summing the percentages of natural gas use shown in Table 3.2, 86% of natural gas use at a beef plant is used to create water and steam in the summer, while in the winter, it is only 50%. The difference in the percentages during the summer and winter is due to additional natural gas consumption during the winter months due to space heating requirements. Multiplying these percentages by the total natural gas use shown in Figure 3.7 gives an estimation of daily boiler gas use throughout the year, which is shown in Figure 3.8.

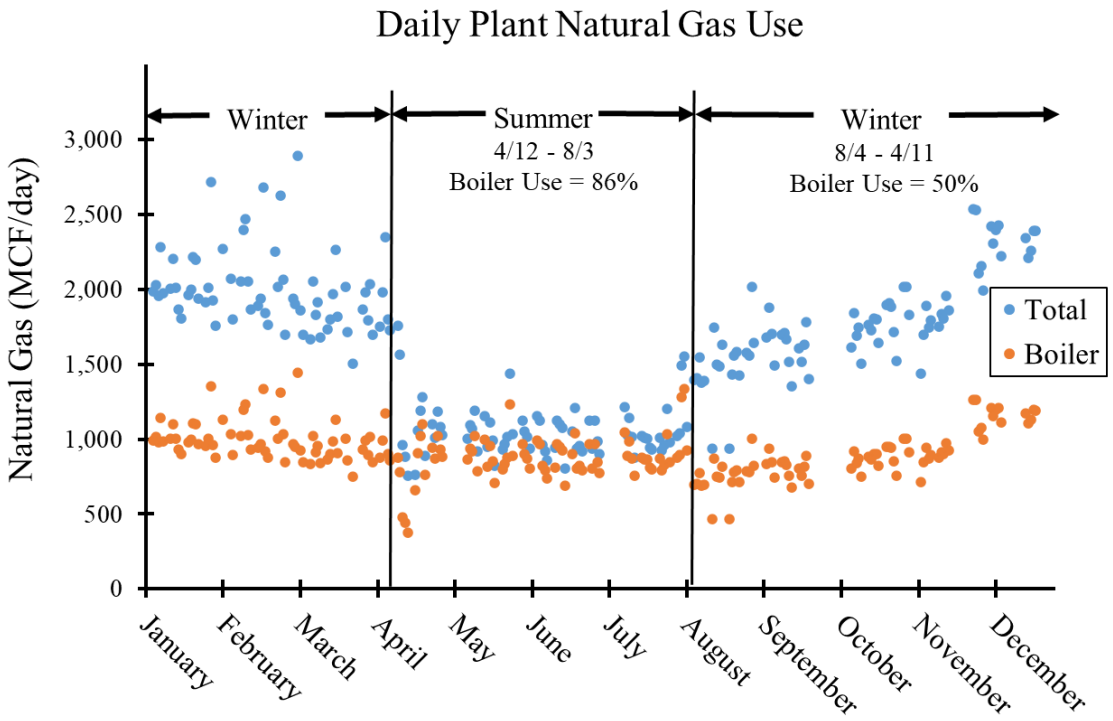

Figure 3.8 Daily natural gas consumption by the primary boilers at a beef processing facility

Considering Figure 3.8, although total plant gas use decreases significantly in the summer, boiler natural gas use remains somewhat constant throughout the year at approximately 1000 MCF/day. This makes sense considering that boiler gas use is dependent on plant operation which is continuous throughout the year. Once daily boiler natural gas use was determined, hourly boiler natural gas use was estimated based on water use trends throughout the day. Figure 3.9 shows hourly water use throughout the day at a beef plant as a percent of the total daily water use. Looking at this trend, water use decreases sharply from midnight to 6:00 am. During these hours, the plant undergoes a cleaning shift, and no cattle are processed, so water use decreases significantly.

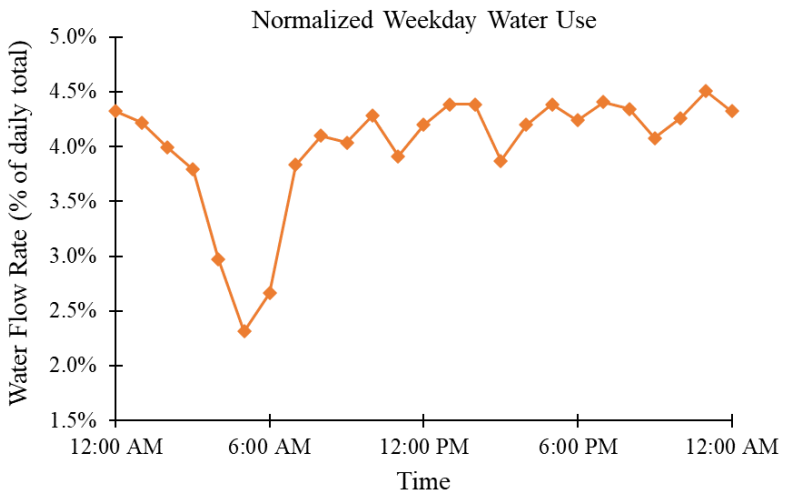

Figure 3.9 Water use trend throughout the day at a beef processing facility [80].

Assuming hourly natural gas use correlates with hourly water use, an hourly natural gas use dataset for every boiler operation hour throughout the year was produced. Figure 3.10 shows hourly boiler natural gas use throughout the year.

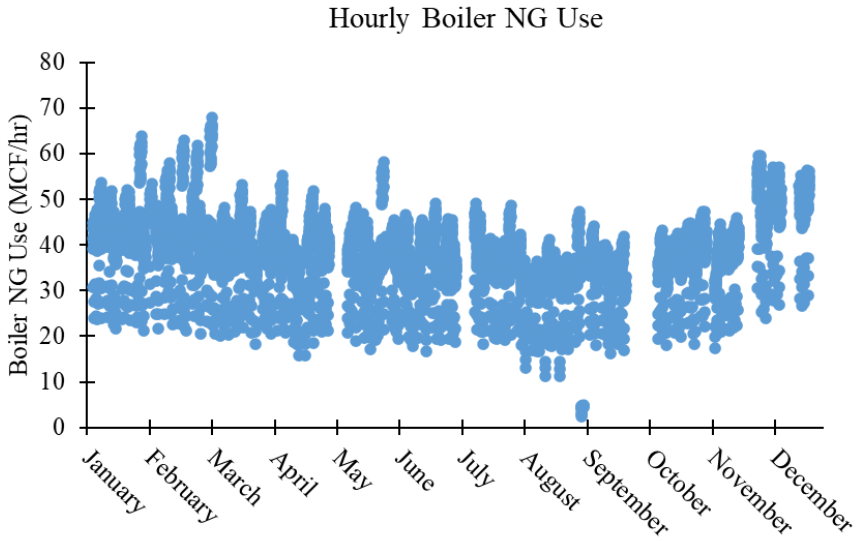

Figure 3.10 Hourly boiler natural gas use throughout the year.

Considering this, boiler natural gas use varies between 20 MCF/hr and 60 MCF/hr consistently throughout the year, depending on the hour of the day. The average hourly boiler natural gas use throughout the year was found to be 37.95 MCF/hour. With hourly boiler natural

gas use determined, the thermodynamics of the boiler can be assessed. The assumptions made for the boiler thermodynamic model are listed in Table 3.3.

Table 3.3 Assumptions made when modeling the boiler system at a beef processing facility.

Boiler Assumptions	Value
η_{boiler}	80% [88]
HHV of Natural Gas	40.6 MJ/m^3 [89]
$\%_{\text{excess air}}$	15%
$moles_{\text{air}}$	9.53
$\rho_{\text{air,stp}}$	1.189 kg/m^3
$C_{\text{p,exhaust}}$	1.93[90]
$T_{\text{exhaust,in}}$	400°F (204 °C) [91]
$T_{\text{exhaust,out}}$	250°F (121 °C) [91]
$C_{\text{p,pg}}$	4.04 kJ/kg-K
$T_{\text{pg,in}}$	87°C
$T_{\text{pg,out}}$	97°C
Operation Hours	5184 hrs/year

The waste heat recovery system is modeled as a 30% propylene glycol-water mixture loop that extracts heat from the plant exhaust gas and sends it to the TCCS or ORC (a schematic is provided in Figure A.2 of the Appendix). An intermediary loop was included in the model due to likelihood of physical constraints at a beef plant that would complicate the colocation of the waste heat technology and the plant boiler. The total thermal output of the boiler is calculated as

$$\dot{Q}_{\text{boiler}} = \dot{V}_{\text{fuel}} * HHV_{\text{fuel}} * \eta_{\text{boiler}} \tag{3.18}$$

where $\dot{V}_{\text{fuel}}$ is the volumetric flow rate of natural gas, HHV_{fuel} is the higher heating value of natural gas, and η_{boiler} is the thermal efficiency of the boiler. The waste heat available in the exhaust gas stream is calculated by assuming 15% excess air beyond a stoichiometric mixture at STP conditions (100 kPa, 20°C). Assuming the exhaust air is cooled from 400°F (204.4°C) to 250°F (121.1°C), heat recoverable in the exhaust heat exchanger is determined as

$$\dot{Q}_{\text{recoverable}} = \dot{M}_{\text{exhaust}} * C_{\text{p,exhaust}} * (T_{\text{exhaust,in}} - T_{\text{exhaust,out}}) \quad (3.19)$$

Applying this analysis to the natural gas hourly data set, hourly boiler waste heat availability is determined throughout the year at a beef processing plant as is shown in Figure 3.11.

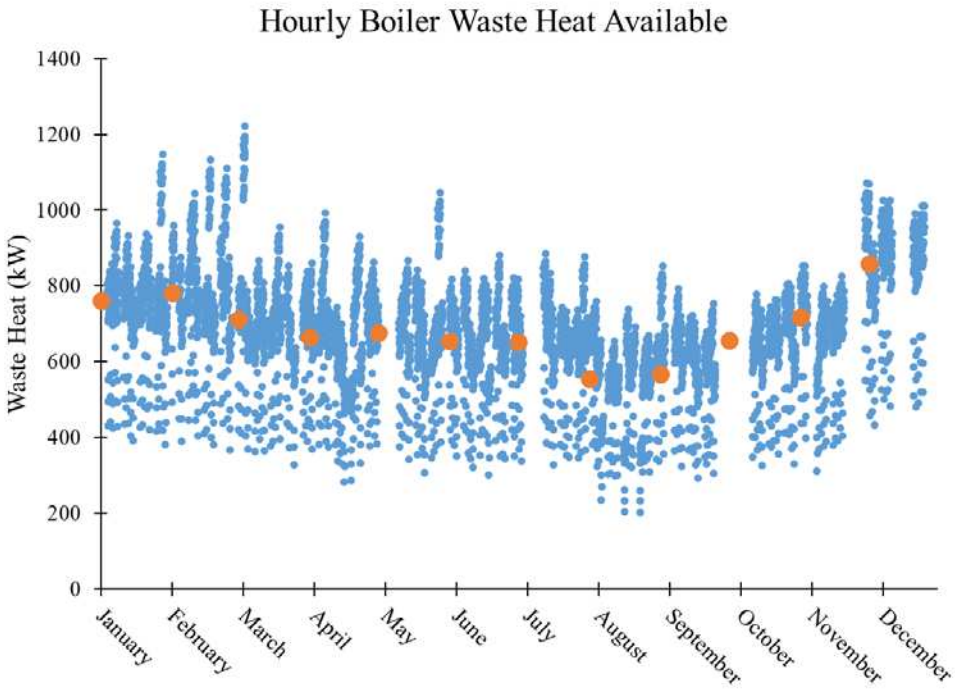

Figure 3.11 Hourly waste heat available throughout the year at a plant of capacity 3200 head/day. Monthly average waste heat values are designated with orange dots. For the TCCS model, waste heat input is assumed to be 685 kW for all operation hours.

Using this methodology, the average waste heat available throughout the year is found to be 685 kW, over 5,184 hours of operation. Although boiler waste heat is relatively constant throughout the year, there are some variations from month to month. This variation is due to the fluctuation of natural gas use and the proportion of usage in summer and winter months. Boiler waste heat also varies throughout the day and week, depending on plant activity. Assuming thermal properties of the propylene glycol mixture, the mass flow rate of the propylene glycol (PG) mixture, and the heat transfer efficiency of the exhaust air to propylene glycol heat exchanger are determined as

$$\dot{Q}_{\text{recoverable}} = \dot{M}_{\text{pg}} * C_{\text{p,pg}} * (T_{\text{pg,out}} - T_{\text{pg,in}}) \quad (3.20)$$

$$\dot{Q}_{\text{recoverable}} = C_{\text{min}} * \varepsilon_{\text{br}} * (T_{exhaust,in} - T_{\text{pg,in}}) \quad (3.21)$$

where $\dot{M}_{\text{pg}}$ and $C_{\text{p,pg}}$ are mass flow rate and average specific heat of the PG mixture, respectively, $T_{\text{pg,in}}$ and $T_{\text{pg,out}}$ are the heat exchanger inlet and outlet temperatures of PG. In Equation (3.21), ε_{br} is the effectiveness of the boiler recovery heat exchanger, which is calculated based on the temperature assumptions listed in Table 3.3, and C_{min} is the minimum heat capacity rate between the exhaust and PG streams. Another finding of the boiler model is feedwater flow rate. The mass flow rate of feedwater entering the boiler is calculated based on the total thermal output of the boiler, as well as known percentages of boiler thermal energy being allocated to produce steam or hot water at varying temperatures. Based on the data provided in Table 3.2, Table 3.4 shows the breakdown of boiler thermal energy use for all hot water streams required at a beef processing facility.

Table 3.4 Breakdown of boiler energy use

Water Temperature	% of Boiler Energy Use		
	Summer	**Winter**	**Average**
90 F water	6.86%	7.60%	7.23%
110 F water	3.26%	3.40%	3.33%
140 F water	59.0%	58.8%	58.9%
Hot water (180 F)	25.3%	24.8%	25.1%
Steam	5.58%	5.20%	5.39%

Using the average percentages in the far-right column of Table 3.4, mass flow rate of boiler feedwater at varying outlet temperatures is calculated as shown in Equation (3.22) through (3.26), and total boiler feedwater flow rate is calculated using Equation (3.27). The temperature of water entering the boiler was assumed to be constant at 60° F (15.56°C) throughout the year.

$$\dot{Q}_{\text{boiler}} = \frac{\dot{M}_{\text{w},90} * \left(h_{\text{w},90} - h_{\text{w},60}\right)}{\%_{90}} \tag{3.22}$$

$$\dot{Q}_{\text{boiler}} = \frac{\dot{M}_{\text{w},110} * \left(h_{\text{w},110} - h_{\text{w},60}\right)}{\%_{110}} \tag{3.23}$$

$$\dot{Q}_{\text{boiler}} = \frac{\dot{M}_{\text{w},140} * \left(h_{\text{w},140} - h_{\text{w},60}\right)}{\%_{140}} \tag{3.24}$$

$$\dot{Q}_{\text{boiler}} = \frac{\dot{M}_{\text{w},180} * \left(h_{\text{w},180} - h_{\text{w},60}\right)}{\%_{180}} \tag{3.25}$$

$$\dot{Q}_{\text{boiler}} = \frac{\dot{M}_{\text{w},212} * \left(h_{\text{w},212} - h_{\text{w},60}\right)}{\%_{212}} \tag{3.26}$$

$$\dot{M}_{w,total} = \dot{M}_{w,90} + \dot{M}_{w,110} + \dot{M}_{w,140} + \dot{M}_{w,180}\, \dot{M}_{w,212} \tag{3.27}$$

The average thermal output of the boiler was found to be 9.7 MW, and the average feedwater flow rate of the boiler was found to be 52.4 kg/s. The hourly variation of boiler thermal output and feedwater flow rate is plotted in Figure 3.12.

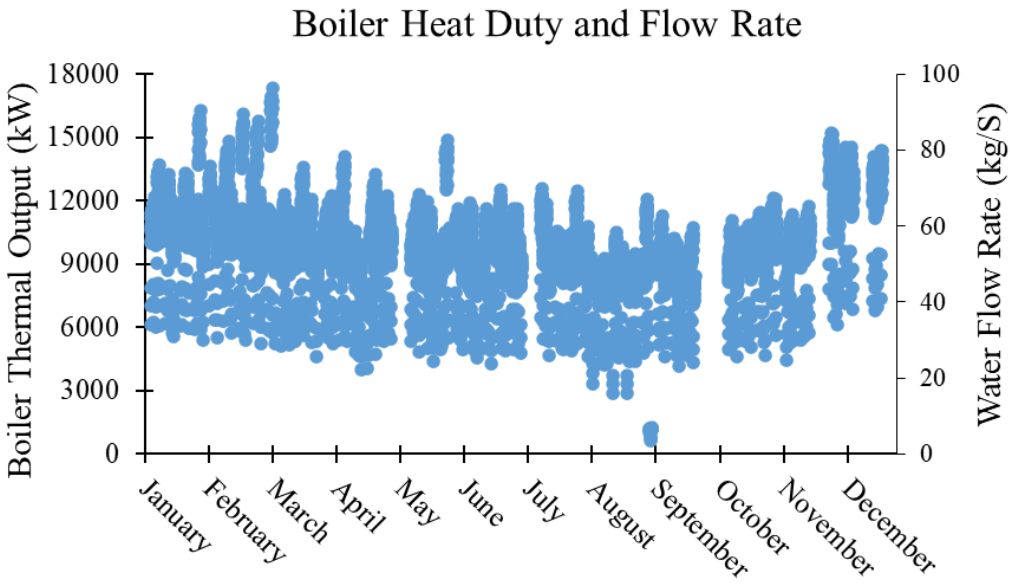

Figure 3.12 Hourly boiler thermal output and feedwater flow rate throughout the year at a plant of capacity 3200 head/day.

3.2.3. FWE Model

The feedwater economizer is modeled similarly to the boiler heat recovery loop, however instead of rejecting heat to a PG-water heat recovery loop, heat from the boiler exhaust is rejected to feedwater entering the boiler. A schematic of the feedwater economizer is shown in Figure 3.13.

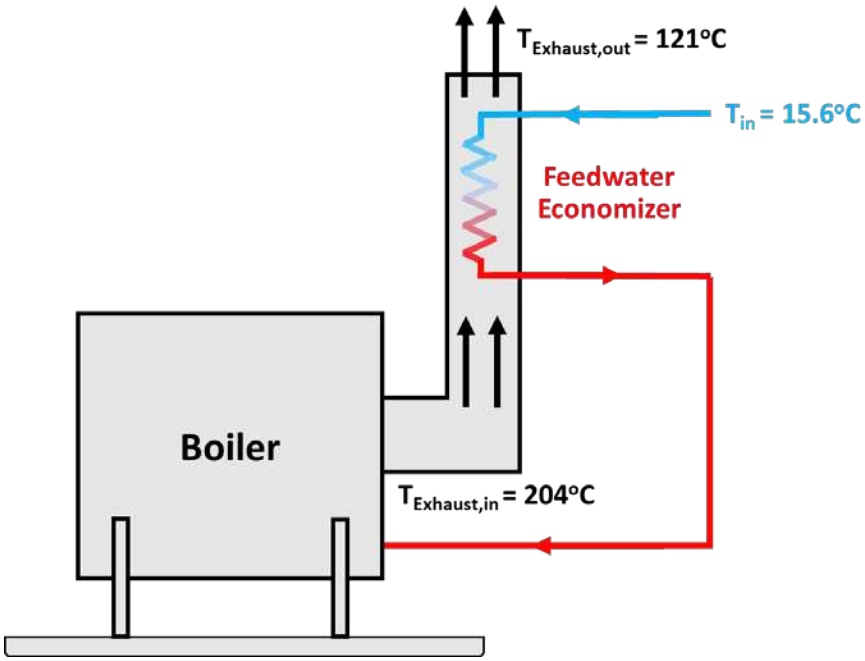

Figure 3.13 Schematic diagram of the feedwater economizer model.

The feedwater economizer could be retrofitted to the primary boiler at a beef processing facility to recover waste heat from the boiler exhaust for feedwater heating. By increasing the inlet temperature of the boiler water through feedwater heating, the heat duty of the boiler is lowered, and natural gas consumption can be reduced, leading to energy savings. The assumptions made for the feedwater economizer are similar to those made for the boiler heat recovery unit (shown in Table 3.3), however the feedwater economizer heat exchanger rejects heat to boiler feedwater instead of a PG-water mixture. Boiler feedwater is assumed to enter the heat exchanger at 15.56°C (60°F) throughout the year. The heat rejected to the feedwater economizer is calculated as shown in Equation (3.28) through Equation (3.30).

$$\dot{Q}_{\mathrm{FWE}} = \dot{M}_{\mathrm{exhaust}} * C_{\mathrm{p,exhaust}} * (T_{exhaust,in} - T_{\mathrm{exhaust,out}}) \quad (3.28)$$

$$\dot{Q}_{\mathrm{FWE}} = \dot{M}_{\mathrm{w,total}} * C_{\mathrm{p,w}} * (T_{\mathrm{w,out}} - T_{\mathrm{w,in}}) \quad (3.29)$$

$$\dot{Q}_{\mathrm{FWE}} = C_{\mathrm{min}} * \varepsilon_{\mathrm{FWE}} * (T_{exhaust,in} - T_{\mathrm{w,in}}) \quad (3.30)$$

After heat recovered by the FWE is calculated, hourly natural gas savings are determined by converting the heat recovered into a quantity of natural gas, as shown in Equation (3.31).

$$Savings_{\mathrm{gas,FWE}} = \frac{\dot{Q}_{\mathrm{FWE}}\ (MJ)}{HHV_{\mathrm{fuel}}(\frac{MJ}{m^3})} * 0.0353\ \frac{MCF}{m^3} \quad (3.31)$$

Where HHV_{fuel} is the higher heating value of natural gas, which is assumed to be 40.6 MJ/m^3. One important distinction between the FWE and the PG-water heat recovery calculation that should be noted is that heat recovered by the FWE is somewhat less than heat recovered by the PG-water loop, due to the impact that economizing has on natural gas consumption. When water entering the boiler is preheated, the boiler requires less natural gas to produce heated water and steam. When natural gas consumption is reduced, the mass flow of exhaust decreases, resulting in less heat being rejected to the FWE. Because boiler natural gas consumption is dependent on feedwater heating, and feedwater heat rejection is dependent on boiler natural gas, the model works iteratively to determine natural gas reduction where heating demands are still satisfied. The model outputs for the FWE will be discussed in detail in Section 4.1.

3.2.4. ORC Model

The second technology considered in this study is the Organic Rankine Cycle. The ORC is a thermodynamic cycle that generates power by expanding a superheated vapor through a power generating device such as a turbine or expander. For the application of a beef processing plant, an ORC could be used to generate auxiliary power which could be used to reduce overall grid electricity consumption that is required by a plant. The ORC is also configured to reject condenser

heat to the feedwater entering the boiler, which would allow for additional energy savings in the form of a reduction in required boiler natural gas consumption. The ORC modeled in this work uses R134a as the working fluid and is driven by boiler exhaust gas waste heat. The fixed inputs for the baseline ORC thermodynamic model are shown in Table 3.5. The heat duty of the ORC boiler was set to be 631 kW, which is 54 kW less than the waste heat found to be produced by the boiler in Section 3.2.2. This was done to account for the reduction in waste heat that will occur when boiler feedwater heating is provided. Along with a fixed heat duty, several other assumptions were made regarding the boiler including PG-water inlet and outlet temperature, as well as heat exchanger effectivenesses for the two-phase and superheated region. For the ORC condenser, the condenser water flow rate was set to be equivalent to the average feedwater flow rate of 52.4 kg/s, found with the boiler model. Further, condenser water inlet temperature was set to 15.56°C (60° F) to match the inlet temperature of plant boiler water.

Table 3.5 Fixed inputs for the baseline ORC thermodynamic model.

System	Input	Value	Unit
Boiler	$\dot{Q}_{boil}$	631	kW
	$T_{pg,in}$	97	°C
	$T_{pg,out}$	87	°C
	$\varepsilon_{b,tp}$	0.35	-
	$\varepsilon_{b,sh}$	0.7	-
Recuperator	ε_{recup}	0.7	
Condenser	$\dot{m}_{cond,w}$	52.4	kg/s
	$T_{cond,w,in}$	15.56	°C
	$\varepsilon_{c,tp}$	0.7	-
	$\varepsilon_{c,sc}$	0.1	-
Turbine	η_{turb}	0.8	-
	η_{gen}	0.95	-
Pump	η_{pump}	0.65	-

A complete process flow diagram of the ORC configured to provide auxiliary power and boiler feedwater heating at a beef processing plant is shown in Figure 3.14.

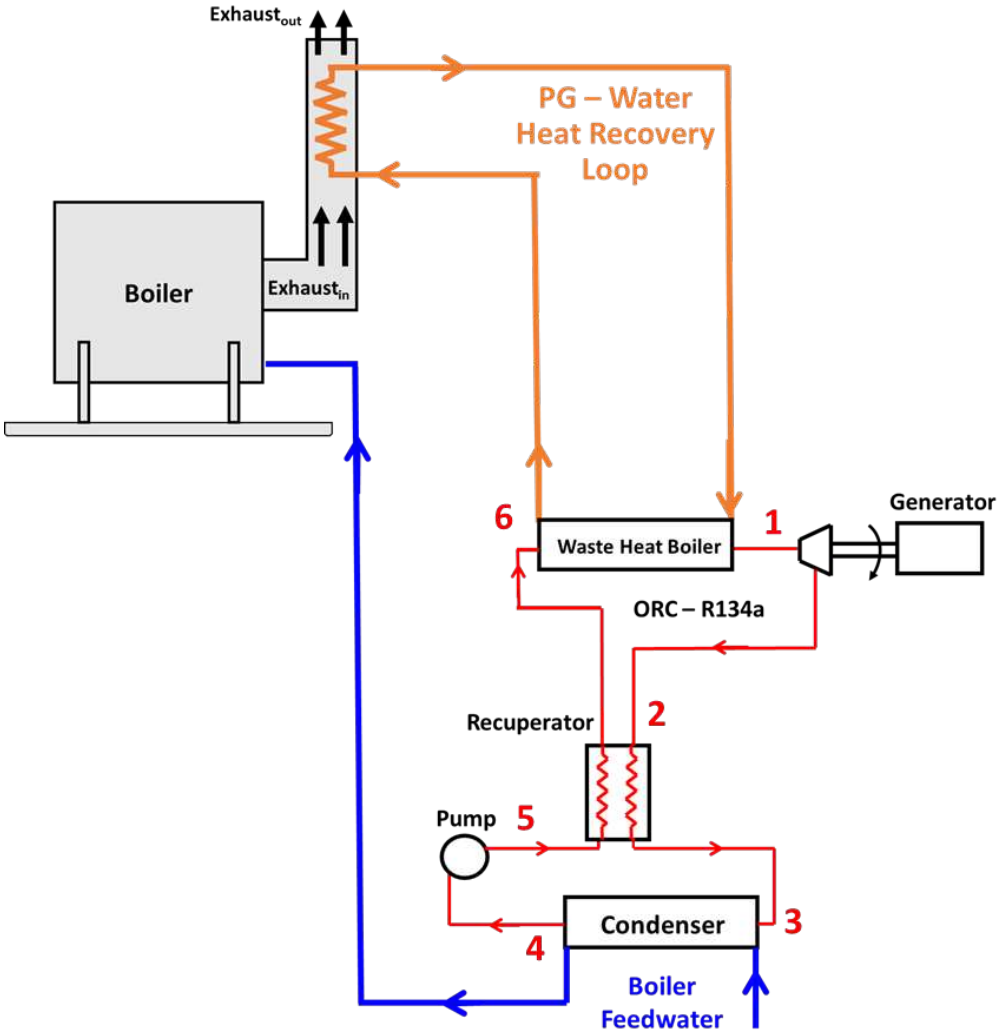

Figure 3.14 Process flow diagram of an ORC used to provide auxiliary power and boiler feedwater heating at a beef plant

In modeling the ORC, the condenser and waste heat boiler were divided into three distinct regions where each region represents a different working fluid phase. The boiler and condenser were divided into three subsections: subcooled, two-phase, and superheated. The boiler, condenser, and recuperator were all modeled as counter flow plate and frame heat exchangers. To describe the cycle, waste heat boils the working fluid (6-1 in Figure 3.14) which is then expanded

through a high-efficiency centrifugal turbine (1-2). The working fluid exits the turbine and enters the recuperator (2-3) where some of the heat is rejected to working fluid leaving entering the boiler. After the recuperator, the working fluid is condensed (3-4), rejecting heat to feedwater entering the beef plant water boiler. Then, the working fluid is compressed to the boiler pressure (4-5) with the pump, recuperated (5-6), and re-enters the boiler to repeat the cycle. A Temperature-entropy diagram of the ORC with R134a as the working fluid is shown in Figure 3.15.

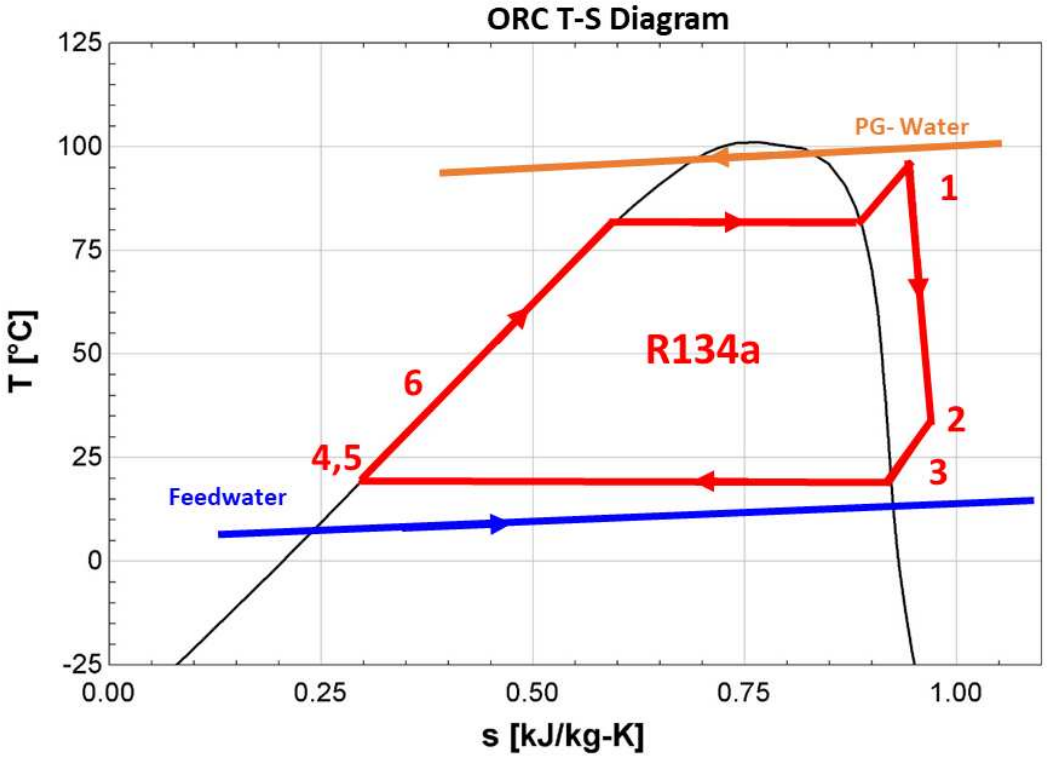

Figure 3.15 Temperature-Entropy diagram of the organic Rankine cycle with R134a as the working fluid. The PG-Water mixture that vaporizes the working fluid in the ORC boiler (orange), and boiler feedwater that condenses the working fluid (blue) are overlayed.

The heat exchangers of the ORC are modeled by solving an energy balance for each fluid region. There are seven distinct heat exchanger regions in the ORC: the superheated, two-phase, and subcooled regions of both the condenser and boiler, and the single-phase region of the recuperator. For each heat exchanger region, three energy balance equations are used to evaluate

heat transfer on the refrigerant side, heat transfer on the external stream side, and heat transfer efficiency between the two streams. The energy balance for heat transfer on the refrigerant side is solved for using Equation (3.32):

$$\dot{Q} = \dot{m}_{\mathrm{r}} * (h_{\mathrm{r,in}} - h_{\mathrm{r,out}}) \tag{3.32}$$

where $\dot{Q}$ is the heat transfer rate, $\dot{m}_{\mathrm{r}}$ is the mass flow rate of refrigerant, and $h_{\mathrm{r,in}}$ and $h_{\mathrm{r,out}}$ are the enthalpies of the refrigerant at inlet and outlet, respectively. On the external stream side of the heat exchanger, the energy balance is solved for using Equation (3.33):

$$\dot{Q} = \dot{m}_{\mathrm{ext}} * C_{\mathrm{p}} * (T_{\mathrm{ext,in}} - T_{\mathrm{ext,out}}) \tag{3.33}$$

where $\dot{m}_{\mathrm{ext}}$ is the mass flow rate of the external stream, C_{p} is the specific heat capacity of the external fluid, and $T_{\mathrm{ext,in}}$ and $T_{\mathrm{ext,out}}$ are the enthalpies of the external stream at inlet and outlet, respectively. For the recuperator, which is an internal heat exchanger, two versions of Equation (43) are used, to describe heat transfer on the superheated (2-3 in Figure 3.15) and subcooled (5-6) sides of the heat exchanger. The heat transfer effectiveness is then used to relate heat exchanger performance with external and internal temperature gradients as shown below in Equation (3.34):

$$\dot{Q} = \varepsilon * C_{\mathrm{min}} * (T_{\mathrm{hot,in}} - T_{\mathrm{cold,in}}) \tag{3.34}$$

where ε is the heat exchanger effectiveness, and C_{min} is minimum heat capacity rate between the refrigerant and external stream, which is the product of the mass flow rate and specific heat capacity. $T_{\mathrm{hot,in}}$ and $T_{\mathrm{cold,in}}$ are the inlet temperatures of the hot side and cold side, respectively. ORC Turbine work is evaluated using Equation (3.35) and Equation (3.36).

$$\dot{W}_{\text{turb}} = \dot{M}_{\text{r}} * \left(h_{\text{r,in}} - h_{\text{r,out}}\right) \tag{3.35}$$

$$\eta_{\text{turb}} = \frac{h_{\text{r,in}} - h_{\text{r,out,s}}}{h_{\text{r,in}} - h_{\text{r,out}}} \tag{3.36}$$

where $h_{\text{r,in}}$ and $h_{\text{r,out}}$ are the enthalpies of the working fluid at turbine inlet and outlet, respectively, and $h_{\text{r,out,s}}$ is the enthalpy at the turbine outlet assuming constant entropy. η_{turb} is the isentropic efficiency of the turbine, which is assumed constant as shown in Table 3.5. ORC pump work is evaluated using Equation (3.37) and (3.38).

$$\dot{W}_{\text{pump}} = \dot{M}_{\text{r}} * \left(h_{\text{r,out}} - h_{\text{r,in}}\right) \tag{3.37}$$

$$\eta_{\text{pump}} = \frac{h_{\text{r,out,s}} - h_{\text{r,in}}}{h_{\text{r,out}} - h_{\text{r,in}}} \tag{3.38}$$

Overall efficiency of the ORC is calculated as shown in Equation (3.39) as:

$$\eta_{\text{ORC}} = \frac{\dot{W}_{\text{turb}}}{\dot{Q}_{\text{boil}} + \dot{W}_{\text{pump}}} \tag{3.39}$$

where $\dot{W}_{\text{turb}}$ is the power output of the turbine, $\dot{Q}_{\text{boil}}$ is the total heat input to the boiler, and $\dot{W}_{\text{pump}}$ is the work input of the pump. Finally, the electricity and natural gas savings of the ORC are calculated using Equation (3.40) and Equation (3.41):

$$Savings_{\text{elec,ORC}} = \dot{W}_{\text{turb}} * \eta_{\text{gen}} - \dot{W}_{\text{pump}} \tag{3.40}$$

$$Savings_{\text{gas,ORC}} = \frac{\dot{Q}_{\text{cond}} * 3600 * 0.0353}{1000 * HHV_{\text{ng}}} \tag{3.41}$$

Where η_{gen} is the assumed generator efficiency in Table 3.5, and the factors used in Equation (3.41) are used to convert condenser heat rejection ($\dot{Q}_{\text{cond}}$) in kW to a quantity of natural gas (MCF). Table 3.6 shows the thermodynamic state points of the ORC, which are solved for using

EES. Because the ORC does not interact with the PRS, performance remains constant throughout the year based on the fixed inputs in Table 3.5.

Table 3.6 Thermodynamic state points of the ORC

State Point	Temperature	Enthalpy	Pressure	Entropy
	°C	kJ kg^{-1}	kPa	kJ kg^{-1} K^{-1}
1	95.2	303	2770	0.947
2	33.5	275	556	0.97
3	24.5	266	556	0.941
4	18.7	77.5	556	0.295
5	20.5	80.3	2770	0.298
6	26.8	89.1	2770	0.327

The baseline ORC operates at a pressure ratio of 5, with a high temperature at the turbine inlet of 95.2^{o} C and a low temperature at the condenser outlet of 18.7^{o}C. This concludes the discussion of the baseline ORC thermodynamic model. The results from the ORC thermodynamic model are presented in Section 4.1. In the following section, the baseline DMS thermodynamic model will be described.

3.2.5. DMS Model

The third technology considered in this research to reduce energy use at a beef processing plant is a dedicated mechanical subcooler. As discussed in Section 2.2.3.4, a DMS is a small, secondary vapor compression cycle that is coupled to the PRS at the condenser outlet. By providing subcooling to the PRS at the condenser outlet, the PRS refrigerant enters the evaporator at a lower quality, allowing for an increased refrigeration effect (illustrated in Figure 2.16). If the overall cooling load of the PRS is fixed, the mass flow rate of ammonia refrigerant can be reduced, allowing for a reduction in PRS compressor work which results in energy savings. The fixed inputs for the baseline DMS thermodynamic model are shown in Table 3.7. The condenser water mass flow and temperature are made equivalent to the boiler feedwater. The DMS compressor work is

set at 98% of the ORC turbine output to create a fair comparison the DMS and the TCCS. The working fluid of the DMS is selected to be R134a, like the ORC and TCCS.

Table 3.7 Fixed inputs for the baseline DMS thermodynamic model

System	Input	Value	Unit
Evaporator	$\boldsymbol{\varepsilon_{ch,tp}}$	0.7	-
	$\boldsymbol{\varepsilon_{ch,sh}}$	0.7	-
Condenser	$\boldsymbol{\dot{m}_{cond,w}}$	52.4	kg/s
	$\boldsymbol{T_{cond,w,in}}$	15.56	^{o}C
	$\boldsymbol{\varepsilon_{cc,tp}}$	0.7	-
	$\boldsymbol{\varepsilon_{cc,sc}}$	0.1	-
Compressor	$\boldsymbol{\dot{W}_{comp,DMS}}$	79	kW
	$\boldsymbol{\eta_{comp}}$	0.8	-

The one input for DMS model that does vary throughout the year is the pressure of ammonia at the PRS condenser outlet. Due to the impact of ambient weather, the PRS compressor work required varies throughout the year, altering the high side pressure of the ammonia stream. In general, the high-side pressure of the ammonia stream is the highest during the summer months due to lowered cooling tower performance when it is hot and humid. The high side pressure variation of the PRS is shown in Figure 3.6a. A full schematic diagram of the DMS is shown in Figure 3.16. Like the ORC, the DMS is also configured to provide natural gas savings by rejecting heat from the condenser directly to the feedwater entering the boiler.

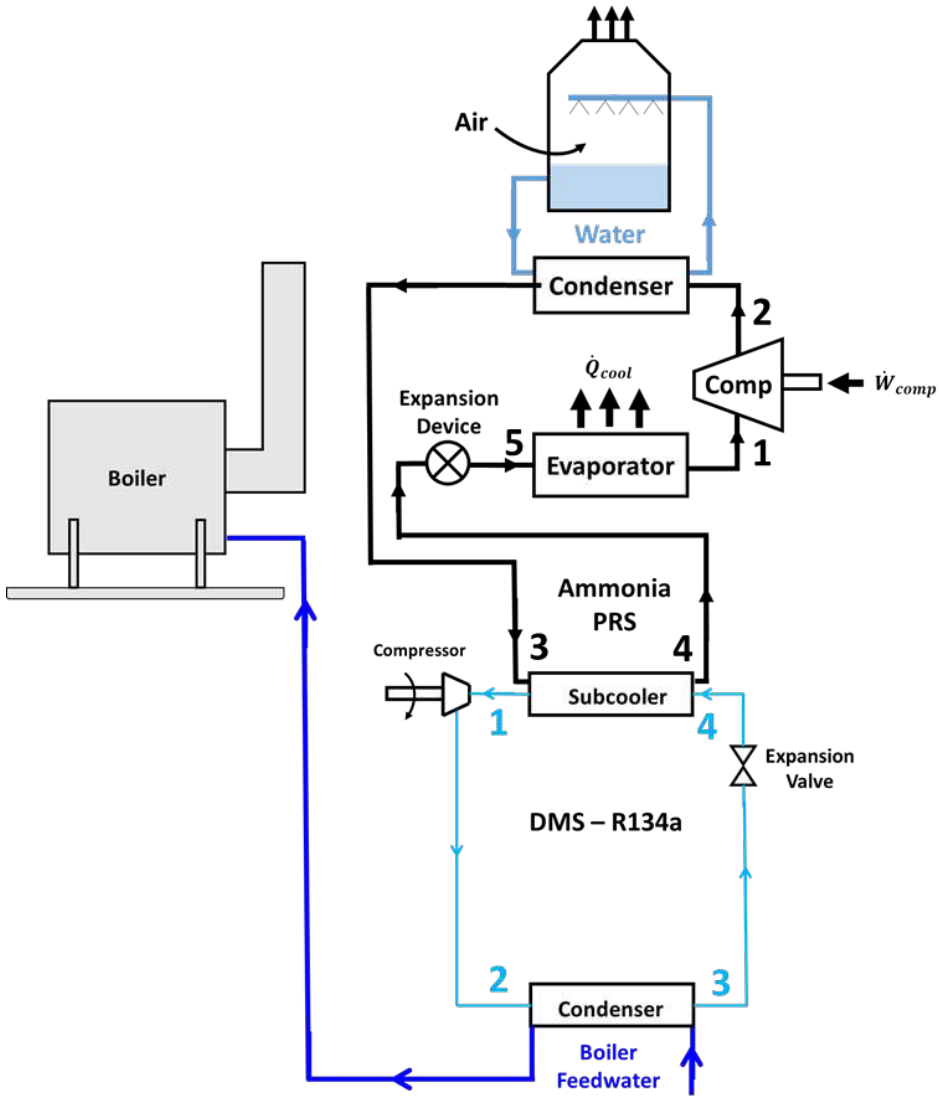

Figure 3.16 Process flow diagram of a dedicated mechanical subcooler used to provide auxiliary PRS subcooling and boiler feedwater heating at a beef plant

To describe the DMS, the working fluid is compressed to a high pressure (1-2 in Figure 3.16) and is then condensed through a condensing heat exchanger (2-3). The working fluid is then passed through an isenthalpic expansion valve which decreases temperature and pressure (3-4). Finally, the working fluid is evaporated in the subcooler, providing subcooling to the PRS (4-1). A temperature entropy diagram of the DMS with R134A configured to provide subcooling to the ammonia PRS is shown in Figure 3.17.

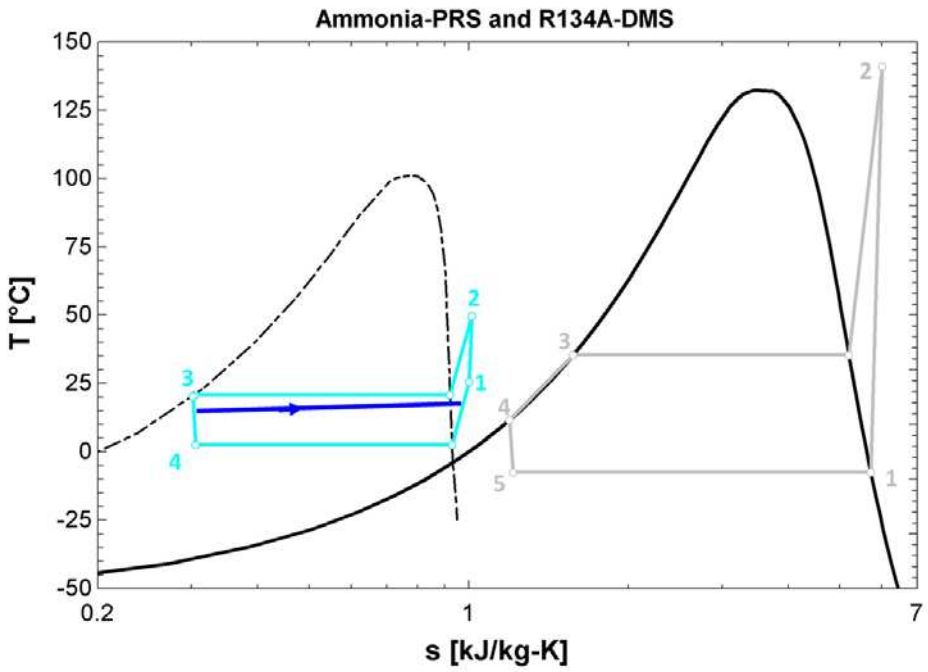

Figure 3.17 Temperature-Entropy diagram of the R134a DMS and Ammonia PRS. The ammonia stream is shown in gray, the DMS stream is shown in light blue, and the boiler feedwater stream is shown in dark blue. The ammonia vapor dome is shown in solid black, and the R134a vapor dome is shown in dashed black.

The heat exchangers of the DMS, including the condenser and subcooler, are evaluated in the same way as the heat exchangers of the ORC (Equation (3.32)-(3.34)). Although the PRS compressor work input is set, the amount of subcooling provided to the PRS still varies, due to the varying condition of the ammonia stream (Figure 3.6a), which allows for the DMS to provide subcooling. The COP of the DMS is calculated as shown in Equation (3.42).

$$COP_{\text{DMS}} = \frac{\dot{Q}_{\text{subcool}}}{\dot{W}_{\text{comp,DMS}}} \tag{3.42}$$

Where $\dot{Q}_{\text{subcool}}$ is the amount of subcooling provided by the PRS, and $\dot{W}_{\text{comp,DMS}}$ is the work input, which is a fixed. The overall work input required for the PRS and DMS is calculated as:

$$\dot{W}_{\text{overall,PRS+DMS}} = \dot{W}_{\text{comp,PRS}} + \dot{W}_{\text{comp,DMS}} \tag{3.43}$$

Where $\dot{W}_{\text{comp,PRS}}$ is the PRS compressor work input at the reduced PRS mass flow rate, which is calculated as discussed in Section 3.2.1. The improved COP of the PRS is then calculated as:

$$COP_{\text{PRS}} = \frac{\dot{Q}_{\text{overall}}}{\dot{W}_{\text{overall,PRS+DMS}}} \tag{3.44}$$

Where $\dot{Q}_{\text{overall}}$ is the assumed overall PRS cooling load of 9.3 MW, which is assumed to be constant throughout the year. Finally, electricity and natural gas savings provided by the DMS are calculated as shown in Equation (3.45) and Equation (3.46).

$$Savings_{\text{elec,DMS}} = \dot{W}_{\text{PRS,initial}} - \dot{W}_{\text{overall,PRS+DMS}} \tag{3.45}$$

$$Savings_{\text{gas,DMS}} = \frac{\dot{Q}_{\text{cond}} * 3600 * 0.0353}{1000 * HHV_{\text{ng}}} \tag{3.46}$$

The baseline DMS thermodynamic simulation was run on EES, and accounts for hourly PRS pressure variation found with the beef plant refrigeration model. The thermodynamic results of the baseline DMS model will be discussed in Section 4.1 In the following section, the baseline TCCS thermodynamic model will be discussed in detail.

3.2.6. TCCS Model

The final technology considered in this study is the Turbo-compression cooling system. The TCCS is a thermally driven cooling technology that could be implemented at a beef processing facility to provide PRS subcooling in the same way as the DMS. The primary distinction between the TCCS and the DMS is that the TCCS is driven by waste heat, while the DMS requires electrical work input to the compressor. While the performance improvement of the DMS comes as a tradeoff with additional compressor work, a thermally driven subcooler is bound only by waste heat availability. The TCCS model consists of two thermodynamic cycles: a power cycle (ORC) and a cooling cycle (VCRC) which are mechanically coupled between the ORC turbine and VCRC

Compressor. In essence, the TCCS serves as a combination of the two technologies discussed in the previous sections. A complete schematic diagram of the TCCS implemented at a beef processing facility is shown in Figure 3.18.

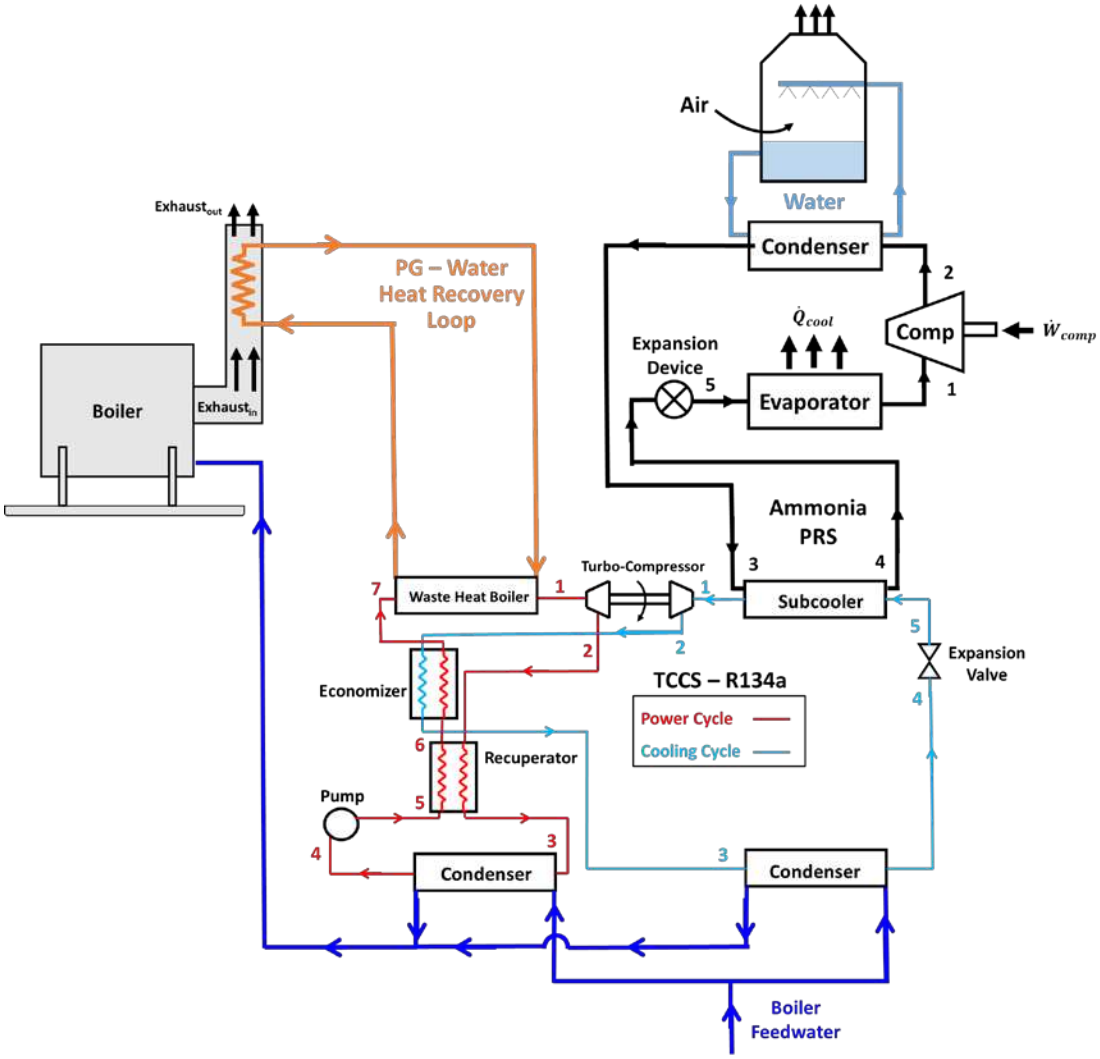

Figure 3.18 Process flow diagram for a TCCS used to provide PRS mechanical subcooling and boiler feedwater heating.

To explain the cycle, the power cycle uses waste heat from the primary plant boilers to vaporize a high-pressure refrigerant (red 7-1 in Figure 3.18). The superheated, high-pressure refrigerant is then expanded through the centrifugal turbine of the turbo-compressor (red 1-2). Power produced in the turbine is directly transferred to the compressor of the turbo-compressor

using a common shaft. A recuperator is used to recover some of the heat of the turbine discharge to preheat the refrigerant entering the boiler (red 2-3). After the recuperator, the refrigerant is condensed (red 3-4), and pumped back up to the boiler pressure (red 4-5). In the cooling cycle, a low-pressure, two-phase refrigerant is boiled in the evaporator to produce the desired cooling effect (blue 5-1). The evaporator of the TCCS is coupled to the PRS condenser outlet to provide subcooling to the high-pressure, saturated liquid ammonia (black 3-4). The refrigerant in the TCCS cooling cycle leaves the evaporator and enters the compressor of the turbo-compressor as a low-pressure, superheated vapor (blue 1-2). After being compressed, the refrigerant in the TCCS cooling cycle is sent to the economizer where some of the heat is rejected to preheat the refrigerant entering the boiler of the TCCS power cycle (blue 2-3 and red 6-7). After the economizer, the refrigerant is condensed (blue 3-4), and throttled (blue 4-5) down to the evaporator pressure. A Temperature entropy diagram of the TCCS cooling and power cycles shown in Figure 3.19a-b.

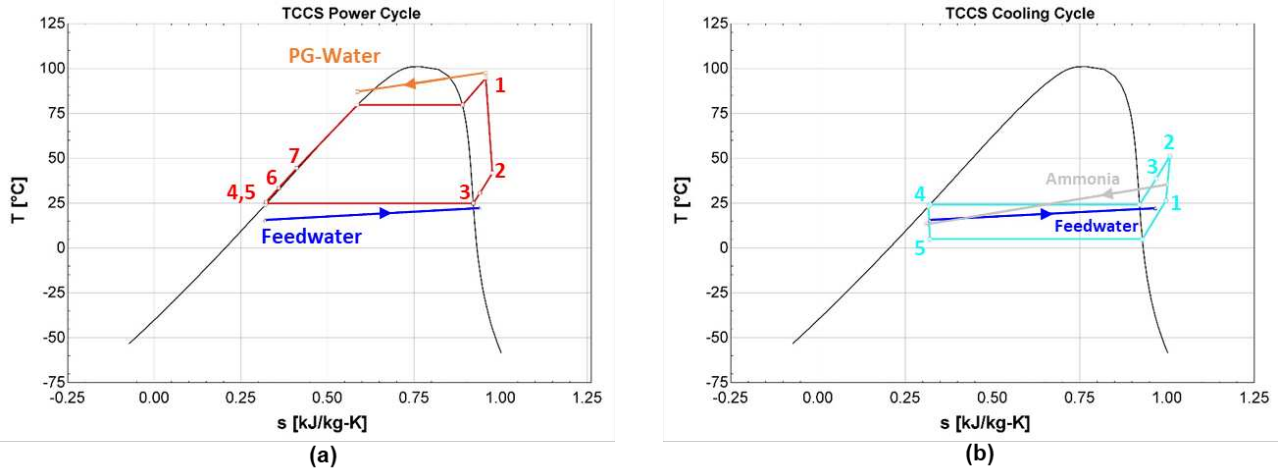

Figure 3.19 Temperature-Entropy diagrams of the R134a TCCS (a) power cycle and (b) cooling cycle. The ammonia stream being subcooled is shown in gray, the boiler feedwater streams are shown in dark blue, and the PG-water stream is shown in orange. The R1434a vapor dome is shown in solid black.

The TCCS is thermodynamically modeled to evaluate the subcooling provided to the PRS based on ambient weather conditions, high-side pressure of the ammonia refrigeration system, and

waste heat available from the plant boiler exhaust. To simplify the analysis, it is assumed that the system is operating under steady state conditions, heat loss and pressure from all components and piping are negligible, and the expansion process of the cooling cycle is isenthalpic. Furthermore, heat exchanger effectivenesses and turbomachinery isentropic efficiencies are assumed to be constant. Also, work required to operate auxiliary systems, such as the waste heat recovery and condenser water loops, is neglected. Table 3.8 lists the fixed inputs for the TCCS model at the baseline effectiveness values.

Table 3.8 Fixed inputs for the baseline TCCS thermodynamic model.

System		Input	Value	Unit
Power Cycle	Boiler	$\dot{Q}_{boil}$	631	kW
		$T_{pg,in}$	97	C
		$T_{pg,out}$	87	C
		$\varepsilon_{b,tp}$	0.35	-
		$\varepsilon_{b,sh}$	0.7	-
	Recuperator	ε_{recup}	0.7	
	Condenser	$\dot{m}_{cond,w}$	21.7	kg/s
		$T_{cond,w,in}$	15.56	C
		$\varepsilon_{c,tp}$	0.7	-
		$\varepsilon_{c,sc}$	0.1	-
	Turbine	η_{turb}	0.8	-
		η_{mech}	0.98	-
	Pump	η_{pump}	0.65	-
	Economizer	ε_{econ}	0.7	-
Cooling Cycle	Evaporator	$\varepsilon_{ch,tp}$	0.7	-
		$\varepsilon_{ch,sh}$	0.7	-
	Condenser	$\dot{m}_{cond,w}$	30.7	kg/s
		$T_{cond,w,in}$	15.56	C
		$\varepsilon_{cc,tp}$	0.7	-
		$\varepsilon_{cc,sc}$	0.1	-
	Compressor	η_{comp}	0.8	-

One key difference between the TCCS model and the ORC and DMS models is the condenser water flow rate. In the DMS and ORC models, each system only has as single condenser which receives the full 52.4 kg/s flow of boiler feedwater. Because the TCCS has two condensers

for both the power and cooling cycle, the mass flow is split between the two condensers, with the sum flow being equivalent to 52.4 kg/s. The mass flow of boiler feedwater was split at a ratio of roughly 60:40 between the two condensers, with greater flow going to the cooling cycle condenser. This was done because the cooling cycle condenser operates at a slightly lower pressure and requires more heat rejection than the power cycle condenser, and preliminary simulations showed that when split 60:40, the outlet temperatures of feedwater from both condensers were similar. The heat exchangers of the TCCS are modeled by solving an energy balance for each fluid region in the same way as the ORC and DMS models. One additional heat exchanger included in the TCCS is the cross-cycle economizer, which further improves the performance of the TCCS by transferring heat from the working fluid at the cooling cycle condenser outlet to the working fluid at the power cycle boiler inlet. The turbomachinery components including the pump, and turbo-compressor are also modeled using energy balances in the same way as the DMS and ORC. The pump and compressor of the turbo-compressor were modeled using an energy balance as shown in Equation (3.47), and the isentropic efficiency was calculated using Equation (3.48)

$$\dot{W}_{\text{pump/comp}} = \dot{M}_{\text{r}} * \left(h_{\text{r,out}} - h_{\text{r,in}}\right) \tag{3.47}$$

$$\eta = \frac{h_{\text{r,out,s}} - h_{\text{r,in}}}{h_{\text{r,out}} - h_{\text{r,in}}} \tag{3.48}$$

where $h_{\text{r,out,s}}$ is the enthalpy at pump or compressor outlet assuming constant entropy. Turbine work is evaluated similarly, as

$$\dot{W}_{\text{turb}} = \dot{M}_{\text{r}} * \left(h_{\text{r,in}} - h_{\text{r,out}}\right) \tag{3.49}$$

$$\eta_{\text{turb}} = \frac{h_{\text{r,in}} - h_{\text{r,out,s}}}{h_{\text{r,in}} - h_{\text{r,out}}} \tag{3.50}$$

Compressor work is also equated to turbine work as a function of the turbo-compressor mechanical shaft efficiency as

$$\dot{W}_{\text{comp}} = \dot{W}_{\text{turb}} * \eta_{\text{mech}} \tag{3.51}$$

The performance of the TCCS is estimated with the overall COP of the TCCS, which is calculated as

$$COP_{\text{TCCS}} = \frac{\dot{Q}_{\text{subcool}}}{\dot{Q}_{\text{boiler}} + \dot{W}_{\text{pump}}} \tag{3.52}$$

Where $\dot{Q}_{\text{subcool}}$ is the total amount of cooling provided by the TCCS, used to subcool the beef plant's refrigeration cycle. The overall work input required for the PRS and DMS is calculated as

$$\dot{W}_{\text{overall,PRS+TCCS}} = \dot{W}_{\text{comp,PRS}} + \dot{W}_{\text{pump,TCCS}} \tag{3.53}$$

Where $\dot{W}_{\text{pump,TCCS}}$ is the work required to operate the pump of the power cycle of the TCCS. Finally, electricity and natural gas savings provided by the TCCS are calculated as shown in Equation (3.54) and Equation (3.55).

$$Savings_{\text{elec,TCCS}} = \dot{W}_{\text{PRS,initial}} - \dot{W}_{\text{overall,PRS+TCCS}} \tag{3.54}$$

$$Savings_{\text{gas,TCCS}} = \frac{(\dot{Q}_{\text{cond,CC}} + \dot{Q}_{\text{cond,PC}}) * 3600 * 0.0353}{1000 * HHV_{\text{ng}}} \tag{3.55}$$

In Equation (3.55), $\dot{Q}_{\text{cond,CC}}$ and $\dot{Q}_{\text{cond,PC}}$ are the heat rejected from the condensers of the TCCS cooling cycle and power cycle, respectively. This concludes the discussion of the TCCS thermodynamic model. In the next section, a brief discussion of the primary thermodynamic model inputs will be presented.

3.2.7. Summary of Thermodynamic Model inputs

In summary, six distinct thermodynamic models are produced in this work to assess energy use and potential energy savings at a beef processing facility with a 3200 head/day capacity. The purpose of this section is to review the models described in the previous sections, and reiterate the

critical assumptions and inputs used in each simulation. Table 3.9 compares each thermodynamic model based on the fixed and varying inputs required.

Table 3.9 Comparison of inputs for each thermodynamic model.

Model (Operation Hours)	Input	Value
PRS (8760 hrs)	$\dot{Q}_{\text{cool}}$ Condenser Pressure Evaporator Pressure	9.3 MW f(TMY3) 322 kPa
Boiler (5184 hrs)	$\dot{Q}_{\text{boiler}}$, $\dot{Q}_{\text{exhaust}}$, $\dot{M}_{\text{water}}$ $\Delta T_{\text{exhaust}}$ $\Delta T_{\text{pg-water}}$	f(NG data) (204 −121) = 83°C (97 − 87) = 10°C
FWE (5184 hrs)	$\dot{Q}_{\text{boiler}}$, $\dot{Q}_{\text{exhaust}}$, $\dot{M}_{\text{water}}$ $\Delta T_{\text{exhaust}}$ $T_{\text{feedwater,in}}$	f(NG_data) (204 −121) = 83°C 15.56°C
ORC (5184 hrs)	$\dot{Q}_{\text{boil}}$ ε_{HX} $\eta_{\text{turb}}/\eta_{\text{pump}}$ $\dot{M}_{\text{cond,water}}$	631 kW Fixed 0.8/0.65 52.4 kg/s
DMS (5184 hrs)	$\dot{W}_{\text{comp}}$ ε_{HX} η_{comp} $\dot{Q}_{\text{subcool}}$ $\dot{M}_{\text{cond,water}}$ $T_{\text{cond,water,in}}$	$\dot{W}_{\text{turb,orc}} * 0.98$ fixed 0.8 f(PRS) 52.4 kg/s 15.56°C
TCCS (5184 hrs)	$\dot{Q}_{\text{boil}}$ ε_{HX} $\eta_{\text{turb}}/\eta_{\text{pump}}/\eta_{\text{comp}}$ $\dot{Q}_{\text{subcool}}$ $\dot{M}_{\text{cond,water,pc}}$ $\dot{M}_{\text{cond,water,cc}}$ $T_{\text{cond,water,in}}$	631 kW Fixed 0.8/0.65/0.8 f(PRS) 21.7 kg/s 30.7 kg/s 15.56°C

The first two models described in this work are the beef plant refrigeration and boiler models. As discussed in Section 1.1, the refrigeration system and boiler are the two systems at a plant that consume the most electricity and natural gas, respectively. Thus, to understand energy use at a beef processing plant, it is critical to accurately model these two systems. The PRS is thermodynamically modeled as an ammonia VCRC with a wet cooling tower and is simulated at

an hourly resolution for a year's worth of weather data (8,760 hours) taken from the TMY3 database. The PRS was simulated for five different TMY3 datasets corresponding to the following cities: Fresno, California; Denver, Colorado; Atlanta, Georgia; Grand Island, Nebraska; and Atlanta, Georgia. These cities were selected due to their varying climates, and because they are in states that are all considered top livestock producers. The primary fixed inputs of the PRS model, which remain constant throughout the year, are the overall cooling load of 9.3 MW, and evaporator pressure of 322 kPa (~32 PSIG). The cooling load was estimated based on beef plant refrigeration compressor data and an assumed COP, then scaled to estimate the cooling needs of a plant processing 3200 head/day. Although a fixed cooling load isn't a realistic assumption, it was chosen to better understand the impact of ambient weather conditions on PRS performance.

The plant boiler is thermodynamically modeled to estimate overall boiler load, feedwater flow rate, and exhaust waste heat availability. The boiler model is simulated for 5,184 hours, based on the natural gas data set used in this work, which is reflective of the number of processing hours at a beef plant. Unlike the PRS model, the boiler model does not take into consideration ambient weather, and thus, is modeled the same across the five locations. The primary input to the boiler model is natural gas and water use data, and several assumptions are made regarding the boiler heat recovery unit and water temperatures.

After modeling the refrigeration and boiler systems, four technologies are investigated that achieve electricity and natural gas savings at a beef plant. The first technology discussed is the feedwater economizer. The FWE model is like the boiler model, but instead of boiler heat being rejected to PG-water, it is rejected to feedwater entering the boiler. Over 5,184 operation hours, the FWE model calculates exhaust waste heat and water flow rate from natural gas data, then determines gas savings yielded by preheating the water entering the boiler. A constant feedwater

economizer inlet water temperature of 15.56°C (60°F) is assumed, which is based on the approximate temperature of groundwater. Exhaust inlet and outlet temperatures of 204°C (400°F) and 121°C (250°F) are also assumed based on the expected performance of a feedwater economizer heat exchanger.

The second energy saving technology is the organic Rankine cycle. The ORC is thermodynamically modeled to generate supplemental electricity for the plant with a power generating turbine to yield electricity savings, and boiler feedwater heating with the condenser to yield natural gas savings. The primary inputs for the ORC model are waste heat to the boiler, heat exchanger effectivenesses, turbomachine efficiencies, and condenser water flow rate and inlet temperature. To keep consistent with the TCCS model, waste heat input to the ORC was assumed to be constant at 631 kW for all 5,184 operation hours of the year. Furthermore, condenser water flow rate was also assumed to be constant at 52.4 kg/s. For this reason, the ORC operates constantly throughout the year. Additionally, because the ORC model does not account for ambient weather, ORC performance is also the same across the five plant locations.

The third energy saving technology is the DMS. The DMS is modeled to provide subcooling to the PRS, which yields compressor electricity savings, as well as boiler feedwater heating with the condenser to provide natural gas savings. The primary fixed inputs for the DMS model are a set compressor work input, heat exchanger effectiveness, turbomachinery efficiencies, as well as condenser water flow rate and temperature. To keep consistent with the TCCS model, the DMS was simulated for 5,184 hours of the year when the boiler is being operated. Furthermore, work input to the DMS was set constant for all hours at 79 kW (in the baseline model), equivalent to 98% of the work generated in the turbine of the ORC. In the system optimization study, discussed in Section 3.5, compressor work input was varied along with effectiveness in accordance

to the ORC turbine output. To create a fair comparison of natural gas savings produced by the ORC and DMS, the condenser water flow rate and inlet temperature were also set at 52.4 kg/s and 15.56°C. The one input that varies for the DMS model throughout the year is pressure of ammonia at the subcooler inlet. Because ammonia pressure is based on the PRS model, which considers ambient weather, DMS performance varies throughout the year and between locations. Depending on the condition of the ammonia stream, the DMS varies mass flow and operation pressures, resulting in a varying amount of subcooling being provided to the PRS.

The final technology modeled is the TCCS, which acts as a combination of the ORC and DMS. The TCCS provides waste heat driven subcooling to the PRS to yield compressor electricity savings, and boiler feedwater heating with the condensers to yield natural gas savings. The primary fixed inputs for the TCCS model are waste heat, heat exchanger effectiveness, turbomachine efficiencies, as well as the mass flow and inlet temperature of condenser water. The TCCS is operated for 5,184 hours of the year when boiler waste heat is available. A fixed waste heat input and condenser water flow were selected due to computation limitations. The TCCS EES simulation, which solves 5,184 times for each operation hour, took significantly longer to run when waste heat, condenser water flow, and ammonia pressure were all set to the time varying amounts. To reduce computation time, the waste heat input for the TCCS was selected as 631 kW, which is the average boiler waste heat output (plotted in Figure 3.11), minus 54 kW to account for the impact of boiler feedwater heating. Additionally, total condenser water flow rate was set at the average boiler feedwater flow rate of 52.4 kg/s (split 60:40 between the two condensers). To verify that the assumption of constant waste heat would not impact overall performance results, an additional simulation was performed calculating the performance of the TCCS in Fresno with a

varying waste heat input. The performance of the TCCS in Fresno with both varied and constant waste heat inputs is plotted in Figure 3.20.

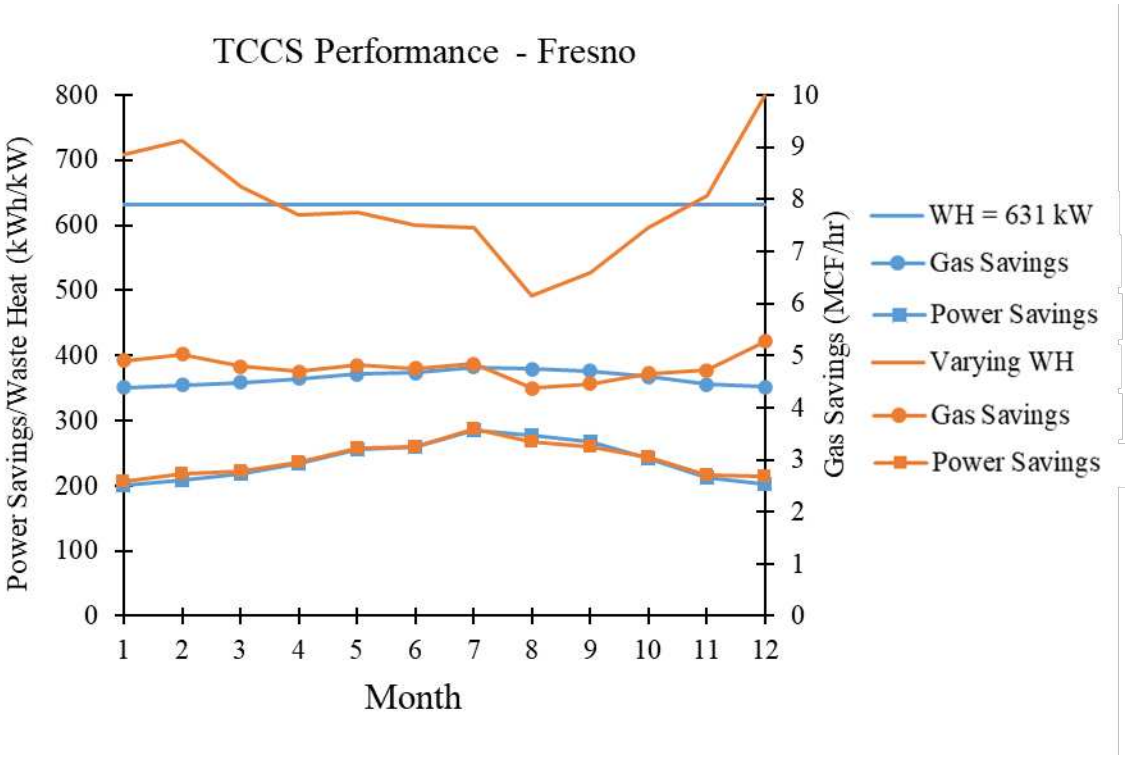

Figure 3.20 Average monthly power and gas savings achieved by the TCCS in Fresno with the assumed constant waste heat (shown in blue) and varying waste heat (shown in orange).

In Figure 3.20, the orange lines represent the performance results from the TCCS model with the varying waste heat, and the blue lines represent TCCS performance with the constant waste heat input of 631 kW. Although slight variations between the blue and orange savings trends occur, the total annual savings calculated in each simulation were found to be similar in magnitude. For both constant and varied waste heat, the TCCS in Fresno yielded a total annual savings of $350,000. The total gas and electricity savings produced by the TCCS with varied waste heat (shown in blue) were found to be $186,000 and $164,000, respectively. In comparison, the gas and electricity savings produced by the TCCS with constant waste heat were found to be $183,000 and

$167,000, respectively. Considering the low variation in total annual savings between the two simulations, the assumption of a constant waste heat input is reasonable.

This concludes the discussion of the thermodynamic models produced in this work. The results of the baseline thermodynamic models are discussed in Section 4.1. The thermodynamic results from the optimization study are discussed in Section 4.4.1 In the following section, the heat exchanger models for the ORC, DMS, and TCCS will be described in detail.

3.3. Plate and Frame Heat Exchanger Modeling

Once thermodynamic performance is determined, the goal of the heat exchanger model is to evaluate the size and performance of stainless-steel plate and frame heat exchangers to be used within the ORC, DMS, and TCCS. Determining the size of heat exchangers is a critical step in calculating capital cost, and thus, overall economic performance of each technology option. The FWE was the only technology option for which a heat exchanger simulation was not conducted. This is because the capital cost of the FWE was determined using a supplier quote, rather than by summing the costs of each individual component.

The anatomy of a counterflow plate and frame heat exchanger is shown in Figure 3.21. Plate frame heat exchangers consist of a heat transfer plate pack, gaskets, a fixed end plate, a moving end plate, long bolts that span the length of the plate pack, and a frame. The heat transfer plate pack consists of thin plates (~0.0003 m – 0.0007 m) that are separated by gaskets. After the plates and gaskets are compressed between the two end plates using the long bolts, alternating channels for the hot and cold heat transfer fluids are formed, shown in red and blue on Figure 3.21 [92]. The gaskets are used to keep the fluids in their respective flow channels. The channel spacing is typically on the order of 0.005 m. To describe the heat exchanger, the fluids enter the device in the inlet header and are distributed to each alternating flow channel. Then, the fluid will flow up

or down the plates and recollect in the return header to exit the device. The plates typically have corrugated herringbone patterns to increase heat transfer surface area and induce additional turbulence to improve heat transfer performance.

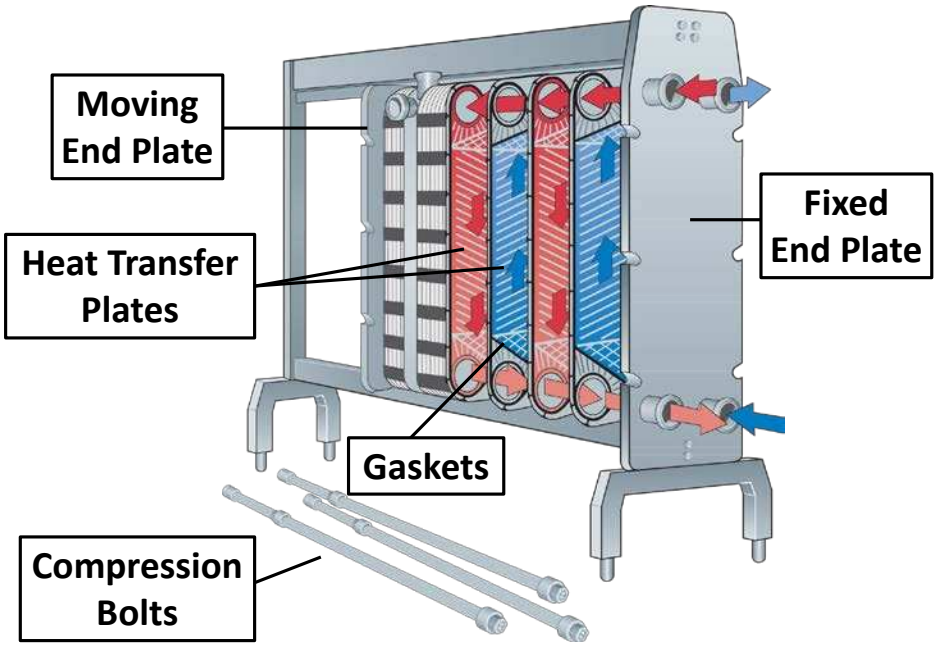

Figure 3.21 Plate Frame Heat Exchanger Construction [92].

The advantages of using plate frame heat exchangers for this application of the ORC, DMS, and TCCS which include small footprint, and ease of scalability. Plate frame heat exchangers are compact, resulting in a lower overall footprint of each of the technologies, which may allow for more flexibility when considering technology integration at a beef plant. Furthermore, the heat duty of each heat exchanger can be easily modified by adding or removing plates, which would allow for the plant operators to scale up or down the technologies if needed. Each heat exchanger modeled in this study was chosen to be a counter-flow, stainless steel plate and frame heat exchanger.

The technique used to model the plate and frame heat exchangers for the ORC, DMS, and TCCS is based on the technique used in a previous investigation conducted by Young et al. [93].

This technique aims to calculate how much heat exchanger area is required to achieve the necessary heat duty based on heat exchanger effectivenesses, calculated mass flows, and temperature differences which are determined by the thermodynamic model. Heat exchanger area is determined through the calculation of two properties for each heat exchanger region: number of transfer units (NTU) and overall heat transfer coefficient (U). In the following sections, the calculation of these properties will be discussed in detail.

3.3.1. Epsilon-NTU Heat Exchanger Method

In determining the cost of a heat exchanger, it is critical to calculate heat transfer area. To determine the area of each heat exchanger, the epsilon-NTU method is used for each region of each heat exchanger. The NTU method is often used when evaluating counter-flow heat exchangers where inlet and outlet temperatures are known. NTU, which stands for number of transfer units, is calculated for a counterflow heat exchanger as a function of heat exchanger effectiveness and heat capacity ratio. Figure 3.22a-d provides a schematic of a single plate in each of the heat exchangers in the ORC, DMS, and TCCS. As discussed in the previous section, each plate in the heat exchanger is connected in parallel with a gasket in between each plate. The gasket is depicted in gray, keeping the two streams in the heat exchanger separate. All four heat exchanger types (boiler, condenser, subcooler, and single phase) were modeled as counter flow devices. Each working fluid phase occupies a certain area of every refrigerant plate. In Figure 3.22a, the refrigerant enters the boiler at the bottom header as a subcooled liquid and is heated by the PG-water mixture. As it travels upward through the channel, energy is transferred to the refrigerant until it becomes a superheated vapor, exiting the device at the outlet header. The PG-water flows through the boiler in the opposite direction, entering the device in the upper manifold and traveling downward, transferring heat to the refrigerant until it exits at the lower manifold. In the subcooler,

shown in Figure 3.22b, the DMS or TCCS refrigerant enters the device at the lower manifold inlet header as a two-phase mixture and flow transferring energy to the PRS ammonia stream flowing in the opposite direction. The DMS or TCCS refrigerant exits the device at the upper manifold as a superheated vapor, while the PRS refrigerant exits at the lower manifold as a subcooled liquid.

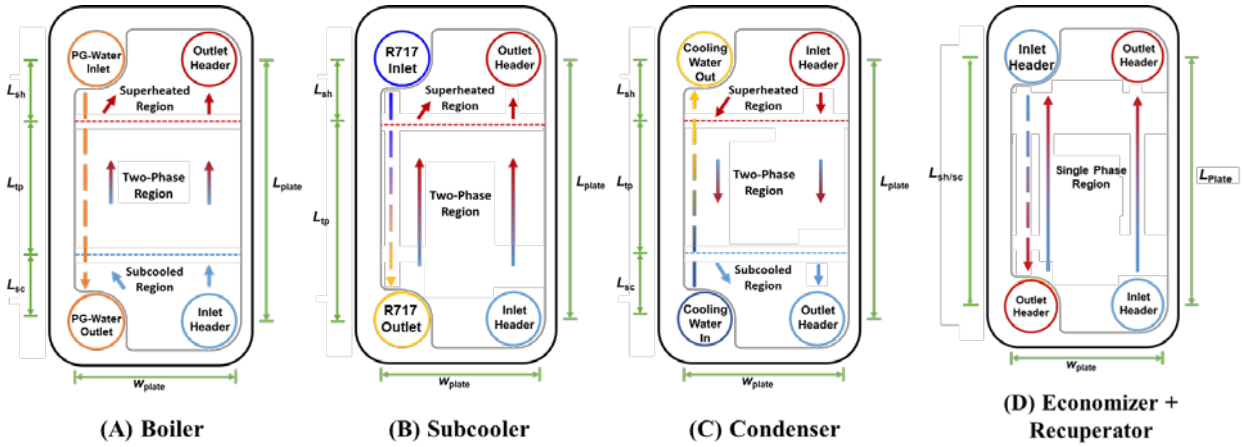

Figure 3.22 Flow path and working fluid regions for a single plate in the (A) TCCS/ORC boiler (B) TCCS/DMS subcooler (C) condensers and (D) recuperator and economizer.

In the condenser plates, shown in Figure 3.22c, the ORC, DMS, or TCCS refrigerant enters at the top header as a superheated vapor. The refrigerant is condensed to the liquid phase as it travels down the plates to the outlet header of the lower manifold. The cooling water stream enters at the bottom header and absorbs heat from the refrigerant as it travels upward through the device to the upper manifold. In the economizer and recuperator plates, shown in Figure 3.22d, the ORC, DMS, or TCCS refrigerant enters on both sides of the device, traveling in counterflow. On either side, the single phase refrigerant is either subcooled or superheated as it travels upward or downward through the device. For each region of each heat exchanger, the NTU is calculated based on heat exchanger effectiveness as shown in Equation (3.56)

$$NTU = \frac{1}{C_r - 1} \ln\left(\frac{\varepsilon - 1}{\varepsilon C_r - 1}\right) \tag{3.56}$$

where C_r is the heat capacity ratio which is defined as $C_r = C_{min}/C_{max}$. If $C_r = 1$, a different *NTU* equation is required, however that was never found to be the case in this research. In the two phase heat exchanger regions, where the heat capacity ratio is equal to zero, Equation (3.56) simplifies accordingly. Number of transfer units (NTU) for each heat exchanger region is then calculated using Equation (3.57).

$$NTU_{region} = \frac{U_{region} A_{region}}{C_{min}} \tag{3.57}$$

Where U_{region} is the overall heat transfer coefficient, A_{region} is the heat exchange area of each distinct region (subcooled, two-phase, or superheated), and C_{min} is the minimum heat capacity rate. Summing the areas of each region, total heat exchanger area required is calculated as shown in Equation (3.58).

$$A_{total} = A_{sc} + A_{tp} + A_{sh} \tag{3.58}$$

With total heat exchange area determined, the total number of plates required for each heat exchanger is calculated using Equation (3.59).

$$A_{total} = A_{plate}\left(N_{plate} - 1\right) = w_{plate}(L_{sc} + L_{tp} + L_{sh})(N_{plate} - 1) \tag{3.59}$$

The corrugation pattern was not accounted for in the area calculation, as this information was not provided by the heat exchanger manufacturer but was accounted for in the heat transfer calculation. Equation (3.58) and (3.59) were modified to be used for the subcooler and single-phase heat exchanger, which consist of less regions than the condensers and boiler. The subcooler does not have a subcooled region, because the working fluid is a two-phase mixture at the exit of the expansion valve, while the economizer and recuperator consist of a singular region where the fluid exists as either a subcooled liquid or superheated vapor.

Along with the calculation of NTU, it is necessary to also calculate U_{region}, which is the overall heat transfer coefficient in each heat exchanger region. The overall heat transfer coefficient U is calculated as shown in Equation (3.60):

$$U = \frac{1}{h_{\text{r}}} + R_{\text{wall}} + \frac{1}{h_{\text{w}}} \tag{3.60}$$

where h_{r} is the heat transfer coefficient on the refrigerant side, R_{wall} is the wall resistance of the heat exchanger plate, and h_{w} is the heat transfer coefficient of the external stream (PG-water, boiler feedwater, or ammonia). The wall resistance is based on the plate material and thickness and is defined as $R_{\text{wall}} = t_{\text{plate}}/k_{\text{plate}}$, where t_{plate} is the thickness of the plate from plate heat exchanger quotes and data sheets, and k_{plate} is the conductivity of the plate, which is selected to be made of stainless steel. Table 3.10 shows the geometry specifications of the plates in this study.

Table 3.10 Plate geometry inputs for the heat exchanger model [93].

Input	Value	Units
$\boldsymbol{L_{\text{plate}}}$	1.32	m
$\boldsymbol{w_{\text{plate}}}$	1.17	m
$\boldsymbol{t_{\text{plate}}}$	0.0007	m
$\boldsymbol{s_{\text{plate}}}$	0.0045	m
$\boldsymbol{D_{\text{header}}}$	0.35	m
$\boldsymbol{k_{\text{stainless}}}$	13.3	W m^{-1} K^{-1}

With the overall heat transfer coefficient *U*, and the number of transfer units *NTU* determined for each heat exchanger region, the area of each region in each heat exchanger is determined using Equation (3.57). In the next section, the calculation of heat transfer coefficient will be discussed in detail.

3.3.2. Determination of Overall Heat Transfer Coefficient

There are many correlations for heat transfer coefficient that are available in the literature, describing boiling, condensing, and single-phase flow through plate and frame heat exchangers.

In this study, three correlations were used to determine the heat transfer coefficient in each heat exchanger region. A summary of the correlations used for each fluid in each heat exchanger region is shown in Table 3.11. The correlations used in this study are the same as those used in prior TCCS research conducted by Young et al. [93], with the exception of the external stream correlations, where the Thonon correlation was used instead of the Dittus-Boelter correlation.

Table 3.11 Summary of heat transfer correlations used for each heat exchanger region [93].

Heat Exchanger	Fluid Side	Subcooled	Two-Phase	Superheated
Condenser	**R134a**	Thonon [94]	Kuo [95]	Thonon
	Feedwater	Thonon		
Boiler	**R134a**	Thonon	Hsieh [96]	Thonon
	PG -Water	Thonon		
Economizer & Recuperator	**R134a**	Thonon	-	
	R134a	-		Thonon
Subcooler	**R134a**	-	Hsieh	Thonon
	Ammonia	-	Thonon	

The Kuo correlation was used to calculate condensing heat transfer of R134a refrigerant. The Kuo correlation was developed for the condensation of R410a in compact plate frame heat exchangers, and is shown in Equation (3.61) [95]:

$$h_{\mathrm{r,cond}} = h_{\mathrm{r,l}}\left[0.25Co^{-0.45}Fr_l^{0.25} + Bo^{0.75}\right] \tag{3.61}$$

Where $h_{\mathrm{r,l}}$ is the single-phase heat transfer coefficient for liquid refrigerant in a plate heat exchanger, *Co* is the convection number, Fr_l is the Froude number, and *Bo* is the boiling number. As shown in Table 3.11, the Kuo correlation was used to calculate condensation heat transfer in the condensers (including the ORC, DMS, and TCCS condensers). The single-phase liquid heat transfer coefficient, $h_{\mathrm{r,l}}$, is defined by Kuo as shown in Equation (3.62):

$$h_{\mathrm{r,l}} = 0.2092\left(\frac{k_{\mathrm{l}}}{D_{\mathrm{hyd,chan}}}\right)Re_{\mathrm{l}}^{0.78}Pr_{\mathrm{l}}^{1/3}\left(\frac{\mu_{\mathrm{ave}}}{\mu_{\mathrm{wall}}}\right)^{0.14} \tag{3.62}$$

Where k_{l} is the conductivity of the liquid phase refrigerant, $D_{\mathrm{hyd,chan}}$ is the hydraulic diameter of the channel, Re_l is the Reynolds number of the liquid, Pr_l is the Prandtl number, and μ is the viscosity of the liquid refrigerant. In this study, the ratio of the average and wall viscosities of refrigerant was assumed to be unity. The hydraulic diameter of the channel is also defined by Kuo and is calculated in Equation (3.63):

$$D_{\mathrm{hyd,chan}} = \frac{4(A_c)}{P_{wetted}} = \frac{4(w_{\mathrm{plate}} s_{\mathrm{plate}})}{2(w_{\mathrm{plate}} + s_{\mathrm{plate}})} = 0.008966 \text{ [m]} \tag{3.63}$$

Where w_{plate} is the width of a single plate and s_{plate} is the spacing between each plate, which are both defined in Table 3.10. For the current study, the hydraulic diameter yields a value of 0.009 m for the fixed plate dimensions. The dimensionless numbers used in the Kuo correlation are calculated as shown in Equation (3.64) through Equation (3.68).

$$Re_{\mathrm{l}} = \frac{uL}{\nu} = \frac{4\dot{m}_{\mathrm{plate}}}{P_{\mathrm{wetted}}\,\mu_l} \tag{3.64}$$

$$\mathrm{Pr}_{\mathrm{l}} = \frac{\mu_{\mathrm{l}} c_l}{k_{\mathrm{l}}} \tag{3.65}$$

$$Co = \frac{\rho_{\mathrm{g}}}{\rho_{\mathrm{l}}}\left[\frac{1-x}{x}\right]^{0.5} \tag{3.66}$$

$$Fr_{\mathrm{l}} = \frac{G_{\mathrm{plate}}^2}{\rho_{\mathrm{l}}^2 g D_{\mathrm{hyd,chan}}} \tag{3.67}$$

$$Bo = \frac{q}{G_{\mathrm{plate}} i_{\mathrm{fg}}} \tag{3.68}$$

Where c_l is the liquid specific heat capacity, x is the quality, G is the refrigerant mass flux, g is the acceleration due to gravity, and i_{fg} is the refrigerant enthalpy of vaporization. The mass flow term $\dot{m}_{\mathrm{plate}}$ is the mass flow of a fluid through a single plate, which is calculated as shown in Equation (3.69):

$$\dot{m}_{\text{plate}} = \frac{\dot{m}}{0.5(N_{\text{plate}} - 1)} \tag{3.69}$$

Where N_{plate} is the number of plates total in the heat exchanger, and the calculation in the denominator represents the number of channels where either the refrigerant or external stream is flowing. Refrigerant mass flux, or G_{plate}, is calculated as shown in Equation (3.70):

$$G_{\text{plate}} = \frac{\dot{m}_{\text{plate}}}{s_{\text{plate}} w_{\text{plate}}} \tag{3.70}$$

The next correlation used in this study is the Hsieh correlation, which was determined for boiling R410a in a vertical plate heat exchanger. The Hsieh correlation was used for the two-phase region of refrigerant blowing through the boiler and subcooler, and is shown in Equation (3.71) [96]:

$$h_{\text{r,boil}} = h_{\text{r,l}}(88Bo^{0.5}) \tag{3.71}$$

where $h_{\text{r,l}}$ is the single-phase heat transfer coefficient calculated in Equation (3.62) and *Bo* is the boiling number calculated in Equation (3.68). The final correlation used in this study is the Thonon correlation, which is used for all single-phase flow in the heat exchangers examined in this study. The Thonon correlation is defined in Equation (3.72) [94].

$$h = 0.2998 Re_{\text{plate}}^{0.645} \text{Pr}^{1/3} \frac{k}{D_{\text{hyd,chan}}} \tag{3.72}$$

The Reynolds number range for the Thonon correlation is 50 < *Re* < 15,000. In some instances, the calculated Reynold's number was found to be outside of this region, which resulted in artificially high or low heat transfer coefficients, resulting in unrealistic heat exchanger areas. To avoid unrealistic results, the Reynold's number was set at either the minimum value of 50 or the maximum value of 15,000, which is consistent with the methodology used in Young et al. [93]. This concludes the calculation procedure for heat transfer coefficients for all regions of the heat

exchangers considered in this study. In the next section the economic model will be discussed in detail.

3.4. Economic Modeling

The economic model uses the outputs from the thermodynamic and heat exchanger models to estimate the capital cost and annual savings of the four technology options. Annual savings, or OPEX, of each technology is calculated from total annual electricity and natural gas savings, as well as EIA utility cost data for 2019 [81,82]. The capital cost, or CAPEX, of the ORC, DMS, and TCCS is calculated by determining the individual cost of all major components including heat exchangers, turbomachinery, piping, heat recovery, refrigerant, as well as other miscellaneous items. The CAPEX of the FWE was determined using a supplier quote [97]. The cost models were modified by the Chemical Engineering Plant Cost Index (CEPCI) for 2019 to more accurately represent present day cost [98]. With CAPEX and OPEX calculated, two other economic metrics are calculated including simple payback period, and net present value (NPV) of each technology option. The following sections will discuss in detail the calculations of OPEX, CAPEX, payback period, and NPV for each technology option.

3.4.1. Annual Savings

The thermodynamic models discussed in sections 3.2.3 through 3.2.6 describe how hourly natural gas and electricity savings are determined for the FWE, ORC, DMS, and TCCS. Each model is assumed to operate for 5,184 hours of the year based on boiler operation hours. To reiterate, the FWE reduces boiler natural gas use by preheating boiler feedwater using heat recovered from the exhaust gas. The ORC recovers heat from the boiler exhaust gas to vaporize a refrigerant which is used to generate electrical power in a turbine, offsetting the amount of grid electricity required at a beef plant. Further energy savings are achieved by the ORC by using the

ORC condenser heat to preheat boiler feedwater, resulting in boiler natural gas savings. The DMS provides subcooling to the PRS at a beef processing facility, which results in electricity savings via a reduction in overall PRS compressor work required to produce the overall refrigeration load. Like the ORC, the condenser heat produced by the DMS is also used to preheat boiler feedwater, resulting in boiler natural gas savings. The final technology option considered in this study is the TCCS, which is a waste heat driven subcooler, producing electricity savings in the same way as the DMS. Like the ORC and DMS, the condenser heat produced by the TCCS condensers is rejected to the boiler feedwater resulting in natural gas savings. With hourly energy savings determined, hourly monetary savings are calculated for each technology option as shown in Equation (3.73) through Equation (3.76):

$$Savings_{\text{total,FWE}} = Savings_{\text{gas,FWE}} * Cost_{\text{gas}} \tag{3.73}$$

$$Savings_{\text{total,ORC}} = Savings_{\text{gas,ORC}} * Cost_{\text{gas}} + Savings_{\text{elec,ORC}} * Cost_{\text{elec}} \tag{3.74}$$

$$Savings_{\text{total,DMS}} = Savings_{\text{gas,DMS}} * Cost_{\text{gas}} + Savings_{\text{elec,DMS}} * Cost_{\text{elec}} \tag{3.75}$$

$$Savings_{\text{total,TCCS}} = Savings_{\text{gas,TCCS}} * Cost_{\text{gas}} + Savings_{\text{elec,TCCS}} * Cost_{\text{elec}} \tag{3.76}$$

Where $Cost_{\text{gas}}$ is the cost of natural gas in \$/MCF, and $Cost_{\text{elec}}$ is the cost of electricity in \$/kWh. The utility cost data that was used in this study was based on the EIA's monthly industrial natural gas and electricity prices for 2018, for each location are shown considered in this study. Figure 3.23 shows the variation in electricity and natural gas costs throughout the year in each city modeled.

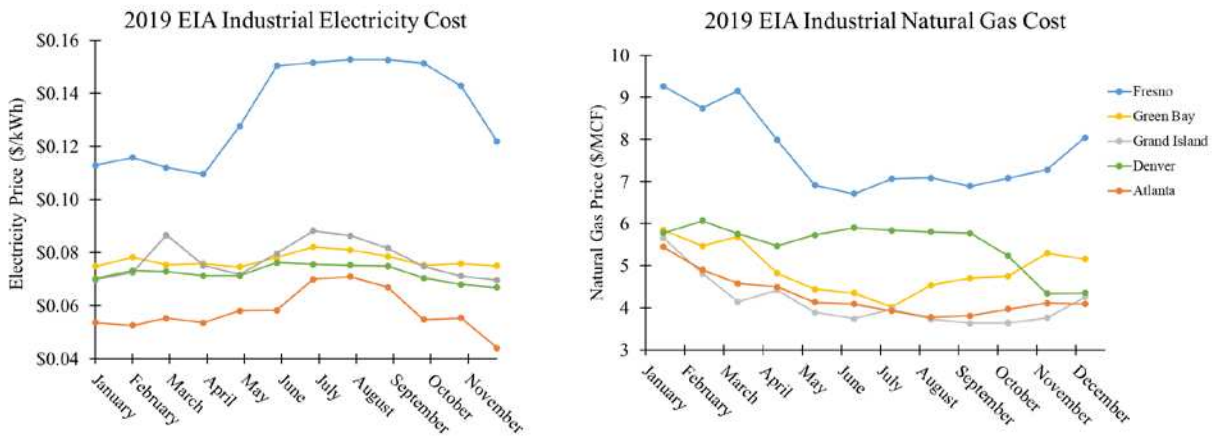

Figure 3.23 EIA industrial natural gas prices for five different states in 2019 [81,82].

After determining the hourly monetary savings achieved by each technology option, the overall annual savings, or OPEX, was calculated by summing all savings produced throughout the year. In the next section, the capital cost and simple payback period calculations for each technology option will be discussed in detail.

3.4.2. Cost Model and Simple Payback Period

The capital cost of each system was calculated as the sum of costs of each individual component. In this analysis, all major pieces of equipment were accounted for, including heat exchangers, turbomachinery, piping, refrigerant, heat recovery and other miscellaneous components. To estimate capital cost, it was necessary to choose a single point of operation for the TCCS and DMS, since the heat exchanger heat duties and turbomachinery work duties vary based on PRS operation. In this study, a PRS high-side pressure of 1367 kPa was selected as the operation point at which system cost would be determined. This pressure corresponds to the operational high-side pressure of the PRS during average summer ambient conditions in Denver, Colorado, calculated as shown in Appendix section A.1. Also, the baseline cost of each technology is assumed to be the same across the five locations considered in this study. In the following

subsections, the cost equations will be presented that were used to determine the overall system cost of the FWE, ORC, DMS, and TCCS.

3.4.2.1. Component Costing

The cost of the heat exchangers is based on the total area calculated in section 3.3.2. The cost of a plate and frame heat exchanger, taken from Brown, is calculated as shown in Equation (3.77) [99]:

$$cost_{\mathrm{HX}} = 475 * (A_{\mathrm{total}})^{0.54} * f_{\mathrm{pressure}} * \frac{CEPCI_{2019}}{CEPCI_{2005}} \tag{3.77}$$

Where $cost_{\mathrm{HX}}$ is the cost in dollars, A_{total} is the total area in ft^2, f_{pressure} is the pressure cost multiplier, and $CEPCI$ is the Chemical Engineering Plant Cost Index value for the designated year. $CEPCI_{2019}$ is equivalent to 607.5 and $CEPCI_{2005}$ is equal to 468 [98,100]. In the original cost model, there are two additional cost multipliers, for the gasket type and material, however in this analysis both are assumed to be 1. The pressure cost multiplier is equivalent to 1.23 for heat exchangers with a working pressure of 235-370 psig (1620-2551 kPa) and 1.35 for heat exchangers with a working pressure between greater than 370 psig (2551 kPa).

The next component for which cost was determined was the piping. Pipe cost is based on several factors including length and diameter. Table 3.12 lists pipe runs for each technology option as well as their working fluid phase and assumed diameter.

Table 3.12 Pipe Diameters for the ORC, DMS, and TCCS.

System	Pipe Run	Phase	Diameter (in.)
TCCS - PC	Boiler to Turbine	SH	3
	Turbine to Recuperator	SH	3
	Recuperator to Condenser	SH	3
	Condenser to Pump	SC	2
	Pump to Recuperator	SC	2
	Recuperator to Economizer	SC	2
	Economizer to Boiler	SC	2
TCCS - CC	Evaporator to compressor	SH	3
	Compressor to Economizer	SH	3
	Economizer to Condenser	SH	3
	Condenser to Expansion Valve	SC	2
ORC	Boiler to Turbine	SH	3
	Turbine to Recuperator	SH	3
	Recuperator to Condenser	SH	3
	Condenser to Pump	SC	2
	Pump to Recuperator	SC	2
	Recuperator to Boiler	SC	2
DMS	Evaporator to compressor	SH	3
	Compressor to Condenser	SH	3
	Condenser to Expansion Valve	SC	2

The cost model for steel system piping was taken from brown, and calculates piping cost as shown in Equation (3.78) [99]:

$$cost_{\text{pipe}} = f_{\text{material}} * 10 * \left(0.1N_{\text{fittings}} + 0.924\right) D_{\text{pipe}}^{0.83} L_{\text{pipe}} \frac{CEPCI_{2019}}{CEPCI_{2005}} \tag{3.78}$$

where $cost_{\text{pipe}}$ is the cost in dollars, $f_{material}$ is the piping material cost multiplier, which is 1.2 in this study for the sleeted material of 304L SS (schedule 10). $N_{fittings}$ is the number of fittings per 100 feet of pipe (equal to 16.67 in this work, or 1 fitting per 6 feet of pipe), D_{pipe} is the pipe diameter, and L_{pipe} is the length of pipe. In this study, all pipes were assumed to have a length of 2 meters (6.562 feet) and a diameter of either 2 or 3 inches, depending on the working fluid phase, as shown in Table 3.12.

The next piece of equipment considered in the cost model is the power cycle pump, which contributes to the overall cost of both the ORC and DMS. The pump cost model was adopted from Couper et al., and is calculated as shown in Equation (3.79) [101]:

$$cost_{\text{pump}} = F_{\text{type}} * cost_{base} * \frac{CEPCI_{2019}}{CEPCI_{1985}} \tag{3.79}$$

where $cost_{\text{pump}}$ is the cost in dollars, F_{type} is the pump type cost multiplier, and $cost_{\text{base}}$ is the base cost of the machine. $CEPCI_{1985}$ is equivalent to 325. F_{type} is calculated in Equation (3.80):

$$F_{\text{type}} = exp\left(b_1 + b_2 ln\left(\dot{V}\sqrt{H}\right) - b_3 ln\left(\dot{V}\sqrt{H}\right)^2\right) \tag{3.80}$$

where b_1, b_2, and b_3 are constants that depend on the type of pump, $\dot{V}$ is the flow rate in gallons per minute and H is the head delivered by the pump in feet. The pump in this study was selected to be a single stage centrifugal pump operating at 3550 RPM, which defines b_1, b_2, and b_3 as 0.0632, 0.2744, and -0.0253, respectively. $Cost_{\text{base}}$ of the pump is calculated as shown in Equation (3.81):

$$cost_{\text{base}} = 3exp\left(8.883 - 0.6019\left(ln\left(\dot{V}\sqrt{H}\right)\right) + 0.0519\left(ln\left(\dot{V}\sqrt{H}\right)^2\right)\right) \tag{3.81}$$

The next pieces of equipment considered in the cost model are the ORC turbine and the DMS compressor. The cost model for these items are also defined in Couper et al. and are shown in Equation (3.82) and (3.83) [101]:

$$cost_{\text{comp}} = 1810 * \left(\dot{W}_{\text{comp}}\right)^{0.71} * \frac{cepci_{2019}}{cepci_{1985}} \tag{3.82}$$

$$cost_{\text{turb}} = 378 * \left(\dot{W}_{\text{turb}}\right)^{0.81} * \frac{cepci_{2019}}{cepci_{1985}} \tag{3.83}$$

where $cost_{\text{comp}}$ and $cost_{\text{turb}}$ are the cost of the machines in dollars, and $\dot{W}$ is in horsepower. The compressor selected for the DMS is a screw compressor, and the cost model is applicable for compressors with work inputs between 10-800 HP and includes the cost of a driver. The turbine

selected for the ORC is a pressure discharge turbine, and the cost model is applicable for turbines with a power output of between 20-5000 HP.

The next piece of equipment included in the cost model is the turbocompressor, which was developed by Barber-Nichols, Inc. The cost model is based on a logarithmic fit of two different design points, 6 KW and 10 kW turbine power, of a high efficiency centrifugal turbocompressor. The cost model is a function of turbine power and is shown in Equation (3.84) [93]:

$$cost_{\mathrm{TC}} = cost_{6\ \mathrm{kw}} \left(\frac{\dot{W}_{\mathrm{turbine}}}{6\ kW} \right)^{\frac{\log\left(\frac{cost10kW}{cost6kW}\right)}{\log\left(\frac{10\mathrm{kw}}{6\mathrm{kw}}\right)}} \tag{3.84}$$

where $cost_{6\mathrm{kW}}$ and $cost_{10\mathrm{kW}}$ are the known costs for a 6 kW and 10 kW turbomachine, and $\dot{W}_{\mathrm{turbine}}$ is the actual work developed in the turbine of the turbocompressor.

The next piece of equipment included in the cost model is the heat recovery unit, which recovers heat from the boiler exhaust and delivers heat to the ORC and TCCS boilers. The cost of these items were estimated based on data published by a maker of feedwater economizers and is calculated as a function of waste heat delivered from the boiler exhaust as shown in Equation (3.85) [97]:

$$cost_{\mathrm{HR}} = 36.6(\dot{Q}_{\mathrm{boil}}) \tag{3.85}$$

where $cost_{\mathrm{HR}}$ is the cost of the heat recovery unit in dollars, and $\dot{Q}_{\mathrm{boil}}$ is the heat delivered to the ORC and TCCS boiler in kW. For the ORC and TCCS, $\dot{Q}_{\mathrm{boil}}$ is the fixed waste heat input of 631 kW. This equation is also used to calculate the cost of the FWE. For the FWE, $\dot{Q}_{\mathrm{boil}}$ is assumed to be the maximum waste heat delivered to the FWE which was found to be 1157 kW.

The final components included in the cost model are miscellaneous components, which include the chassis to house each system, as well as electronics and instrumentation to operate and monitor each system. The chassis, electronics, and instrumentation were each set at a fixed cost of

$1,500, $3,000, and $750, respectively [93]. In the next section, the calculations of refrigerant charge and cost will be discussed in detail.

3.4.2.2. Refrigerant Charge

The cost of refrigerant in the ORC, DMS, and TCCS was calculated by determining the total mass of refrigerant in each system's heat exchangers and pipes. To calculate mass, the internal volume of each exchanger is calculated, and multiplied by the density of refrigerant in each section. The total mass of refrigerant in the boiler, condenser and subcooler plate and frame heat exchanger are calculated as shown in Equation (3.86):

$$m_{\text{boil/cond/subcool}} = m_{\text{header,i}} + m_{\text{channel}} + m_{\text{header,o}} \tag{3.86}$$

where $m_{\text{header,i}}$ is the mass of refrigerant in the inlet header of the heat exchanger, m_{channel} is the mass of refrigerant in the working fluid channels, and $m_{\text{header,o}}$is the mass of refrigerant in the outlet header. For the economizer and recuperator, which are internal heat exchangers with refrigerant on both sides, the total mass of refrigerant in the heat exchanger is calculated as shown in Equation (3.87):

$$m_{\text{econ/recup}} = m_{\text{header,sc,i}} + m_{\text{channel,sc}} + m_{\text{header,sc,o}} + m_{\text{header,sh,i}} + m_{\text{channel,sh}} + m_{\text{header,sh,o}} \tag{3.87}$$

where header and channel terms with the 'sc' and 'sh' designation represent the mass of refrigerant on the subcooled and superheated sides of the heat exchanger, respectively. The refrigerant charge in the headers of each heat exchanger are calculated as shown in Equation (3.88):

$$m_{\text{header}} = \rho_{\text{header}} \left(\frac{\pi D^2}{4} \right) * L_{\text{header}} \tag{3.88}$$

where ρ_{header} is the density of refrigerant in the header, D is the header diameter which is set to 0.35m as shown in Table 3.10, and L_{header} is the length of the header, which is calculated in Equation (3.89):

$$L_{\text{header}} = \left(N_{\text{plates}} * t_{\text{plate}}\right) + S_{\text{plate}}(N_{\text{plates}} - 2) \tag{3.89}$$

where N_{plates} is total number of plates in the heat exchanger, t_{plate} is the plate thickness, and S_{plate} is the spacing between plates (or channel width). Plate thickness and spacing are also fixed inputs which are listed in Table 3.10. The total channel volume of the boiler, condenser, subcooler, economizer, and recuperator are calculated in Equations (3.90) through (3.92).

$$V_{\text{channel,boil/cond}} = V_{\text{ch,sc}} + V_{\text{ch,tp}} + V_{\text{ch,sh}} \tag{3.90}$$

$$V_{\text{channel,subcool}} = V_{\text{ch,tp}} + V_{\text{ch,sh}} \tag{3.91}$$

$$V_{\text{channel,econ/recup}} = V_{\text{ch,sc}} + V_{\text{ch,sh}} \tag{3.92}$$

The volume of refrigerant in the specific regions of each heat exchanger are calculated as shown in Equation (3.93):

$$V_{\text{ch,region}} = A_{\text{region}}(S_{\text{plate}}) \tag{3.93}$$

where A_{region} is the total area of each region calculated in the heat exchanger model. Once volume in each region is calculated, the mass of refrigerant in each heat exchanger region can be determined using Equation (3.94):

$$m_{\text{ch,region}} = \rho_{\text{region}}(V_{\text{ch,region}}) \tag{3.94}$$

where $m_{\text{ch,region}}$ is the mass of refrigerant in the specified region and ρ_{region} is the density of the refrigerant in the region. For the two-phase regions of the boiler, condensers, and subcooler density is calculated as the average between the density of the working fluid as a saturated liquid and saturated vapor, shown in Equation (3.95):

$$\rho_{\text{tp}} = 0.5(\rho_{\text{l}} + \rho_{v}) \tag{3.95}$$

After refrigerant charge in the heat exchangers is determined, mass of refrigerant in the pipes of the ORC, DMS and TCCS is calculated as shown in Equation (3.96):

$$m_{\text{ref,piping}} = \rho_{\text{piping}}(V_{\text{piping}}) = \rho_{\text{piping}}\left(\left(\frac{\pi D^2}{4}\right) * L_{\text{pipe}}\right) \tag{3.96}$$

where ρ_{piping} is the density of refrigerant in the pipe, and V_{piping} is the internal volume of the pipe. The internal volume of the pipe is calculated using D which is the pipe diameter, and L which is the pipe length, both of which are fixed as discussed in the component costing section. Once the mass of refrigerant is calculated for the heat exchangers and pipes, the cost of refrigerant is calculated as shown in Equation (3.97):

$$cost_{\text{ref,total}} = m_{\text{ref,total}} * cost_{\text{ref,specific}} \tag{3.97}$$

where $m_{\text{ref,total}}$ is the total charge of the system and $cost_{\text{ref,specific}}$ is the cost per kilogram of refrigerant. In this study, the cost of R134a is assumed to be \$11 kG^{-1} [93]. In the next section the calculation of overall system cost and payback period will be discussed.

3.4.2.3. Simple Payback Period

Once the cost has been estimated for each individual component, the total install cost (or CAPEX) of the ORC, DMS, and TCCS is calculated as shown in Equation (3.98) through (3.100):

$$cost_{\text{ORC,total}} = f_{\text{install}}(cost_{\text{HX}} + cost_{\text{ref}} + cost_{\text{turb}} + cost_{\text{pump}} + cost_{\text{piping}} + cost_{\text{hr}} + cost_{\text{misc}}) \tag{3.98}$$

$$cost_{DMS,\text{total}} = f_{\text{install}}(cost_{\text{HX}} + cost_{\text{ref}} + cost_{\text{comp}} + cost_{\text{piping}} + cost_{\text{misc}}) \tag{3.99}$$

$$cost_{\text{TCCS,total}} = f_{\text{install}}(cost_{\text{HX}} + cost_{\text{ref}} + cost_{TC} + cost_{\text{pump}} + cost_{\text{piping}} + cost_{\text{misc}}) \tag{3.100}$$

where $cost_{system}$ is the total installation cost of the ORC, DMS, and TCCS in dollars, $f_{install}$ is the installation factor, $cost_{HX}$ is the total heat exchanger cost, $cost_{ref}$ is the total refrigerant cost, $cost_{turb}$ is the turbine generator cost, $cost_{pump}$ is the power cycle pump cost, $cost_{piping}$ is the total piping cost, $cost_{HR}$ is the cost of the heat recovery unit, and $cost_{misc}$ is the cost of miscellaneous items including chassis, instrumentation, and electronics. Two different installation factors were used for the ORC, DMS, and TCCS. For the ORC and DMS, an installation factor of 1.2 was used, while a factor of 1.6 was used for the TCCS. The ORC and DMS factor was based on an install factor determined for a commercial chiller unit, while the TCCS install factor was based on an install factor determined for an Absorption chiller, which is an alternative waste heat driven cooling system [102,103]. An install factor of 1.2 was also used for the FWE. Considering these factors, it makes sense to use a slightly higher install factor for the TCCS due to its increase in components and complexity over the other three technologies. After total install cost is calculated for each technology, payback period can be determined. The simple payback period is the total cost of the technology divided by the annual cost savings, as shown in Equation (3.101):

$$Payback\ Period = \frac{cost_{\text{total,technology}}}{Annual\ Savings} = \frac{f_{install} * \sum cost_{\text{component}}}{\sum_{i=1}^{5184} Savings_{\text{hourly}}} \tag{3.101}$$

where $cost_{\text{total,technology}}$ is the total install cost of the technology, and $Annual\ Savings$ is the total yearly savings of a technology, which is calculated as the sum of all hourly savings throughout all operation hours in the year. This concludes the discussion of capital cost and simple payback period. In the next section, the calculation of net present value (NPV) will be discussed.

3.4.3. Net Present Value

In addition to calculating payback period, annual savings and capital cost of each technology were also used to determine the net present value of each technology option. Net

present value is a useful metric to assess the economic viability of an investment as it takes into consideration cash flow throughout the lifetime of a project, taking into account the time value of money, along with operational costs throughout the lifetime of each technology option. The constant inputs for the NPV calculation are shown in Table 3.13, which were chosen in accordance with the 'nth' plant design considerations [104]. In this analysis, the capital cost, and annual savings of the TCCS, ORC, and DMS were assumed to be constant. The lifetime of each system in this analysis is assumed to be 10 years. An internal rate of return was chosen to be 10% for all systems because each technology represents a new technology at a beef plant, representing some risk. All systems were assumed to be built over a 3-year period with a startup time of 6 months, which is consistent with prior TCCS investigations [93]. The startup time implies that the system is only providing 50% of the total annual savings for the first 6 months of operation as the system is commissioned and troubleshooting is performed. To investigate the economic impact of construction period and start up time, NPV of each technology was recalculated assuming a 1-year construction period and startup time of 3 months. The maintenance of each system was chosen to be 3% of the total capital cost for each year of operation. The loan period of is assumed to be 10 years, and the loan interest rate is assumed to be 8% with payments made yearly. The loan principal for each system is assumed to be 40% of the total equipment and facilities cost. The tax rate used was based on the corporate income tax rate for each of the five locations [105]. The depreciation schedule was chosen to occur over 7 years in modified accelerated cost recovery system (MACRS), which is the current depreciation schedule in the United States.

Table 3.13 Fixed inputs for the NPV analysis.

Fixed Inputs	Value
Project Lifetime	10 Years
IRR	10%
Construction Period	3 Years [93]
Startup Time	0.5 Years [93]
Maintenance Cost	3% of Capex (yearly)
Loan Period	10 Years
Loan Interest Rate	8%
Loan Principal	40%
Tax Rate	7.2% (average) [105]
Depreciation Schedule	MACRS (7 year)

The goal of the analysis is to determine the NPV of each technology over a 10-year lifetime. Net present value is determined by calculating the costs, or negative cash flows, and benefits, or positive cash flows of an investment. The NPV of an investment is calculated as shown in Equation (3.102):

$$NPV = NPB - NPC \tag{3.102}$$

where *NPV* is the net present value, *NPB* is the net present benefits, and *NPC* is the net present costs. *NPB* and *NPC* are calculated as shown in Equation (3.103) and (3.104):

$$NPB = \frac{1}{(1+IRR)^{y}} \sum_{y=1}^{10} (Annual\ Benefit) \tag{3.103}$$

$$NPC = \frac{1}{(1+IRR)^{y}} \sum_{y=1}^{10} (Annual\ Cost) \tag{3.104}$$

where *IRR* is the assumed internal rate of return, and *y* is the year of operation. The calculation of $1/(1+IRR)^{y}$ is representative of the discount factor, which in this analysis is the factor that

brings both annual benefits and costs into the present. The annual benefit is calculated as shown in Equation (3.105):

$$annual\ benefit = annual\ aavings - loan - operational\ cost - tax \tag{3.105}$$

where *annual savings* is the yearly savings of each technology, *loan* represents the annual loan payment, *operational cost* represents annual cost associated with maintaining the system, and *tax* represents income tax associated with the annual earnings of the system. The annual cost is calculated as shown in Equation (3.106):

$$annual\ cost = CAPEX + interest \tag{3.106}$$

Where *CAPEX* is the annual equipment capital, and *interest* is the annual loan interest payment. Using this methodology, the NPV of all four technologies was calculated. This concludes the economic modeling block. The next section will detail the optimization study that was conducted to determine optimal system size of the ORC, DMS, and TCCS to minimize payback period and maximize NPV.

3.5. System Optimization

Finally, after the complete evaluation of both the thermodynamic and economic models of the technologies was completed, a system optimization routine was completed to investigate the relationship between heat exchanger size, performance, and overall system economics. The strategy used in the optimization study was to vary the input heat exchanger effectiveness values for each system to see if an optimal economic point could be achieved. In this study, an optimal economic point is one where the technology payback period is minimized, or NPV is maximized. The optimization parameter was selected to be heat exchanger effectiveness for several reasons. First, there are many heat exchanger effectiveness inputs, which altogether have a profound impact on the overall performance of each technology. Each heat exchanger considered in this study has

between one and three effectiveness inputs, depending on the number of regions in the device. Secondly, heat exchangers are the most expensive individual component in a thermal energy system, which in some instances can account for as much as 75% of the total system cost [93].

For these reasons, heat exchanger effectiveness inputs are an ideal optimization parameter. Baseline heat exchanger effectiveness inputs for the TCCS, ORC, and DMS are shown in Table 3.14. The only two heat exchanger regions that effectiveness was not set as a fixed input were the superheated regions in both the power and cooling cycle condensers, due to variable constraints.

Table 3.14 Baseline effectiveness inputs for the TCCS, ORC, and DMS systems.

HX	Region	TCCS	ORC	DMS
		Effectiveness (ε)		
Boiler	**tp**	0.35	0.35	N/A
	sh	0.7	0.7	N/A
Recuperator	**-**	0.7	0.7	N/A
PC Condenser	**tp**	0.7	0.7	N/A
	sc	0.1	0.1	N/A
Economizer	**-**	0.7	N/A	N/A
Subcooler	**tp**	0.7	N/A	0.7
	sh	0.7	N/A	0.7
CC Condenser	**tp**	0.7	N/A	0.7
	sc	0.1	N/A	0.1

The optimization process used in this study involves altering all the effectiveness values in each system by +/- 10% of their baseline value shown in Table 3.14, which leads to a new calculation of both annual savings and overall system cost. With these two parameters determined, payback period and NPV can then be recalculated. For the TCCS and DMS, effectiveness values were varied from +10% to -50% before an optimal point was found. When the TCCS effectiveness values were varied by -40% and lower, it was necessary to remove the economizer entirely for the

simulation to solve. For the ORC, effectiveness values were varied between +10% and -70% before an economic conclusion was determined. At the lowest effectiveness input of -70%, it was necessary to remove the recuperator entirely for the simulation to solve.

The only technology that was not included in the optimization routine was the FWE. The FWE as not included in the optimization study for several reasons. Firstly, because the capital cost of the FWE is based off a supplier quote, there is no model in this study that relates heat exchanger effectiveness to capital cost. In section 3.2.3, a model is developed to relate FWE performance to annual savings, however, FWE effectiveness is not set, but rather solved for as a function of boiler exhaust and feedwater inlet and outlet temperatures. Finally, an optimization study was not considered for the FWE because the initial payback period was found to be much lower than the other three technologies, deeming an optimization study unnecessary.

CHAPTER 4. Results and Discussion

Using the optimization routine described in Section 3.5, a minimum payback period and maximum net present value was determined for the ORC, DMS and TCCS. Once optimized, these three technologies each represent competitive economic alternatives to the FWE as potential technologies to reduce energy use and produce savings at a beef processing facility. In the following sections, the baseline thermodynamic, heat transfer, and economic performance of these technologies will be presented. After presenting the baseline results, the optimization process will be described, which seeks to evaluate the tradeoff between system performance and economics for the ORC, DMS, and TCCS.

4.1. Baseline Thermodynamic Performance

In this study, four technologies were thermodynamically modeled to provide energy savings at a beef processing plant. The technologies include a feedwater economizer, an organic Rankine cycle, a dedicated mechanical subcooler, and a turbo compression cooling system. The first technology modeled was the FWE. The FWE is the simplest of the four technologies, generating savings by preheating water entering the plant boiler by recycling heat that is rejected in the beef plant boiler's exhaust. By preheating boiler feedwater, the economizer enables the boiler to operate at a lower natural gas consumption rate while still providing the overall heated water demand, resulting in energy savings. A thermodynamic simulation of the boiler and FWE was conducted, which determines economizer gas savings as a function of boiler natural gas data, plant water data, as well as thermodynamic assumptions which are discussed in section 3.2.3. The boiler considered in this study has an average thermal output of 9.7 MW, and an average feedwater

flow rate of 52.4 kg/s. Figure 4.1 shows the hourly natural gas savings throughout the year of the FWE.

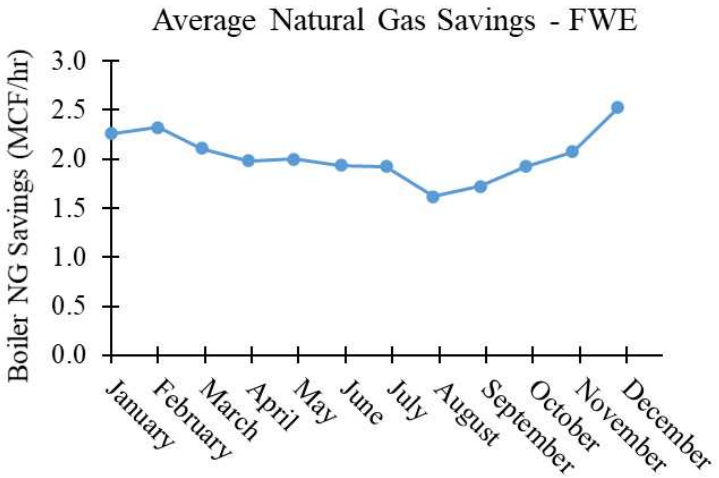

Figure 4.1 Hourly natural gas savings produced by the FWE throughout the year, averaged by month.

On average, the FWE reduces boiler natural gas consumption by 2.02 MCF/hr. For a boiler which operates at an average of 38 MCF/hr, this corresponds to approximately a 5% reduction, which is consistent with values found in the literature [91].The trend of FWE fuel savings throughout the year is directly correlated with overall boiler natural gas use. When the hot water demand of the plant increases, the boilers must consume an increased amount of fuel to meet that demand, which results in greater amounts of waste heat being rejected in the exhaust, allowing for greater amounts of economizing and increased fuel savings. Table 4.1 shows the outputs from the FWE thermodynamic model.

Table 4.1 FWE thermodynamic model outputs

Model Output	Value	Unit
$\dot{Q}_{\mathbf{FWE}}$	646	kW
$T_{\mathbf{w,out}}$	18.4	°C
$\varepsilon_{\mathbf{FWE}}$	0.441	-
Average Fuel Savings	2.02	MCF/hr
Annual Fuel Savings	10535	MCF

On average the economizer was found to recover 646 kW of exhaust heat from the boiler, heating the feedwater from 15.6°C to 18.4°C. The effectiveness of the economizer heat exchanger was calculated to be 0.441, and the total annual fuel savings was calculated to be 10535 MCF. Because the boiler and FWE models are not reliant on ambient weather conditions, the fuel savings of the FWE is the same across all five locations.

The next technology considered is the organic Rankine Cycle, which is discussed in section 3.2.4. The ORC is a thermodynamic cycle that generates power by expanding a superheated refrigerant through a power generating turbine. Considering the application of beef processing, an ORC could be installed to generate additional electricity, offsetting the amount of grid that taken from the grid, and thus resulting in energy savings. The thermal energy source of the ORC was selected to be the heated exhaust gas from the plant boiler. Additionally, the ORC in this work is configured to provide further energy savings by rejecting the heat in the condenser to the feedwater entering the boiler, which allows for a reduction in boiler natural gas consumption. The ORC thermodynamic model outputs are shown in Table 4.2.

Table 4.2 Thermodynamic results of the ORC model

Output	Value	Unit
$\dot{m}_{\mathbf{ORC}}$	2.96	kg/s
$\dot{m}_{\mathbf{pg-water}}$	15.6	kg/s
$\dot{Q}_{\mathbf{recup}}$	25.9	kW
$\dot{Q}_{\mathbf{cond}}$	559	kW
$\dot{W}_{\mathbf{turb}}$	80.7	kW
$\dot{W}_{\mathbf{pump}}$	8.18	kW
$\varepsilon_{\mathbf{b,sc}}$	0.99	-
$\varepsilon_{\mathbf{c,sh}}$	0.828	-
$T_{\mathbf{cond,w,out}}$	18.1	°C
$Savings_{\mathbf{elec,ORC}}$	68.5	kW
$Savings_{\mathbf{gas,ORC}}$	1.75	MCF/hr
$\eta_{\mathbf{ORC}}$	12.6	%

Like the FWE, the ORC is not dependent on ambient weather conditions and thus performance does not vary between locations or throughout the year. The ORC, which accepts 631 kW of waste heat from the boiler exhaust, operates at a thermal efficiency of 12.6%, producing 80.7 kW of work in the turbine. This work is transferred into electricity with a generator, resulting in hourly electricity savings of 68.5 kW. The heat rejected in the ORC condenser was found to be 559 kW, which corresponds to a 1.75 MCF/hr. reduction in boiler natural gas consumption. In total, the ORC was found to produce an average annual electricity savings of 355,000 kWh, and a total annual natural gas savings of 9,062 MCF.

The next technology considered in this work is the dedicated mechanical subcooler. The DMS is a small, secondary vapor compression cycle that provides condenser subcooling to the primary refrigeration system at beef processing plant. By providing subcooling at the PRS condenser outlet, the PRS refrigerant enters the evaporator as a lower quality two-phase refrigerant, allowing for a reduction in PRS compressor work to produce the overall cooling load. When overall PRS compressor work is reduced, the plant can reduce the amount of electricity that is taken from the grid, which results in energy savings. The DMS was simulated at an hourly resolution, providing subcooling to a PRS in five different cities with varying ambient conditions: ambient conditions impact refrigeration performance due to the PRS condenser cooling tower, which increases or decreases the high-side pressure of the PRS depending on the ambient temperature, pressure, and relative humidity. Figure 4.2a-b shows the operating temperatures and mass flows of the DMS and PRS throughout the year, averaged between the five different cities.

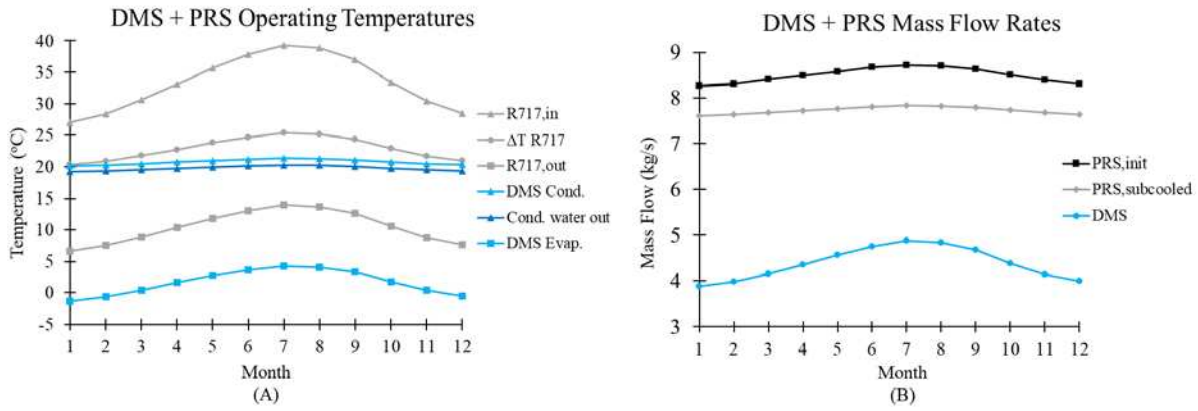

Figure 4.2 Operating temperatures (A) and Mass flows (B) of the PRS and DMS throughout the year. Temperature data shown is averaged from the five different cities considered in this study.

The thermodynamic simulation was produced using EES, and accounts for hourly PRS pressure variation which was determined in the beef plant refrigeration model. During the summer months, the DMS capitalizes on the inefficiencies of the PRS by operating at a higher evaporator temperature, lower pressure ratio, and higher mass flow rate. For example, in July, the PRS operates at its lowest efficiency due to hot and humid ambient conditions (Figure 3.6d). This results in a high PRS condenser pressure of 1530 kPa, and subcooler inlet temperature of 39.3°C (Figure 4.2a). The DMS adjusts to the high temperature and pressure of ammonia by operating at a high evaporator temperature of 4.3°C. Looking at the DMS condenser temperature, variation throughout the year is low because the inlet temperature of water to the DMS condenser is set constant at 15.56°C. With a high evaporator temperature and relatively constant condenser temperature, the pressure ratio is much lower in July, so the DMS can operate at an increased mass flow rate of 4.88 kg/s (Figure 4.2b). When operating at a higher mass flow rate, more subcooling is provided to the PRS resulting greater reduction in PRS mass flow rate. In July, the PRS mass flow is reduced by 0.89 kg/s (from 8.72 kg/s-7.83 kg/s). In contrast, the PRS performs the most efficiently in December, when ambient weather conditions are cold and dry, operating at a lower condenser pressure of 1080 kPa, and saturation temperature of 27°C. To account for the lower pressure and

temperature of ammonia, the DMS operates at a low evaporator temperature of -1.31°C, resulting in an increased DMS pressure ratio. At a greater pressure ratio, and fixed compressor work input, the DMS must operate at a lower mass flow rate of 3.9 kg/s. Therefore, less subcooling is provided to the PRS, and the reduction in PRS mass flow rate is lower. In December, the PRS mass flow is reduced by 0.65 kg/s (from 8.26 kg/s to 7.61 kg/s).

When greater subcooling is provided at higher mass flow rates, the DMS condenser heat rejection must increase as well. Heat transfer in the DMS heat exchangers as well as DMS performance for each location throughout the year are plotted in Figure 4.3a-b. Considering Figure 4.3a, Condenser heat rejection is consistently 79 kW greater than subcooling, which is equivalent to the amount of DMS compressor work being added.

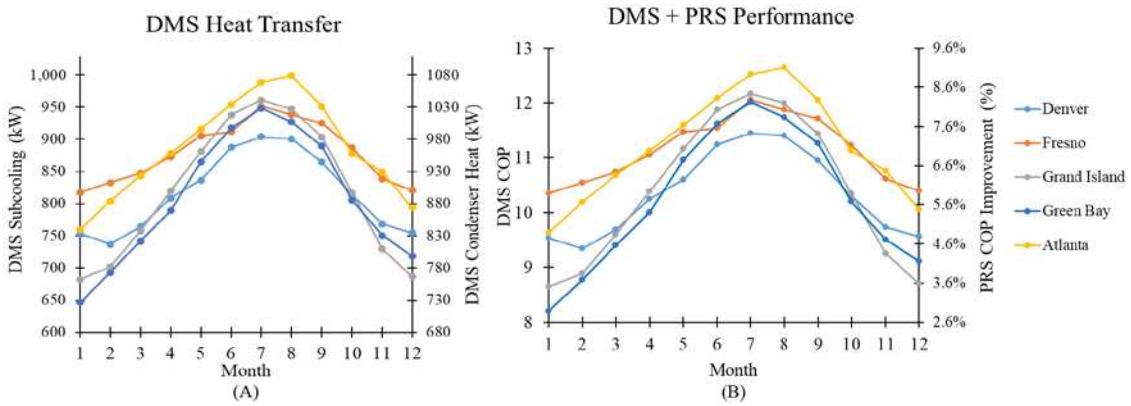

Figure 4.3 (A) DMS Subcooler and Condenser Heat Transfer in five locations throughout the year. (B) COP of the DMS, and PRS COP improvement provided by the DMS in five locations throughout the year.

Considering these results, the COP of the DMS was found to range from 8.2-12.7 throughout the year, which is much higher than the COP of a standard performing VCRC. This is a result of several factors, including the high temperature and pressure of the ammonia stream being subcooled and the comparatively low temperature of feedwater being used to cool DMS refrigerant in the condenser. Again, performance correlates well with wet bulb temperature, which

reduces PRS performance. In Atlanta in August, when wet bulb temperature is 22.5°C, The DMS achieves its highest COP of 12.7, improving the PRS cycle COP by 9.1%, while providing 1000 kW of subcooling and 1079 kW of heat rejection in the Feedwater. The performance of the DMS was the lowest in Green Bay in December, when wet bulb temperature is the lowest of any month in any city at -11.1°C. Recalling from Section 3.2.1, this is the month and city where the PRS performed best, achieving a COP of 5.3, due to low condenser water temperatures allowing for low ammonia condenser pressures. At low ammonia pressure and temperatures, the DMS operates at a lower evaporator temperature, which increases the pressure ratio and reduces efficiency. In Green Bay in December, the DMS COP is 8.2, improving the PRS only by 2.7%, while providing 648 kW of subcooling and 727 kW of condensing. Although performance is lowered, the general performance of the DMS is still very high throughout the year because of the high pressure and temperature of the ammonia stream and the low temperature of condenser water.

Finally, electricity and natural gas savings provided by the DMS are calculated for each operation hour. Average hourly energy savings provided by the DMS during each month are plotted in Figure 4.4. Hourly Electricity savings ranged from 40-260 kWh, and natural gas savings ranged from 2.3-3.4 MCF/hr. In general, energy savings correlate well with wet bulb temperature and PRS condenser pressure trends. For Example, in Denver, the wet bulb temperature decreases slightly from January to February, resulting in a decrease om PRS condenser pressure from 1110 kPa in January to 1090 kPa in February (Figure 3.6a). As a result, the DMS performs less efficiently, so subcooling and heat rejection are less. Looking at the Denver trend in Figure 4.3a, from January to February, average subcooling decreased from 754 kW-738 kW, and average condenser heat rejection decreased from 834 kW-817 kW. Thus, average hourly gas and electricity savings (Figure 4.4) decrease, from 104kWh-95kWh and 2.65MCF/hr-2.56MCF/hr, respectively.

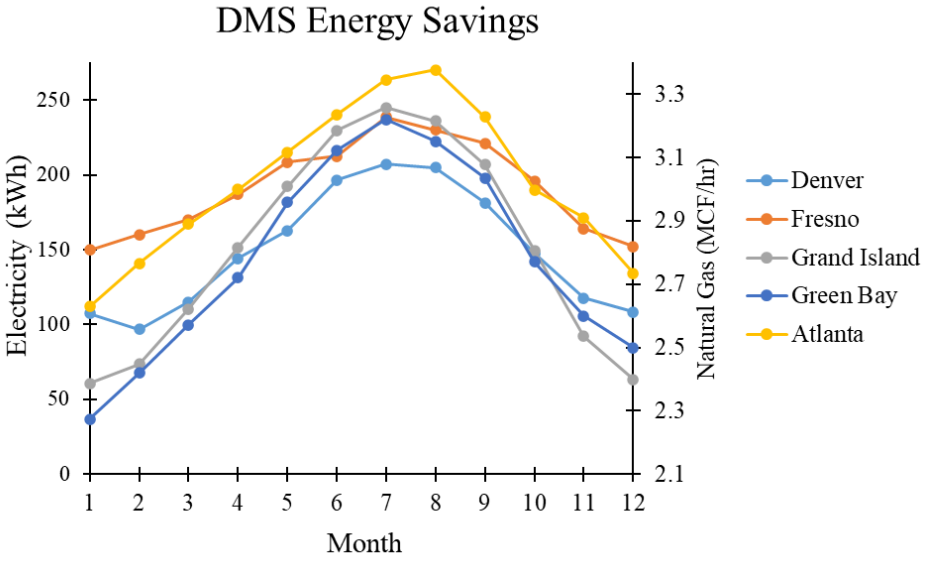

Figure 4.4 Operating temperatures (A) and Mass flows (B) of the TCCS and DMS throughout the year. Temperature data shown is averaged from the five different cities considered in this study.

The final technology considered in this research is the turbocompression cooling system. The TCCS produces energy savings in the same way as the DMS, by providing subcooling to the PRS. However, unlike the DMS, the TCCS is a thermally driven cooling technology, which uses waste heat to drive the turbine of a power cycle which is directly coupled to the compressor of a cooling cycle used to provide PRS subcooling. Thus, while the amount of subcooling that the DMS can provide comes as a tradeoff with additional compressor work, the thermally driven TCCS subcooler is bound primarily by waste heat availability. Like the ORC and DMS, the TCCS was also configured to provide natural gas savings via condenser heat rejection. The thermodynamic model of the TCCS was ran for all boiler operation hours in the year to determine thermodynamic state points, flow rates, heat duties, and energy savings. The primary inputs for the TCCS model are waste heat, which was found from the boiler model to be 631 kW, and PRS high-side pressure, which varies throughout the year based on ambient weather conditions. Figure 4.5a-b shows the

operating temperatures and mass flows of the TCCS and PRS throughout the year, averaged between the five different cities.

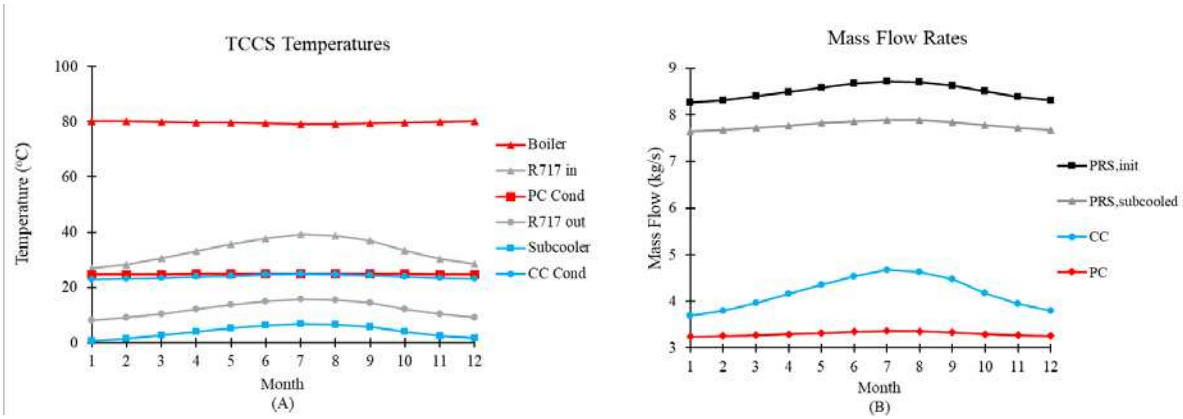

Figure 4.5 Operating temperatures (A) and mass flows (B) of the TCCS and DMS throughout the year. Temperature data shown is averaged from the five different cities considered in this study.

Looking at yearly performance, the TCCS power cycle operates the same throughout the year, operating at average boiler and condenser temperatures of 80°C and 25°C, respectively, and a refrigerant mass flow rate of 3.3 kg/s. The TCCS power cycle operates the same throughout the year because of the fixed waste heat input, as well as the fixed condenser water flow rate and temperature. The TCCS cooling cycle operates in the same way as the DMS, at a lower pressure ratio and increased mass flow rate during the summer months, when the PRS condenser pressure is greater. In July, the TCCS operates at its highest average subcooler temperature (6.8°C) and mass flow rate (4.67 kg/s). In January, when the PRS condenser pressure is lowest, the TCCS operates at the lowers subcooler temperature (0.7°C) and cooling cycle mass flow rate (3.7 kg/s).

Figure 4.6A shows the average heat transfer that occurs in each of the TCCS heat exchangers, and Figure 4.6B shows the performance of the TCCS as well as the performance improvement provided by the TCCS to the PRS. Comparing the TCCS to the ORC and DMS reveals that cooling and power cycles of the TCCS both perform less efficiently than the standalone

ORC and DMS. This is due to lowered condenser water flow rate being distributed to each of the TCCS condensers, which reduces the efficiency of each sub cycle. Comparing the power cycle of the TCCS to the ORC, the average efficiency of the ORC is 12.6% (Table 4.2), while the average efficiency of the TCCS power cycle is 12.3%. Thus, slightly less work is delivered to the cooling cycle of the TCCS than the DMS. Adding to this, cooling cyle condenser water flow rate is lower (52.4 kg/s in the DMS versus 30.7 kg/s in the TCCS cooling cycle), resulting in a lower cooling cycle refrigerant flow rate. In July, the average mass flow rate of the DMS is 4.88 kg/s (Figure 4.2b), versus the TCCS cooling cycle which is 4.67 kg/s (Figure 4.5b). As a result, the TCCS is only able to provide 891 kW of subcooling to the PRS (Figure 4.6a), versus the DMS, which provides an average of 952 kW.

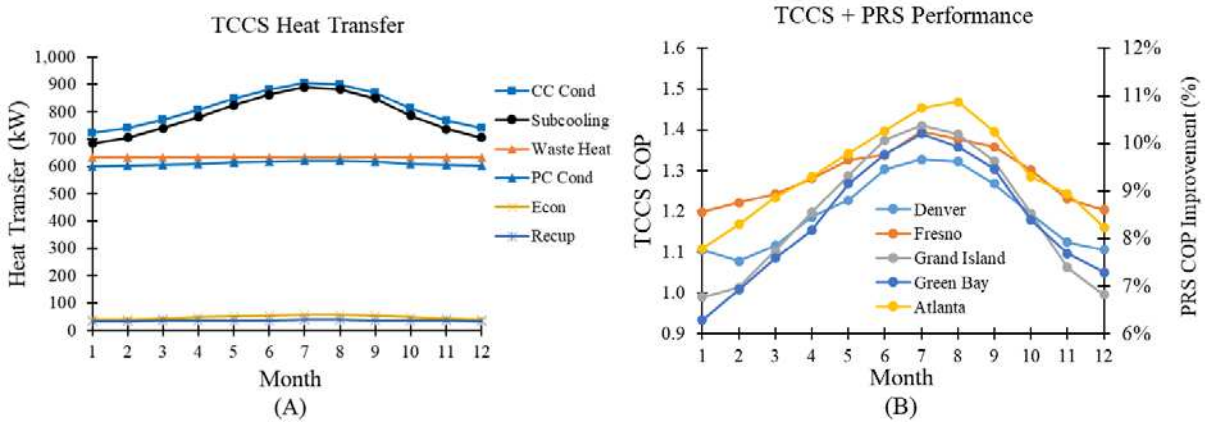

Figure 4.6 (A) TCCS Subcooler and Condenser Heat Transfer averaged between five locations throughout the year. (B) COP of the TCCS, and PRS COP improvement provided by the TCCS in five locations throughout the year.

Considering Figure 4.6b, the COP of the TCCS varies between 0.95-1.5, throughout the year, resulting in a PRS COP improvement ranging from 7%-11%. In general, the COP of the TCCS found in this work was found to be higher than most other thermally activated cooling systems, as discussed in Section 2.3.1 of this document. There are two primary reasons for this, which include the high temperature and pressure of the PRS ammonia stream, as well as the high

flow rate and relatively low temperature of the TCCS condenser cooling water. Considering that the feedwater enters the condenser at 15.56°C, and the PRS ammonia temperature enters the subcooler at 20°C-40°C at any point in the year, the PRS could in theory be subcooled with the feedwater alone. Because of this, the TCCS can provide high levels of subcooling with very little work input, resulting in highly efficient operation. The DMS also benefits from the high temperature of PRS ammonia compared to the low temperature of condenser feedwater, but the TCCS still provides more overall energy savings than the DMS due to the significantly lower electrical work input. The only electrical work input required for the TCCS is the power cycle pump, which only requires around 8 kW, while the DMS is driven by an electrical compressor which requires 79 kW. Natural gas and electricity savings provided by the TCCS throughout the year in five locations are shown in Figure 4.7.

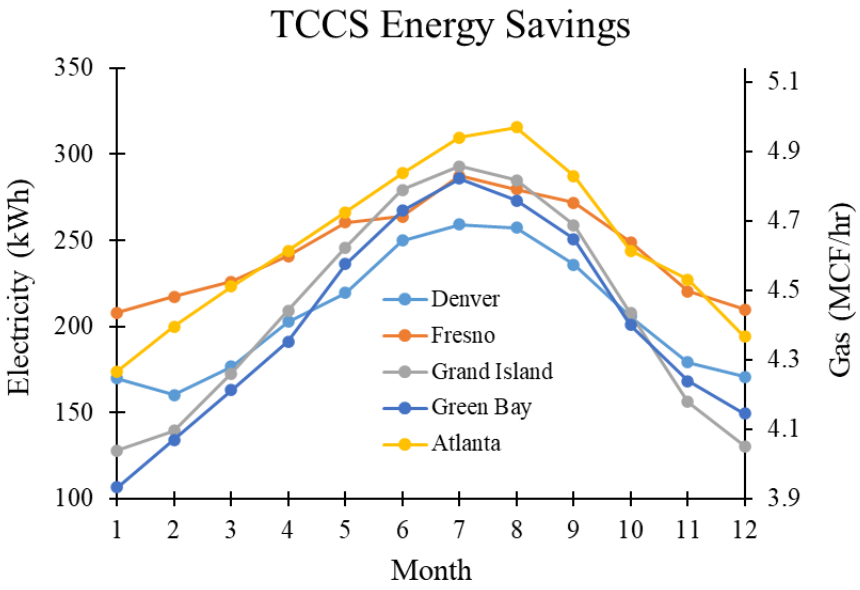

Figure 4.7 Monthly average Natural gas and electricity savings achieved by the TCCS at a beef processing plant located in five different cities.

Average hourly electricity savings of the TCCS range from 100-320 kWh throughout the year, which is approximately 60 kWh greater than the savings provided by the DMS. Although the

DMS provides more subcooling than the TCCS due to higher condenser water flow, it is setback by the electrical input to the compressor. Average hourly gas savings of the TCCS range from 4-5 MCF/hr, which is greater than the DMS or ORC, due to the high levels of heat rejected in the TCCS condensers (shown in Figure 4.6). In the next section, the annual savings provided by each technology will be presented.

4.2. Annual Savings

Once the thermodynamic models have been solved for each hour of operation, annual savings produced by each technology are calculated. Savings vary greatly from city to city due to differences in utility costs as shown in Figure 4.8.

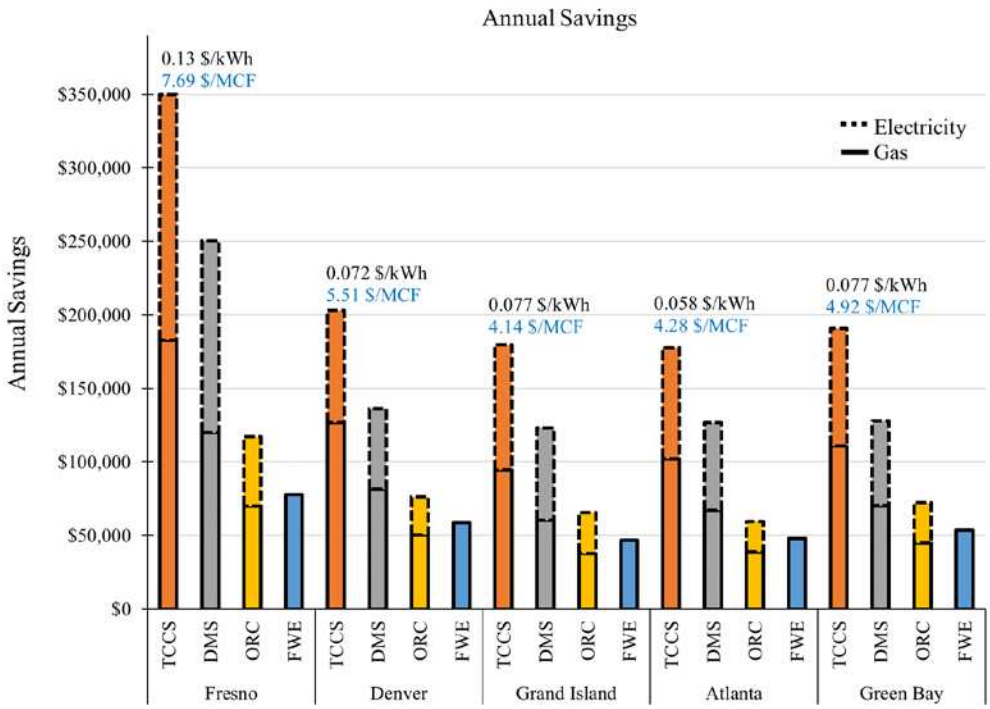

Figure 4.8 Bar graph showing economic savings for each technology in each state. Gas savings for each technology are shown for each technology in solid black, while electricity savings are shown in dashed black. The average gas and electricity prices for each location are shown in light blue and black.

For all five cities, the TCCS yields the highest annual savings of the four technology options, with savings ranging from $178,000 - $350,000 per year. Comparing cities, utility costs

had the largest impact on annual savings. For example, in Fresno, where the average cost of electricity and natural gas are highest, annual savings achieved by each option are also the highest. In Fresno, the TCCS achieved the greatest savings of any technology option in any location at $350,000 per year. However, in Atlanta, where utility costs are roughly half of those in Fresno, savings are also cut in half. In Atlanta, the TCCS achieved the lowest annual savings of $177,800 per year. Although annual TCCS dollar savings are much less in Atlanta than Fresno, the quantity of electricity and natural gas saved by the TCCS in the two cities is similar. In Fresno, the TCCS produced annual electricity and gas savings of 1,240,000 kWh and 23,700 MCF, respectively. In Atlanta, the TCCS performed similarly, producing the annual savings of 1,274,000 kWh and 23,800 MCF per year. This makes sense, considering the similarities in climate between the two locations, which heavily influence the performance of both the TCCS and PRS. Comparing climates, the average wet bulb temperatures in Fresno and Atlanta are very similar, at 12.1^{o}C 12.7^{o}C, respectively. In contrast, Denver, Grand Island, and Green Bay have colder climates than Fresno and Atlanta, so energy savings are produced by the TCCS and DMS are lower. The average energy savings produced by the TCCS in Denver, Grand Island, and Green Bay are 1,050,000 kWh and 22,700 MCF per year, representative of a 16% reduction in electricity savings and a 4% reduction in natural gas savings. Although climate does affect the annual savings achieved by the TCCS and DMS, the difference in annual savings between cities is mostly a result of varied utility costs. However, for the FWE and ORC, which are not climate dependent, annual savings across the five cities vary solely as a function of utility costs.

Natural gas and electricity savings achieved by each technology in each location are compared in Table 4.3. Comparing technologies, the TCCS achieves the most savings of the four technologies, with annual savings ranging from $177,800-$350,000 per year. This is reasonable

considering the high levels of hourly natural gas and electricity saved by the TCCS, as discussed in Section 4.1. The DMS and ORC are the two options that saved the second and third most annually, with savings ranging from $123,000-$250,000, and $58,500-$115,000 per year, respectively. The technology option that saved the least annually was the FWE, with savings ranging from $46,700-$77,900. This is reasonable considering that the FWE only reduces natural gas consumption, unlike the other technologies which reduce natural gas and electricity consumption.

Table 4.3 Natural gas and electricity savings of each technology in each location.

Technology	Fresno	Denver	Atlanta	Grand Island	Green Bay
	Natural Gas				
TCCS	$183,000	$127,000	$102,000	$94,400	$111,000
DMS	$120,000	$81,200	$67,000	$60,400	$70,300
ORC	$69,900	$50,400	$38,900	$37,700	$44,600
FWE	$77,800	$58,700	$48,000	$46,700	$53,600
	Electricity				
TCCS	$167,000	$76,200	$75,800	$85,300	$80,100
DMS	$130,000	$55,000	$59,600	$62,900	$57,700
ORC	$44,800	$25,700	$19,600	$26,200	$28,100

Comparing electricity and natural gas savings produced by the TCCS, DMS, and ORC, feedwater heating produces slightly greater annual savings than electricity production or PRS subcooling. For the TCCS, DMS, and ORC, natural gas savings accounted for an average of 57%, 53%, and 63% of the total annual savings, respectively. Feedwater heating is more lucrative than electricity generation or subcooling for several reasons, including the high levels of condenser heat rejected to the feedwater, as well as the cost of natural gas versus the cost of electricity. When only considering annual savings, the TCCS would seem to be the most economically viable technology. However, to fully understand the economic viability of a technology, it is also critical to estimate the capital cost, payback period, and cash flow. In the next section the results from the cost model and cash flow analysis will be presented

4.3. Economic Results

After determining thermodynamic performance and annual savings of each technology option, installation cost was estimated to determine payback period, cash flow, and net present value. The total installation cost of each technology is broken down by component in Figure 4.9.

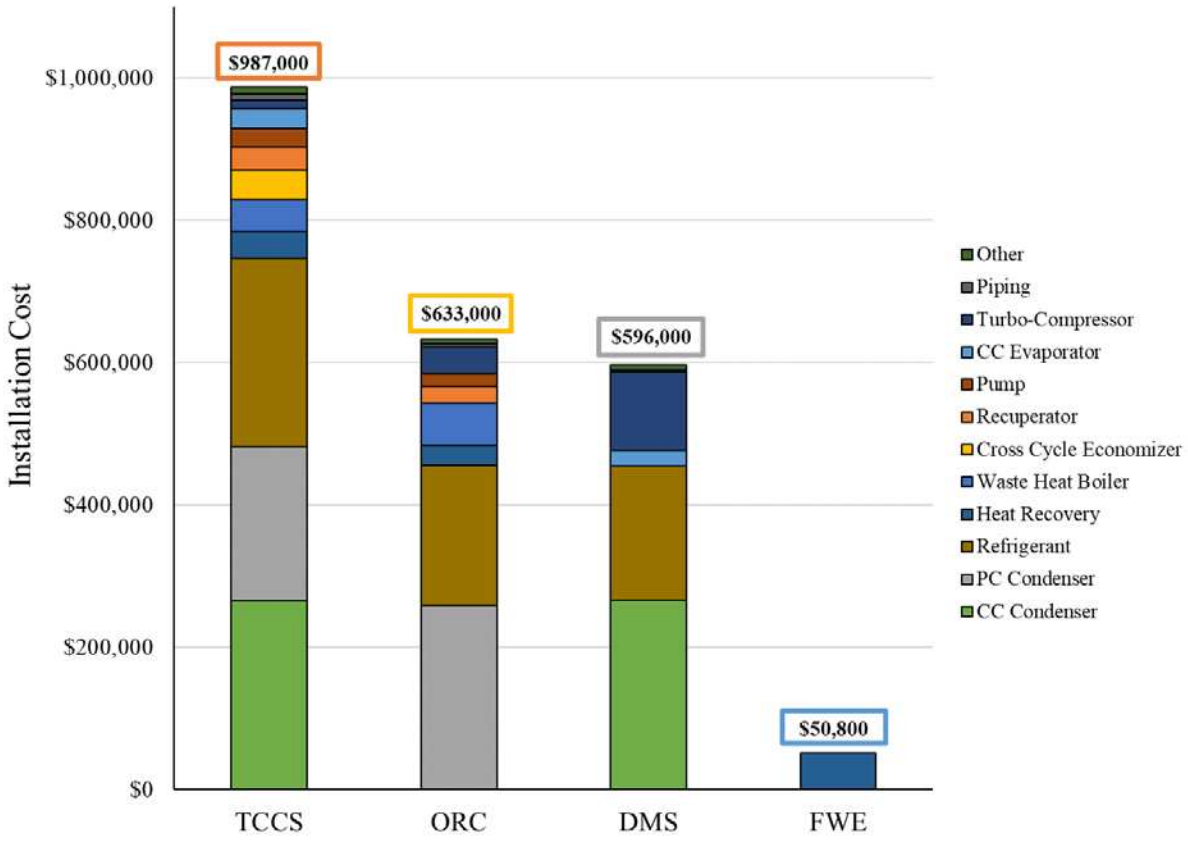

Figure 4.9 Breakdown of installation cost for each technology option.

Comparing the technologies, the TCCS was the option which was found to have the highest installation cost at $987,000. The second and third most capital-intensive technologies were found to be the ORC and the DMS, with installation costs of $633,000 and $596,000, respectively. The least capital-intensive technology was found to be the FWE, with an install cost of $50,800. The cost of the FWE is not broken down by component because a supplier quote was used to estimate the overall system cost. Intuitively, these results make sense considering the TCCS is the most

complex technology with the most components, while the ORC and DMS have less complexity, and the FWE is the smallest and most simplistic technology. Considering individual component costs, the heat exchangers were found to be the most expensive components in each system. Figure 4.10 breaks down the percent contributed to overall cost of each component type. For the TCCS, DMS, and ORC, heat exchangers accounted for 68%, 58%, and 48% of the total cost, respectively. The second most expensive component type was found to be refrigerant, which accounted for 27% of the TCCS cost, 31% of the ORC cost, and 32% of the DMS cost.

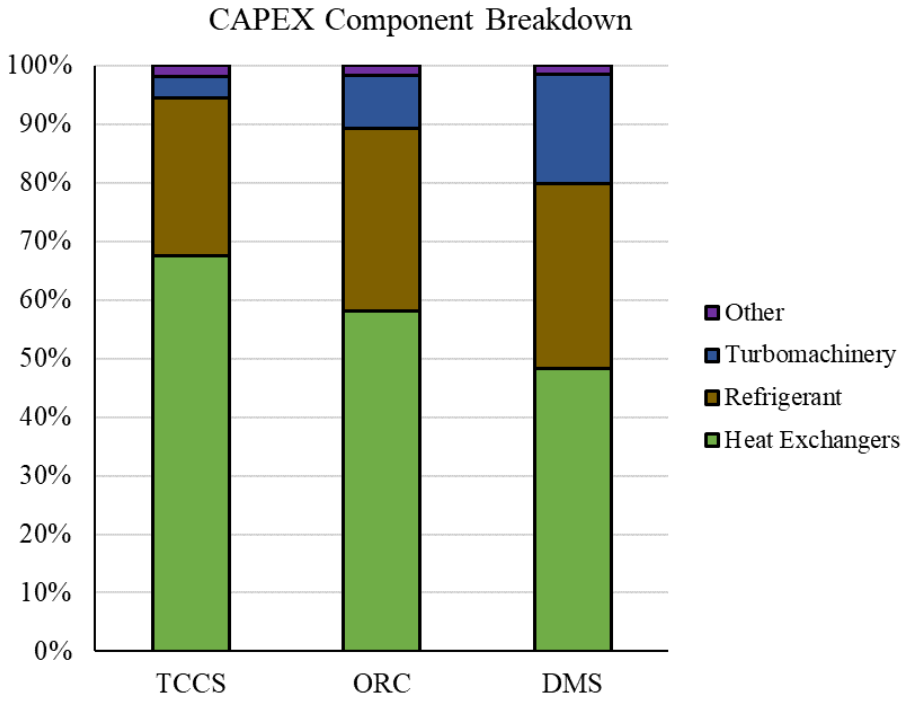

Figure 4.10 Breakdown of installation cost based on component type.

The heat exchanger values for each heat exchanger in the TCCS, ORC, and DMS are provided in Table 4.4 and Table 4.5, including effectiveness values, number of plates, total heat duty, log mean temperature difference (LMTD), thermal conductance (UA), and cost based on the total heat exchanger area. The LMTD, and UA values listed are reflective of the two-phase regions of the boiler, condensers, and subcooler, which are the regions with the highest heat duties.

Table 4.4 Characteristics of the TCCS heat exchangers at baseline effectiveness.

HX	TCCS					
	Boiler	**PC Cond.**	**Recup.**	**Econ.**	**Subcooler**	**CC Cond.**
ε_{sc}	0.865	0.1	0.7	0.7	N/A	0.1
ε_{tp}	0.35	0.7	N/A	N/A	0.7	0.7
ε_{sh}	0.7	0.664	N/A	N/A	0.7	0.83
N_{plates}	42	1254	22	36	30	1845
Q (kW)	631	614	37	53	818	842
LMTD	13.1	5.4	6.4	6.0	16.4	5.0
UA (kW K^{-1})	27	109	6	9	45	155
Cost	28,633	134,785	20,165	26,458	17,735	166,010

The two most expensive heat exchangers of the TCCS are the cooling and power cycle condensers, with component costs of $166,010 and $134,785, respectively. The condensers are much more expensive than the other heat exchangers due to a combination of high heat duties, and low LMTD's. The LMTD, which is reflective of the temperature driving force in a heat exchanger, is calculated based on the temperature differences between the hot and cold fluids in the device. If a heat exchanger has a low LMTD, it will transfer heat less effectively, requiring greater heat transfer area to satisfy the overall heat duty. In the case of the power and cooling cycle condensers, the LMTD values are the lowest out of all the heat exchangers, at 5.4 and 5 respectively, while still having high heat duties of 614 kW and 842 kW. Therefore, large amounts of heat transfer area are required, which increase overall cost.

Table 4.5 Characteristics of the ORC and DMS heat exchangers at baseline effectiveness.

HX	ORC			DMS	
	Boiler	**Cond.**	**Recup.**	**Subcooler**	**Cond.**
ε_{sc}	0.989	0.1	0.7	N/A	0.1
ε_{tp}	0.35	0.7	N/A	0.7	0.7
ε_{sh}	0.7	0.828	N/A	0.7	0.919
N_{plates}	113	2982	21	32	3157
Q (kW)	631	559	26	875	954
LMTD	11.0	2.0	5.1	17.6	3.1
UA (kW K^{-1})	27	264	5	44	264
Cost	49,387	215,197	19,037	18,065	221,919

Like the TCCS, the most expensive heat exchangers in the ORC and DMS were also found to be the condensers, with component costs of $215,197 and $221,919, respectively. Comparing the ORC condenser to the power cycle condenser of the TCCS, the ORC condenser is significantly more expensive, even though the condenser heat rejection is similar (559 kW in the ORC condenser vs. 614 kW in the TCCS power cycle condenser). As the refrigerant enters the ORC condenser, it is cooled by a 52.4 kg/s stream of feedwater, while the flow of feedwater into the TCCS power cycle condenser is only 21.7 kg/s. With a higher rate of water entering the condenser, the ORC can operate at a significantly lower temperature, which allows for increased cycle performance but also a lower heat exchanger LMTD. The LMTD of the power cycle condenser was found to be 2, compared to 5.4 in the TCCS power cycle condenser. At a lower LMTD, heat is transferred less efficiently, so a larger, and thus, more expensive heat exchanger is required. The same reasoning can be used to explain the cost discrepancy between the TCCS cooling cycle condenser and the DMS condenser. The rate of water entering the DMS condenser is 52.4 kg/s, while the rate of water entering the TCCS cooling cycle condenser is 30.7 kg/s. This increased feedwater flow rate allows the DMS to operate at a lower condensing temperature, which again, increases overall cycle performance, but decreases heat exchanger efficiency, as seen by the lowered LMTD in the DMS condenser versus the TCCS cooling cycle condenser (3.1 versus 5).

With the installation cost and annual savings of each technology determined, payback period can be calculated. Figure 4.11 displays the simple payback period of each of the four technologies in the five plant locations considered in this study.

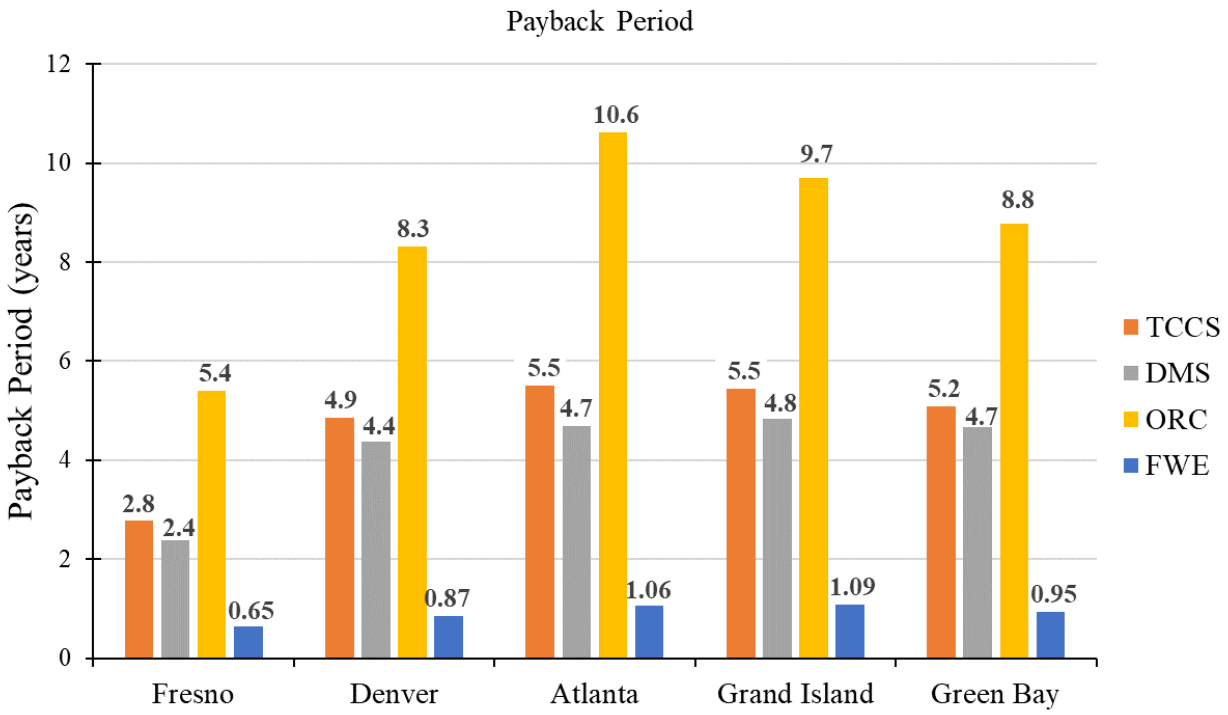

Figure 4.11 Simple payback period of four technologies in five locations.

The technology option with the fastest payback period is the FWE. With an average payback of 0.92 years, the FWE pays itself off significantly faster than the other three technologies. The option with the second fasted payback is the DMS, with an average payback period of 4.19 years. The TCCS has a comparable payback to the DMS, paying itself off in 4.78 years, on average. The technology with the slowest payback period was the ORC, with an average payback period of 8.56 years. Comparing cities, each technology achieved its fastest payback period in the city of Fresno. This makes sense, considered the high utility costs in Fresno that generate a significant increase in annual savings, as discussed in Section 4.2.

Another calculation made with capital cost and annual savings determined is simple cash flow. Figure 4.12 shows a simple cash flow diagram for each system using the capital costs from Figure 4.9, and the average annual savings produced by each technology across the five plant locations from Figure 4.8.

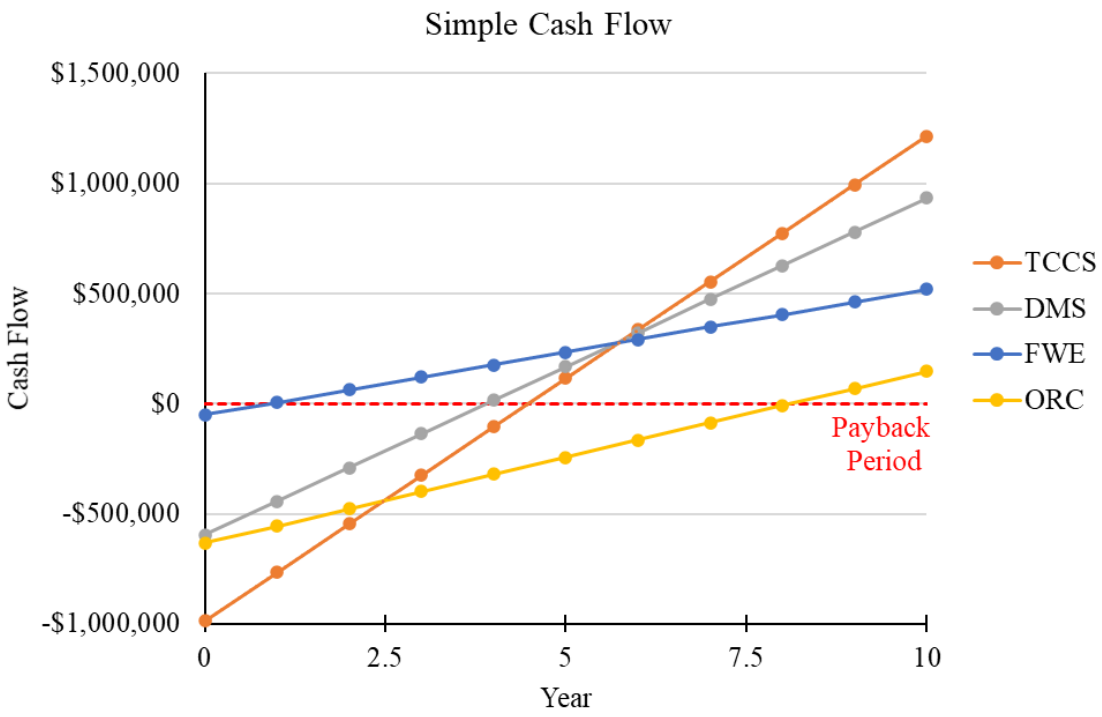

Figure 4.12 Simple cash flow of four technologies over a 10-year period.

The simple cash flow diagram is useful when considering the economics of a technology over its entire lifetime, which in this study is assumed to be 10 years. The cash flow for each technology starts in the negative region because of the initial capital investment that is required for purchase and installation. Each year, the four technologies yield financial savings by reducing energy consumption at a plant, so the total cash flow rises, until reaching the red dashed line, which represents the payback period. The TCCS yielded a cash flow of $1,215,000 over a 10-year lifetime, which is the greatest of all four technologies. The DMS, FWE, and ORC yielded 10-year cash flows of $933,00, $519,00, and $139,000, respectively.

The final economic calculation made in is net present value. While simple cash flow is a useful indicator of project value over the entire project lifetime, NPV accounts for the increased value of money in the present versus the value of money in the future. Figure 4.13 displays the NPV of each technology in each location.

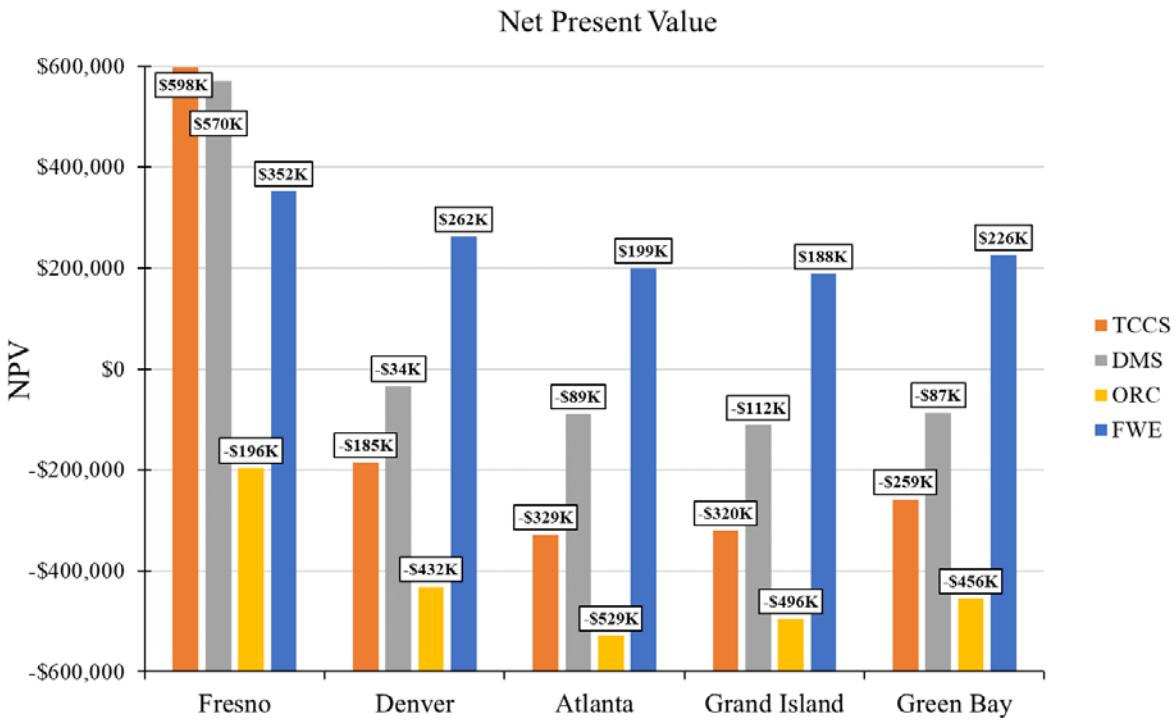

Figure 4.13 NPV of four technologies in five plant locations.

As discussed in section 3.4.3, the NPV considers the present value of money through the discount factor, reducing the value of future cash flows to account for the delay. For this reason, technologies with quicker payoffs result in higher net present values. A positive NPV means that the projected earnings of a technology exceed the anticipated costs, indicating that the technology is profitable. Considering Figure 4.13, the FWE is the only technology that achieves a positive NPV across all five locations, with an average NPV of $245,000. Only in Fresno, where the annual savings are highest, does TCCS and DMS to achieve a positive NPV. The average NPV of the TCCS and DMS are much lower than the FWE, at -$99,000 and $50,000, respectively. This makes sense when considering that the average payback period of the TCCS and DMS are 4.78 and 4.19 years, making up a significant portion of the 10-year project lifetime. The ORC achieves an average NPV of -$422,000, which is significantly less than the other technologies. This low NPV is reasonable considering that the average payback period of the ORC is 8.56 years, taking up

nearly the entire 10-year project lifetime to pay off. Comparing locations, the NPV is significantly higher in Fresno for each technology than the other four cities. This is due to the high cost of electricity and natural gas in Fresno compared to the other four cities, which leads to much greater annual savings (Figure 4.8).

Considering the results from the baseline technology models, the economics of the FWE were found to be much more favorable than the TCCS, DMS, and ORC. The FWE achieved the lowest payback period of the four technologies, with an average payback period less than one year across the five cities. Furthermore, the FWE was the only technology that achieved a positive NPV in all five cities. Although the simple cash flow analysis (summarized in Figure 4.12) suggests that the TCCS, DMS, and ORC are more valuable over the 10-year project lifetime, the NPV calculation shows otherwise. Net present value, which gives a more realistic assessment of project worth compared to simple cash flow, was found to be negative for the TCCS, DMS, and ORC in all locations except in Fresno. In Fresno, where the utility costs are much higher than any other city, the TCCS and DMS achieves slightly higher NPV's than the FWE. Although NPV's for the TCCS and DMS are greater in Fresno than the FWE, the payback periods achieved of both technologies are still four times greater than the FWE (2.8 years for the TCCS and 2.4 years for the DMS versus 0.65 years for the FWE, as shown in Figure 4.11). Therefore, unless a plant is in a city with high utility costs, and payback period isn't a priority, then the FWE is the most economically viable technology.

In conclusion, the baseline modeling efforts suggest that, although the TCCS, DMS, and ORC, produce high annual savings when installed at a beef processing facility, they are unable to compete economically with the much simpler FWE due to high capital costs, which delay system payback and reduce NPV. For this reason, an optimization study was conducted to seek how

thermodynamic performance of the TCCS, DMS, and ORC impact economic performance. In the following section, an optimization study will be presented which investigates the tradeoff between the thermodynamics and economics of the TCCS, DMS, and ORC. The goal of the optimization study is to vary thermodynamic performance of these three systems to quantify a minimum payback period and maximum NPV and determine whether these technologies can compete economically with the FWE.

4.4. System Optimization

The goal of the optimization study in this work was to vary heat exchanger effectiveness inputs for the baseline TCCS, DMS, and ORC models to determine the minimum payback period and maximum net present value and discover if these technologies can be optimized to be more economically competitive with the FWE. Heat exchanger effectiveness values were raised or lowered by 10% increments and OPEX, CAPEX, payback period, and NPV were recalculated. Since the initial heat exchanger effectiveness values (shown in Table 3.14) were high, effectiveness values could only be increased by 10%, but were decreased by 50% for the TCCS and DMS, and by 70% for the ORC. At -40% effectiveness, it was necessary to remove the cross-cycle economizer entirely from the TCCS model, and at -70%, the recuperator from the ORC model, due to thermodynamic constraints. In the following subsections, the relationship between heat exchanger effectiveness, thermodynamic performance, and system economics of the ORC, DMS, and TCCS will be discussed in detail.

4.4.1. Thermodynamic Performance and Annual Savings

Heat exchanger effectiveness inputs were found to have a dramatic impact on the thermodynamic performance of the ORC, DMS, and TCCS. Starting with the ORC, heat exchanger

effectiveness values were varied from +10% to -70% of the baseline values shown in Table 3.14. Table 4.6 compares the thermodynamic results for the ORC at each effectiveness.

Table 4.6 Comparison of ORC operation at varying effectiveness values.

Δε	$\dot{M}_{orc}$	p_{boil}	p_{cond}	$\dot{Q}_{cond}$	$\dot{Q}_{boil}$	$\dot{Q}_{recup}$	$\dot{W}_{pump}$	$\dot{W}_{turb}$	η_{orc}
	[kg/s]	**[kPa]**	**[kPa]**	**[kW]**	**[kW]**	**[kW]**	**[kW]**	**[kW]**	**[%]**
10%	2.96	2870	551	557	631	28	9	83	13%
0%	2.96	2773	556	559	631	26	8	81	13%
-10%	2.96	2649	563	561	631	24	8	78	12%
-20%	2.96	2488	571	563	631	22	7	75	12%
-30%	2.98	2272	583	567	631	20	6	70	11%
-40%	3.00	1972	598	574	631	19	5	63	10%
-50%	3.05	1539	622	585	631	18	4	49	8%
-60%	3.20	889	663	615	631	17	1	17	3%
-70%	3.31	734	730	630.6	631	0	0.02	0.37	0.06%

Recalling from Section 3.2.4, the ORC operates at a fixed waste heat input of 631 kW, and a fixed feedwater mass flow rate of 52.4 kg/s that enters the condenser at a temperature of 15.56°C. As heat exchanger effectiveness values are lowered, heat transfer occurring in the ORC heat exchangers becomes less efficient, resulting in several changes in ORC operation. Considering the boiler, when effectiveness values are lowered, the mass flow of refrigerant increases, and boiler pressure decreases for the refrigerant to accept the overall heat input of 631 kW. As effectiveness values were lowered from +10% to -70%, ORC refrigerant mass flow increased from 2.95 kg/s - 3.31 kg/s, and boiler pressure decreased from 2870-734 kPa. Considering the ORC condenser, as heat exchanger effectivenesses are lowered and refrigerant mass flow increases, the condenser pressure must increase to effectively cool the ORC refrigerant from a superheated vapor to a subcooled liquid. As effectiveness values were lowered, the cooling load in the condenser increased from 557 kW-620.6 kW due to the increase in refrigerant mass flow. Although refrigerant mass flow is greater at lower effectiveness values, work is generated in the ORC turbine

drops off sharply, from 83 kW-0.37 kW, due to the decreased ORC pressure ratio. The decrease in pressure ratio also causes a decrease in recuperator heat duty, from 28 kW – 17 kW. Overall, the thermal efficiency of the ORC varied from 13% - 0.06% across the effectiveness values considered. As effectiveness values are lowered past -50%, a large reduction in turbine work occurs due to the significant decrease in pressure ratio. As a result, the ORC generates almost no electrical savings via turbine work, essentially operating in the same way as the feedwater economizer.

Like the ORC, the DMS also experienced a reduction in performance at lowered heat exchanger effectiveness values. Table 4.7 compares thermodynamic performance of the DMS across the range of effectiveness values considered. The values shown reflect DMS performance when the PRS is operating at a high-side pressure of 1367 kPa, which is the operation point at which system costs were evaluated.

Table 4.7 Comparison of DMS operation at varying effectiveness values.

Δε	$\dot{M}_{\mathbf{dms}}$	$p_{\mathbf{cond}}$	$p_{\mathbf{evap}}$	$\dot{Q}_{\mathbf{subcool}}$	$\dot{Q}_{\mathbf{cond}}$	$\dot{W}_{\mathbf{comp}}$	$COP_{\mathbf{dms}}$
	[kg/s]	**[kPa]**	**[kPa]**	**[kW]**	**[kW]**	**[kW]**	**-**
10%	4.79	585	327	935	1016	81	11.5
0%	4.53	589	322	875	954	79	11.1
-10%	4.26	593	316	811	887	77	10.6
-20%	3.95	597	310	742	815	73	10.1
-30%	3.60	601	305	667	735	69	9.7
-40%	3.19	605	302	582	643	61	9.5
-50%	2.65	605	311	479	527	48	9.9

Recalling from Section 3.2.5, the DMS provides supplementary cooling to the PRS at the condenser outlet, subcooling the PRS ammonia from a saturated liquid to a subcooled liquid. The temperature and pressure of the PRS ammonia stream is dependent on ambient weather conditions, and the feedwater entering the DMS condenser is set at 52.4 kg/s and an inlet temperature of 15.56°C. The work input to the compressor of the DMS, which is set at 98% of the work generated

in the ORC turbine, varied from 81 kW to 48 kW across the effectiveness values considered. When compressor work input and heat exchanger effectiveness values are lowered, the DMS operates at a lower refrigerant mass flow and higher pressure ratio to provide subcooling to the PRS. As effectiveness values were lowered from +10% to -40%, DMS refrigerant mass flow decreased from 4.79 kg/s to 3.19 kg/s, and pressure ratio increased from 1.79 to 2. At lower mass flows, and higher-pressure ratio, the performance of the DMS decreases, with subcooling decreasing from 935 kW to 582 kW, and COP decreasing from 11.5 to 9.5. As discussed earlier, the DMS can achieve such a high COP for several reasons, including the high temperature and pressure of the ammonia stream being subcooled as well as the low temperature of feedwater used to cool the condenser.

At -50% effectiveness, the performance of the DMS increased slightly, as the pressure ratio decreased from 2 to 1.94, resulting in a COP increase from 9.5 to 9.9. This is reflective of the point where cooling provided by the condenser feedwater begins to outweigh the cooling created via vapor compression. Because the temperature of the feedwater stream entering the condenser is lower than the temperature of ammonia entering the subcooler, cooling can be provided to the ammonia solely through the feedwater without adding any compressor work to the DMS refrigerant. As a result, as compressor work added approaches zero, the COP of the DMS will increase somewhat artificially. However, this is not indicative of more cooling being provided – subcooling still decreased from 582 kW to 479 kW when heat exchanger effectivenesses were lowered from -40% to -50% and compressor work was reduced from 61 kW to 48 kW.

The performance of the TCCS also decreased at lower effectiveness values. Table 4.8 shows the thermodynamic results from the TCCS model when effectiveness values were varied between +10% and -50%. The values shown reflect TCCS performance when the PRS is operating

at a high-side pressure of 1367 kPa. Recalling from Section 3.2.6, the TCCS accepts 631 kW of heat from the plant boiler exhaust to drive a power cycle turbine which is directly coupled to a compressor which drives a cooling cycle, used to provide subcooling to the PRS. The power and cooling cycle reject heat to the boiler feedwater, which is split between two condensers at a flow rate of 21.7 kg/s and 30.7 kg/s, respectively.

Table 4.8 Comparison of TCCS thermodynamic results across effectiveness variations.

$\Delta\varepsilon$	**TCCS - Power Cycle**						
	$\dot{M}_{pc}$	$p_{ratio,pc}$	$\dot{Q}_{cond,pc}$	$\dot{W}_{pump}$	$\dot{W}_{turb}$	$\dot{Q}_{recup}$	η_{pc}
	[kg/s]	-	[kW]	[kW]	[kW]	[kW]	-
10%	3.38	4.2	624	8.8	83	43	13%
0%	3.32	3.9	614	8.2	79	37	12%
-10%	3.27	3.7	605	7.6	74	33	12%
-20%	3.23	3.3	599	6.8	68	29	11%
-30%	3.21	2.9	595	5.7	60	26	9%
-40%	3.17	2.4	586	4.4	49	23	8%
-50%	3.29	1.6	605	2.2	28	22	4%
$\Delta\varepsilon$	**TCCS - Cooling Cycle**					**Overall**	
	$\dot{M}_{cc}$	$p_{ratio,cc}$	$\dot{Q}_{cond,cc}$	$\dot{Q}_{subcool}$	COP_{cc}	$\dot{Q}_{econ}$	COP_{tccs}
	[kg/s]	-	[kW]	[kW]	-	[kW]	-
10%	4.6	1.84	898	884	10.8	67	1.38
0%	4.3	1.86	842	818	10.6	53	1.28
-10%	4.0	1.88	781	749	10.4	40	1.17
-20%	3.7	1.89	714	676	10.2	29	1.06
-30%	3.3	1.9	637	596	10.1	18	0.94
-40%	2.8	1.86	554	506	10.5	0	0.80
-50%	2.1	1.62	407	379	13.8	0	0.60

Considering the TCCS power cycle, performance generally decreases with lowered heat exchanger effectiveness. As effectiveness values were lowered from +10% to -50%, the turbine work output decreased from 83 kW-28 kW, resulting in a thermal efficiency decreasing from 13% to 4%. Unlike the ORC, the mass flow of refrigerant through the power cycle decreased, from 3.38 kg/s-3.17 kg/s, as heat exchanger effectiveness was reduced to -40%, and then increased slightly to 3.29 kg/s at -50%. Power cycle condenser heat rejection showed the same trend – decreasing

from 624 kW at +10% to 586 kW at -40%, then increasing to 605 kW at -50%. There are two primary factors that distinguish the TCCS power cycle model from the ORC model: condenser water flow rate, which is lower for the TCCS power cycle, and the cross-cycle economizer, which transfers heat to the TCCS power cycle refrigerant at the boiler inlet from the TCCS cooling cycle at the compressor outlet. Since feedwater flow rate in both the ORC and TCCS models are fixed, it is likely the case that the removal of the economizer at -40% is the reason for this trend. As effectiveness values of the TCCS heat exchangers are lowered from +10% to -40%, economizer heat duty decreases from 67 kW- 18 kW. At -50%, it was necessary to remove the economizer entirely due to thermodynamic constraints.

The performance of the TCCS cooling cycle followed the same trend as the performance of the DMS. At lower effectiveness values, less work is delivered from the turbine to the compressor of the TCCS, thus, the cooling cycle must operate at a lower refrigerant mass flow rate which results in less PRS subcooling and condenser heat rejection. As effectiveness values were lowered compressor work input decreased from 82 kW-27 kW, reducing TCCS cooling cycle mass flow from 4.6 kg/s-2.8 kg/s. In turn, TCCS subcooling and cooling cycle condenser heat rejection fell from 884 kW to 379 kW, and 898 kW to 407 kW, respectively.

Like the DMS, a slight increase in TCCS cooling cycle performance was observed at the lowest heat exchanger effectiveness values. When heat exchanger effectiveness values were lowered from -30% to -50%, the pressure ratio of the cooling cycle decreased from 1.9 to 1.62, and COP of the cooling cycle increased from 10.1 to 13.8. As discussed earlier, this improvement in performance is likely due to the unique boundary conditions of the subcooling cycle – where condenser feedwater enters the cycle at a lower temperature than the ammonia in the PRS. Although the COP of the cooling cycle increases slightly from -30% to -50%, the amount of

condenser heat rejected and subcooling still decreases. Furthermore, the overall COP of the TCCS decreased across the range of effectiveness values, from 1.38-0.6.

Once the thermodynamic models have been evaluated at varying effectiveness, annual savings is calculating in the same way as the baseline, using the method described in Section 3.4.1. The annual gas and electricity savings produced by each technology at varying effectiveness values are shown in Figure 4.14. Savings shown are the average result across the five plant locations.

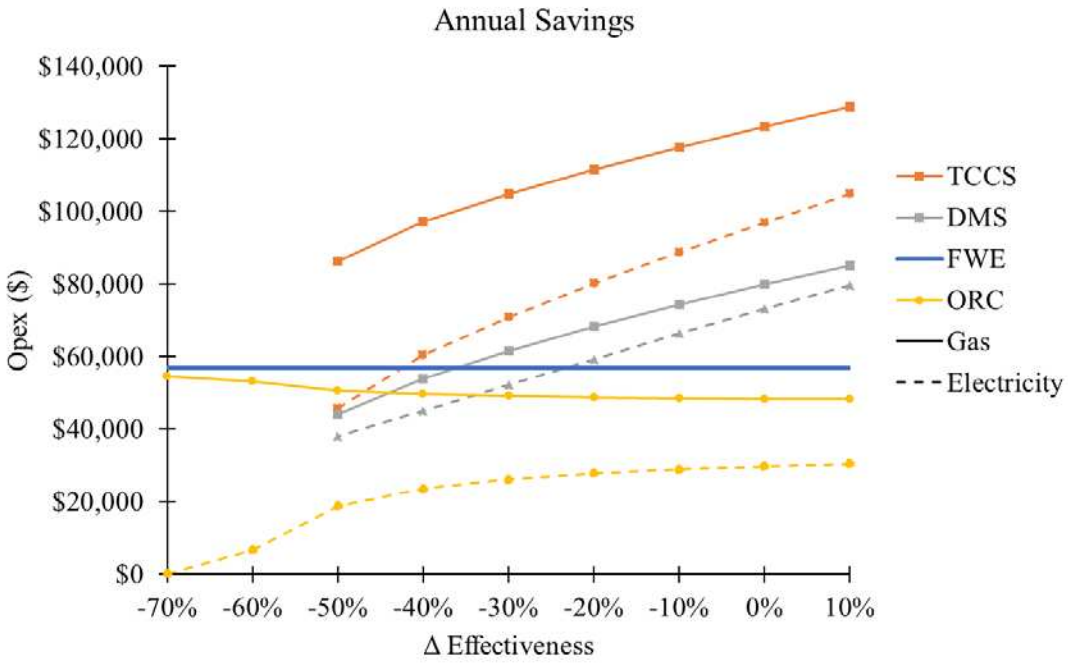

Figure 4.14 Annual savings produced by each technology via electricity and natural gas reduction.

The savings produced by the TCCS, DMS, FWE, and ORC are shown in orange, grey, blue, and yellow, respectively. Savings that are achieved by electricity generation or PRS subcooling are designated with dashed lines, while savings produced by feedwater heating are designated with solid lines. The FWE, shown in solid blue, saves $57,000 annually, which is the average of the savings across the five cities, shown in Table 4.3. The FWE was not considered in the optimization study, and thus savings are constant across the range of effectiveness values.

Looking at the TCCS, as effectiveness values lowered from +10% to -50%, gas and electricity savings decreased from $129,000-$86,200 and $105,000-$45,600, respectively. For the DMS, gas and electricity savings decreased from $85,000-$44,200 and $79,700-$37,900, respectively. For both the TCCS and DMS, the reduction seen in gas and electricity savings is consistent with the thermodynamic results, which show lowered amounts of subcooling and condenser heat rejection at lower heat exchanger effectiveness values.

For the ORC, electricity savings decrease steadily between +10% and -50% effectiveness, from $30,400-$18,800, and drop off sharply at effectiveness values between -50% and -70%. Conversely, ORC gas savings steadily increase as effectiveness values are lowered, rising from $48,200-$54,600. To explain this, as effectiveness values for the ORC heat exchangers are lowered to the extreme, the ORC must operate at an increasingly smaller pressure ratio, resulting in a large decline in the amount of work generated in the turbine. Furthermore, mass flow of ORC refrigerant and ORC condenser pressure increase, resulting in greater heat rejection to the condenser. At -70% effectiveness, the ORC generates almost no offset in electric revenue, producing savings almost entirely through boiler feedwater heating. In summary, heat exchanger effectiveness is found to have a dramatic impact on the annual savings produced by the TCCS, DMS, and ORC. As heat exchanger effectiveness values were lowered, a significant decrease in savings is observed for the three technologies, which is reasonable considering the decrease in thermodynamic performance. In the next section, the relationship between heat exchanger effectiveness and capital cost will be discussed in detail.

4.4.2. Capital Cost

To reiterate, the goal of the optimization study was to find a point where the TCCS achieves a minimum payback period and maximum net present value. The inputs that were varied to find

this point were heat exchanger effectiveness values, which have a profound impact on the overall performance of the ORC, DMS, and TCCS. As heat exchanger effectiveness values are lowered, the performance of each cycle was found to lower as well. This resulted in a large reduction in both gas and electricity savings for both the DMS and TCCS. For the ORC, as effectiveness values were lowered to -70% of their baseline value, electricity savings went away entirely, while gas savings increased, approaching the savings achieved by the FWE. Like annual savings, capital cost was found to have a direct relationship with heat exchanger effectiveness. For all three technology options, as heat exchanger effectiveness values were lowered, the overall system cost lowered also. Recalling the results discussed in section 4.3, the most expensive components for the TCCS, DMS, and ORC was found to be the heat exchangers, which accounted for 68%, 58%, and 48% of the total cost, respectively.

Starting with the ORC, effectiveness values were varied between +10% and -70%, and capital cost was recalculated. Table 4.9 shows the cost breakdown of the ORC in dollars at varying effectiveness values. Cost items not included in Table 4.9 include the exhaust to PG-water heat exchanger, piping, and other costs, which are assumed constant. As effectiveness values were varied from +10% to -70%, the total install cost of the ORC decreased from $723,000-$95,000.

Table 4.9 Cost breakdown of the ORC at varying effectiveness.

Δε	**Cond.**	**Boiler**	**Recup.**	**Refrig.**	**Turbine**	**Pump**	**Total**	**Install**
10%	240,625	56,367	22,711	202,888	32,026	15,921	602,000	723,000
0%	215,197	49,386	19,037	164,885	31,392	15,909	528,000	633,000
-10%	192,319	29,446	16,227	130,094	30,594	15,893	446,000	536,000
-20%	172,090	20,898	12,710	105,057	29,526	15,873	388,000	466,000
-30%	153,583	16,680	10,959	84,597	27,993	15,845	341,000	410,000
-40%	136,178	13,243	9,435	67,332	25,559	15,806	299,000	359,000
-50%	111,875	8,370	6,574	46,509	21,032	15,749	242,000	290,000
-60%	52,051	6,381	5,635	11,289	8,946	15,765	132,000	158,000
-70%	22,513	3,838	-	2,278	402	17,981	79,000	95,000

Considering the pump, which raises the pressure of the ORC refrigerant from the condenser to the boiler pressure, cost stayed relatively constant from +10% to -60%, which is reasonable considering that as effectiveness values are lowered ORC mass flow increases, but pressure ratio decreases. At -70%, pump cost increases slightly, due to the removal of the recuperator which increases ORC mass flow rate. Pump costs ranged from $15,921-$17,981 across the range of effectiveness values. The cost of the turbine, which converts thermal energy into mechanical work, decreased from $32,026 - $402 as effectiveness was varied from +10% to -70%. The significant reduction in turbine cost is a direct result of a reduction in turbine work, which approaches zero at -70% effectiveness. Across the range of effectiveness values, turbomachinery accounted for an average of 13.7% of total system cost.

Considering the cost of heat exchangers and refrigerant, as effectiveness values are lowered, there is a dramatic reduction in heat transfer area. As heat transfer area decreases, overall heat exchanger area decreases resulting in a lowered heat exchanger cost. As effectiveness values were lowered, the cost of the condenser decreased from $240,625-$22,513, the cost of the boiler decreased from $56,367-$3,838, and the cost of the recuperator decreased from $22,711-$5,635. Across the range of effectiveness values, heat exchangers accounted for an average of 60% of total system cost. Furthermore, as heat transfer area decreases, internal volume decreases leading to a reduction in refrigerant cost. Refrigerant cost decreased by a factor of 100, from $202,888 to $2,278, between +10% and -70%, accounting for an average of 22% of total system cost.

The cost results for the heat exchangers and refrigerant are somewhat counterintuitive, as one would expect heat exchangers with lower effectiveness to cost more, requiring greater surface area to transfer heat. The reduction in surface area and heat exchanger cost can be explained by a combination of increased overall heat transfer coefficient and increase in log mean temperature

difference. Considering the condenser and boiler, which are the two most expensive heat exchangers in the ORC, Table 4.10 shows the heat transfer results across the range of effectiveness values.

Table 4.10 Characteristics of the ORC condenser and boiler with varying effectiveness values.

	Condenser				**Boiler**			
Δε	**U**	**LMTD**	**A**	N_{plates}	**U**	**LMTD**	**A**	N_{plates}
	W m^{-2} k^{-1}	**-**	**m^2**	**-**	**W m^{-2} k^{-1}**	**-**	**m^2**	**-**
10%	61	1.7	5662	3667	789	9	221	144
0%	62	2.0	4604	2982	934	11	173	113
-10%	63	2.5	3739	2422	1775	13	66	44
-20%	64	3.0	3043	1972	2392	16	42	28
-30%	65	3.7	2465	1597	3102	20	28	19
-40%	65	4.5	1973	1278	4004	26	18	13
-50%	75	5.8	1371	889	5217	36	11	8
-60%	244	7.9	332	216	6147	57	7	5
-70%	909	11.2	70	47	10131	63	3	3

The overall heat transfer coefficient and LMTD values shown are reflective of heat transfer in the two-phase regions of the condenser and boiler, which are responsible for the largest heat duty. The area values shown are reflective of the overall heat transfer area of the condenser and boiler, which each consist of a subcooled, two-phase, and superheated region. Considering the boiler, as effectiveness values are lowered, refrigerant pressure in the boiler decreases, resulting in a greater LMTD. As effectiveness values lowered from +10% to -70% the LMTD in the two-phase region of the boiler increased from 9 to 63, which is reasonable considering the decrease in refrigerant pressure in the boiler at lower effectiveness values. Overall heat transfer coefficient in the boiler also increased as effectiveness values were lowered, from 789-10131 W m^{-2} k^{-1}. Both factors combined are responsible for the large reduction in heat transfer area, from 221-3 m^2, and number of plates, from 144-3 plates. With this reduction in boiler size, boiler cost was reduced from $56,332-$3,834 across the range of effectiveness values. Looking at the condenser, as

effectiveness values are varied from +10% to -70%, the LMTD increases from 1.7 to 11.2, and the overall heat transfer coefficient increases from 61-909 W m^{-2} k^{-1}. Combined, increased LMTD and heat transfer coefficients are responsible for the large reduction in condenser heat transfer area, decreasing from 5662-70 m^2, and number of plates, from 3667-47 plates. With the reduction in condenser size, condenser cost was reduced from $240,625-$22,513 across the range of effectiveness values.

In summary, the average cost of the ORC across between +10% and -60% is equivalent to $447,000, or $7,050/kW turbine work (excluding from this average is the ORC cost calculated at -70% effectiveness, due to extremely low turbine work output). ORC costs calculated in the present study are compared to the costs published by Lemmens et al. in Figure 4.15. The cost data shown in yellow represents the ORC costs calculated in the present study in terms of installation cost per kW turbine work (2019 dollars). The cost values in green represent the data from the literature representing the cost of ORC that uses a heat recovery system as a fuel source. The hollow green diamonds represent ORC modules (M), which comprise of the essential components of the ORC without installation, and the solid green diamonds represent ORC projects (P), which include all expenses needed to integrate and install the ORC module into an existing plant [106]. The data from Lemmens was converted from 2014 euros to 2014 dollars by assuming a euro to dollar conversion rate of 1.25$/€, and 2014 dollars were converted to 2019 dollars assuming a 2014 and 2019 CEPCI values of 576.1 and 607.5, respectively. The average cost of an ORC project from the literature was found to be $4230/kW, and the average cost of an ORC module was found to be $14,700/kW. Although the correlation between system cost and work output is of low significance, the costs calculated in the present study have similar magnitude to the costs published in the literature.

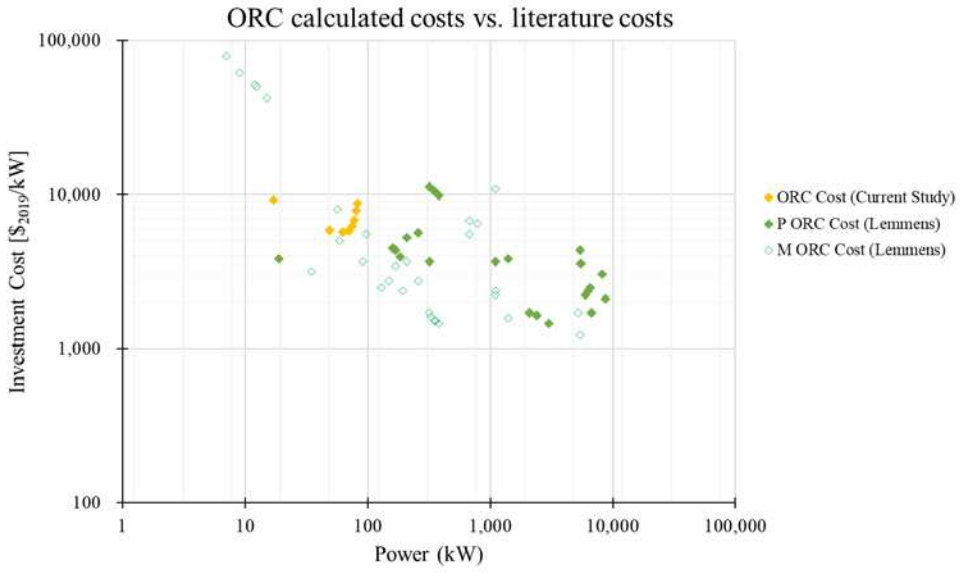

Figure 4.15 ORC costs calculated in the present study versus ORC cost in literature [106].

The next technology that will be discussed is the DMS. Table 4.11 shows the cost breakdown for the DMS in dollars across the range of effectiveness values considered. Cost items not shown in Table 4.11 include the cost of piping, and the cost of miscellaneous items, which are assumed constant across the range of effectiveness values. As effectiveness values were varied from +10% to -50%, the total install cost of the DMS decreased from $676,000-$303,000. Looking at the compressor, cost decreased from $94,400 to $65,296 as effectiveness values were varied from +10% to -50%. At lower effectiveness values, less work is delivered to the compressor which results in a lower component cost. Across the range of effectiveness values, the compressor accounted for an average of 22% of total DMS system cost.

Table 4.11 Cost breakdown of the DMS at varying effectiveness.

Δε	**Cond.**	**Subcooler**	**Refrig.**	**Comp.**	**Total**	**Install**
10%	247,823	21,359	192,301	94,400	563,000	676,000
0%	221,919	18,065	157,050	92,761	497,000	596,000
-10%	197,864	15,379	127,295	90,689	438,000	526,000
-20%	176,505	13,073	103,343	87,910	388,000	465,000
-30%	156,908	11,166	83,421	83,895	342,000	411,000
-40%	138,419	9,460	66,454	77,465	299,000	359,000
-50%	120,462	7,769	51,735	65,296	252,000	303,000

Considering the cost of heat exchangers and refrigerant, cost decreased with effectiveness in the same way as the ORC. At lower effectiveness values, heat transfer area decreases resulting in a smaller internal volume which reduces the amount of system refrigerant. Refrigerant cost decreased from $192,301 to $51,735 across the range of effectiveness values, accounting for an average of 27% of the total system cost. Like the ORC, the reduction in heat transfer area is a result of increased overall heat transfer coefficients and LMTD. Table 4.12 shows the heat transfer results for the condenser and subcooler devices across the range of effectiveness values.

Table 4.12 Characteristics of the DMS heat exchangers with varying effectiveness values.

	Condenser				**Subcooler**			
Δε	**U**	**LMTD**	**A**	N_{plates}	**U**	**LMTD**	**A**	N_{plates}
	W m^{-2} k^{-1}	**-**	**m^2**	**-**	**W m^{-2} k^{-1}**	**-**	**m^2**	**-**
10%	61.0	2.7	5980	3873	2043	16	64	42
0%	61.2	3.1	4874	3157	2443	18	47	31
-10%	62.3	3.5	3940	2553	2880	20	35	24
-20%	63.3	4.0	3189	2066	3376	22	26	18
-30%	64.2	4.4	2565	1662	3707	24	19	13
-40%	65.1	4.8	2033	1318	3906	26	14	10
-50%	66.0	5.1	1572	1019	4112	27	10	7

Although the heat duty in the condenser and subcooler of the DMS (shown in Table 4.7) are relatively similar, the condenser requires much greater heat transfer area due to small LMTD and overall heat transfer coefficients, leading to greater component cost. The LMTD of the two-phase region of the condenser varied from 2.7-5.1, and the heat transfer coefficient varied from 61-66 W m^{-2} k^{-1} as effectiveness was varied from +10% to -50%. Comparatively, the subcooler operates at a higher LMTD, with values ranging from 16-27, and higher overall heat transfer coefficient ranging from 2043-4112 W m^{-2} k^{-1}, resulting in significantly lower heat transfer area. Across effectiveness values the cost of the condenser varied from $247,823-$120,462, while the

cost of the subcooler varied from $21,359-$7,769. Together, the DMS heat exchangers accounted for an average of 49% of total system cost across the effectiveness values considered.

The final technology considered in the optimization study is the TCCS. Table 4.13 shows the cost breakdown of the TCCS in dollars as heat exchanger effectiveness inputs were varied between +10% and -50%. Component costs are organized into three categories: power cycle, cooling cycle, and cross cycle. Total component and install cost are shown in the bottom right.

Table 4.13 Cost breakdown of the TCCS at varying effectiveness.

	Power Cycle				**Cooling Cycle**	
	Boiler	**Cond.**	**Recup.**	**Pump**	**Subcooler**	**Cond.**
10%	35,172	150,583	24,299	15,981	21,072	185,832
0%	28,633	134,785	20,165	15,955	17,735	166,010
-10%	22,096	98,655	15,526	15,926	15,016	147,853
-20%	18,520	63,183	13,251	15,893	12,682	119,481
-30%	15,293	39,248	11,362	15,851	10,808	89,333
-40%	12,535	24,258	9,680	15,795	9,073	70,570
-50%	7,866	16,947	6,801	15,720	7,254	63,104
	Cross-Cycle				**Total**	**Install**
	Econ.	**TC**	**Refrig.**			
10%	35,965	6,704	206,091		716,000	1,146,000
0%	26,458	6,570	165,730		617,000	987,000
-10%	18,544	6,416	116,800		492,000	787,000
-20%	14,547	6,225	70,038		369,000	590,000
-30%	11,435	5,960	38,403		272,000	436,000
-40%	0	5,547	22,606		205,000	328,000
-50%	0	4,539	17,610		175,000	279,000

As effectiveness values were lowered from +10% to -50%, the total installation cost of the TCCS decreased from $1,146,000-$279,000. The most expensive components of the TCCS were the heat exchangers, which accounted for on average 70% of the total component cost of the TCCS. The two most expensive heat exchangers are the cooling and power cycle condensers, with component costs ranging from $185,832-$63,104, and $150,583-$16,947, respectively. Like the ORC and DMS, the cost of the TCCS heat exchangers decreased as effectiveness values were

lowered. Table 4.14 shows the heat transfer results for the power cycle condenser, boiler, cooling cycle condenser, and subcooler, which are the four primary heat exchangers in the TCCS.

Table 4.14 Characteristics of the TCCS heat exchangers at varying effectiveness values.

Δε	**PC Condenser**				**Boiler**			
	U	**LMTD**	**A**	N_{plates}	**U**	**LMTD**	**A**	N_{plates}
	W m^{-2} k^{-1}	**-**	**m^2**	**-**	**W m^{-2} k^{-1}**	**-**	**m^2**	**-**
10%	60.4	4.52	2376	1,540	1533	11	92	61
0%	60.6	5.40	1936	1,254	1947	13	63	42
-10%	90.0	6.41	1086	704	2350	15	46	31
-20%	173	7.63	476	309	2863	18	33	23
-30%	351	9.18	197	129	3531	22	23	16
-40%	722	11.1	81	53	4340	28	16	12
-50%	1272	14.3	42	28	5684	41	10	8
Δε	**CC Condenser**				**Subcooler**			
	U	**LMTD**	**A**	N_{plates}	**U**	**LMTD**	**A**	N_{plates}
	W m^{-2} k^{-1}	**-**	**m^2**	**-**	**W m^{-2} k^{-1}**	**-**	**m^2**	**-**
10%	60.4	4.37	3508	2,273	26.46	14.5	62	41
0%	60.5	4.99	2848	1,845	29.1	16.4	45	30
-10%	61.6	5.60	2297	1,489	31.95	18.1	33	23
-20%	76	6.19	1549	1,004	39.03	19.8	24	17
-30%	107	6.74	904	586	51.53	21.3	18	13
-40%	136	7.15	584	379	62.24	22.3	13	9
-50%	129	6.80	475	308	59.01	21.1	9	7

Considering these results, the increased cost of the condensers compared to the subcooler and boiler can be explained by low LMTD and heat transfer coefficients which increase the number of plates and overall heat transfer area of the devices. As effectiveness was lowered, overall heat transfer coefficients and LMTD values increase, resulting in lowered heat exchanger area. In summary, the installation costs of the ORC, DMS, and TCCS at varying heat exchanger effectiveness values, as well as the FWE installation cost, are plotted in Figure 4.16.

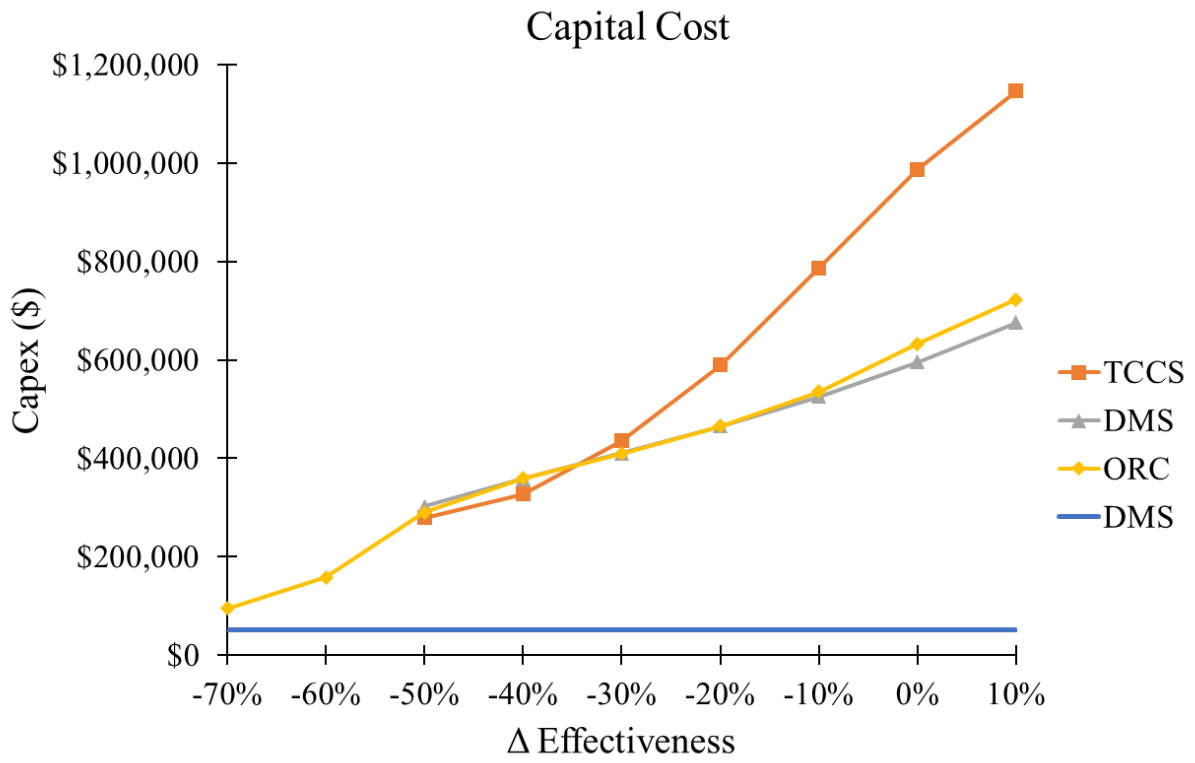

Figure 4.16 Capital cost of the TCCS, DMS, ORC, and FWE.

The total costs of the TCCS, DMS, and ORC were all found to decrease as effectiveness values were lowered. At +10% effectiveness, the TCCS is by far the most expensive technology, exceeding the cost of the DMS and ORC by approximately $450,000. However, as effectiveness values are lowered the cost of the TCCS decreases rapidly compared to the ORC and DMS, and by -30%, only exceeds the ORC and DMS costs by $26,000. The cost of the ORC, DMS, and TCCS then decrease at roughly the same rate from -30% to -50%. The minimum capital cost for the TCCS and DMS both occur at the lowest effectiveness value of -50%. The cost of the ORC, which was varied to -70% effectiveness, continues to decrease, approaching the capital cost of the FWE. This is reasonable considering the similar performance characteristics between the FWE and ORC at extremely low effectiveness values. In the next section, the relationship between heat exchanger effectiveness and system economics will be discussed.

4.4.3. System Economics

With capital costs and annual savings recalculated at varying heat exchanger effectiveness, economic parameters including payback period and net present value can be redetermined. To reiterate, the goal of the system optimization study was to vary heat exchanger effectiveness inputs to find a minimum payback period and maximum net present value for the ORC, DMS, and TCCS. Figure 4.17 shows the payback period of each technology across the range of effectiveness values. Each line represents the average payback period of a technology across the five plant locations considered in this study. The calculated payback period of each technology is designated by color, and the boxed values represent the minimum payback period achieved by each technology.

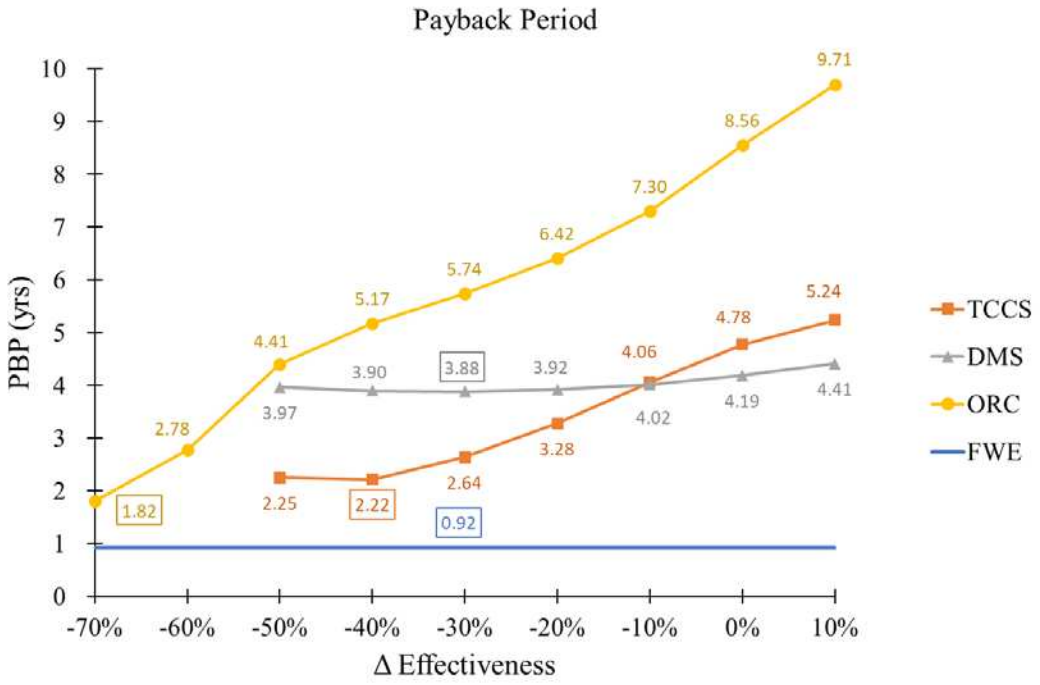

Figure 4.17 Payback period of the ORC, DMS, and TCCS at varying effectiveness compared to the FWE.

Considering these results, the FWE was found to have a significantly lower payback period than the other technologies due to its high annual savings and low capital cost. The ORC achieved a minimum payback period of 1.82 years at -70% effectiveness, the DMS achieved a minimum

payback of 3.88 years at -30% effectiveness, and the TCCS achieved a minimum payback period of 2.22 years at -40% effectiveness. Net present value was also recalculated for each technology at varying effectiveness values. Figure 4.18 shows the NPV of each technology across the range of effectiveness values. Each line represents the average NPV of a technology across the five plant locations considered.

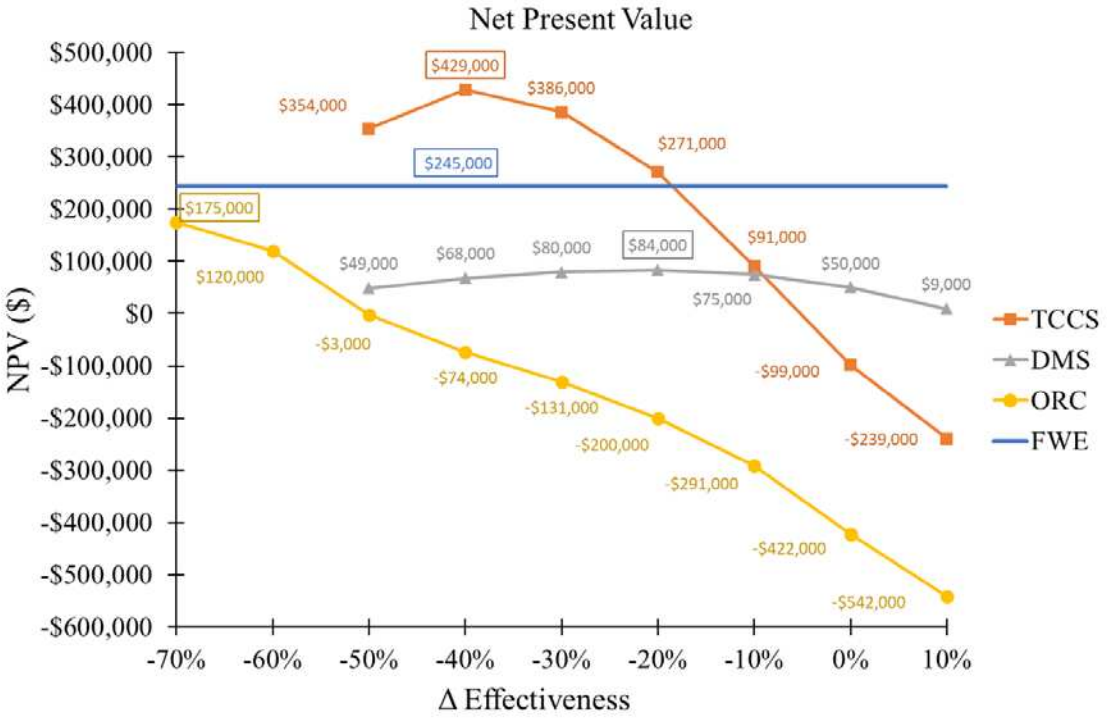

Figure 4.18 NPV of the ORC, DMS, and TCCS at varying effectiveness compared to the FWE.

Again, the boxed value designates the maximum average NPV achieved by each technology. The TCCS achieved the highest NPV of $429,000 at an effectiveness value of -40%. The FWE achieved the second greatest average NPV of $245,000. The ORC achieved the third highest NPV of $175,000 at -70% effectiveness, and the DMS achieved the fourth highest NPV of $84,000. Looking at both payback period and NPV, each technology was optimized at a lowered effectiveness. This is counterintuitive, as one would expect the highest performing system to also be the most economically viable. For the TCCS, payback period is minimized and NPV is

maximized at -40% of the original effectiveness values. The DMS achieves minimum payback at -30% effectiveness, but a maximum NPV at -20% effectiveness. From -20% to -30% effectiveness, DMS payback period only decreases by a factor of 1%, but NPV decreases by a factor of 5%, so it can be concluded that the DMS is economically optimized for at -20%. The ORC was the only technology that didn't experience a true maximum or minimum, but rather, the payback period and NPV of the ORC approached the values of the FWE as heat exchanger effectiveness values were lowered to -70%. This may indicate that the ORC is never as economical as the much simpler FWE, even when the ORC is configured to generate power and feedwater heating.

As mentioned in Section 3.4.3, one additional calculation was made in the economic analysis to investigate the impact of construction period and startup time on NPV. Figure 4.18 displays the calculated NPV of each technology assuming a 3-year construction period with a 6 month start up time, which is consistent with the values used in prior TCCS research [93]. To investigate the significance of this assumption, NPV's were recalculated assuming a much shorter construction period and startup time of 1-year and 3 months, respectively. Figure 4.19 compares the NPV's calculated with varying construction periods and startup times. When assuming the shorter construction period, the NPV of all four technologies increased. For the TCCS, DMS, and ORC, the NPV increased by an average of $62,000, $44,000, and $34,000, respectively, across effectiveness values considered. The NPV of the FWE increased by $10,000, from $245,000 to $255,000. Considering these results, reducing the construction period does impact the magnitude of NPV, and further investigations should be diligent in assuming an appropriate construction period and startup time for each technology.

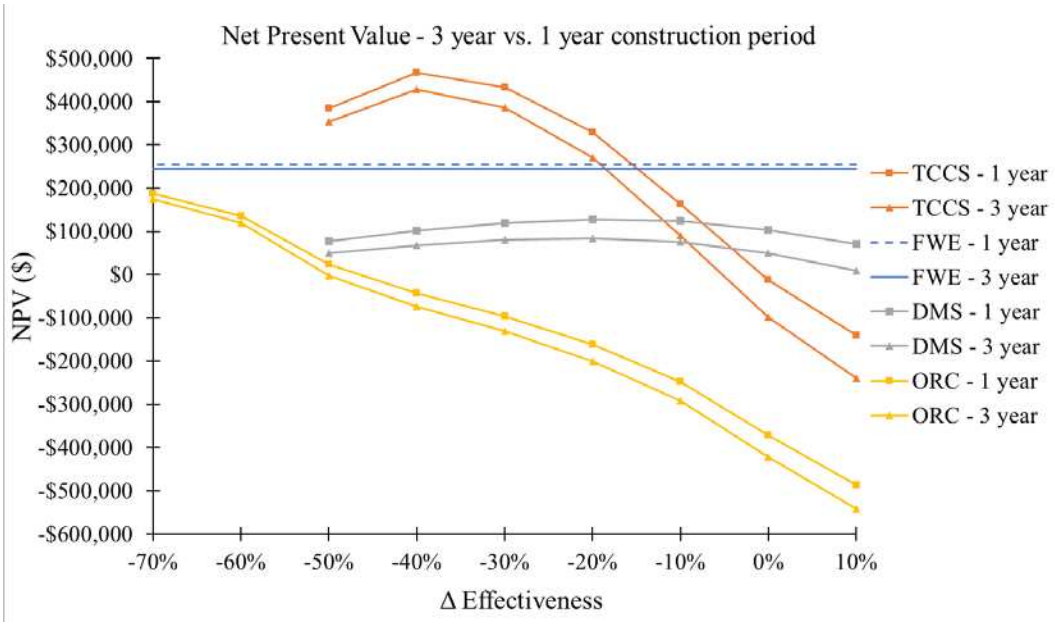

Figure 4.19 Net present values of each technology assuming a 3-year versus 1-year construction period.

Comparing the technologies that performed the best economically, the FWE was still found to have the lowest payback period even after the ORC, DMS, and TCCS were optimized. Although the ORC achieved the second lowest payback period of 1.82 years, it does so at such low effectiveness values that almost no electrical offset is produced by the ORC turbine, essentially operating as a feedwater heater. The technology option that yields the highest NPV is the TCCS. At -40% effectiveness, the TCCS achieves an average NPV of $429,000 (Figure 4.18), which is greater than the NPV of the FEW by a factor of $184,000.

In conclusion, the optimization study sought to find an appropriate system size for the ORC, DMS, and TCCS that minimizes payback period and maximizes net present value. The FWE was not considered in the optimization study due to its significantly lower payback period and higher net present value that made it much more competitive than the other technologies. Further, a heat exchanger simulation was not performed for the FWE, and capital cost was determined using a supplier quote, and thus would require a different optimization procedure. Considering all

four technologies, the FWE and TCCS were the technology options that achieved the lowest payback period and highest NPV. A plant could install either of these technologies to reduce energy consumption and save money. If the priority of a plant is to install a technology with a low payback period, then the FWE is the most economically viable. However, if a plant is more concerned with installing a technology with a high NPV, than the TCCS is the most economically viable.

CHAPTER 5. Conclusions and Recommendations

The present study examines the use of four different technologies to produce energy savings at a beef processing facility: a feedwater economizer, an electrically driven dedicated mechanical subcooler, an organic Rankine cycle, and a thermally driven TCCS subcooler. The ORC, DMS, and TCCS working fluid was selected to be R134a. Using water and natural gas data, waste heat availability throughout the year is determined at a beef processing facility. Using ambient weather data from five different cities, a beef plant ammonia refrigeration system with condenser cooling towers is thermodynamically modeled to evaluate baseline refrigeration performance. Then, a detailed thermodynamic, heat exchanger, and economic model was developed to study the technical and economic performance of the FWE, ORC, DMS, and TCCS. In the thermodynamic analysis, the heat exchangers were divided into regions based on working fluid phase (subcooled, two-phase, or superheated), and a first law analysis was used to determine heat duties, as well as work inputs/outputs of the turbomachinery. Thermodynamic performance of the ORC and FWE were determined based on the average waste heat input to either system from the boiler exhaust, and average boiler feedwater mass flow rate. Thermodynamic performance of both the DMS and TCCS were calculated at an hourly resolution, providing boiler feedwater heating and PRS subcooling, which operates at a varying high-side pressure depending on ambient conditions in each plant location. The performance of all four technologies was evaluated for 5,184 hours of the year in each plant location, based on when the boiler operation hours. Annual savings yielded by each technology were then calculated from the hourly energy savings and monthly gas and electricity prices in each city. In the heat exchanger analysis, heat transfer correlations from the literature were used to calculate the size and performance of the plate and frame heat exchangers. Then, the capital cost of the FWE, ORC, DMS, and TCCS was determined using

component cost models and supplier quotes. All major pieces of equipment were accounted for including heat exchangers, turbomachines, refrigerant, heat recovery, and piping. The capital cost of the ORC was further investigated by comparing costs determined in the present study to costs published in the literature. Next, simple payback period of each system in each plant location was calculated based on the initial capital expenditures and the yearly energy savings. Additionally, a cash flow analysis was performed to calculate the net present value of each technology. Within the cash flow analysis, two different construction periods and startup times were considered to determine variation in NPV. Finally, an optimization study was conducted with the goal of increasing the economic viability of the ORC, DMS, and TCCS. The ORC, DMS and TCCS were optimized by varying the heat exchanger effectiveness values in increments of ±10%, until the minimum payback period and maximum net present value were achieved.

Comparing the four technologies, the FWE achieved the lowest average simple payback period of 0.92 years. The FWE recovers 646 kW of heat from the boiler exhaust to preheat feedwater that enters the boiler. In doing so, feedwater is heated from 15.56^{o}C to 18.4^{o}C, resulting in an average hourly natural gas savings of 2.02 MCF/hr. Throughout the year, the FWE was found to save a total of 10,535 MCF in natural gas. The FWE achieved the second highest average NPV of $245,000. The ORC achieved the second lowest payback period of 1.82 years when heat exchanger effectiveness values were lowered by -70% of the original effectiveness values. To achieve this payback, the ORC must operate at an extremely low pressure ratio, producing no work in the turbine and rejecting all boiler heat to the condenser, effectively operating as a feedwater heater. At -70%, the ORC achieves a net present value of $175,000, which is the second lowest NPV when compared to the FWE, and optimized DMS and TCCS. The TCCS achieves the third lowest payback of 2.22 years, and highest NPV of $429,000 when effectiveness values were

lowered by -40%. At -40% effectiveness, the TCCS provides 506 kW of cooling to the PRS, rejecting a total of 1,140 kW of heat in the condensers to the boiler feedwater. The overall COP of the TCCS at -40% was found to be 0.8, which is a significant reduction in performance from the COP of 1.28 at the original effectiveness values. Although this reduction in performance results in a reduction in the average annual savings, from $220,000 at 0% to $157,000 at -40%, there is an even larger reduction in TCCS capital cost. This reduction in cost is a direct result of a large reduction in heat transfer area when effectiveness values are lowered. At lower heat exchanger effectiveness values, overall heat transfer coefficient and LMTD were found to increase significantly, resulting in smaller required heat transfer areas and lower heat exchanger costs. Additionally, with smaller heat exchangers, the internal volume decreases leading to lowered refrigerant costs. Between -0% and -40%, TCCS heat exchanger cost decreased from $417,000 to $149,000, and refrigerant cost decreased from $166,000 to $22,600. Reduction in refrigerant and heat exchanger costs combined to produce a large decrease in system cost, from $987,000 at 0% to $328,000 at -40%. The DMS shows the least economic promise of any technology, achieving a minimum payback period of 3.88 years at -30% effectiveness, and a maximum NPV of $84,000 at-20% effectiveness. At -20% effectiveness, the DMS receives a work input of 73 kW to the compressor to provide 742 kW of subcooling to the PRS, rejecting 815 kW of heat to the boiler feedwater in the condenser. The COP of the DMS at -20% is 10.1, which is significantly higher than the performance of a standard vapor compression chiller due to the high temperature and pressure of the PRS ammonia entering the subcooler, and relatively low temperature of the DMS condenser feedwater. Although the amount of subcooling provided to the PRS by the DMS is greater than the amount provided by the TCCS, the annual savings are less due to the electrical input required to the DMS compressor and lower amount of heat rejected to the feedwater in the

condenser. Overall, the two technologies that are most economically viable are the FWE and the TCCS. If the plant wishes to install a simple technology with a low payback, then the FWE would make the most economic sense. However, if a plant is more concerned with choosing the technology option with the highest NPV, but a slightly longer payback period, then the TCCS should be selected.

5.1. Future Studies

Several aspects of this work require further investigation. The key parts of the future work for this study include:

- Collecting better data regarding a beef processing plant's boiler and refrigeration systems. With regards to the boiler, this study would benefit from hourly waste heat data throughout the year, forgoing the need for a boiler model. By placing temperature and flow sensors in the exhaust stacks of boilers at a facility, hourly waste heat could be measured to know how much energy input is available at any given time. With regards to the refrigeration system, more data regarding the performance of the compressor, condensers, and evaporators would allow for a more accurate estimation of baseline performance. One assumption that could be revised is the assumption of overall cooling load. In this study, overall cooling load is assumed to be a constant 9.3 MW throughout the year. The overall cooling load is likely to fluctuate throughout the year based on several factors, such as head processed, storage time, and refrigeration system maintenance. In general, the overall system analysis would greatly benefit from more refrigeration system data such as refrigerant mass flow, condenser and evaporator pressures and temperatures, and compressor performance. Other factors which are not included in the baseline model are pressure drops, which are likely to occur in large refrigeration system.

- Different sizes of plants should also be considered in future studies. In the current study, a generic plant is considered that processes 3200 head of cattle per day, which is based on the national average of plants found in the review of literature. Plant capacity varies wildly, with some plants processing 500 head per day while others process 6,000 head per day. The number of cattle processed has a large impact on the amount of refrigeration required, and waste heat available, thus impacting the performance and savings achievable by a waste heat driven cooling device. Moving forward, the analysis will become more thorough if replicated for plants of varying size and capacity, to better understand how this impacts performance and economics of the TCCS.
- Heat Exchanger models that include pressure drop should be investigated. In the current study, pressure drop is neglected, which is unlikely considering the number of plates calculated for each heat exchanger. More realistic performance results would be obtained if pressure drops in the heat exchangers and pipes of each system were considered. The heat exchanger model could be further improved by taking a more rigorous approach to selecting appropriate heat transfer correlations. In the present study, the correlations used were taken directly from prior TCCS research conducted by Young et al. However, in some instances, the calculated Reynold's number were outside of the ranges designated by the correlations. In these instances, the Reynold's numbers were set to the maximum or minimum value specified by the correlation. In these instances, different correlations could be used that are appropriate for the calculated Reynold's number, leading to more accurate performance results.
- Consideration of different heat exchanger types and working fluids will be critical to the further commercialization of the TCCS. In this study, plate and frame heat exchangers were

selected as the heat exchanger type, and R134a was selected as the working fluid. There is a high likelihood that R134a will be phased out of use in the future, due to its high GWP which is damaging to the environment. However, there are many other types of refrigerants that are less environmentally harmful and may be more suitable for the application of beef processing. Similarly, there are many types of heat exchangers beyond plate and frame, including shell and tube and spiral heat exchangers, that may perform better or be more suitable for the application of beef processing.

- A detailed analysis of the waste heat produced at a beef processing facility. In the present study, the only waste heat stream that is considered is boiler exhaust, however other waste heat streams could be utilized which will result in additional savings. Examples of other waste heat streams at a beef plant that could be utilized include waste heat from wastewater, space heating, and process heating. In addition, investigating varying waste heat loads will be critical to estimating the performance of the TCCS. In the current study, the average waste heat availability and feedwater mass flow rate was assumed constant for all operation hours. Boiler waste heat availability and boiler feedwater flow rate will vary throughout the day based on plant activity, and throughout the year based on ambient conditions and other factors. One simulation was conducted, which confirmed that total annual savings were relatively unchanged with the assumed constant waste heat versus varying waste heat. However, a more thorough investigation is required, because understanding how the TCCS operates under varying waste heat conditions and condenser water flow rates will be a critical step toward the commercialization of this technology.
- Future work should investigate different types of food processing facilities other than just beef processing facilities. Many other types of food, such as dairy, fruits and vegetables,

also require large amounts of process heating and refrigeration during processing. For this reason, these types of facilities could also benefit from the installation of a waste heat driven cooling technology such as the TCCS.

- A more thorough Cost validation of each technology should also be included in future work. In the present study, only the ORC costs were compared to cost data published in the literature. This work would be improved by also comparing the TCCS, DMS, and FWE costs to published costs.

References

[1] "U.S. Energy Facts Explained - Consumption and Production - U.S. Energy Information Administration (EIA)" [Online]. Available: https://www.eia.gov/energyexplained/us-energy-facts/. [Accessed: 16-Oct-2019].

[2] "Use of Energy in Explained - U.S. Energy Information Administration (EIA)" [Online]. Available: https://www.eia.gov/energyexplained/use-of-energy/. [Accessed: 27-Jul-2020].

[3] "Waste Heat Recovery Technologies and Applications | Elsevier Enhanced Reader" [Online]. Available: https://reader.elsevier.com/reader/sd/pii/S2451904918300015?token=7E6201930EF6DEB4DDE4453083F1D155D166EDDB941BB134647C5E5B65DC2C06ED3D051372E6DF47D59A22097FF896A9. [Accessed: 14-May-2020].

[4] Compton, M., Willis, S., Rezaie, B., and Humes, K., 2018, "Food Processing Industry Energy and Water Consumption in the Pacific Northwest," Innovative Food Science & Emerging Technologies, 47, pp. 371–383.

[5] 2007, *Energy Trends in Selected Manufacturing Sectors*, United States Environmental Protection Agency, Washington DC, USA.

[6] 2014, *Manufacturing Energy Consumption Survey (MECS) - Data - U.S. Energy Information Administration (EIA)*, United States Energy Information Administration, Washington DC, USA.

[7] 2018, *Emissions Impossible: How Big Meat and Dairy Are Heating up the Planet*, Institute for Agriculture and Trade Policy, Minneapolis, Minnesota.

[8] "The Paris Agreement | UNFCCC" [Online]. Available: https://unfccc.int/process-and-meetings/the-paris-agreement/the-paris-agreement. [Accessed: 08-Apr-2020].

[9] "Implications of Future US Diet Scenarios on Greenhouse Gas Emissions | Center for Sustainable Systems" [Online]. Available: http://css.umich.edu/publication/implications-future-us-diet-scenarios-greenhouse-gas-emissions. [Accessed: 02-Oct-2020].

[10] Brückner, S., Liu, S., Miró, L., Radspieler, M., Cabeza, L. F., and Lävemann, E., 2015, "Industrial Waste Heat Recovery Technologies: An Economic Analysis of Heat Transformation Technologies," Applied Energy, 151, pp. 157–167.

[11] "(6) The Modeling of Air-Cooled Absorption Chiller Integration in CHP System," ResearchGate [Online]. Available: https://www.researchgate.net/publication/255585417_The_Modeling_of_Air-Cooled_Absorption_Chiller_Integration_in_CHP_System. [Accessed: 14-May-2020].

[12] "A Novel Flue Gas Waste Heat Recovery System for Coal-Fired Ultra-Supercritical Power Plants | Elsevier Enhanced Reader" [Online]. Available: https://reader.elsevier.com/reader/sd/pii/S1359431114002130?token=C06908F6451C88F2156A9380258C5FA91F554EB6B0CD28E148FD13A10FE56FEE9C495ECCCFA4B13ADAAA820EBBDE6D6B. [Accessed: 24-Sep-2019].

[13] Aneke, M., Agnew, B., Underwood, C., and Menkiti, M., 2012, "Thermodynamic Analysis of Alternative Refrigeration Cycles Driven from Waste Heat in a Food Processing Application," International Journal of Refrigeration, 35(5), pp. 1349–1358.

[14] Bombarda, P., Invernizzi, C. M., and Pietra, C., 2010, "Heat Recovery from Diesel Engines: A Thermodynamic Comparison between Kalina and ORC Cycles," Applied Thermal Engineering, 30(2), pp. 212–219.

[15] 2020, "Wake Up! Supersonic Cold Spray Converts Waste Energy To Electricity," CleanTechnica [Online]. Available: https://cleantechnica.com/2020/04/17/10-quadrillion-btu-

in-untapped-waste-energy-gets-supersonic-thermoelectric-treatment/. [Accessed: 14-May-2020].
[16] Yari, M., and Mahmoudi, S. M. S., 2010, "Utilization of Waste Heat from GT-MHR for Power Generation in Organic Rankine Cycles," Applied Thermal Engineering, 30(4), pp. 366–375.
[17] "Options to Maximise Process Heat Recovery at Red Meat Processing Facilities" [Online]. Available: https://www.ampc.com.au/uploads/cgblog/id87/2013_5011-Options-to-Maximise-Process-Heat-Recovery-at-Red-Meat-Processing-Facilities.pdf. [Accessed: 18-Sep-2019].
[18] Hempstead, C., and Worthington, W. E., 2005, *Encyclopedia of 20th-Century Technology*, Routledge.
[19] "A History of Mechanical Engineering | The MIT Press" [Online]. Available: https://mitpress.mit.edu/books/history-mechanical-engineering. [Accessed: 19-May-2020].
[20] Moran, M. J., Shapiro, H. N., and Boettner, D. D., 2010, *Fundamentals of Engineering Thermodynamics, 7th Edition*, Wiley Global Education.
[21] Çengel, Y. A., and Boles, M. A., 2011, *Thermodynamics: An Engineering Approach*, McGraw-Hill.
[22] Kornhauser, A. A., 1990, "The Use of an Ejector As a Refrigerant Expander."
[23] Park, C., Lee, H., Hwang, Y., and Radermacher, R., 2015, "Recent Advances in Vapor Compression Cycle Technologies," International Journal of Refrigeration, 60, pp. 118–134.
[24] Huff, H. J., Lindsay, D., and Radermacher, R., 2002, "Positive Displacement Compressor And Expander Simulation."
[25] Huff, H. J., and Radermacher, R., 2003, *CO2 Compressor - Expander Analysis*, Air-Conditioning And Refrigeration Technology Institute.
[26] Nickl, J., Will, G., Quack, H., and Kraus, W. E., 2005, "Integration of a Three-Stage Expander into a CO2 Refrigeration System," International Journal of Refrigeration, 28(8), pp. 1219–1224.
[27] Wang, M., Zhao, Y., Cao, F., Bu, G., and Wang, Z., 2012, "Simulation Study on a Novel Vane-Type Expander with Internal Two-Stage Expansion Process for R-410A Refrigeration System," International Journal of Refrigeration, 35(4), pp. 757–771.
[28] Subiantoro, A., and Ooi, K. T., 2013, "Economic Analysis of the Application of Expanders in Medium Scale Air-Conditioners with Conventional Refrigerants, R1234yf and CO2," International Journal of Refrigeration, 36(5), pp. 1472–1482.
[29] Jiautheen, P. B., and Annamalai, M., 2014, "Review on Ejector of Vapor Jet Refrigeration System," Int. J. Air-Cond. Ref., 22(03), p. 1430003.
[30] Sarbu, I., and Sebarchievici, C., 2017, "Chapter 7 - Solar Thermal-Driven Cooling Systems," *Solar Heating and Cooling Systems*, I. Sarbu, and C. Sebarchievici, eds., Academic Press, pp. 241–313.
[31] Disawas, S., and Wongwises, S., 2004, "Experimental Investigation on the Performance of the Refrigeration Cycle Using a Two-Phase Ejector as an Expansion Device," International Journal of Refrigeration, 27(6), pp. 587–594.
[32] Li, D., and Groll, E. A., 2005, "Transcritical CO2 Refrigeration Cycle with Ejector-Expansion Device," International Journal of Refrigeration, 28(5), pp. 766–773.
[33] Lawrence, N., and Elbel, S., 2013, "Theoretical and Practical Comparison of Two-Phase Ejector Refrigeration Cycles Including First and Second Law Analysis," International Journal of Refrigeration, 36(4), pp. 1220–1232.

[34] Lawrence, N., and Elbel, S., 2014, "Experimental Investigation of a Two-Phase Ejector Cycle Suitable for Use with Low-Pressure Refrigerants R134a and R1234yf," International Journal of Refrigeration, 38, pp. 310–322.
[35] Boumaraf, L., Haberschill, P., and Lallemand, A., 2014, "Investigation of a Novel Ejector Expansion Refrigeration System Using the Working Fluid R134a and Its Potential Substitute R1234yf," International Journal of Refrigeration, 45, pp. 148–159.
[36] Hafner, A., Försterling, S., and Banasiak, K., 2014, "Multi-Ejector Concept for R-744 Supermarket Refrigeration," International Journal of Refrigeration, 43, pp. 1–13.
[37] Visentin, C., Prodi, N., Cappelletti, F., Torresin, S., and Gasparella, A., 2018, "Flashing Liquid Expander Energy Reduction in Refrigeration Systems," Purdue e-pubs.
[38] Dutta, A. K., Yanagisawa, T., and Fukuta, M., 2001, "An Investigation of the Performance of a Scroll Compressor under Liquid Refrigerant Injection," International Journal of Refrigeration, 24(6), pp. 577–587.
[39] Cho, H., Chung, J. T., and Kim, Y., 2003, "Influence of Liquid Refrigerant Injection on the Performance of an Inverter-Driven Scroll Compressor," International Journal of Refrigeration, 26(1), pp. 87–94.
[40] Pawale, K., Sali, N. V., and Deshpande, G., 2014, "Vapor Compression Refrigeration System with Refrigerant Injection: A Review," Elixir Mechanical Engineering, (72).
[41] Winandy, E. L., and Lebrun, J., 2002, "Scroll Compressors Using Gas and Liquid Injection: Experimental Analysis and Modelling," International Journal of Refrigeration, 25(8), pp. 1143–1156.
[42] Heo, J., Jeong, M. W., and Kim, Y., 2010, "Effects of Flash Tank Vapor Injection on the Heating Performance of an Inverter-Driven Heat Pump for Cold Regions," International Journal of Refrigeration, 33(4), pp. 848–855.
[43] Lee, H., Hwang, Y., Radermacher, R., and Chun, H.-H., 2013, "Potential Benefits of Saturation Cycle with Two-Phase Refrigerant Injection," Applied Thermal Engineering, 56(1), pp. 27–37.
[44] Lee, H., Hwang, Y., Radermacher, R., and Chun, H.-H., 2015, "Performance Investigation of Multi-Stage Saturation Cycle with Natural Working Fluids and Low GWP Working Fluids," International Journal of Refrigeration, 51, pp. 103–111.
[45] Lee, H., Hwang, Y., Song, I., and Jang, K., 2015, "Transient Thermal Model of Passenger Car's Cabin and Implementation to Saturation Cycle with Alternative Working Fluids," Energy, 90, pp. 1859–1868.
[46] Wang, X., Hwang, Y., and Radermacher, R., 2008, "Investigation of Potential Benefits of Compressor Cooling," Applied Thermal Engineering, 28(14), pp. 1791–1797.
[47] Domanski, P. A., Didion, D. A., and Doyle, J. P., 1994, "Evaluation of Suction-Line/Liquid-Line Heat Exchange in the Refrigeration Cycle," International Journal of Refrigeration, 17(7), pp. 487–493.
[48] Klein, S. A., Reindl, D. T., and Brownell, K., 2000, "Refrigeration System Performance Using Liquid-Suction Heat Exchangers," International Journal of Refrigeration, 23(8), pp. 588–596.
[49] Mastrullo, R., Mauro, A. W., Tino, S., and Vanoli, G. P., 2007, "A Chart for Predicting the Possible Advantage of Adopting a Suction/Liquid Heat Exchanger in Refrigerating System," Applied Thermal Engineering, 27(14), pp. 2443–2448.
[50] Lorentzen, G., and Pettersen, J., 1993, "A New, Efficient and Environmentally Benign System for Car Air-Conditioning," International Journal of Refrigeration, 16(1), pp. 4–12.

[51] Rozhentsev, A., and Wang, C.-C., 2001, "Some Design Features of a CO2 Air Conditioner," Applied Thermal Engineering, 21(8), pp. 871–880.
[52] Hafner, A., 2000, "Experimental Study on Heat Pump Operation of Prototype CO2 Mobile Air Conditioning System," pp. 177–184.
[53] Cho, H., Ryu, C., and Kim, Y., 2007, "Cooling Performance of a Variable Speed CO2 Cycle with an Electronic Expansion Valve and Internal Heat Exchanger," International Journal of Refrigeration, 30(4), pp. 664–671.
[54] Jarall, S., 2012, "Study of Refrigeration System with HFO-1234yf as a Working Fluid," International Journal of Refrigeration, 35(6), pp. 1668–1677.
[55] Zilio, C., Brown, J. S., Schiochet, G., and Cavallini, A., 2011, "The Refrigerant R1234yf in Air Conditioning Systems," Energy, 36(10), pp. 6110–6120.
[56] Lee, T.-J., Kim, K.-B., Lee, S.-W., and Lee, G.-H., 2011, "Development of Performance Analysis Program and the Study of Substitution Refrigerant R1234yf for Vehicle Refrigerant Compressor," Korean Journal of Air-Conditioning and Refrigeration Engineering, 23(11), pp. 699–704.
[57] Navarro-Esbrí, J., Molés, F., and Barragán-Cervera, Á., 2013, "Experimental Analysis of the Internal Heat Exchanger Influence on a Vapour Compression System Performance Working with R1234yf as a Drop-in Replacement for R134a," Applied Thermal Engineering, 59(1), pp. 153–161.
[58] Cho, H., Lee, H., and Park, C., 2013, "Performance Characteristics of an Automobile Air Conditioning System with Internal Heat Exchanger Using Refrigerant R1234yf," Applied Thermal Engineering, 61(2), pp. 563–569.
[59] Pottker, G., and Hrnjak, P., 2015, "Experimental Investigation of the Effect of Condenser Subcooling in R134a and R1234yf Air-Conditioning Systems with and without Internal Heat Exchanger," International Journal of Refrigeration, 50, pp. 104–113.
[60] Zubair, S. M., Yaqub, M., and Khan, S. H., 1996, "Second-Law-Based Thermodynamic Analysis of Two-Stage and Mechanical-Subcooling Refrigeration Cycles," International Journal of Refrigeration, 19(8), pp. 506–516.
[61] Khan, J.-R., and Zubair, S. M., 2000, "Design and Rating of an Integrated Mechanical-Subcooling Vapor-Compression Refrigeration System," Energy Conversion and Management, 41(11), pp. 1201–1222.
[62] Qureshi, B. A., and Zubair, S. M., 2012, "The Impact of Fouling on Performance of a Vapor Compression Refrigeration System with Integrated Mechanical Sub-Cooling System," Applied Energy, 92, pp. 750–762.
[63] Couvillion, R. J., Larson, M. W., and Somerville, M. H., 1988, "Analysis of a Vapor-Compression Refrigeration System with Mechanical Subcooling," ASHRAE transactions, 94, pp. 641–660.
[64] Thornton, J. W., Klein, S. A., and Mitchell, J. W., 1994, "Dedicated Mechanical Subcooling Design Strategies for Supermarket Applications," International Journal of Refrigeration, 17(8), pp. 508–515.
[65] Khan, J.-R., and Zubair, S. M., 2000, "Design and Rating of Dedicated Mechanical-Subcooling Vapour Compression Refrigeration Systems," Proceedings of the Institution of Mechanical Engineers, Part A: Journal of Power and Energy, 214(5), pp. 455–471.
[66] Hrnjak, P., 2012, "Effect of Condenser Subcooling of the Performance of Vapor Compression Systems: Experimental and Numerical Investigation," *Purdue E-Pubs*.

[67] Qureshi, B. A., and Zubair, S. M., 2012, "The Effect of Refrigerant Combinations on Performance of a Vapor Compression Refrigeration System with Dedicated Mechanical Sub-Cooling," International Journal of Refrigeration, 35(1), pp. 47–57.
[68] Srikhirin, P., Aphornratana, S., and Chungpaibulpatana, S., 2001, "A Review of Absorption Refrigeration Technologies," Renewable and Sustainable Energy Reviews, 5(4), pp. 343–372.
[69] Tassou, S. A., Lewis, J. S., Ge, Y. T., Hadawey, A., and Chaer, I., 2010, "A Review of Emerging Technologies for Food Refrigeration Applications," Applied Thermal Engineering, 30(4), pp. 263–276.
[70] Little, A. B., and Garimella, S., 2011, "Comparative Assessment of Alternative Cycles for Waste Heat Recovery and Upgrade," Energy, 36(7), pp. 4492–4504.
[71] "Dry Air Turbo-Compression Cooling | ASME Power Conference | ASME Digital Collection" [Online]. Available: https://asmedigitalcollection.asme.org/POWER/proceedings/POWER2016/50213/V001T04A003/365735. [Accessed: 08-Jun-2020].
[72] Garland, S. D., Bandhauer, T. M., Grauberger, A. M., Iii, J. R. S., Young, D. N., Eisemann, K., Fuller, R., Noall, J., Shull, J., Sami, R. V., Reinke, M. J., and Gabbey, L. W., 2018, "EXPERIMENTAL INVESTIGATION OF A WASTE HEAT DRIVEN TURBO-COMPRESSION CHILLER," Begel House Inc.
[73] Garland, S. D., Noall, J., and Bandhauer, T. M., 2018, "Experimentally Validated Modeling of a Turbo-Compression Cooling System for Power Plant Waste Heat Recovery," Energy, 156, pp. 32–44.
[74] Young, D., Gibson, S. C., and Bandhauer, T. M., 2018, "Working Fluid Selection and Technoeconomic Optimization of a Turbocompression Cooling System," J. Thermal Sci. Eng. Appl, 10(6).
[75] Gibson, S. C., Young, D., and Bandhauer, T. M., 2018, "Technoeconomic Optimization of Turbocompression Cooling Systems," American Society of Mechanical Engineers Digital Collection.
[76] Garland, S. D., 2017, "Waste Heat Driven Turbo-Compression Cooling."
[77] "JBS," JBS USA [Online]. Available: https://jbssa.com/. [Accessed: 25-Jun-2020].
[78] "Tyson Foods Inc. - Tyson Foods Facts" [Online]. Available: https://ir.tyson.com/about-tyson/facts/default.aspx. [Accessed: 25-Jun-2020].
[79] "US & Canada Protein Processing Locations | Cargill" [Online]. Available: https://www.cargill.com/page/locations/protein-processing. [Accessed: 25-Jun-2020].
[80] Li, S., Ziara, R. M. M., Dvorak, B., and Subbiah, J., 2018, "Assessment of Water and Energy Use at Process Level in the U.S. Beef Packing Industry: Case Study in a Typical U.S. Large-Size Plant," Journal of Food Process Engineering, 41(8), p. e12919.
[81] "Electricity Data Browser - Average Retail Price of Electricity" [Online]. Available: https://www.eia.gov/electricity/data/browser/#/topic/7?agg=1,0&geo=g000110g00g4&endsec=2&linechart=ELEC.PRICE.US-IND.M&columnchart=ELEC.PRICE.US-IND.M&map=ELEC.PRICE.US-IND.M&freq=M&start=201901&end=201912&ctype=linechart&ltype=pin&rtype=s&maptype=0&rse=0&pin=. [Accessed: 14-Jun-2020].
[82] "U.S. Natural Gas Prices" [Online]. Available: https://www.eia.gov/dnav/ng/ng_pri_sum_dcu_nus_m.htm. [Accessed: 14-Jun-2020].

[83] "TMY - NSRDB" [Online]. Available: https://nsrdb.nrel.gov/about/tmy.html. [Accessed: 17-May-2021].
[84] Mitchell, J. W., and Braun, J. E., 2012, *Principles of Heating, Ventilation, and Air Conditioning in Buildings*, John Wiley & Sons.
[85] "Cooling Tower and Condenser Water Design Part 3: Understanding Tonnage, Range, and Approach —," James M. Pleasants Company [Online]. Available: https://jmpcoblog.com/hvac-blog/cooling-tower-and-condenser-water-design-part-3-understanding-tonnage-range-and-approach. [Accessed: 19-May-2021].
[86] "BAC Series 3000 Single Cell Data" [Online]. Available: https://www.baltimoreaircoil.com/english/wp-content/uploads/2015/06/S3000A.pdf. [Accessed: 24-Aug-2020].
[87] Pearson, A., 2008, "Refrigeration with Ammonia," International Journal of Refrigeration, 31(4), pp. 545–551.
[88] "Use Feedwater Economizers for Waste Heat Recovery" [Online]. Available: https://www.energy.gov/sites/prod/files/2014/05/f16/steam3_recovery.pdf. [Accessed: 20-Apr-2020].
[89] "Fuels - Higher and Lower Calorific Values" [Online]. Available: https://www.engineeringtoolbox.com/fuels-higher-calorific-values-d_169.html. [Accessed: 10-Jun-2020].
[90] "Thermodynamic Properties of Engine Exhaust Gas for Different Kind of Fuels," ResearchGate [Online]. Available: https://www.researchgate.net/publication/281688983_Thermodynamic_Properties_of_Engine_Exhaust_Gas_for_Different_Kind_of_Fuels. [Accessed: 29-Jun-2020].
[91] "Use Feedwater Economizers for Waste Heat Recovery."
[92] 2015, "Heat Exchangers," Dairy Processing Handbook [Online]. Available: https://dairyprocessinghandbook.tetrapak.com/chapter/heat-exchangers. [Accessed: 12-Mar-2021].
[93] Young, D. N., 2017, "Technoecomonic Optimization and Working Fluid Selection for an Engine Coolant Driven Turbo-Compression Cooling System," Text, Colorado State University.
[94] Ayub, Z., 2003, "Plate Heat Exchanger Literature Survey and New Heat Transfer and Pressure Drop Correlations for Refrigerant Evaporators," Heat Transfer Engineering, 24, pp. 3–16.
[95] Kuo, W. S., Lie, Y. M., Hsieh, Y. Y., and Lin, T. F., 2005, "Condensation Heat Transfer and Pressure Drop of Refrigerant R-410A Flow in a Vertical Plate Heat Exchanger," International Journal of Heat and Mass Transfer, 48(25), pp. 5205–5220.
[96] Hsieh, Y. Y., and Lin, T., 2002, "Saturated Flow Boiling Heat Transfer and Pressure Drop of Refrigerant R-410A in a Vertical Plate Heat Exchanger."
[97] Burton, H., *Boiler Economizer Systems*, Cain Industries.
[98] 2020, "2019 Chemical Engineering Plant Cost Index Annual Average," Chemical Engineering.
[99] Brown, T., 2016, *Engineering Economics and Economic Design for Process Engineers*, CRC Press.
[100] Riekmann, T., 2009, *German and International Cost Indices | Index (Economics) | Inflation*.

[101] Couper, J. R., Penney, W. R., and PhD, J. R. F., 2009, *Chemical Process Equipment - Selection and Design (Revised 2nd Edition)*, Gulf Professional Publishing.
[102] "Updated Buildings Sector Appliance and Equipment Costs and Efficiency" [Online]. Available: https://www.eia.gov/analysis/studies/buildings/equipcosts/. [Accessed: 29-Oct-2020].
[103] "Absorption Chillers for CHP Systems" [Online]. Available: https://www.energy.gov/sites/prod/files/2017/06/f35/CHP-Absorption%20Chiller-compliant.pdf. [Accessed: 29-Oct-2020].
[104] Jones, S. B., Meyer, P. A., Snowden-Swan, L. J., Padmaperuma, A. B., Tan, E., Dutta, A., Jacobson, J., and Cafferty, K., 2013, *Process Design and Economics for the Conversion of Lignocellulosic Biomass to Hydrocarbon Fuels: Fast Pyrolysis and Hydrotreating Bio-Oil Pathway*, PNNL-23053; NREL/TP-5100-61178, Pacific Northwest National Lab. (PNNL), Richland, WA (United States).
[105] Cammenga, J., "State Corporate Income Tax Rates and Brackets," Tax Foundation.
[106] Lemmens, S., 2016, "Cost Engineering Techniques and Their Applicability for Cost Estimation of Organic Rankine Cycle Systems," Energies, 9(7), p. 485.

A. Sample Calculations

In this section, representative calculations are shown for the primary refrigeration system, the beef plant boiler model, the TCCS subcooling model, and the economic model. Starting with two ambient conditions, the high side pressure of the ammonia refrigeration system will be determined using the PRS model. In the following section, a sample calculation will be carried out to illustrate how waste heat availability is determined from plant natural gas use data. Then, sample calculations will be shown for the TCCS model which determine the performance of the TCCS providing subcooling to the PRS and feedwater heating to the boiler based on waste heat available, and the high side pressure of the PRS. Finally, heat exchanger sizing and capital cost equations will be presented which allow for the determination of the overall cost and payback period of the TCCS.

A.1 Beef Plant Refrigeration Sample Calculations

Starting with the beef plant refrigeration model, representative calculations will be shown to determine the performance of the PRS for two ambient weather conditions. The calculations shown are an attempt to illustrate the results from Engineering Equation Solver, which carries out the modeling process described in Section 3.2.1 to determine performance of the PRS, as well as high-side refrigeration pressure as a function of ambient conditions. The two ambient weather conditions are the average weather conditions in the summer (May – October) and winter (November – April) months for the city of Denver. Assumptions made for the PRS model, as well as average summer and winter ambient weather conditions, and high-side pressure guesses are shown in Table A.1. A process flow diagram of the PRS with condenser cooling towers is shown in Figure A.1. With the assumptions and listed in Table A.1, EES can solve for the thermodynamic state points of the PRS. Thermodynamic state points for PRS during the summer and winter

average conditions are shown in Table A.2 and Table A.3, respectively. In the first part of this section, representative calculations for the Beef plant PRS will be carried out, describing the thermodynamic performance of the PRS at the guessed high-side pressure value. In the second part of this section, representative calculations for the condenser cooling tower will be carried out, to verify that the PRS is able to operate during the summer and winter ambient condition.

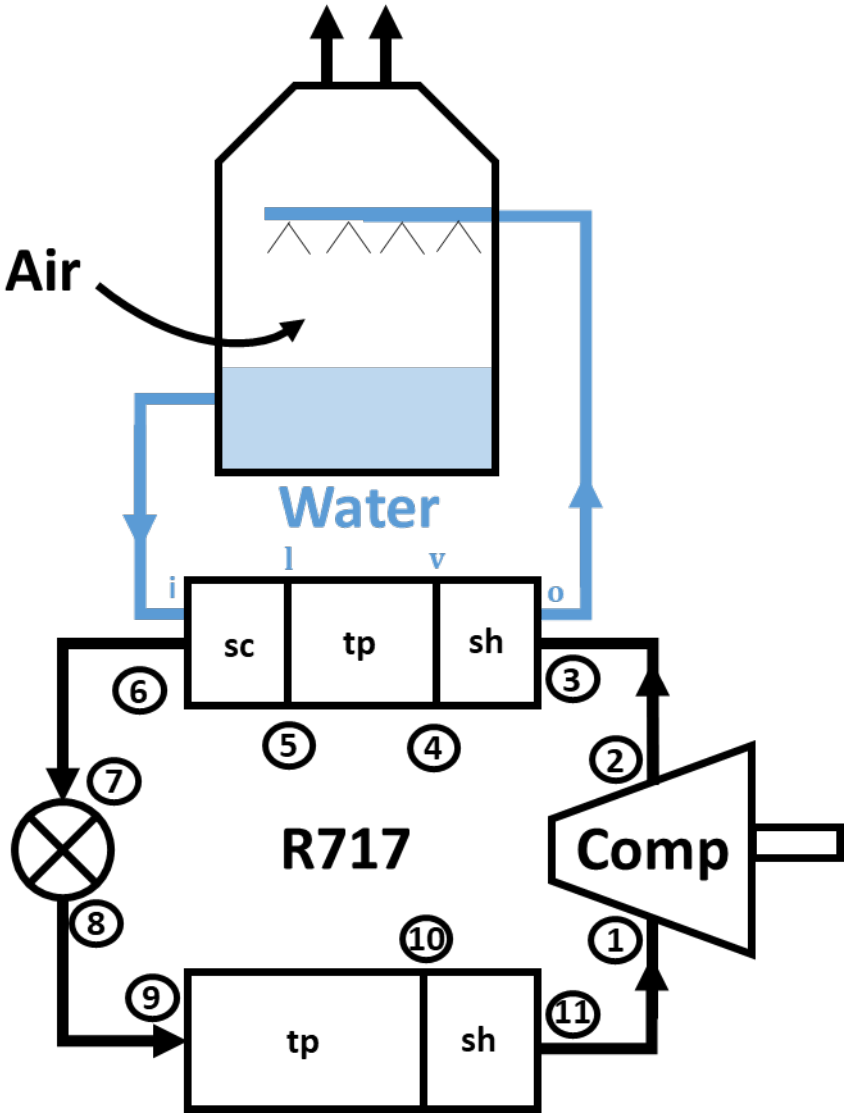

Figure A.1 Process flow diagram of the PRS with state points designated.

Table A.1 Average summer and winter TMY3 ambient weather conditions for Denver, CO.

Model		Assumption	Summer	Winter
working fluids		Refrigerant	Ammonia	Ammonia
		Condensing Fluid	Water	Water
		Cooling Tower Fluid	Air	Air
		Evaporator fluid	Water	Water
VC Cycle	Pressures	Low Side Pressure	322 kPa	322 kPa
		High Side Pressure (guess)	1367 kPa	1144 kPa
	Evaporator	$T_{\mathrm{w,in}}$	10.4°C	10.4°C
		$T_{\mathrm{w,out}}$	6.67°C	6.67°C
		$\varepsilon_{\mathrm{tp}}$	0.208	0.208
		$\varepsilon_{\mathrm{sh}}$	0	0
		$\dot{Q}_{\mathrm{cool}}$	9.3 MW	9.3 MW
	Compressor	η_{comp}	65%	65%
	Condenser	$\Delta \mathrm{T}_{\mathrm{cond,w}}$	5.55°C	5.55°C
		$\varepsilon_{\mathrm{tp}}$	0.31	0.31
		$\varepsilon_{\mathrm{sc}}$	0	0
Cooling Tower		$T_{a,\mathrm{in}}$	16.8°C	2.62°C
		RH	51.6%	56.10%
		P_{atm}	82.4 kPa	81.8 kPa
		$\varepsilon_{\mathrm{ct}}$	0.65	0.65
		Air Flow	650000 CFM	650000 CFM

Table A.2 PRS Thermodynamic State Points (summer ambient conditions).

Ammonia	Primary Refrigeration System				
	Temperature	Enthalpy	Pressure	Entropy	Quality
	°C	kJ kg^{-1}	kPa	kJ kg^{-1} K^{-1}	-
1	-7.47	1454	322	5.721	
2	141	1775	1367	6.009	
3	141	1775	1367	6.009	
4	35.4	1488	1367	5.204	1
5	35.4	368	1367	1.573	0
6	35.4	368	1367	1.572	
7	35.4	368	1367	1.572	
8	-7.47	368	322	1.635	0.1572
9	-7.47	368	322	1.635	0.1572
10	-7.47	1454	322	5.721	1
11	-7.47	1454	322	5.721	

Table A.3 PRS Thermodynamic State Points (winter ambient conditions).

Ammonia	Primary Refrigeration System				
	Temperature	Enthalpy	Pressure	Entropy	Quality
	°C	kJ kg^{-1}	kPa	kJ kg^{-1} K^{-1}	-
1	-7.47	1454	322	5.721	
2	120.5	1730	1144	5.98	
3	120.5	1730	1144	5.98	
4	29.3	1486	1144	5.27	1
5	29.3	338.3	1144	1.477	0
6	29.3	338.3	1144	1.477	
7	29.3	338.3	1144	1.477	
8	-7.47	338.3	322	1.523	0.1342
9	-7.47	338.3	322	1.523	0.1342
10	-7.47	1454	322	5.721	1
11	-7.47	1454	322	5.721	

A.1.1. Beef plant refrigeration Thermodynamic Calculations

With the state points shown in Table A.2 and A.3, the PRS thermodynamic performance can be evaluated. The PRS sample calculations at the summer operation condition (Table A.2) will be carried out first. Starting with the PRS compressor, the work input and isentropic efficiency is calculated as shown in Equation (A.1) and Equation (A.2).

$$\dot{W}_{\text{comp,summer}} = \dot{M}_{\text{r,summer}} * (h_2 - h_1) = 8.57 * (1775 - 1454) = 2751\ kW \quad \text{(A.1)}$$

$$\eta_{\text{comp,summer}} = \frac{h_{2,s} - h_1}{h_2 - h_1} = \frac{1663 - 1454}{1775 - 1454} = 0.651 \quad \text{(A.2)}$$

The ammonia refrigerant leaves the compressor as a high pressure superheated vapor and is then sent to the superheated region of the condenser. The heat duty of the superheated region of the PRS condenser is calculated as shown in Equation (A.3) through (A.5).

$$\dot{Q}_{\text{cond,sh,summer}} = \dot{M}_{\text{r,summer}} * (h_3 - h_4) = 8.57 * (1775 - 1488) = 2460\ kW \quad \text{(A.3)}$$

$$\dot{Q}_{\text{cond,sh,summer}} = \dot{M}_{\text{w,summer}} * C_{\text{p,w}} * (T_{\text{o}} - T_{\text{v}}) = 519 * 4.18 * (26.7 - 25.6) \quad \text{(A.4)}$$

$$= 2386\ kW$$

$$\dot{Q}_{\text{cond,sh,summer}} = \varepsilon_{sh} * C_{min} * (T_3 - T_v) = 0.73 * 29 * (141 - 25.6) \quad \text{(A.5)}$$

$$= 2443\ kW$$

Due to rounding errors, there are slight differences between the calculated heat duty values. These errors, however, do not occur in the EES simulation. Next, the refrigerant enters the two-phase region of the condenser. The heat duty of the two-phase region of the condenser is calculated as shown in Equation (A.6) through (A.8).

$$\dot{Q}_{\text{cond,tp,summer}} = \dot{M}_{\text{r,summer}} * (h_4 - h_5) = 8.57 * (1488 - 368) = 9598\ kW \quad \text{(A.6)}$$

$$\dot{Q}_{\text{cond,tp,summer}} = \dot{M}_{w,\text{summer}} * C_{\text{p,w}}(T_v - T_l) = 519 * 4.18 * (25.6 - 21.1) \quad \text{(A.7)}$$

$$= 9762\ kW$$

$$\dot{Q}_{\text{cond,tp,summer}} = \varepsilon_{\text{tp}} * C_{min} * (T_4 - T_l) = 0.31 * 2172 * (35.4 - 21.1) \quad \text{(A.8)}$$

$$= 9628\ kW$$

Because the effectiveness of the subcooled region of the PRS condenser was selected to be zero, ammonia leaves the PRS condenser as a saturated liquid. Thus, the total condenser heat duty required of the PRS is calculated as shown in Equation (A.9).

$$\dot{Q}_{\text{cond,total,summer}} = \dot{Q}_{\text{cond,sh}} + \dot{Q}_{\text{cond,tp}} = 2430 + 9663 = 12093\ kW \quad \text{(A.9)}$$

Once the ammonia is condensed, it is isenthalpically throttled to the low-side pressure of the PRS and sent to the evaporator. The heat duty of the PRS evaporator is calculated as shown in Equation (A.10) through (A.11). Because the effectiveness of the superheated region of the evaporator was set to zero, the PRS refrigerant leaves the evaporator as a saturated vapor.

$$\dot{Q}_{\text{evap,tp,summer}} = \dot{M}_{\text{r,summer}} * (h_{10} - h_9) = 8.57 * (1454 - 368) = 9307\ kW \quad \text{(A.10)}$$

$$\dot{Q}_{\text{evap,tp,summer}} = \dot{M}_{\text{chill}} * C_{\text{p,tp}} * \left(t_{\text{chill,v}} - t_{\text{chill,o}}\right) = 595 * 4.2 * (10.4 - 6.67) \quad \text{(A.11)}$$

$$= 9321\ kW$$

$$\dot{Q}_{\text{evap,tp,summer}} = \varepsilon_{\text{subcool,tp}} * C_{\text{min}} * \left(t_{\text{chill,v}} - t_9\right) \quad \text{(A.12)}$$

$$= 0.208 * 2500 * (10.4 - (-7.47)) = 9292\ kW$$

Again, due to rounding errors, the calculated heat duty of the evaporator does not exactly equal the assumed 9.3 MW heat duty. However, these differences only occur in the representative calculations and not in the EES simulation. With heat duty and compressor work calculated, overall COP of the PRS can is calculated during the summer ambient condition as shown in Equation (A.13).

$$COP_{\text{prs,summer}} = \frac{\dot{Q}_{\text{cool}}}{\dot{W}_{\text{comp,summer}}} = \frac{9307}{2751} = 3.38 \quad \text{(A.13)}$$

This concludes the representative calculation for the PRS at the summer ambient condition. Next, a representative calculation will be shown for the PRS at the winter ambient condition. Starting with the compressor, work input and compressor efficiency are calculated as shown in Equation (A.14) and Equation (A.15).

$$\dot{W}_{\text{comp,winter}} = \dot{M}_{\text{r,winter}} * (h_2 - h_1) = 8.34 * (1730 - 1454) = 2302\ kW \quad \text{(A.14)}$$

$$\eta_{\text{comp,winter}} = \frac{h_{2,s} - h_1}{h_2 - h_1} = \frac{1633 - 1454}{1730 - 1454} = 0.649 \quad \text{(A.15)}$$

Heat duty of the superheated region of the PRS condenser is calculated as shown in Equation (A.16) through (A.18).

$$\dot{Q}_{\text{cond,sh,winter}} = \dot{M}_{\text{r,winter}} * (h_3 - h_4) = 8.34 * (1730 - 1486) = 2035\ kW \quad \text{(A.16)}$$

$$\dot{Q}_{\text{cond,sh,winter}} = \dot{M}_{\text{w,winter}} * C_{\text{p,w}} * (T_{\text{o}} - T_{\text{v}}) = 500 * 4.18 * (20.1 - 19.1) \quad \text{(A.17)}$$

$$= 2090\ kW$$

$$\dot{Q}_{\text{cond,sh,winter}} = \varepsilon_{sh} * C_{min} * (T_3 - T_v) = 0.744 * 27 * (121 - 19.1) \quad \text{(A.18)}$$

$$= 2047\ kW$$

Heat duty of the two-phase region of the PRS condenser is calculated as shown in Equation (A.19) through (A.21), and total PRS condenser heat duty is calculated in Equation (A.22).

$$\dot{Q}_{\text{cond,tp,winter}} = \dot{M}_{\text{r,winter}} * (h_4 - h_5) = 8.34 * (1486 - 338) = 9574\ kW \quad \text{(A.19)}$$

$$\dot{Q}_{\text{cond,tp,winter}} = \dot{M}_{w,\text{winter}} * C_{\text{p,w}}(T_v - T_l) = 500 * 4.19 * (19.1 - 14.6) \quad \text{(A.20)}$$

$$= 9428\ kW$$

$$\dot{Q}_{\text{cond,tp,winter}} = \varepsilon_{\text{tp}} * C_{min} * (T_4 - T_l) = 0.31 * 2091 * (29.3 - 14.6) \quad \text{(A.21)}$$

$$= 9529\ kW$$

$$\dot{Q}_{\text{cond,total,winter}} = \dot{Q}_{\text{cond,sh}} + \dot{Q}_{\text{cond,tp}} = 2057 + 9510 = 11567\ kW \quad \text{(A.22)}$$

The PRS refrigerant leaves the condenser and is throttled to the evaporator pressure. The total evaporator heat duty is calculated as shown in Equation (A.23) through Equation (A.25).

$$\dot{Q}_{\text{evap,tp,winter}} = \dot{M}_{\text{r,winter}} * (h_{10} - h_9) = 8.34 * (1454 - 338) = 9307\ kW \quad \text{(A.23)}$$

$$\dot{Q}_{\text{evap,tp,winter}} = \dot{M}_{\text{chill}} * C_{\text{p,tp}} * \left(t_{\text{chill,v}} - t_{\text{chill,o}}\right) = 595 * 4.2 * (10.4 - 6.67) \quad \text{(A.24)}$$

$$= 9321\ kW$$

$$\dot{Q}_{\text{evap,tp,winter}} = \varepsilon_{\text{subcool,tp}} * C_{\text{min}} * \left(t_{\text{chill,v}} - t_9\right) \quad \text{(A.25)}$$

$$= 0.208 * 2500 * (10.4 - (-7.47)) = 9292\ kW$$

Finally, the performance of the PRS during the winter ambient condition is illustrated by the COP, which is calculated in Equation (A.26).

$$COP_{\text{prs,winter}} = \frac{\dot{Q}_{\text{cool}}}{\dot{W}_{\text{comp,winter}}} = \frac{9307}{2302} = 4.04 \quad \text{(A.26)}$$

This concludes the representative PRS thermodynamic calculations for both the summer and winter ambient condition. Table A.4 shows the primary results from these hand calculations, compared to the results which from the EES simulation.

Table A.4 PRS thermodynamic sample calculation results compared to EES simulation results.

value	Summer		Winter		Units
	hand calc	EES Calc	Hand Calc	EES Calc	
$\dot{W}_{\text{comp}}$	2751	2753	2302	2303	kW
$\dot{Q}_{\text{cond,sh}}$	2430	2455	2057	2036	kW
$\dot{Q}_{\text{cond,tp}}$	9663	9597	9510	9567	kW
$\dot{Q}_{\text{cond,total}}$	12093	12052	11567	11603	kW
$\dot{Q}_{evap}$	9307	9300	9307	9300	kW
COP	3.38	3.38	4.04	4.04	-

A.1.2. Beef Plant Condenser Cooling Tower Thermodynamic Calculations

Now that the VCRC portion of the PRS has been evaluated at the guessed high-side pressure, the cooling tower portion of the model is used to evaluate if the guessed pressure is reasonable. A high-side pressure value is reasonable if the cooling tower can reject the necessary amount of heat from the VCRC condenser. In other words, if cooling tower heat rejection is equivalent to condenser heat rejection, then the high-side pressure guess is appropriate. Cooling tower heat rejection is based on several factors, including water temperature calculated by the VCRC portion of the model, TMY3 ambient conditions, as well as the assumptions listed in Table A.1.

To start the cooling tower analysis, EES uses the input TMY3 data to calculate the properties of air including humidity ratio, enthalpy, and density. Table A.5 shows the properties that are calculated initially for the cooling tower analysis for the summer and winter conditions.

Table A.5 Calculated air and water inlet properties for PRS cooling tower model.

Calculated Property	Summer	Winter
$\omega_{a,in}$	0.00753 $kg_w\,kg_a^{-1}$	0.00316 $kg_w\,kg_a^{-1}$
$h_{a,in}$	35.9 kJ kg^{-1}	10.6 kJ kg^{-1}
$\rho_{a,in}$	0.986 kg m^{-3}	1.03 kg m^{-3}

The summer cooling tower calculation will be shown first. To start, mass flow rate of air through the tower is calculated as the product of air density and volumetric flow rate as shown in Equations (A.27).

$$\dot{M}_{a,summer} = \rho_{a,in} * \dot{V}_a = 0.986 * (307) = 303 \frac{kg}{s} \quad \text{(A.27)}$$

Then, saturated enthalpy of air at the cooling tower inlet water temperature is calculated as shown in Equation (A.28).

$$h_{\text{a,sat,in,summer}} = enthalpy(air, t = 26.7, P = 82.4, RH = 1) = 97.2\frac{kj}{kg} \quad \text{(A.28)}$$

This property allows for the simulation to evaluate the maximum amount of cooling that can be provided by the tower if the air leaves the tower fully saturated and at the same temperature of warm water entering the tower. Maximum condenser cooling of the tower is calculated as shown in Equation (A.29).

$$\dot{Q}_{\text{ct,max,summer}} = \dot{M}_{\text{a}} * \left(h_{\text{a,sat,in}} - h_{\text{a,in}}\right) = 303 * (97.3 - 35.9) = 18574\ kW \quad \text{(A.29)}$$

To determine the actual amount of heat that can be rejected in the cooling tower, the maximum heat rejection is multiplied by the assumed cooling tower effectiveness as shown in Equation (A.30).

$$\dot{Q}_{\text{ct,summer}} = \varepsilon_{\text{ct}} * \dot{Q}_{\text{ct,max,summer}} = 0.65 * 18574\ kW = 12073\ kW \quad \text{(A.30)}$$

To validate the performance of the cooling tower, cooling tower outlet air properties including enthalpy, temperature and humidity ratio are calculated as shown in Equation (A.31) through (A.33).

$$h_{\text{a,out,summer}} = \frac{\dot{Q}_{\text{ct,summer}}}{\dot{M}_{\text{a}}} + h_{\text{a,in}} = \frac{12073}{303} + 35.9 = 75.8\frac{kJ}{kg} \quad \text{(A.31)}$$

$$T_{\text{a,out,summer}} = temperature(air, h = 75.8, P = 82.4, RH = 1) = 22.3^{\text{o}}C \quad \text{(A.32)}$$

$$\omega_{\text{a,out,summer}} = humrat(air, h = 75.8, P = 82.4, RH = 1) = 0.021\frac{kg_{\text{w}}}{kg_{\text{a}}} \quad \text{(A.33)}$$

With humidity ratio of the air at inlet and outlet determined, cooling tower water loss due to evaporation can be calculated as shown in Equation (A.34).

$$\dot{M}_{\text{w,loss,summer}} = \dot{M}_{\text{a}} * \left(\omega_{\text{a,out}} - \omega_{\text{a,in}}\right) = 303 * (0.021 - 0.00753) = 4.08\frac{kg}{s} \quad \text{(A.34)}$$

Finally, mass flow rate of water leaving the cooling tower is calculated as shown in Equation (A.35).

$$\dot{M}_{\mathrm{w,out,summer}} = \dot{M}_{\mathrm{w,in}} - \dot{M}_{\mathrm{w,loss}} = 519 - 4.08 = 515\,\frac{kg}{s} \tag{A.35}$$

Because the outlet temperature and relative humidity of air are of sensible degree, and the amount of water being evaporated into the air is around 1%, the cooling tower model is reasonable. This concludes the representative calculation for the PRS cooling tower at the summer ambient condition. Next, the same calculations will be shown for the winter ambient condition. Cooling tower air mass flow rate during the winter condition is calculated as shown in Equation (A.36).

$$\dot{M}_{\mathrm{a,winter}} = \rho_{\mathrm{a,in}} * \dot{V}_{\mathrm{a}} = 1.03 * (307) = \ 316\,\frac{kg}{s} \tag{A.36}$$

Saturated enthalpy of air at the cooling tower inlet water temperature is calculated as shown in Equation (A.37).

$$h_{\mathrm{a,sat,in,winter}} = enthalpy(air, t = 20.1, P = 81.8, RH = 1) = 67\,\frac{kj}{kg} \tag{A.37}$$

Maximum cooling by the tower is calculated as shown in Equation (A.38).

$$\dot{Q}_{\mathrm{ct,max,winter}} = \dot{M}_{\mathrm{a}} * \left(h_{\mathrm{a,sat,in}} - h_{\mathrm{a,in}}\right) = 316 * (67 - 10.6) = 17834\ kW \tag{A.38}$$

Actual cooling duty of the tower is then calculated as shown in Equation (A.39).

$$\dot{Q}_{\mathrm{ct,winter}} = \varepsilon_{\mathrm{ct}} * \dot{Q}_{\mathrm{ct,max,winter}} = 0.65 * \ 17834\ kW = 11592\ kW \tag{A.39}$$

Then enthalpy, temperature, and humidity ratio of the air at the cooling tower are calculated as shown in Equations (A.40) through (A.42).

$$h_{\mathrm{a,out,winter}} = \frac{\dot{Q}_{\mathrm{ct,winter}}}{\dot{M}_{\mathrm{a}}} + \ h_{\mathrm{a,in}} \ = \frac{11592}{316} + 10.6 = 47.3\,\frac{kJ}{kg} \tag{A.40}$$

$$T_{\mathrm{a,out,winter}} = temperature(air, h = 47.3, P = 81.8, RH = 1) = 14.6^{\mathrm{o}}C \tag{A.41}$$

$$\omega_{\mathrm{a,out,winter}} = humrat(air, h = 47.3, P = 81.8, RH = 1) = 0.0129\,\frac{kg_{\mathrm{w}}}{kg_{\mathrm{a}}} \tag{A.42}$$

Finally, water loss and mass flow of water leaving the cooling tower are calculated in Equation (A.43) and Equation (A.44).

$$\dot{M}_{\mathrm{w,loss,winter}} = \dot{M}_{\mathrm{a}} * \left(\omega_{\mathrm{a,out}} - \omega_{\mathrm{a,in}}\right) = 316 * (0.0129 - 0.00316) = 3.08 \frac{kg}{s} \quad \text{(A.43)}$$

$$\dot{M}_{\mathrm{w,out,winter}} = \dot{M}_{\mathrm{w,in}} - \dot{M}_{\mathrm{w,loss}} = 500 - 3.08 = 497 \frac{kg}{s} \quad \text{(A.44)}$$

This concludes the representative calculations for the PRS cooling tower operating at the average summer and winter ambient condition. The primary results from these calculations are shown alongside the results from the EES simulation in Table A.6. Several findings from these calculations validate the cooling tower and PRS. Firstly, looking at the amount of water lost to evaporation, the water loss is around 1%, which is reasonable for a standard performing cooling tower. Secondly, comparing heat rejection in the cooling tower ($\dot{Q}_{\mathrm{ct}}$) to heat rejection in the condenser ($\dot{Q}_{\mathrm{cond}}$), the two values only differ by several kilowatts. Considering the rounding errors associated with the sample calculations, as well as the errors associated with constant specific heat assumptions made in both the cooling tower and VCRC models, this difference is small enough to assume that the PRS model has converged on appropriate high-side pressures for both the summer and winter condition. Using this technique, high-side pressure, and condenser water temperature for the PRS was evaluated for every hour of the year.

Table A.6 Cooling tower sample calculation results compared to EES simulation results.

value	Summer		Winter		Units
	hand calc	EES Calc	Hand Calc	EES Calc	
m_dot_air	303	303	316	316	kg/s
Q_ct_max	18574	18546	17834	17858	kW
Q_ct	12073	12055	11592	11608	kW
m_w_loss	4.08	4.07	3.08	3.08	kg/s
m_w_out	515	515	497	497	kg/s

The high-side pressure value determined with the PRS and Cooling tower models serve as direct inputs for the TCCS subcooling model. The high-side pressure of the ammonia stream, which fluctuates based on ambient conditions, impacts the amount of subcooling that can be provided to the PRS by the TCCS. The high side pressure of the ammonia stream during both the summer and winter ambient condition are shown in Table A.7. Waste heat, which is also an input for the TCCS model, is calculated in the next section of the appendix.

Table A.7 Results from the PRS model that are used as direct inputs for the TCCS subcooling model

TCCS Model Input	Summer	Winter
High Side Pressure	1367 kPa	1144 kPa

A.2 Beef Plant Boiler Model Sample Calculations

The beef plant boiler model is used to determine exhaust waste heat available from a beef plant's primary water boilers. Waste heat is transferred from the boiler exhaust gas to the TCCS via waste heat recovery loop that uses a propylene glycol – water mixture as the working fluid. As the exhaust leaves the boiler stack, it heats the PG-water mixture, which is then pumped to the waste heat boiler of the TCCS where it vaporizes the refrigerant, which is chosen to be R134A. A schematic diagram of the waste heat recovery system is shown in Figure A.2. The assumptions made for the sample waste heat calculation are shown in Table A.8, using an hourly natural gas flow rate that corresponds to the yearly average waste heat value of 685 kW.

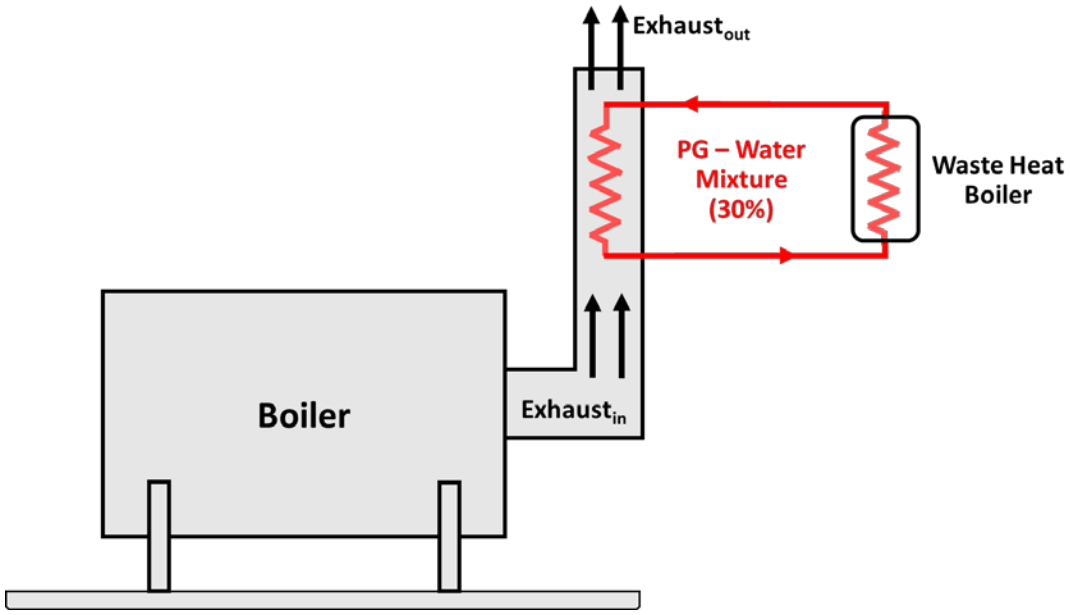

Figure A.2 Schematic diagram of the boiler exhaust waste heat recovery system.

Table A.8 Assumptions made for boiler waste heat sample calculation.

Boiler Assumptions	Value
η_{boiler}	80%
HHV of Natural Gas	40.6 MJ/m^3 [89]
$\%_{\text{excess air}}$	15%
$moles_{\text{air}}$	9.53
$\rho_{\text{air,stp}}$	1.189 kg/m^3
$C_{\text{p,exhaust}}$	1.93[90]
$T_{\text{exhaust,in}}$	400°F (204 °C) [91]
$T_{\text{exhaust,out}}$	250°F (121 °C) [91]
$C_{\text{p,pg}}$	4.04 kJ/kg-K
$T_{\text{pg,in}}$	87°C
$T_{\text{pg,out}}$	97°C
$T_{\text{feedwater,in}}$	15.56°C (60°F)
Average Boiler NG consumption	37.95 MCF/hr (0.3 m^3/s)

A.2.1. Boiler Thermodynamic Calculations

To start, total thermal output of the boiler is calculated based on the volumetric flow rate of natural gas, the higher heating value of natural gas, and the assumed boiler efficiency using Equation (A.45)

$$\dot{Q}_{\text{boiler}} = \dot{V}_{\text{fuel}} * HHV_{\text{fuel}} * \eta_{\text{boiler}} = 0.299 * 40.6 * 0.8 = 9.71\ MW \tag{A.45}$$

To determine waste heat available, first, volumetric flow rate of exhaust air is calculated based on the chemical reaction of air and natural gas combusting in the boiler. The chemical reaction of combustion is shown in Equation (A.46).

$$H_4\ + 2O_2\ + 7.53N_2 \rightarrow CO2 + 2H_2O + 7.53N_2 + Heat\ (40.6\frac{MJ}{m^3}) \tag{A.46}$$

Assuming 15% excess air beyond a stoichiometric mixture, volumetric flow rate of air entering the boiler is calculated as shown in Equation (A.47).

$$\dot{V}_{\text{air}} = \dot{V}_{\text{ng}} * (1 + \%_{\text{excess air}}) * (moles_{\text{air}}) = 0.299 * (1 + 0.15) * (9.53) \tag{A.47}$$

$$= 3.28\frac{m^3}{s}$$

Mass flow rate of air entering the boiler is then calculated as the product of volumetric flow rate of air and the density of air at STP conditions (100 kPa, 20°C), as shown in Equation (A.48). Mass flow rate of the exhaust air is then evaluated as the product of the mass flow rate of air and natural gas entering the boiler as shown in Equation (A.49).

$$\dot{M}_{\text{air,in}} = \dot{V}_{\text{air}} * \rho_{\text{air,stp}} = 3.28 * 1.189 = 3.9\frac{kg}{s} \tag{A.48}$$

$$\dot{M}_{\text{exh}} = \dot{M}_{\text{air,in}} + \frac{\dot{M}_{\text{air,in}}}{(1 + \%_{\text{excess air}}) * (moles_{\text{air}})} = 3.9 + \frac{3.9}{(1 + 0.15) * 9.53} \tag{A.49}$$

$$= 4.26\frac{kg}{s}$$

Once mass flow rate of exhaust has been determined, heat Transfer from the exhaust to the PG-water mixture is evaluated using Equation (A.50) through (A.52).

$$\dot{Q}_{\text{recoverable}} = \dot{M}_{\text{exh}} * C_{\text{p,exh}} * \left(t_{\text{exh,in}} - t_{\text{exh,out}}\right) = 4.26 * 1.93 * (204 - 121) \quad \text{(A.50)}$$

$$= 682\ kW$$

$$\dot{Q}_{\text{recoverable}} = \dot{M}_{pg} * C_{\text{p,pg}} * \left(T_{\text{pg,out}} - T_{\text{pg,in}}\right) = 16.9 * 4.04 * (97 - 87) \quad \text{(A.51)}$$

$$= 683\ kW$$

$$\dot{Q}_{\text{recoverable}} = \varepsilon_{\text{br}} * C_{\text{min}} * \left(T_{\text{exh,in}} - T_{\text{pg,in}}\right) = 0.71 * 8.21 * (204 - 87) \quad \text{(A.52)}$$

$$= 682\ kW$$

Again, the minor differences in values solved for with Equation (A.50) through (A.52) are the result of rounding errors. After determining waste heat recovered, it is assumed that there negligible pressure and enthalpy drop in the PG-water mixture loop, and that the waste heat transferred from the exhaust air to the PG-water mixture is equivalent to the heat transferred from the PG-water mixture to the refrigerant circulating through the power cycle of the TCCS. Once the average waste heat was determined to be 685 kW, the actual was heat input assumed for the FWE, TCCS, and ORC, was reduced by 54 kW (resulting in a waste heat input of 631 kW) to account for the reduction in natural gas use when the boiler water is economized by each system.

In addition to calculating waste heat available, the boiler model is also used to determine boiler feedwater water mass flow rate. Determining boiler water mass flow rate is critical, as this value is used to set the flow rate of water that is used for condenser cooling in the TCCS, DMS, and ORC systems. Boiler water flow rate is calculated based on known percentages of thermal energy being used to heat water to various temperatures, as tabulated in Table 3.2. At a plant, feedwater is sent to the boiler, and heated from the inlet temperature of 60°F to one of five temperatures: 90° F, 110° F, 140° F, 180° F, or 212° F. Using this information, the known

percentages in Table 3.2, and the total boiler thermal output of the boiler, mass flow of each stream is calculated. The sum of all four streams is taken to estimate total feedwater flow rate. The calculation of boiler water flow rates is shown in Equation (A.53) through (A.68). Table A.9 compares the values found in the representative calculations to the values determined from the EES boiler simulation.

$$\dot{Q}_{\text{boiler}} = \frac{\dot{M}_{\text{w,90}} * \left(h_{\text{w,90}} - h_{\text{w,60}}\right)}{\%_{90}} = \frac{10 * (135 - 65.4)}{.072} = 9.67\ MW \quad \text{(A.53)}$$

$$\dot{Q}_{\text{boiler}} = \frac{\dot{M}_{\text{w,110}} * \left(h_{\text{w,110}} - h_{\text{w,60}}\right)}{\%_{110}} = \frac{2.76 * (182 - 65.4)}{.033} = 9.75\ MW \quad \text{(A.54)}$$

$$\dot{Q}_{\text{boiler}} = \frac{\dot{M}_{\text{w,140}} * \left(h_{\text{w,140}} - h_{\text{w,60}}\right)}{\%_{140}} = \frac{30.7 * (251 - 65.4)}{.589} = 9.67\ MW \quad \text{(A.55)}$$

$$\dot{Q}_{\text{boiler}} = \frac{\dot{M}_{\text{w,180}} * \left(h_{\text{w,180}} - h_{\text{w,60}}\right)}{\%_{180}} = \frac{8.72 * (344 - 65.4)}{.251} = 9.68\ MW \quad \text{(A.56)}$$

$$\dot{Q}_{\text{boiler}} = \frac{\dot{M}_{\text{w,212}} * \left(h_{\text{w,212}} - h_{\text{w,60}}\right)}{\%_{212}} = \frac{0.2 * (2676 - 65.4)}{.054} = 9.67\ MW \quad \text{(A.57)}$$

$$\dot{M}_{w,total} = \dot{M}_{w,90} + \dot{M}_{w,110} + \dot{M}_{w,140} + \dot{M}_{w,180}\ \dot{M}_{w,212} \quad \text{(A.58)}$$

$$= 10 + 2.76 + 30.7 + 8.72 + 0.2 = 52.4\,\frac{kg}{s}$$

Table A.9 Comparison of Boiler results between the representative calculation and the EES simulation.

Value	hand Calc	EES value	Unit
Q_boiler	9.69	9.7	MW
V_air	3.28	3.27	m^3/s
M_air_in	3.90	3.89	kg/s
M_exh	4.26	4.24	kg/s
Q_recover	682	683	kW
m_dot_w	52.4	52.4	kg/s

A.3 Representative Calculations for TCCS Subcooling

Using the inputs determined in the previous appendices, a representative calculation will be carried out to demonstrate how the TCCS provides subcooling and feedwater heating at a beef processing facility for a given high-side PRS pressure, waste heat input, and condenser water flow rate. Figure A.3 shows the TCCS with the state points and external flows labeled while Table A.10 lists the model inputs that are determined by both the beef plant boiler and PRS models. The assumptions made for the TCCS model are listed in Table 3.8 of the modeling section. Table A.11 and Table A.12 show the TCCS thermodynamic state points solved for with EES using the winter and summer input conditions. Results will be verified by showing hand calculations for the summer input condition, then results from both the winter and summer models will be presented.

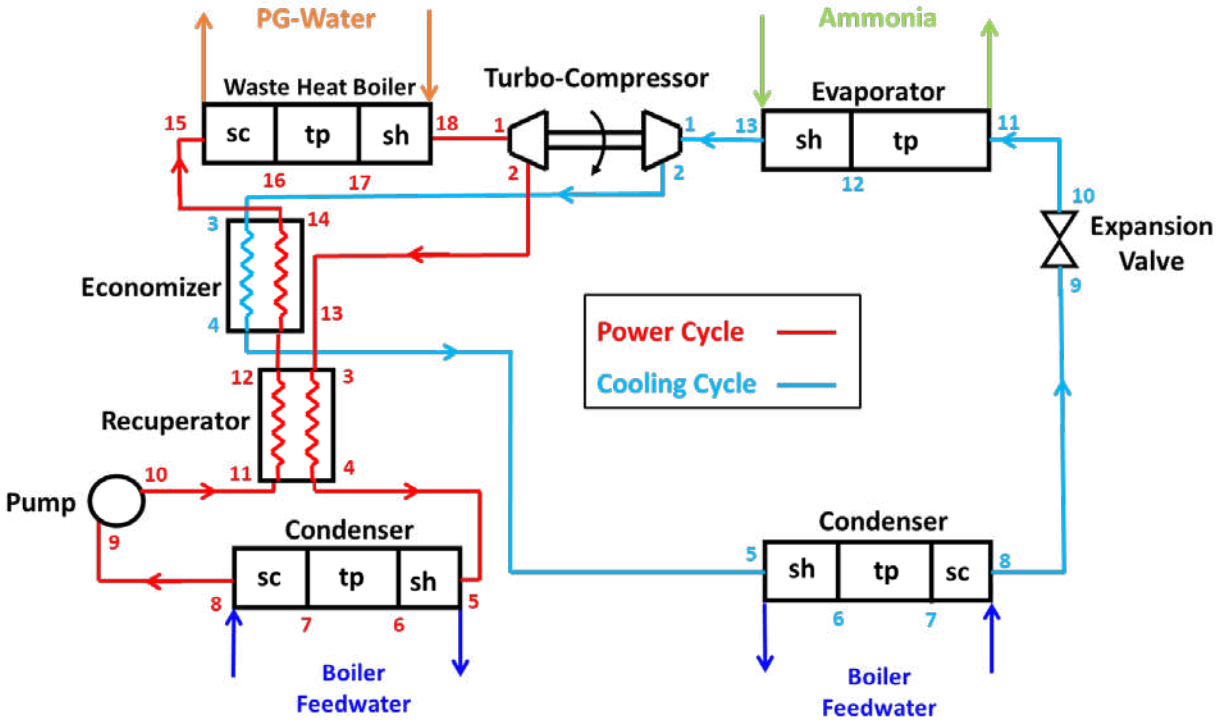

Figure A.3 Process flow diagram of the turbo-compression cooling system with state points and external flows designated.

Table A.10 TCCS Model Inputs as determined by the PRS and boiler models.

TCCS Model Input	Summer	Winter
High Side Pressure	1367 kPa	1144 kPa
$\dot{Q}_{\text{recoverable}}$	631 kW	631 kW
$\dot{M}_{w,cond,cc}$	30.7 kg/s	
$\dot{M}_{w,cond,pc}$	21.7 kg/s	
$T_{w,cond,in}$	15.56° C (60° F)	

Table A.11 TCCS thermodynamic state points for summer input condition.

Summer								
R134a	**Power Cycle**				**Cooling Cycle**			
	T	**H**	**P**	**S**	**T**	**H**	**P**	**S**
	^{o}C	**kJ kg^{-1}**	**kPa**	**kJ kg^{-1} K^{-1}**	**^{o}C**	**kJ kg^{-1}**	**kPa**	**kJ kg^{-1} K^{-1}**
1	94.6	305	2620	0.957	26.5	273	349	0.997
2	41.8	281	664	0.976	51.3	291	650	1.01
3	41.8	281	664	0.976	51.3	291	650	1.01
4	30.6	270	664	0.94	38.8	278	650	0.969
5	30.6	270	664	0.94	38.8	278	650	0.969
6	24.9	264	664	0.921	24.2	264	650	0.921
7	24.9	86.2	664	0.324	24.2	85.2	650	0.32
8	24	84.9	664	0.319	23.3	84	650	0.316
9	24	84.9	664	0.319	23.3	84	650	0.316
10	25.6	87.4	2620	0.322	4.95	84	349	0.32
11	25.6	87.4	2620	0.322	4.95	84	349	0.32
12	33.5	98.6	2620	0.359	4.95	253	349	0.929
13	33.5	98.6	2620	0.359	26.5	273	349	0.997
14	44.5	115	2620	0.411				
15	44.5	115	2620	0.411				
16	79.7	174	2620	0.586				
17	79.7	281	2620	0.89				
18	94.6	305	2620	0.957				

Table A.12 TCCS thermodynamic state points for winter input condition.

Winter								
R134a	Power Cycle				Cooling Cycle			
	T	H	P	S	T	H	P	S
	°C	kJ kg^{-1}	kPa	kJ kg^{-1} K^{-1}	°C	kJ kg^{-1}	kPa	kJ kg^{-1} K^{-1}
1	94.7	305	2640	0.956	21.2	269	314	0.991
2	41.2	281	660	0.975	49	289	632	1
3	41.2	281	660	0.975	49	289	632	1
4	30.3	270	660	0.94	37.9	278	632	0.969
5	30.3	270	660	0.94	37.9	278	632	0.969
6	24.7	264	660	0.921	23.3	263	632	0.921
7	24.7	86	660	0.323	23.3	83.9	632	0.316
8	23.8	84.7	660	0.319	22.5	82.8	632	0.312
9	23.8	84.7	660	0.319	22.5	82.8	632	0.312
10	25.5	87.2	2640	0.322	1.94	82.8	314	0.317
11	25.5	87.2	2640	0.322	1.94	82.8	314	0.317
12	33.2	98.1	2640	0.358	1.94	252	314	0.93
13	33.2	98.1	2640	0.358	21.2	269	314	0.991
14	42	111	2640	0.399				
15	42	111	2640	0.399				
16	80.1	174	2640	0.589				
17	80.1	281	2640	0.889				
18	94.7	305	2640	0.956				

Starting with the turbine, state points 1-2, work generated is evaluated as the product of mass flow rate and change in enthalpy through the turbine, and the isentropic efficiency relation as shown in Equation (A.59) and Equation (A.60).

$$\dot{W}_{\text{turb}} = \dot{M}_{\text{pc}} * (h_1 - h_2) = 3.32 * (305 - 281) = 79.7\ kW \tag{A.59}$$

$$\eta_{\text{turb}} = \frac{h_2 - h_1}{h_{2,\text{s}} - h_1} = \frac{281 - 305}{275 - 305} = 0.8 \tag{A.60}$$

After the power cycle refrigerant is expanded through the turbine, it enters the recuperator where it transfers heat to the refrigerant at the power cycle pump outlet as shown in Equation (A.61) through (A.63).

$$\dot{Q}_{\text{pc,recup}} = \dot{M}_{\text{pc}} * \left(h_{\text{pc},3} - h_{\text{pc},4}\right) = 3.32 * (281 - 270) = 36.5\ kW \tag{A.61}$$

$$\dot{Q}_{\text{pc,recup}} = \dot{M}_{\text{pc}} * \left(h_{\text{pc},12} - h_{\text{pc},11}\right) = 3.32 * (98.6 - 87.4) = 37.1\ kW \tag{A.62}$$

$$\dot{Q}_{\text{pc,recup}} = \varepsilon_{\text{r}} * C_{\min} * \left(T_{\text{pc},3} - T_{\text{pc},11}\right) = 0.7 * 3.28 * (41.8 - 25.6) \tag{A.63}$$

$$= 37.2\ kW$$

The minor differences in results are once again due to rounding errors. After the power cycle refrigerant has been recuperated, it enters the condenser (state points 5 through 8), being condensed from a superheated vapor to a subcooled liquid. The heat duty of the superheated region of the power cycle condenser is calculated as shown in Equation (A.64) through (A.66).

$$\dot{Q}_{\text{pc,cond,sh}} = \dot{M}_{\text{pc}} * \left(h_{\text{pc,5}} - h_{\text{pc,6}}\right) = 3.32 * (270 - 264) = 19.9\ kW \quad \text{(A.64)}$$

$$\dot{Q}_{\text{pc,cond,sh}} = \dot{M}_{\text{pc,cond}} * C_{\text{p,pc,cond,1}} * \left(t_{\text{pc,cond,o}} - t_{\text{pc,cond,v}}\right) \quad \text{(A.65)}$$

$$= 21.7 * 4.18 * (22.3 - 22.1) = 18.1\ kW$$

$$\dot{Q}_{\text{pc,cond,sh}} = \varepsilon_{\text{pc,cond,sh}} * C_{\min} * \left(t_{\text{pc,5}} - t_{\text{pc,cond,v}}\right) \quad \text{(A.66)}$$

$$= 0.664 * 3.42 * (30.6 - 22.1) = 19.3\ kW$$

The heat duty of the two-phase region of the power cycle condenser is calculated as shown in Equation (A.67) through (A.69).

$$\dot{Q}_{\text{pc,cond,tp}} = \dot{M}_{\text{pc}} * \left(h_{\text{pc,6}} - h_{\text{pc,7}}\right) = 3.32 * (264 - 86.2) = 590\ kW \quad \text{(A.67)}$$

$$\dot{Q}_{\text{pc,cond,tp}} = \dot{M}_{\text{pc,cond}} * C_{\text{p,pc,cond,2}} * \left(t_{\text{pc,cond,v}} - t_{\text{pc,cond,l}}\right) \quad \text{(A.68)}$$

$$= 21.7 * 4.19 * (22.1 - 15.6) = 591\ kW$$

$$\dot{Q}_{\text{pc,cond,tp}} = \varepsilon_{\text{pc,cond,tp}} * C_{\min} * \left(t_{\text{pc,6}} - t_{\text{pc,cond,l}}\right) = 0.7 * 90.8 * (24.9 - 15.6) \quad \text{(A.69)}$$

$$= 591\ kW$$

The heat duty of the subcooled region of the power cycle condenser is calculated as shown in Equation (A.70) through (A.72).

$$\dot{Q}_{\text{pc,cond,sc}} = \dot{M}_{\text{pc}} * \left(h_{\text{pc,7}} - h_{\text{pc,8}}\right) = 3.32 * (86.2 - 84.9) = 4.32\ kW \quad \text{(A.70)}$$

$$\dot{Q}_{\text{pc,cond,sc}} = \dot{M}_{\text{pc,cond}} * C_{\text{p,pc,cond,3}} * \left(t_{\text{pc,cond,l}} - t_{\text{pc,cond,i}}\right) \quad \text{(A.71)}$$

$$= 21.7 * 4.19 * (15.6 - 15.56) = 3.64\ kW$$

$$\dot{Q}_{\text{pc,cond,sc}} = \varepsilon_{\text{pc,cond,sc}} * C_{\min} * \left(t_{\text{pc,7}} - t_{\text{pc,cond,i}}\right) \quad \text{(A.72)}$$

$$= 0.1 * 4.72 * (24.9 - 15.56) = 4.41\ kW$$

After the power cycle refrigerant has been condensed to a subcooled liquid, the refrigerant is pressurized to the high-side pressure of the power cycle with the pump. The work input of the pump is calculated as the product of the power cycle mass flow rate and the change in enthalpy,

shown in Equation (A.73), where enthalpies are determined using the pump isentropic efficiency calculation shown in Equation (A.74).

$$\dot{W}_{\text{pump}} = \dot{M}_{\text{pc}} * (h_{10} - h_9) = 3.32 * (87.4 - 84.9) = 8.3\ kW \tag{A.73}$$

$$\eta_{\text{pump}} = \frac{h_{10,s} - h_9}{h_{10} - h_9} = \frac{86.5 - 84.9}{87.4 - 84.9} = 0.64 \tag{A.74}$$

After the refrigerant is pressurized with the pump, it receives heat from the recuperative heat exchanger. The refrigerant then enters the economizer, where it receives heat from the cooling cycle refrigerant at the compressor outlet as shown in Equation (A.75).

$$\dot{Q}_{\text{econ}} = \dot{M}_{\text{pc}} * \left(h_{\text{pc},14} - h_{\text{pc},13}\right) = 3.32 * (115 - 98.6) = 54.4\ kW \tag{A.75}$$

Finally, the power cycle refrigerant is vaporized in the waste heat boiler (state points 15 through 18), receiving heat from the PG-Water waste heat recovery loop. The total boiler heat duty, which is the sum of heat added to the refrigerant in the three regions of the boiler, is set by the waste heat availability as calculated in the previous section. The heat duty of the subcooled region of the power cycle boiler is calculated as shown in Equation (A.76) through (A.78).

$$\dot{Q}_{\text{pc,boil,sc}} = \dot{M}_{\text{pc}} * \left(h_{\text{pc},16} - h_{\text{pc},15}\right) = 3.32 * (174 - 115) = 196\ kW \tag{A.76}$$

$$\dot{Q}_{\text{pc,boil,sc}} = \dot{M}_{\text{pg}} * C_{\text{p,pg,1}} * \left(t_{\text{pg,l}} - t_{\text{pg,o}}\right) = 15.6 * 4.03 * (90.1 - 87) \tag{A.77}$$

$$= 195\ kW$$

$$\dot{Q}_{\text{pc,boil,sc}} = \varepsilon_{\text{pc,boil,sc}} * C_{\min} * \left(t_{\text{pg,l}} - t_{\text{pc},15}\right) = 0.865 * 4.96 * (90.1 - 44.5) \tag{A.78}$$

$$= 196\ kW$$

The heat duty of the two-phase region of the power cycle boiler is calculated as shown in Equation (A.79) through (A.80).

$$\dot{Q}_{\mathrm{pc,boil,tp}} = \dot{M}_{\mathrm{pc}} * \left(h_{\mathrm{pc},17} - h_{\mathrm{pc},16}\right) = 3.32 * (281 - 174) = 355\ kW \quad \text{(A.79)}$$

$$\dot{Q}_{\mathrm{pc,boil,tp}} = \dot{M}_{\mathrm{pg}} * C_{\mathrm{p,pg},2} * \left(t_{\mathrm{pg,v}} - t_{\mathrm{pc,cond,l}}\right) = 15.6 * 4.04 * (95.7 - 90.1) \quad \text{(A.80)}$$

$$= 353\ kW$$

$$\dot{Q}_{\mathrm{pc,boil,tp}} = \varepsilon_{\mathrm{pc,boil,tp}} * C_{\min} * \left(t_{\mathrm{pg,v}} - t_{\mathrm{pc},16}\right) = 0.35 * 63.1 * (95.7 - 79.7) \quad \text{(A.81)}$$

$$= 353\ kW$$

Finally, the heat duty of the superheated region of the power cycle boiler is calculated as shown in Equation (A.82) through (A.84).

$$\dot{Q}_{\mathrm{pc,boil,sh}} = \dot{M}_{\mathrm{pc}} * \left(h_{\mathrm{pc},18} - h_{\mathrm{pc},17}\right) = 3.32 * (305 - 281) = 79.7\ kW \quad \text{(A.82)}$$

$$\dot{Q}_{\mathrm{pc,boil,sh}} = \dot{M}_{\mathrm{pg}} * C_{\mathrm{p,pg},3} * \left(t_{\mathrm{pg,i}} - t_{\mathrm{pg,v}}\right) = 15.6 * 4.05 * (97 - 95.7) \quad \text{(A.83)}$$

$$= 82.1\ kW$$

$$\dot{Q}_{\mathrm{pc,boil,sh}} = \varepsilon_{\mathrm{pc,boil,sh}} * C_{\min} * \left(t_{\mathrm{pg,l}} - t_{\mathrm{pc},17}\right) = 0.7 * 6.63 * (97 - 79.7) \quad \text{(A.84)}$$

$$= 80.3\ kW$$

The cooling cycle of the TCCS is powered by the compressor of the turbo-compressor. Beginning with the compressor, compressor work input is set using three equations. The first equation sets compressor work equivalent to the product of turbine work and the mechanical shaft efficiency as shown in Equation (A.85). The second equation sets compressor work equivalent to the cooling cycle mass flow and the change in enthalpy through the compressor as shown in Equation (A.86). The third equation evaluates the enthalpy at the cooling cycle compressor inlet and outlet based on the compressor isentropic efficiency as shown in Equation (A.87).

$$\dot{W}_{\text{comp}} = \dot{W}_{\text{turb}} * \eta_{mech} = 79.7 * 0.98 = 78.1\ kW \tag{A.85}$$

$$\dot{W}_{\text{comp}} = \dot{M}_{\text{cc}} * (h_2 - h_1) = 4.33 * (291 - 273) = 77.9\ kW \tag{A.86}$$

$$\eta_{\text{comp}} = \frac{h_{2,\text{s}} - h_1}{h_2 - h_1} = \frac{287 - 273}{291 - 273} = 0.778 \tag{A.87}$$

The high-pressure cooling cycle refrigerant is then sent to the cross-cycle economizer, where it rejects heat to the power cycle refrigerant prior to the waste heat boiler. Economizer heat duty is calculated with Equation (A.75), (A.88), and (A.99).

$$\dot{Q}_{\text{econ}} = \dot{M}_{\text{cc}} * \left(h_{\text{cc},2} - h_{\text{cc},3}\right) = 4.33 * (291 - 278) = 56.3\ kW \tag{A.88}$$

$$\dot{Q}_{\text{econ}} = \varepsilon_{\text{econ}} * C_{\min} * \left(t_{\text{cc},3} - t_{\text{cc},13}\right) = 0.7 * 4.27 * (51.3 - 33.5) \tag{A.89}$$

$$= 53.2\ kW$$

After the economizer, the high-pressure cooling cycle refrigerant is sent to the condenser. The heat duty of the superheated region of the condenser is calculated as shown in Equation (A.90) through (A.92).

$$\dot{Q}_{\text{cc,cond,sh}} = \dot{M}_{\text{cc}} * \left(h_{\text{cc},5} - h_{\text{cc},6}\right) = 4.33 * (278 - 264) = 60.6\ kW \tag{A.90}$$

$$\dot{Q}_{\text{cc,cond,sh}} = \dot{M}_{\text{cc,cond}} * C_{\text{p,cc,cond},1} * \left(t_{\text{cc,cond,o}} - t_{\text{cc,cond,v}}\right) \tag{A.91}$$

$$= 30.7 * 4.18 * (22.1 - 21.6) = 64.2\ kW$$

$$\dot{Q}_{\text{cc,cond,sh}} = \varepsilon_{\text{cc,cond,sh}} * C_{\min} * \left(t_{\text{cc},5} - t_{\text{cc,cond,v}}\right) \tag{A.92}$$

$$= 0.83 * 4.45 * (38.8 - 21.6) = 63.5\ kW$$

The heat duty of the two-phase region of the cooling cycle condenser is calculated as shown in Equations (A.93) through (A.95).

$$\dot{Q}_{\mathrm{cc,cond,tp}} = \dot{M}_{\mathrm{cc}} * \left(h_{\mathrm{cc},6} - h_{\mathrm{cc},7}\right) = 4.33 * (264 - 85.2) = 774\ kW \quad \text{(A.93)}$$

$$\dot{Q}_{\mathrm{cc,cond,tp}} = \dot{M}_{\mathrm{cc,cond}} * C_{\mathrm{p,cc,cond},2} * \left(t_{\mathrm{cc,cond,v}} - t_{\mathrm{cc,cond,l}}\right) \quad \text{(A.94)}$$

$$= 30.7 * 4.19 * (21.6 - 15.6) = 772\ kW$$

$$\dot{Q}_{\mathrm{cc,cond,tp}} = \varepsilon_{\mathrm{cc,cond,tp}} * C_{\min} * \left(t_{\mathrm{cc},6} - t_{\mathrm{cc,cond,l}}\right) = 0.7 * 129 * (24.2 - 15.6) \quad \text{(A.95)}$$

$$= 777\ kW$$

The heat duty of the subcooled region of the power cycle condenser is calculated as shown in Equation (A.96) through (A.98).

$$\dot{Q}_{\mathrm{cc,cond,sc}} = \dot{M}_{\mathrm{cc}} * \left(h_{\mathrm{cc},7} - h_{\mathrm{cc},8}\right) = 4.33 * (85.2 - 84) = 5.2\ kW \quad \text{(A.96)}$$

$$\dot{Q}_{\mathrm{cc,cond,sc}} = \dot{M}_{\mathrm{cc,cond}} * C_{\mathrm{p,cc,cond},3} * \left(t_{\mathrm{cc,cond,l}} - t_{\mathrm{cc,cond,i}}\right) \quad \text{(A.97)}$$

$$= 30.7 * 4.19 * (15.6 - 15.56) = 5.15\ kW$$

$$\dot{Q}_{\mathrm{cc,cond,sc}} = \varepsilon_{\mathrm{cc,cond,sc}} * C_{\min} * \left(t_{\mathrm{cc},7} - t_{\mathrm{cc,cond,i}}\right) = 0.1 * 6.15 * (24.2 - 15.56) \quad \text{(A.98)}$$

$$= 5.31\ kW$$

The subcooled refrigerant is then expanded through the isenthalpic expansion valve (State points 8 to 9) and enters the evaporator (PRS ammonia subcooler) as a two-phase mixture. The cooling duty of the two-phase region in the evaporator is calculated as shown in Equation (A.99) through (A.101).

$$\dot{Q}_{\text{cc,subcool,tp}} = \dot{M}_{\text{cc}} * \left(h_{\text{cc,12}} - h_{\text{cc,11}}\right) = 4.33 * (253 - 84) = 732\ kW \quad \text{(A.99)}$$

$$\dot{Q}_{\text{cc,subcool,tp}} = \dot{M}_{\text{prs}} * C_{\text{p,prs,1}} * \left(t_{\text{prs,v}} - t_{\text{prs,o}}\right) = 7.81 * 4.77 * (33.1 - 13.4) \quad \text{(A.100)}$$

$$= 734\ kW$$

$$\dot{Q}_{\text{cc,subcool,tp}} = \varepsilon_{\text{cc,subcool,tp}} * C_{\min} * \left(t_{\text{prs,v}} - t_{\text{cc,11}}\right) \quad \text{(A.101)}$$

$$= 0.7 * 37.2 * (33.1 - 4.95) = 733\ kW$$

The cooling duty of the superheated region of the evaporator is calculated as shown in Equation (A.102) through (A.104).

$$\dot{Q}_{\text{cc,subcool,sh}} = \dot{M}_{\text{cc}} * \left(h_{\text{cc,13}} - h_{\text{cc,12}}\right) = 4.33 * (273 - 253) = 86.6\ kW \quad \text{(A.102)}$$

$$\dot{Q}_{\text{cc,subcool,sh}} = \dot{M}_{\text{prs}} * C_{\text{p,prs,2}} * \left(t_{\text{prs,i}} - t_{\text{prs,v}}\right) = 7.81 * 4.87 * (35.3 - 33.1) \quad \text{(A.103)}$$

$$= 83.7\ kW$$

$$\dot{Q}_{\text{cc,subcool,sh}} = \varepsilon_{\text{cc,subcool,sh}} * C_{\min} * \left(t_{\text{prs,v}} - t_{\text{cc,12}}\right) \quad \text{(A.104)}$$

$$= 0.7 * 3.99 * (35.3 - 4.95) = 84.8\ kW$$

The total cooling duty of the TCCS evaporator is evaluated as shown in Equation (A.105).

$$\dot{Q}_{\text{cc,subcool}} = \dot{Q}_{\text{cc,subcool,tp}} + \dot{Q}_{\text{cc,subcool,sh}} = 733 + 85 = 818\ kW \quad \text{(A.105)}$$

Reduced PRS mass flow rate, PRS compressor work, and power savings are evaluated as shown in Equation (A.106) through (A.108).

$$\dot{M}_{\text{r,prs}} = \frac{\dot{Q}_{\text{cool}} - \dot{Q}_{\text{cc,subcool}}}{(h_1 - h_5)} = \frac{9300 - 818}{(1454 - 368)} = 7.81 \frac{kg}{s} \quad \text{(A.106)}$$

$$\dot{W}_{\text{overall,prs+tccs}} = \dot{M}_{\text{r,prs}} * (h_2 - h_1) + \dot{W}_{\text{pump,tccs}} \quad \text{(A.107)}$$

$$= 7.81 * (1775 - 1454) + 8.3 = 2515\ kW$$

$$Power\ Savings = \dot{W}_{\text{overall,prs}} - \dot{W}_{\text{overall,prs+tccs}} = 2753 - 2515 = 238\ kW \quad \text{(A.108)}$$

Natural gas savings that are produced by economizing the heat from each of the TCCS condensers are calculated as shown in Equation (A.109).

$$NG_{\text{savings,tccs}} = (\dot{Q}_{\text{cond,pc}} + \dot{Q}_{\text{cond,cc}}) * 3.6\frac{MJ}{kWh} \div \frac{40.6MJ}{m^3} * 0.0353\frac{MCF}{m^3} \quad \text{(A.109)}$$

$$= \frac{(614 + 842) * 3.6 * 0.0354}{40.6} = 4.57\frac{MCF}{hr}$$

Finally, COP of the TCCS is evaluated as the amount of subcooling provided to the PRS divided by the sum of the waste heat and the power cycle pump work as shown in Equation (A.110).

$$COP_{\text{tccs}} = \frac{\dot{Q}_{\text{cc,subcool}}}{\dot{Q}_{\text{recoverable}} + \dot{W}_{\text{pump,tccs}}} = \frac{818}{631 + 8.3} = 1.28 \quad \text{(A.110)}$$

This concludes the representative calculation for the thermodynamics of the TCCS system. The results from the representative calculations are compared with the results from the EES model in Table A.13. The TCCS thermodynamic results from the EES model for both the summer and winter input condition are shown in Table A.14. The total annual savings, which are calculate by summing the hourly natural gas and electricity savings (multiplied by the cost of natural gas and electricity in each location) throughout the entire year are shown in Table A.15.

Table A.13 Comparison of thermodynamic results between the representative calculation and the EES simulation.

Value	Hand Result	EES Result	Unit
W_turb	79.7	78.9	kW
eta_turb	0.8	0.8	-
Q_pc_recup	36.9	37.2	kW
Q_pc_cond_sh	19.1	19.2	kW
Q_pc_cond_tp	591	590	kW
Q_pc_cond_sc	4.12	4.41	kW
w_pump	8.3	8.2	kW
eta_pump	0.64	0.65	
q_econ	54.6	53.4	kW
q_boil_sc	196	195	kW
q_boil_tp	354	355	kW
q_boil_sh	80.7	80.5	kW
w_comp	78	77.3	kW
eta_comp	0.778	0.8	-
q_cc_cond_sh	62.8	63.4	kW
q_cc_cond_tp	774	773	kW
q_cc_cond_sc	5.22	5.31	kW
q_subcool_tp	733	733	kW
q_subcool_sh	85	84.7	kW
q_subcool_total	818	818	kW
m_r_prs	7.81	7.81	kg/s
w_overall	2515	2520	kW
power saving	238	234	kW
ng saving	4.57	4.57	MCF/hr
COP_tccs	1.28	1.28	-

Table A.14 TCCS thermodynamic results for average summer and winter conditions from EES simulations.

Model		Result	Summer	Winter
TCCS	**Power Cycle**	$\dot{W}_{\text{turb}}$	78.9 kW	78 kW
		$\dot{Q}_{\text{recup}}$	37.2 kW	35.4 kW
		$\dot{Q}_{\text{cond,pc}}$	614 kW	603 kW
		$\dot{W}_{\text{pump}}$	8.2 kW	8.17 kW
		$\dot{Q}_{\text{econ}}$	53.4 kW	42 kW
	Cooling Cycle	$\dot{W}_{\text{comp}}$	77.3 kW	76.5 kW
		$\dot{Q}_{\text{cond,cc}}$	841 kW	751 kW
		$\dot{Q}_{\text{subcool}}$	818 kW	716 kW
		COP_{tccs}	1.28	1.12
		$NG_{savings}$	4.57 MCF/hr	4.25 MCF/hr
	PRS	$\dot{M}_{\text{r,prs}}$	7.81 kg/s	7.7 kg/s
		$\dot{W}_{\text{overall,prs+tccs}}$	2520 kW	2132 kW
		$Power\ Savings$	234 kW	169 kW

Table A.15 Total Annual Savings yielded by TCCS in five different locations.

Location	Gas		Electricity		Total Savings ($)
	Total (MCF)	Savings ($)	Total (kWh)	Savings ($)	
Fresno, CA	23,715	$182,734	1,242,657	$167,214	$349,948
Denver, CO	22,761	$126,783	1,044,893	$76,154	$202,938
Atlanta, GA	23,820	$102,057	1,274,272	$75,774	$177,832
Grand Island, NE	22,853	$94,449	1,078,212	$85,333	$179,783
Green Bay, WI	22,627	$110,740	1,030,161	$80,108	$190,848

A.4 Heat Transfer Calculations

To determine the overall cost of the TCCS, ORC, and DMS, each heat exchanger was sized based on heat transfer calculations for a system operating at the average summer condition of the PRS operating at a high side pressure of 1367 kPa. In this section, representative calculations of heat transfer coefficient and total heat exchanger area for each heat exchanger of the TCCS will be provided. Inputs for the heat transfer calculations included heat exchanger geometry values, which were based on prior TCCS research, and thermodynamic parameters calculated from the thermodynamic model. Each heat exchanger in this work was selected to be a counter flow stainless-steel plate and frame heat exchanger.

Starting with the power cycle boiler, which is used to exchange heat between the PG-water mixture and the R134a working fluid that circulates through the power cycle. In the first region of the boiler, the working fluid is a subcooled liquid. The first step in sizing the boiler is to determine the overall heat transfer coefficient in this region. To determine the overall heat transfer coefficient, the heat transfer coefficient of the working fluid, the PG-water mixture, and the wall resistance are calculated. The heat transfer coefficient of the working fluid was calculated using the Thonon correlation, as shown in Equation (A.111).

$$h_{\mathrm{r,b1}} = 0.2998 Re_{\mathrm{plate}}^{0.645} Pr^{\frac{1}{3}} \frac{k}{D_{hyd}} = 0.2998(1753)^{0.645}(3.13)^{\frac{1}{3}}\left(\frac{0.0754}{0.008966}\right) \qquad \text{(A.111)}$$

$$= 456 \frac{W}{m^2 K}$$

The heat transfer coefficient of the PG-water mixture is also calculated using the Thonon correlation as shown in Equation (A.112).

$$h_{\mathrm{w,b1}} = 0.2998 Re_{\mathrm{plate}}^{0.645} Pr^{\frac{1}{3}} \frac{k}{D_{hyd}} = 0.2998(2175)^{0.645}(4.84)^{\frac{1}{3}}\left(\frac{0.5}{0.008966}\right) \quad \text{(A.112)}$$

$$= 4019 \frac{W}{m^2 K}$$

The wall resistance of the plates is calculated according to Equation (A.112).

$$R_{wall} = \frac{t_{\mathrm{plate}}}{k_{\mathrm{plate,stainless}}} = \frac{0.0007}{13.32} = 5.26 * 10^{-5} \frac{m^2 K}{W} \quad \text{(A.113)}$$

The overall heat transfer coefficient for the subcooled region of the power cycle boiler is then calculated as shown in Equation (A.114).

$$\frac{1}{U_{\mathrm{b1}}} = \frac{1}{h_{\mathrm{r,b1}}} + \mathrm{R}_{\mathrm{wall}} + \frac{1}{h_{\mathrm{w,b1}}} = \frac{1}{456} + 5.26 * 10^{-5} + \frac{1}{4019} = 401 \frac{W}{m^2 K} \quad \text{(A.114)}$$

Once overall heat transfer coefficient is calculated, the next step is to calculate the number of transfer units (NTU) for the subcooled region which is a function of the effectiveness of the heat exchanger and the ratio of heat capacity rates as shown in Equation (A.115).

$$NTU_{\mathrm{pc,b1}} = \frac{1}{C_{\mathrm{r}} - 1} \ln\left(\frac{\varepsilon - 1}{\varepsilon C_{\mathrm{r}} - 1}\right) = \frac{1}{.0787 - 1} \ln\left(\frac{0.865 - 1}{(.865).0787 - 1}\right) = 2.097 \quad \text{(A.115)}$$

The total area of the subcooled region can then be determined using Equation (A.116), which relates area to heat transfer coefficient and number of transfer units.

$$A_{\mathrm{b1}} = \frac{NTU_{\mathrm{pc,b1}}\left(C_{\mathrm{min,b1}}\right)}{U_{\mathrm{b1}}} = \frac{2.097(4949)}{401} = 25.9\, m^2 \quad \text{(A.116)}$$

The length of the power cycle boiler subcooled region is calculated using Equation (A.117).

$$L_{\mathrm{b1}} = \frac{A_{b1}}{\left(N_{\mathrm{plate,boiler}} - 1\right) w_{\mathrm{plate}}} = \frac{25.9}{(41.8 - 1)1.17} = .543\, m \quad \text{(A.117)}$$

In the second region of the boiler, the working fluid changes phase from a saturated liquid to a saturated vapor. The same method is used as for the subcooled region, which is to first calculate overall heat transfer coefficient, then number of transfer units, which can then be used to determine

overall heat exchanger area. For the phase changing working fluid, heat transfer coefficient was determined using the Hsieh correlation, as shown in Equation (A.118).

$$h_{\mathrm{r,b2}} = h_{\mathrm{r,l}}(88 * Bo^{0.5}) = 872(88(0.0035)^{0.5}) = 4540\ \frac{W}{m^2K} \tag{A.118}$$

The wall resistance is found to be the same as in Equation (A.113). To calculate heat transfer coefficient of the PG-water side, the Thonon correlation is used as shown in Equation (A.119).

$$h_{\mathrm{w,b2}} = 0.2998 Re_{\mathrm{plate}}^{0.645} Pr^{\frac{1}{3}} \frac{k}{D_{hyd}} = 0.2998(2370)^{0.645}(4.42)^{\frac{1}{3}}\left(\frac{0.504}{0.008966}\right) \tag{A.119}$$

$$= 4155 \frac{W}{m^2K}$$

The overall heat transfer coefficient for the two-phase region of the boiler is then calculated using Equation (A.120).

$$\frac{1}{U_{\mathrm{b2}}} = \frac{1}{h_{\mathrm{r,b2}}} + \mathrm{R_{wall}} + \frac{1}{h_{\mathrm{w,b2}}} = \frac{1}{4540} + 5.26 * 10^{-5} + \frac{1}{4155} = 1947\ \frac{W}{m^2K} \tag{A.120}$$

After this, the number of transfer units required for the two-phase region of the boiler is calculated using Equation (A.121).

$$NTU_{\mathrm{pc,b2}} = -\ln(1-\varepsilon) = -\ln(1-0.35) = 0.431 \tag{A.121}$$

The area of the two-phase region of the boiler is calculated using Equation (A.122).

$$A_{\mathrm{b2}} = \frac{NTU_{\mathrm{pc,b2}}\left(C_{\mathrm{min,b2}}\right)}{U_{\mathrm{b2}}} = \frac{0.431(63030)}{1947} = 14\ m^2 \tag{A.122}$$

The length of the power cycle boiler two-phase region is calculated using Equation (A.123).

$$L_{\mathrm{b2}} = \frac{A_{b2}}{\left(N_{\mathrm{plate,boiler}} - 1\right) w_{\mathrm{plate}}} = \frac{14}{(41.8-1)1.17} = 0.293\ m \tag{A.123}$$

In the third region of the boiler, the working fluid is a superheated vapor. To calculate the area of this region, the overall heat transfer and number of transfer units is calculated. The heat

transfer coefficient of the superheated vapor is calculated using the Thonon correlation, as shown in Equation (A.124).

$$h_{\mathrm{r,b3}} = 0.2998 Re_{\mathrm{plate}}^{0.645} Pr^{\frac{1}{3}} \frac{k}{D_{hyd}} = 0.2998(15000)^{0.645}(1.5)^{\frac{1}{3}} \left(\frac{0.0213}{0.008966}\right) \quad \text{(A.124)}$$

$$= 403 \frac{W}{m^2 K}$$

As discussed in the modeling section, the Reynolds number in this region was set to 15,000 which is the upper limit of the Thonon correlation. If the Reynolds number was not set, it would exceed 15,000 which was found to be unrealistic based on prior heat exchanger research. The heat transfer coefficient of PG-water in this region was also calculated using the Thonon correlation, as shown in Equation (A.125).

$$h_{\mathrm{w,b3}} = 0.2998 Re_{\mathrm{plate}}^{0.645} Pr^{\frac{1}{3}} \frac{k}{D_{hyd}} = 0.2998(2416)^{0.645}(4.33)^{\frac{1}{3}} \left(\frac{0.505}{0.008966}\right) \quad \text{(A.125)}$$

$$= 4186 \frac{W}{m^2 K}$$

The wall resistance was calculated to be the same as in Equation (A.113). Then, overall heat transfer coefficient in the superheated region is calculated as shown in Equation (A.126).

$$\frac{1}{U_{\mathrm{b3}}} = \frac{1}{h_{\mathrm{r,b3}}} + \mathrm{R_{wall}} + \frac{1}{h_{\mathrm{w,b3}}} = \frac{1}{403} + 5.26 * 10^{-5} + \frac{1}{4186} = 367 \frac{W}{m^2 K} \quad \text{(A.126)}$$

The number of transfer units for the superheated region is then calculated as shown in Equation (A.127).

$$NTU_{\mathrm{pc,b3}} = \frac{1}{C_{\mathrm{r}} - 1} \ln\left(\frac{\varepsilon - 1}{\varepsilon C_{\mathrm{r}} - 1}\right) = \frac{1}{0.1046 - 1} \ln\left(\frac{0.7 - 1}{(0.7)0.1046 - 1}\right) = 1.26 \quad \text{(A.127)}$$

Thus, the area of the superheated region of the boiler is calculated in Equation (A.128).

$$A_{\mathrm{b3}} = \frac{NTU_{\mathrm{pc,b3}}\left(C_{\mathrm{min,b3}}\right)}{U_{\mathrm{b3}}} = \frac{1.26(6619)}{367} = 22.7\ m^2 \quad \text{(A.128)}$$

Finally, the length of the power cycle boiler superheated region is calculated using Equation (A.129).

$$L_{\mathrm{b3}} = \frac{A_{b3}}{\left(N_{\mathrm{plate,boiler}} - 1\right) w_{\mathrm{plate}}} = \frac{22.7}{(41.8 - 1)1.17} = \ 0.476\ m \tag{A.129}$$

Once the heat transfer in all three sections of the power cycle boiler has been assessed, some overall calculations can be made to describe the geometry of the heat exchanger. The overall area of the power cycle boiler is calculated as shown in Equation (A.130).

$$A_{\mathrm{total,boiler}} = A_{\mathrm{b1}} + A_{\mathrm{b2}} + A_{\mathrm{b3}} = 25.9 + 14 + 22.7 = 62.6\ m^2 \tag{A.130}$$

The total length of the of the power cycle boiler is calculated in Equation (A.131).

$$L_{\mathrm{total,boiler}} = L_{\mathrm{b1}} + L_{\mathrm{b2}} + L_{\mathrm{b3}} = 0.543 + 0.292 + 0.476 = \ 1.31\ m \tag{A.131}$$

The number of plates of the power cycle boiler is confirmed in Equation (A.132).

$$N_{\mathrm{plate,b}} - 1 = \frac{A_{\mathrm{total,boiler}}}{A_{\mathrm{plate}}} = 1 + \frac{62.6}{1.544} = 41.5\ Plates \tag{A.132}$$

The power cycle recuperator representative calculations will be discussed next. The power cycle recuperator is used to transfer heat from the superheated working fluid at the turbine outlet to the subcooled working fluid at the boiler inlet. The recuperator is selected to be a stainless steel, counter-flow plate frame heat exchanger, and the area is found using the same method as used for the power cycle boiler. The heat transfer coefficient of the superheated working fluid in the recuperator is calculated using the Thonon correlation as shown in Equation (A.133).

$$h_{\mathrm{r,sh,rec}} = 0.2998 Re_{\mathrm{plate}}^{0.645} Pr^{\frac{1}{3}} \frac{k}{D_{hyd}} = 0.2998(15000)^{0.645}(0.789)^{\frac{1}{3}} \left(\frac{0.0158}{0.008966}\right) \tag{A.133}$$

$$= 241 \frac{W}{m^2 K}$$

The heat transfer coefficient of the subcooled working fluid is also calculated using the Thonon correlation as shown in Equation (A.134).

$$h_{\mathrm{r,sc,rec}} = 0.2998 Re_{\mathrm{plate}}^{0.645} Pr^{\frac{1}{3}} \frac{k}{D_{hyd}} = 0.2998(2652)^{0.645}(3.31)^{\frac{1}{3}}\left(\frac{0.0849}{0.008966}\right) \quad \text{(A.134)}$$

$$= 683 \frac{W}{m^2 K}$$

The wall resistance was calculated to be the same as shown in Equation (A.113). The overall heat transfer coefficient in the recuperator is calculated in Equation (A.135).

$$\frac{1}{U_{\mathrm{rec}}} = \frac{1}{h_{\mathrm{r,sh,rec}}} + \mathrm{R}_{\mathrm{wall}} + \frac{1}{h_{\mathrm{r,sc,rec}}} = \frac{1}{241} + 5.26 * 10^{-5} + \frac{1}{683} = 176 \frac{W}{m^2 K} \quad \text{(A.135)}$$

The number of transfer units for the recuperator is then calculated as shown in Equation (A.136).

$$NTU_{\mathrm{rec}} = \frac{1}{C_{\mathrm{r}} - 1} \ln\left(\frac{\varepsilon - 1}{\varepsilon C_{\mathrm{r}} - 1}\right) = \frac{1}{.702 - 1} \ln\left(\frac{0.7 - 1}{(0.7).702 - 1}\right) = 1.77 \quad \text{(A.136)}$$

Thus, the area of the recuperator is calculated in Equation (A.137).

$$A_{\mathrm{rec}} = \frac{NTU_{\mathrm{rec}}\left(C_{\mathrm{min,rec}}\right)}{U_{\mathrm{rec}}} = \frac{1.77(3272)}{176} = 33\ m^2 \quad \text{(A.137)}$$

The total number of plates of the recuperator is calculated using Equation (A.138).

$$N_{\mathrm{plate,rec}} - 1 = \frac{A_{\mathrm{rec}}}{A_{\mathrm{plate}}} = 1 + \frac{33}{1.544} = 22.4\ Plates \quad \text{(A.138)}$$

Finally, the length of the recuperator is calculated in Equation (A.139).

$$L_{\mathrm{rec}} = \frac{A_{\mathrm{rec}}}{\left(N_{\mathrm{plate,rec}} - 1\right) w_{\mathrm{plate}}} = \frac{33}{(22.4 - 1)1.17} = 1.32\ m \quad \text{(A.139)}$$

The next heat exchanger that will be discussed is the power cycle condenser. Like the power cycle boiler, the power cycle condenser is a counter-flow, stainless steel, plate frame heat exchanger with three regions: subcooled, two-phase, and superheated. The heat transfer coefficient of the superheated refrigerant in the power cycle condenser is calculated using the Thonon correlation as shown in Equation (A.140).

$$h_{\mathrm{r,c1}} = 0.2998 Re_{\mathrm{plate}}^{0.645} Pr^{\frac{1}{3}} \frac{k}{D_{hyd}} = 0.2998(737)^{0.645}(0.82)^{\frac{1}{3}}\left(\frac{0.015}{0.008966}\right) \quad \text{(A.140)}$$

$$= 33.2 \frac{W}{m^2 K}$$

The heat transfer coefficient of the condenser water is also calculated using the Thonon correlation as shown in Equation (A.141).

$$h_{\mathrm{w,c1}} = 0.2998 Re_{\mathrm{plate}}^{0.645} Pr^{\frac{1}{3}} \frac{k}{D_{hyd}} = 0.2998(61.9)^{0.645}(6.62)^{\frac{1}{3}}\left(\frac{0.602}{0.008966}\right) \quad \text{(A.141)}$$

$$= 541 \frac{W}{m^2 K}$$

The wall resistance was calculated to be the same as Equation (A.113). Thus, the overall heat transfer coefficient in the superheated region of the condenser is calculated in Equation (A.142).

$$\frac{1}{U_{\mathrm{c1}}} = \frac{1}{h_{\mathrm{r,c1}}} + \mathrm{R_{wall}} + \frac{1}{h_{\mathrm{w,c1}}} = \frac{1}{33.2} + 5.26 * 10^{-5} + \frac{1}{541} = 31.2 \ \frac{W}{m^2 K} \quad \text{(A.142)}$$

Then, the number of transfer units for this region is calculated using Equation (A.143).

$$NTU_{\mathrm{pc,c1}} = \frac{1}{C_{\mathrm{r}} - 1} \ln\left(\frac{\varepsilon - 1}{\varepsilon C_{\mathrm{r}} - 1}\right) = \frac{1}{.0377 - 1} \ln\left(\frac{0.664 - 1}{(.664).0377 - 1}\right) = 1.11 \quad \text{(A.143)}$$

The total area of the superheated region of the condenser is calculated using Equation (A.144).

$$A_{\mathrm{c1}} = \frac{NTU_{\mathrm{pc,c1}}\left(C_{\mathrm{min,c1}}\right)}{U_{\mathrm{c1}}} = \frac{1.11(3416)}{31.2} = 122 \ m^2 \quad \text{(A.144)}$$

Finally, the length of the superheated region of the condenser is calculated using Equation (A.145).

$$L_{\mathrm{c1}} = \frac{A_{\mathrm{c1}}}{\left(N_{\mathrm{plate,pc,cond}} - 1\right) w_{\mathrm{plate}}} = \frac{122}{(1254 - 1)1.17} = \ .0832 \ m \quad \text{(A.145)}$$

In the next region of the condenser, the working fluid is a two-phase mixture. The heat transfer coefficient in this region is calculated using the Kuo correlation for condensing refrigerants in plate heat exchangers, as shown in Equation (A.146).

$$h_{\mathrm{r,c2}} = h_{\mathrm{r,l}}\left(0.25Co^{-0.45}Fr_{\mathrm{l}}^{0.25} + 75Bo^{0.75}\right) \tag{A.146}$$

$$= 61.4(0.25(0.0267)^{-0.45}(0.00000787)^{0.25} + 75(0.00341)^{0.75})$$

$$= 69.1\ \frac{W}{m^2K}$$

The water side heat transfer coefficient was calculated using the Thonon correlation as shown in Equation (A.147).

$$h_{\mathrm{w,c2}} = 0.2998Re_{\mathrm{plate}}^{0.645}Pr^{\frac{1}{3}}\frac{k}{D_{hyd}} = 0.2998(52.6)^{0.645}(7.95)^{\frac{1}{3}}\left(\frac{0.59}{0.008966}\right) \tag{A.147}$$

$$= 507\frac{W}{m^2K}$$

The overall heat transfer coefficient is then calculated as shown in Equation (A.148)

$$\frac{1}{U_{\mathrm{c2}}} = \frac{1}{h_{\mathrm{r,c2}}} + \mathrm{R_{wall}} + \frac{1}{h_{\mathrm{w,c2}}} = \frac{1}{69.1} + 5.26 * 10^{-5} + \frac{1}{507} = \ 60.6\frac{W}{m^2K} \tag{A.148}$$

The number of transfer units for the two-phase region of the condenser is calculated in Equation (A.149).

$$NTU_{\mathrm{pc,c2}} = -\ln(1-\varepsilon) = -\ln(1-0.7) = 1.2 \tag{A.149}$$

The area of the two-phase region is calculated with Equation (A.150).

$$A_{\mathrm{c2}} = \frac{NTU_{\mathrm{pc,c2}}\left(C_{\mathrm{min,c2}}\right)}{U_{\mathrm{c2}}} = \frac{1.2(90840)}{60.6} = 1800\ m^2 \tag{A.150}$$

Finally, the length of the two-phase region of the condenser is calculated as shown in Equation (A.151).

$$L_{\mathrm{c2}} = \frac{A_{\mathrm{c2}}}{\left(N_{\mathrm{plate,pc,cond}} - 1\right)w_{\mathrm{plate}}} = \frac{1800}{(1254-1)1.17} = 1.23\ m \tag{A.151}$$

In the third region of the condenser, the working fluid is a subcooled liquid. The heat transfer coefficient of the working fluid is calculated using the Thonon correlation as shown in Equation (A.152).

$$h_{\mathrm{r,c3}} = 0.2998 Re_{\mathrm{plate}}^{0.645} Pr^{\frac{1}{3}} \frac{k}{D_{hyd}} = 0.2998(50)^{0.645}(3.33)^{\frac{1}{3}}\left(\frac{0.0833}{0.008966}\right) \tag{A.152}$$

$$= 51.9 \frac{W}{m^2 K}$$

The water side heat transfer coefficient is also calculated using the Thonon correlation as shown in Equation (A.153).

$$h_{\mathrm{w,c3}} = 0.2998 Re_{\mathrm{plate}}^{0.645} Pr^{\frac{1}{3}} \frac{k}{D_{hyd}} = 0.2998(52.6)^{0.645}(7.96)^{\frac{1}{3}}\left(\frac{0.59}{0.008966}\right) \tag{A.153}$$

$$= 507 \frac{W}{m^2 K}$$

The overall heat transfer coefficient in the subcooled region is then calculated as shown in Equation (A.154)

$$\frac{1}{U_{\mathrm{c3}}} = \frac{1}{h_{\mathrm{r,c3}}} + \mathrm{R}_{\mathrm{wall}} + \frac{1}{h_{\mathrm{w,c3}}} = \frac{1}{51.9} + 5.26 * 10^{-5} + \frac{1}{507} = 47 \ \frac{W}{m^2 K} \tag{A.154}$$

The number of transfer units for the subcooled region of the condenser is calculated in Equation (A.155).

$$NTU_{\mathrm{pc,c3}} = \frac{1}{C_{\mathrm{r}} - 1} \ln\left(\frac{\varepsilon - 1}{\varepsilon C_{\mathrm{r}} - 1}\right) = \frac{1}{.0519 - 1} \ln\left(\frac{0.1 - 1}{(.1).0519 - 1}\right) = .106 \tag{A.155}$$

The area of the subcooled region is calculated with Equation (A.156).

$$A_{\mathrm{c3}} = \frac{NTU_{\mathrm{pc,c3}}\left(C_{\mathrm{min,c3}}\right)}{U_{\mathrm{c3}}} = \frac{.106(4718)}{47} = 10.6 \ m^2 \tag{A.156}$$

Finally, the length of the subcooled region of the condenser is calculated as shown in Equation (A.157).

$$L_{\mathrm{c3}} = \frac{A_{\mathrm{c3}}}{\left(N_{\mathrm{plate,pc,cond}} - 1\right) w_{\mathrm{plate}}} = \frac{10.6}{(1254 - 1)1.17} = \ .00723 \ m \tag{A.157}$$

Once the heat transfer in all three sections of the power cycle condenser has been assessed, some overall calculations can be made to describe the geometry of the heat exchanger. The overall area of the power cycle condenser is calculated as shown in Equation (A.158).

$$A_{\text{total,pc,cond}} = A_{\text{c1}} + A_{\text{c2}} + A_{\text{c3}} = 122 + 1800 + 10.6 = \ 1933\ m^2 \tag{A.158}$$

The total length of the of the power cycle condenser is calculated in Equation (A.159).

$$L_{\text{total,boiler}} = L_{\text{b1}} + L_{\text{b2}} + L_{\text{b3}} = 0.124 + 1.18 + 0.0114 = \ 1.32\ m \tag{A.159}$$

The number of plates of the power cycle condenser is confirmed in Equation (A.160).

$$N_{\text{plate,pc.cond}} - 1 = \frac{A_{\text{total,pc,cond}}}{A_{\text{plate}}} = 1 + \frac{1933}{1.544} = 1253\ Plates \tag{A.160}$$

The number of plates calculated in Equation (A.160), 1253 plates, is one plate less than the plate number value solved for by EES due to rounding errors in the sample calculations. The cross-cycle economizer calculations will be discussed next. The cross-cycle economizer is a counterflow stainless steel heat exchanger that exchanges heat between the cooling cycle working fluid at the turbine outlet and the power cycle working fluid at the boiler inlet. The economizer, like the recuperator, is a single-phase heat exchanger, where the cooling cycle fluid is a superheated vapor and the power cycle fluid is a subcooled liquid. The heat transfer coefficient of the superheated working fluid in the economizer is calculated using the Thonon correlation as shown in Equation (A.161).

$$h_{\text{r,sh,econ}} = 0.2998 Re_{\text{plate}}^{0.645} Pr^{\frac{1}{3}} \frac{k}{D_{hyd}} \tag{A.161}$$

$$= 0.2998(15000)^{0.645}(0.774)^{\frac{1}{3}}\left(\frac{0.0164}{0.008966}\right) = 249\frac{W}{m^2K}$$

The heat transfer coefficient of the subcooled working fluid is also calculated using the Thonon correlation as shown in Equation (A.162).

$$h_{\mathrm{r,sc,econ}} = 0.2998 Re_{\mathrm{plate}}^{0.645} Pr^{\frac{1}{3}} \frac{k}{D_{hyd}} = 0.2998(1600)^{0.645}(3.31)^{\frac{1}{3}}\left(\frac{0.0849}{0.008966}\right) \quad \text{(A.162)}$$

$$= 493 \frac{W}{m^2 K}$$

The wall resistance was calculated to be the same as shown in Equation (A.113). The overall heat transfer coefficient in the economizer is calculated in Equation (A.163).

$$\frac{1}{U_{\mathrm{econ}}} = \frac{1}{h_{\mathrm{r,sh,econ}}} + \mathrm{R}_{\mathrm{wall}} + \frac{1}{h_{\mathrm{r,sc,econ}}} = \frac{1}{249} + 5.26 * 10^{-5} + \frac{1}{493} = 164 \ \frac{W}{m^2 K} \quad \text{(A.163)}$$

The number of transfer units for the economizer is then calculated as shown in Equation (A.164).

$$NTU_{\mathrm{econ}} = \frac{1}{C_{\mathrm{r}} - 1} \ln\left(\frac{\varepsilon - 1}{\varepsilon C_{\mathrm{r}} - 1}\right) = \frac{1}{0.897 - 1} \ln\left(\frac{0.7 - 1}{(0.7)0.897 - 1}\right) = 2.09 \quad \text{(A.164)}$$

Thus, the area of the economizer is calculated in Equation (A.165).

$$A_{\mathrm{econ}} = \frac{NTU_{\mathrm{econ}}\left(C_{\mathrm{min,econ}}\right)}{U_{\mathrm{econ}}} = \frac{2.09(4273)}{164} = 54.5 \ m^2 \quad \text{(A.165)}$$

The number of plates of the economizer is calculated using Equation (A.166).

$$N_{\mathrm{plate,econ}} - 1 = \frac{A_{\mathrm{econ}}}{A_{\mathrm{plate}}} = 1 + \frac{54.5}{1.544} = 36.3 \ Plates \quad \text{(A.166)}$$

Finally, the length of the economizer is confirmed in Equation (A.167).

$$L_{\mathrm{econ}} = \frac{A_{\mathrm{econ}}}{\left(N_{\mathrm{plate,econ}} - 1\right) w_{\mathrm{plate}}} = \frac{54.5}{(36.3 - 1)1.17} = \ 1.32 \ m \quad \text{(A.167)}$$

The cooling cycle evaporator heat exchanger will be discussed next. The working fluid enters the chiller as a two-phase mixture. The heat transfer coefficient of the TCCS refrigerant in this region is calculated using the Hsieh correlation, as shown in Equation (A.168).

$$h_{\mathrm{cc,r,E1}} = h_{\mathrm{r,l}}(88 * Bo^{0.5}) = 1257(88(0.00307)^{0.5}) = 6129 \ \frac{W}{m^2 K} \quad \text{(A.168)}$$

The heat transfer coefficient of the ammonia in the two-phase region of the evaporator is calculated using the Thonon correlation, as shown in Equation (A.169)

$$h_{\mathrm{cc,w,E1}} = 0.2998 Re_{\mathrm{plate}}^{0.645} Pr^{\frac{1}{3}} \frac{k}{D_{hyd}} = 0.2998(7453)^{0.645}(1.28)^{\frac{1}{3}}\left(\frac{0.463}{0.008966}\right) \quad \text{(A.169)}$$

$$= 5287 \frac{W}{m^2 K}$$

The overall heat transfer coefficient is then calculated as shown in Equation (A.170)

$$\frac{1}{U_{\mathrm{cc,E1}}} = \frac{1}{h_{\mathrm{cc,r,E1}}} + \mathrm{R_{wall}} + \frac{1}{h_{\mathrm{cc,w,cE1}}} = \frac{1}{6129} + 5.26 * 10^{-5} + \frac{1}{5287} \quad \text{(A.170)}$$

$$= 2470 \ \frac{W}{m^2 K}$$

The number of transfer units for the two-phase region of the evaporator is calculated in Equation (A.171).

$$NTU_{\mathrm{cc,E1}} = -\ln(1-\varepsilon) = -\ln(1-0.7) = 1.2 \quad \text{(A.171)}$$

The area of the two-phase region is calculated with Equation (A.172).

$$A_{\mathrm{cc,E1}} = \frac{NTU_{\mathrm{cc,E1}}\left(C_{\mathrm{min,E1}}\right)}{U_{\mathrm{cc,E1}}} = \frac{1.2(37230)}{2470} = 18.1\ m^2 \quad \text{(A.172)}$$

Finally, the length of the two-phase region of the condenser is calculated as shown in Equation (A.173).

$$L_{\mathrm{cc,E1}} = \frac{A_{\mathrm{cc,E1}}}{\left(N_{\mathrm{plate,evap}} - 1\right) w_{\mathrm{plate}}} = \frac{18.1}{(30.3-1)1.17} = \ 0.528\ m \quad \text{(A.173)}$$

The heat transfer coefficient of the TCCS refrigerant in the superheated region of the evaporator is calculated using the Thonon correlation as shown in Equation (A.174).

$$h_{\mathrm{cc,r,E2}} = 0.2998 Re_{\mathrm{plate}}^{0.645} Pr^{\frac{1}{3}} \frac{k}{D_{hyd}} = 0.2998(15000)^{0.645}(0.813)^{\frac{1}{3}}\left(\frac{0.0126}{0.008966}\right) \quad \text{(A.174)}$$

$$= 194 \frac{W}{m^2 K}$$

The heat transfer coefficient of ammonia in the superheated region of the evaporator is also calculated using the Thonon correlation which is shown in Equation (A.175)

$$h_{\mathrm{cc,w,E2}} = 0.2998 Re_{\mathrm{plate}}^{0.645} Pr^{\frac{1}{3}} \frac{k}{D_{hyd}} = 0.2998(7614)^{0.645}(1.28)^{\frac{1}{3}}\left(\frac{0.457}{0.008966}\right) \quad \text{(A.175)}$$

$$= 5291 \frac{W}{m^2 K}$$

The overall heat transfer coefficient in the superheated region is then calculated as shown in Equation (A.176)

$$\frac{1}{U_{\mathrm{cc,E2}}} = \frac{1}{h_{\mathrm{cc,r,E2}}} + \mathrm{R_{wall}} + \frac{1}{h_{\mathrm{cc,w,E2}}} = \frac{1}{194} + 5.26 * 10^{-5} + \frac{1}{5291} = 185 \ \frac{W}{m^2 K} \quad \text{(A.176)}$$

The number of transfer units for the superheated region of the evaporator is calculated in Equation (A.177).

$$NTU_{\mathrm{cc,E2}} = \frac{1}{C_{\mathrm{r}} - 1} \ln\left(\frac{\varepsilon - 1}{\varepsilon C_{\mathrm{r}} - 1}\right) = \frac{1}{.105 - 1} \ln\left(\frac{0.7 - 1}{(0.7).105 - 1}\right) = 1.26 \quad \text{(A.177)}$$

The area of the region is then calculated with Equation (A.178).

$$A_{\mathrm{cc,E2}} = \frac{NTU_{\mathrm{cc,E2}}\left(C_{\mathrm{min,E2}}\right)}{U_{\mathrm{cc,E2}}} = \frac{1.26(3985)}{185} = 27.1\ m^2 \quad \text{(A.178)}$$

Finally, the length of the superheated region is calculated as shown in Equation (A.179).

$$L_{\mathrm{cc,E2}} = \frac{A_{\mathrm{cc,E2}}}{\left(N_{\mathrm{plate,evap}} - 1\right) w_{\mathrm{plate}}} = \frac{27.1}{(30.3 - 1)1.17} = \ .791\ m \quad \text{(A.179)}$$

Once the heat transfer in both sections of the evaporator has been assessed, some overall calculations can be made to describe the geometry of the heat exchanger. The overall area of the evaporator is calculated as shown in Equation (A.180).

$$A_{\mathrm{total,evap}} = A_{\mathrm{cc,E1}} + A_{\mathrm{cc,E2}} = 18.1 + 27.1 = \ 45.2\ m^2 \quad \text{(A.180)}$$

The total length of the of the power cycle condenser is calculated in Equation (A.181).

$$L_{\mathrm{total,evap}} = L_{\mathrm{cc,E1}} + L_{\mathrm{cc,E2}} = 0.528 + 0.791 = \ 1.32\ m \quad \text{(A.181)}$$

The number of plates of the power cycle condenser is confirmed in Equation (A.182).

$$N_{\text{plate,evap}} - 1 = \frac{A_{\text{total,evap}}}{A_{\text{plate}}} = 1 + \frac{45.2}{1.544} = 30.3\ Plates \tag{A.182}$$

The final heat exchanger to be discussed is the cooling cycle condenser. The cooling cycle condenser is a counterflow, stainless-steel, plate frame heat exchanger which exchanges heat between the working fluid in the cooling cycle and the boiler feedwater. The heat transfer coefficient of the superheated refrigerant in the cooling cycle condenser is calculated using the Thonon correlation as shown in Equation (A.183).

$$h_{\text{cc,r,c1}} = 0.2998 Re_{\text{plate}}^{0.645} Pr^{\frac{1}{3}} \frac{k}{D_{hyd}} = 0.2998(634)^{0.645}(0.793)^{\frac{1}{3}}\left(\frac{0.0155}{0.008966}\right) \tag{A.183}$$

$$= 30.8 \frac{W}{m^2 K}$$

The heat transfer coefficient of the condenser water is also calculated using the Thonon correlation as shown in Equation (A.184).

$$h_{\text{cc,w,c1}} = 0.2998 Re_{\text{plate}}^{0.645} Pr^{\frac{1}{3}} \frac{k}{D_{hyd}} = 0.2998(58.9)^{0.645}(6.71)^{\frac{1}{3}}\left(\frac{0.601}{0.008966}\right) \tag{A.184}$$

$$= 525 \frac{W}{m^2 K}$$

The wall resistance was calculated to be the same as Equation (A.113). Thus, the overall heat transfer coefficient in the superheated region of the condenser is calculated in Equation (A.185).

$$\frac{1}{U_{\text{cc,c1}}} = \frac{1}{h_{\text{cc,r,c1}}} + \text{R}_{\text{wall}} + \frac{1}{h_{\text{cc,w,c1}}} = \frac{1}{30.8} + 5.26 * 10^{-5} + \frac{1}{525} = 29\ \frac{W}{m^2 K} \tag{A.185}$$

Then, the number of transfer units for this region is calculated using Equation (A.186).

$$NTU_{\text{cc,c1}} = \frac{1}{C_{\text{r}} - 1} \ln\left(\frac{\varepsilon - 1}{\varepsilon C_{\text{r}} - 1}\right) = \frac{1}{.0346 - 1} \ln\left(\frac{0.83 - 1}{(.83).0346 - 1}\right) = 1.81 \tag{A.186}$$

The total area of the superheated region of the condenser is calculated using Equation (A.187).

$$A_{\mathrm{cc,c1}} = \frac{NTU_{\mathrm{cc,c1}}\left(C_{\mathrm{min,c1}}\right)}{U_{\mathrm{cc,c1}}} = \frac{1.81(4444)}{29} = 277\ m^2 \tag{A.187}$$

Finally, the length of the superheated region of the condenser is calculated using Equation (A.188).

$$L_{\mathrm{cc,c1}} = \frac{A_{\mathrm{cc,c1}}}{\left(N_{\mathrm{plate,cc,cond}} - 1\right)w_{\mathrm{plate}}} = \frac{277}{(1845-1)1.17} = 0.128\ m \tag{A.188}$$

In the next region of the condenser, the working fluid is a two-phase mixture. The heat transfer coefficient in this region is calculated using the Kuo correlation for condensing refrigerants in plate heat exchangers, as shown in Equation (A.189).

$$h_{\mathrm{cc,r,c2}} = h_{\mathrm{r,l}}\left(0.25Co^{-0.45}Fr_{\mathrm{l}}^{0.25} + 75Bo^{0.75}\right) \tag{A.189}$$

$$= 61.7(0.25(0.0261)^{-0.45}(0.00000618)^{0.25} + 75(0.00341)^{0.75})$$

$$= 69.3\frac{W}{m^2K}$$

The water side heat transfer coefficient was calculated using the Thonon correlation as shown in Equation (A.190).

$$h_{\mathrm{cc,w,c2}} = 0.2998Re_{\mathrm{plate}}^{0.645}Pr^{\frac{1}{3}}\frac{k}{D_{hyd}} = 0.2998(50.7)^{0.645}(7.95)^{\frac{1}{3}}\left(\frac{0.59}{0.008966}\right) \tag{A.190}$$

$$= 495\ \frac{W}{m^2K}$$

The overall heat transfer coefficient is then calculated as shown in Equation (A.191)

$$\frac{1}{U_{\mathrm{cc,c2}}} = \frac{1}{h_{\mathrm{cc,r,c2}}} + \mathrm{R_{wall}} + \frac{1}{h_{\mathrm{cc,w,c2}}} = \frac{1}{69.3} + 5.26 * 10^{-5} + \frac{1}{495} = 60.6\frac{W}{m^2K} \tag{A.191}$$

The number of transfer units for the two-phase region of the condenser is calculated in Equation (A.192).

$$NTU_{\mathrm{cc,c2}} = -\ln(1-\varepsilon) = -\ln(1-0.7) = 1.2 \tag{A.192}$$

The area of the two-phase region is calculated with Equation (A.193).

$$A_{\mathrm{cc,c2}} = \frac{NTU_{\mathrm{cc,c2}}\left(C_{\mathrm{min,c2}}\right)}{U_{\mathrm{cc,c2}}} = \frac{1.2(128600)}{60.6} = 2547\ m^2 \tag{A.193}$$

Finally, the length of the two-phase region of the condenser is calculated as shown in Equation (A.194).

$$L_{\mathrm{cc,c2}} = \frac{A_{\mathrm{cc,c2}}}{\left(N_{\mathrm{plate,cc,cond}} - 1\right)w_{\mathrm{plate}}} = \frac{2547}{(1845-1)1.17} = 1.18\ m \tag{A.194}$$

In the third region of the condenser, the working fluid is a subcooled liquid. The heat transfer coefficient of the working fluid is calculated using the Thonon correlation as shown in Equation (A.195).

$$h_{\mathrm{cc,r,c3}} = 0.2998 Re_{\mathrm{plate}}^{0.645} Pr^{\frac{1}{3}} \frac{k}{D_{hyd}} = 0.2998(50)^{0.645}(3.34)^{\frac{1}{3}}\left(\frac{0.0836}{0.008966}\right) \tag{A.195}$$

$$= 52.1 \frac{W}{m^2 K}$$

The water side heat transfer coefficient is also calculated using the Thonon correlation as shown in Equation (A.196).

$$h_{\mathrm{cc,w,c3}} = 0.2998 Re_{\mathrm{plate}}^{0.645} Pr^{\frac{1}{3}} \frac{k}{D_{hyd}} = 0.2998(50.6)^{0.645}(7.96)^{\frac{1}{3}}\left(\frac{0.59}{0.008966}\right) \tag{A.196}$$

$$= 495 \frac{W}{m^2 K}$$

The overall heat transfer coefficient in the subcooled region is then calculated as shown in Equation (A.197)

$$\frac{1}{U_{\mathrm{cc,c3}}} = \frac{1}{h_{\mathrm{cc,r,c3}}} + \mathrm{R}_{\mathrm{wall}} + \frac{1}{h_{\mathrm{cc,w,c3}}} = \frac{1}{52.1} + 5.26 * 10^{-5} + \frac{1}{495} = 47\ \frac{W}{m^2 K} \tag{A.197}$$

The number of transfer units for the subcooled region of the condenser is calculated in Equation (A.198).

$$NTU_{\mathrm{cc,c3}} = \frac{1}{C_{\mathrm{r}} - 1} \ln\left(\frac{\varepsilon - 1}{\varepsilon C_{\mathrm{r}} - 1}\right) = \frac{1}{.0478 - 1} \ln\left(\frac{0.1 - 1}{(0.1).0478 - 1}\right) = 0.106 \tag{A.198}$$

The area of the subcooled region is calculated with Equation (A.199).

$$A_{\mathrm{cc,c3}} = \frac{NTU_{\mathrm{cc,c3}}\left(C_{\mathrm{min,c3}}\right)}{U_{\mathrm{cc,c3}}} = \frac{0.106(6152)}{47} = 13.9\ m^2 \tag{A.199}$$

Finally, the length of the subcooled region of the condenser is calculated as shown in Equation (A.200).

$$L_{\mathrm{cc,c3}} = \frac{A_{\mathrm{cc,c3}}}{\left(N_{\mathrm{plate,cc,cond}} - 1\right) w_{\mathrm{plate}}} = \frac{13.9}{(1845 - 1)1.17} = \ .00644\ m \tag{A.200}$$

Once the heat transfer in all three sections of the cooling cycle condenser has been assessed, some overall calculations can be made to describe the geometry of the heat exchanger. The overall area of the cooling cycle condenser is calculated as shown in Equation (A.201).

$$A_{\mathrm{total,cc,cond}} = A_{\mathrm{cc,c1}} + A_{\mathrm{cc,c2}} + A_{\mathrm{cc,c3}} = 277 + 2547 + 13.9 = \ 2838\ m^2 \tag{A.201}$$

The total length of the of the cooling cycle condenser is calculated in Equation (A.202).

$$L_{\mathrm{total,cc,cond}} = L_{\mathrm{b1}} + L_{\mathrm{b2}} + L_{\mathrm{b3}} = 0.128 + 1.18 + 0.00644 = \ 1.31\ m \tag{A.202}$$

The number of plates of the cooling cycle condenser is confirmed in Equation (A.203).

$$N_{\mathrm{plate,cc.cond}} - 1 = \frac{A_{\mathrm{total,cc,cond}}}{A_{\mathrm{plate}}} = 1 + \frac{2838}{1.544} = 1839\ Plates \tag{A.203}$$

This concludes the representative heat transfer calculations. Table A.16 shows the hand calculated values compared to the EES calculated values for total heat exchanger area and number of plates for each heat exchanger of the TCCS.

Table A.16 Comparison of heat transfer results between the representative calculation and the EES simulation.

HX	Value	Hand Result	EES Result	Unit
Boiler	Area	62.6	63	m^2
	N_plate	41.5	41.8	Plates
Recuperator	Area	33	32.9	m^2
	N_plate	22.4	22.3	Plates
PC Condenser	Area	1933	1936	m^2
	N_plate	1253	1254	Plates
Cross Cycle Economizer	Area	54.5	54.5	m^2
	N_plate	36.3	36.3	Plates
Chiller	Area	45.2	45.3	m^2
	N_plate	30.3	30.3	Plates
CC Condenser	Area	2838	2847	m^2
	N_plate	1839	1845	Plates

A.5 Economics Sample Calculations

After calculating the total heat exchanger area, and number of plates for all heat exchangers used in the ORC, DMS, and TCCS, the economic model can be carried out. The total heat exchanger cost for the TCCS is found as the sum of the cost of each heat exchanger which include the power cycle boiler, power cycle condenser, power cycle recuperator, cross-cycle economizer, cooling cycle chiller, and cooling cycle condenser. The cost of each heat exchanger is calculated in Equation (A.204) through Equation (A.209)

$$cost_{\text{boiler}} = 475A^{0.54} f_{\text{mat}} f_{\text{pressure}} \frac{CEPCI_{2019}}{CEPCI_{2005}} \tag{A.204}$$

$$= 475(678)^{0.54}(1)(1.35)\left(\frac{607.5}{460}\right) = \$28{,}621$$

$$cost_{\text{pc.cond}} = 475A^{0.54} f_{\text{mat}} f_{\text{pressure}} \frac{CEPCI_{2019}}{CEPCI_{2005}} \quad \text{(A.205)}$$

$$= 475(20839)^{0.54}(1)(1)\left(\frac{607.5}{460}\right) = \$134{,}796$$

$$cost_{\text{rec}} = 475A^{0.54} f_{\text{mat}} f_{\text{pressure}} \frac{CEPCI_{2019}}{CEPCI_{2005}} \quad \text{(A.206)}$$

$$= 475(354)^{0.54}(1)(1.35)\left(\frac{607.5}{460}\right) = \$20{,}150$$

$$cost_{\text{econ}} = 475A^{0.54} f_{\text{mat}} f_{\text{pressure}} \frac{CEPCI_{2019}}{CEPCI_{2005}} \quad \text{(A.207)}$$

$$= 475(587)^{0.54}(1)(1.35)\left(\frac{607.5}{460}\right) = \$26{,}478$$

$$cost_{\text{evap}} = 475A^{0.54} f_{\text{mat}} f_{\text{pressure}} \frac{CEPCI_{2019}}{CEPCI_{2005}} \quad \text{(A.208)}$$

$$= 475(488)^{0.54}(1)(1)\left(\frac{607.5}{460}\right) = \$17{,}751$$

$$cost_{\text{cc,cond}} = 475A^{0.54} f_{\text{mat}} f_{\text{pressure}} \frac{CEPCI_{2019}}{CEPCI_{2005}} \quad \text{(A.209)}$$

$$= 475(30645)^{0.54}(1)(1)\left(\frac{607.5}{460}\right) = \$166{,}003$$

The amount of refrigerant in each heat exchanger was calculated based on the internal volume. The refrigerant charge was calculated for the inlet and outlet headers in each region: subcooled, two-phase, and superheated.

The power cycle boiler refrigerant charge calculation will be presented first. The charge in the inlet header was calculated using Equation (A.210) and the charge in the outlet header was calculated using Equation (A.211)

$$m_{\text{header,i}} = \rho_{\text{liquid}}\left(\frac{\pi D^2}{4}\right) * L_{\text{header}} = 1140\left(\frac{\pi 0.35^2}{4}\right) * 0.2082 = \ 22.8\ kg \tag{A.210}$$

$$m_{\text{header,o}} = \rho_{\text{vapor}}\left(\frac{\pi D^2}{4}\right) * L_{\text{header}} = 126\left(\frac{\pi 0.35^2}{4}\right) * 0.2082 = \ 2.52\ kg \tag{A.211}$$

The charge of refrigerant in the subcooled, two-phase, and superheated plates of the boiler are shown in Equation (A.212) through (A.214).

$$m_{\text{sc}} = \rho_{\text{liquid}}(V_{\text{sc}}) = \rho(A_{\text{sc}})\left(S_{\text{plate}}\right) = 1140(25.9)(0.0045) = \ 133\ kg \tag{A.212}$$

$$m_{tp} = \rho_{\text{ave}}\left(V_{tp}\right) = \frac{\rho_{\text{liquid}} + \rho_{vapor}}{2}\left(A_{tp}\right)\left(S_{\text{plate}}\right) = (542)(14)(0.0045) \tag{A.213}$$

$$= \ 34.1\ kg$$

$$m_{\text{sh}} = \rho_{\text{vapor}}(V_{\text{sh}}) = \rho(A_{\text{sh}})\left(S_{\text{plate}}\right) = 126(23.2)(0.0045) = \ 13.2\ kg \tag{A.214}$$

The total charge in the boiler is then calculated as shown in Equation (A.215).

$$m_{\text{boiler}} = m_{\text{header,i}} + m_{\text{sc}} + m_{\text{tp}} + m_{\text{sh}} + m_{\text{header,o}} \tag{A.215}$$

$$= 22.8 + 133 + 34.1 + 13.2 + 2.52 = \ 206\ kg$$

The recuperator refrigerant charge calculations will be presented next. Because the recuperator is an internal heat exchanger, refrigerant charge must be calculated on both sides of the heat exchanger instead of just one. The inlet and outlet header charge on the subcooled side of the recuperator are calculated as shown in Equation (A.216) and Equation (A.217).

$$m_{\text{header,sc,i}} = \rho_{\text{liquid}}\left(\frac{\pi D^2}{4}\right) * L_{\text{header}} = 1216\left(\frac{\pi 0.35^2}{4}\right) * 0.1069 = \ 12.5\ kg \tag{A.216}$$

$$m_{\text{header,sc,o}} = \rho_{\text{liquid}}\left(\frac{\pi D^2}{4}\right) * L_{\text{header}} = 1186\left(\frac{\pi 0.35^2}{4}\right) * 0.1069 = \ 12.2\ kg \tag{A.217}$$

The inlet and outlet header charge on the superheated side of the recuperator are calculated as shown in Equation (A.218) and Equation (A.219).

$$m_{\text{header,sh,i}} = \rho_{\text{vapor}}\left(\frac{\pi D^2}{4}\right) * L_{\text{header}} = 29.4\left(\frac{\pi 0.35^2}{4}\right) * 0.1069 = \ 0.302\ kg \quad \text{(A.218)}$$

$$m_{\text{header,sh,o}} = \rho_{\text{vapor}}\left(\frac{\pi D^2}{4}\right) * L_{\text{header}} = 31.2\left(\frac{\pi 0.35^2}{4}\right) * 0.1069 = \ 0.321\ kg \quad \text{(A.219)}$$

The refrigerant charge in the subcooled and superheated and regions of the recuperator are calculated in Equation (A.220) and Equation (A.222).

$$m_{\text{sc}} = \rho_{\text{liquid}}(V_{\text{sc}}) = \rho(A_{\text{sc}})\left(S_{\text{plate}}\right) = 1201(15.7)(0.0045) = \ 178\ kg \quad \text{(A.220)}$$

$$m_{\text{sh}} = \rho_{\text{vapor,avg}}(V_{\text{sh}}) = \rho(A_{\text{sh}})\left(S_{\text{plate}}\right) = 30.3(15.7)(0.0045) = \ 4.49\ kg \quad \text{(A.221)}$$

The total charge in the recuperator is then calculated as shown in Equation (A.222).

$$m_{\text{recup}} = m_{\text{header,sc,i}} + m_{\text{sc}} + m_{\text{header,sc,o}} + m_{\text{header,sh,i}} + m_{\text{sh}} + m_{\text{header,sh,o}} \quad \text{(A.222)}$$

$$= 12.5 + 178 + 12.2 + 0.302 + 4.49 + 0.321 = \ 208\ kg$$

The power cycle condenser refrigerant charge calculations will be discussed next. The charge in the inlet header was calculated using Equation (A.223) and the charge in the outlet header was calculated using Equation (A.224)

$$m_{\text{header,i}} = \rho_{\text{vapor}}\left(\frac{\pi D^2}{4}\right) * L_{\text{header}} = 31.2\left(\frac{\pi 0.35^2}{4}\right) * 6.514 = \ 19.6\ kg \quad \text{(A.223)}$$

$$m_{\text{header,o}} = \rho_{\text{liquid}}\left(\frac{\pi D^2}{4}\right) * L_{\text{header}} = 1211\left(\frac{\pi 0.35^2}{4}\right) * 6.514 = \ 759\ kg \quad \text{(A.224)}$$

The charge of refrigerant in the subcooled, two-phase, and superheated plates of the condenser are shown in Equation (A.225) through Equation (A.227).

$$m_{\text{sc}} = \rho_{\text{liquid}}(V_{\text{sc}}) = \rho(A_{\text{sc}})\left(S_{\text{plate}}\right) = 1211(10.6)(0.0045) = \ 57.8\ kg \quad \text{(A.225)}$$

$$m_{tp} = \rho_{\text{ave}}(V_{tp}) = \frac{\rho_{\text{liquid}} + \rho_{vapor}}{2}(A_{tp})(S_{\text{plate}}) = (620)(1804)(0.0045) \quad (A.226)$$

$$= 5033\ kg$$

$$m_{\text{sh}} = \rho_{\text{vapor}}(V_{\text{sh}}) = \rho(A_{\text{sh}})(S_{\text{plate}}) = 31.2(121)(0.0045) = 17\ kg \quad (A.227)$$

The total charge in the power cycle condenser is then calculated as shown in Equation (A.228).

$$m_{\text{pc,cond}} = m_{\text{header,i}} + m_{\text{sh}} + m_{\text{tp}} + m_{\text{sc}} + m_{\text{header,o}} \quad (A.228)$$

$$= 19.6 + 17 + 5033 + 57.8 + 759 = 5886\ kg$$

The cross-cycle economizer refrigerant charge calculations will be discussed next. Because the economizer is also an internal heat exchanger, refrigerant charge must be calculated on both sides of the heat exchanger like the recuperator. The inlet and outlet header charge on the subcooled side of the economizer are calculated as shown in Equation (A.229) and Equation (A.230).

$$m_{\text{header,sc,i}} = \rho_{\text{liquid}}\left(\frac{\pi D^2}{4}\right) * L_{\text{header}} = 1186\left(\frac{\pi 0.35^2}{4}\right) * 0.1797 = 20.5\ kg \quad (A.229)$$

$$m_{\text{header,sc,o}} = \rho_{\text{liquid}}\left(\frac{\pi D^2}{4}\right) * L_{\text{header}} = 1140\left(\frac{\pi 0.35^2}{4}\right) * 0.1797 = 19.7\ kg \quad (A.230)$$

The inlet and outlet header charge on the superheated side of the economizer are calculated as shown in Equation (A.231) and Equation (A.232).

$$m_{\text{header,sh,i}} = \rho_{\text{vapor}}\left(\frac{\pi D^2}{4}\right) * L_{\text{header}} = 27.4\left(\frac{\pi 0.35^2}{4}\right) * 0.1797 = 0.474\ kg \quad (A.231)$$

$$m_{\text{header,sh,o}} = \rho_{\text{vapor}}\left(\frac{\pi D^2}{4}\right) * L_{\text{header}} = 29.1\left(\frac{\pi 0.35^2}{4}\right) * 0.1797 = 0.503\ kg \quad (A.232)$$

The refrigerant charge in the subcooled and superheated and regions of the recuperator are calculated in Equation (A.233) and Equation (A.234).

$$m_{\text{sc}} = \rho_{\text{liquid}}(V_{\text{sc}}) = \rho(A_{\text{sc}})\left(S_{\text{plate}}\right) = 1163(26)(0.0045) = \ 285\ kg \tag{A.233}$$

$$m_{\text{sh}} = \rho_{\text{vapor,avg}}(V_{\text{sh}}) = \rho(A_{\text{sh}})\left(S_{\text{plate}}\right) = 28.3(26)(0.0045) = \ 6.94\ kg \tag{A.234}$$

The total charge in the recuperator is then calculated as shown in Equation (A.235).

$$m_{\text{econ}} = m_{\text{header,sc,i}} + m_{\text{sc}} + m_{\text{header,sc,o}} + m_{\text{header,sh,i}} + m_{\text{sh}} + m_{\text{header,sh,o}} \tag{A.235}$$

$$= 20.5 + 285 + 19.7 + 0.474 + 6.94 + 0.503 = \ 333\ kg$$

The refrigerant charge for the cooling cycle evaporator will be discussed next. The charge in the inlet header was calculated using Equation (A.236) and the charge in the outlet header was calculated using Equation (A.237)

$$m_{\text{header,i}} = \rho_{\text{tp}}\left(\frac{\pi D^2}{4}\right) * L_{\text{header}} = 120\left(\frac{\pi 0.35^2}{4}\right) * 0.1486 = \ 1.72\ kg \tag{A.236}$$

$$m_{\text{header,o}} = \rho_{\text{vapor}}\left(\frac{\pi D^2}{4}\right) * L_{\text{header}} = 15.4\left(\frac{\pi 0.35^2}{4}\right) * 0.1486 = \ 0.22\ kg \tag{A.237}$$

The refrigerant charge in the two phase and superheated regions of the evaporator are calculated as shown in Equation (A.238) and Equation (A.239).

$$m_{tp} = \rho_{\text{ave}}\left(V_{tp}\right) = \frac{\rho_{\text{liquid}} + \rho_{vapor}}{2}\left(A_{tp}\right)\left(S_{\text{plate}}\right) = (68.7)(18.2)(0.0045) \tag{A.238}$$

$$= \ 5.63\ kg$$

$$m_{\text{sh}} = \rho_{\text{vapor}}(V_{\text{sh}}) = \rho(A_{\text{sh}})\left(S_{\text{plate}}\right) = 15.4(27.1)(0.0045) = \ 1.88\ kg \tag{A.239}$$

The total charge in the evaporator is then calculated as shown in Equation (A.240).

$$m_{\text{evap}} = m_{\text{header,i}} + m_{\text{sh}} + m_{\text{tp}} + m_{\text{header,o}} = 1.72 + 1.88 + 5.63 + 0.22 \quad \text{(A.240)}$$

$$= 9.45\ kg$$

The refrigerant charge in the cooling cycle condenser will be discussed next. The charge in the inlet header was calculated using Equation (A.241) and the charge in the outlet header was calculated using Equation (A.242)

$$m_{\text{header,i}} = \rho_{\text{vapor}} \left(\frac{\pi D^2}{4}\right) * L_{\text{header}} = 29.1 \left(\frac{\pi 0.35^2}{4}\right) * 9.583 = 26.8\ kg \quad \text{(A.241)}$$

$$m_{\text{header,o}} = \rho_{\text{liquid}} \left(\frac{\pi D^2}{4}\right) * L_{\text{header}} = 1213 \left(\frac{\pi 0.35^2}{4}\right) * 9.583 = 1118\ kg \quad \text{(A.242)}$$

The charge of refrigerant in the subcooled, two-phase, and superheated plates of the condenser are shown in Equation (A.243) through Equation (A.245).

$$m_{\text{sc}} = \rho_{\text{liquid}}(V_{\text{sc}}) = \rho(A_{\text{sc}})\left(S_{\text{plate}}\right) = 1213(13.8)(0.0045) = 75.3\ kg \quad \text{(A.243)}$$

$$m_{tp} = \rho_{\text{ave}}\left(V_{tp}\right) = \frac{\rho_{\text{liquid}} + \rho_{vapor}}{2}\left(A_{tp}\right)\left(S_{\text{plate}}\right) = (621)(2558)(0.0045) \quad \text{(A.244)}$$

$$= 7148\ kg$$

$$m_{\text{sh}} = \rho_{\text{vapor}}(V_{\text{sh}}) = \rho(A_{\text{sh}})\left(S_{\text{plate}}\right) = 29.1(276)(0.0045) = 36.1\ kg \quad \text{(A.245)}$$

The total charge in the cooling cycle condenser is then calculated as shown in Equation (A.246).

$$m_{\text{cc,cond}} = m_{\text{header,i}} + m_{\text{sh}} + m_{\text{tp}} + m_{\text{sc}} + m_{\text{header,o}} \quad \text{(A.246)}$$

$$= 26.8 + 36.1 + 7148 + 75.3 + 1118 = 8404\ kg$$

After calculating the refrigerant charge in all the heat exchangers, the refrigerant charge in the pipes of the system was determined. Based on the diameter, length, and working fluid phase in the piping in the system, the total charge was calculated to be 26.5 kg. Thus, the total mass of refrigerant in the TCCS is calculated as shown in Equation (A.247).

$$m_{\text{ref,total}} = m_{\text{boiler}} + m_{\text{recup}} + m_{\text{pc,cond}} + m_{\text{econ}} + m_{\text{evap}} + m_{\text{cc,cond}} + m_{\text{pipe}} \quad \text{(A.247)}$$

$$= 206 + 208 + 5886 + 333 + 9.45 + 8404 + 26.5$$

$$= \ 15{,}073\ kg$$

From supplier quotes, the cost per kilogram of R134a was found to be $11 per kg. Thus, the cost of the refrigerant is calculated as shown in Equation (A.248).

$$cost_{\text{ref,total}} = m_{\text{ref,total}} * cost_{\text{ref,spec}} = 15073 * 11 = \$165{,}803 \quad \text{(A.248)}$$

The cost of the pump, turbocompressor, piping, and heat recovery unit will be presented next. The cost of the pump is calculated according to Equation (A.249).

$$cost_{\text{pump}} = f_{\text{type}} Cost_{\text{base}} \frac{CEPCI_{2019}}{CEPCI_{1985}} = 2.12(4027)\left(\frac{607.5}{325}\right) = \$15{,}958 \quad \text{(A.249)}$$

The cost of the turbocompressor was calculated with Equation (A.250).

$$cost_{\text{TC}} = Cost_{6\text{ kw}}\left(\frac{\dot{W}_{\text{turbine}}}{6\ kW}\right)^{\frac{\log\left(\frac{cost10kW}{cost6kW}\right)}{\log\left(\frac{10\text{kw}}{6\text{kw}}\right)}} = 2620\left(\frac{78.8}{6}\right)^{0.356915} = \$6{,}569 \quad \text{(A.250)}$$

The cost of piping depends on the length, diameter, and number of fittings. The total cost of piping in the system was calculated to be $6,418. The cost of heat recovery was determined based on a supplier website cost estimate for a feedwater economizer unit and for the system is estimated to be $23,095. Other costs included in the estimate include cost of miscellaneous components, electronics, and instruments. Miscellaneous component cost was estimated to be $1,500. Electronic cost was estimated to be $3,000. Instrumentation cost was estimated to be $750. The total system cost for the TCCS is calculated using Equation (A.251).

$$cost_{\text{total,tccs}} = f_{\text{install}}\big(cost_{HX} + cost_{\text{refrigerant}} + cost_{\text{pump}} + cost_{\text{TC}} + cost_{\text{piping}} + cost_{heat\ recovery} + cost_{\text{misc}} + cost_{\text{elec}} + cost_{\text{inst}}\big) = 1.6(393{,}799 + 165{,}803 + 15{,}958 + 6{,}569 + 6{,}418 + 23{,}095 + 1{,}500 + 3{,}000 + 750) = \$987{,}027 \quad \text{(A.251)}$$

After finding the total system cost, payback period can be determined. For a TCCS system installed at a beef plant located in Denver, Colorado, annual savings produced by the TCCS were found to total at $202,800 per year. Thus, payback period for the TCCS is calculated as shown in Equation (A.252).

$$Payback\ Period = \frac{Cost_{\text{total,system}}}{Annual\ Savings} = \frac{\$987{,}027}{\$202{,}800/year} = 4.87\ years \quad \text{(A.252)}$$

This concludes the representative calculation for the turbo-compression cooling system using R134a applied to provide subcooling to a primary ammonia refrigeration system at a beef processing facility. The representative economic hand calculations are compared to the results from the EES simulation in Table A.17. The results from the representative cost calculation are calculated per kW of subcooling provided by the TCCS in Table A.18.

Table A.17 Comparison of economic results between the representative calculation and the EES simulation.

Value	Hand Calc	EES Calc	Unit
Cost, Boiler	28,643	28,633	$
Cost, PC Condenser	134,796	134,785	$
Cost, Recuperator	20,150	20,165	$
Cost, Economizer	26,478	26,458	$
Cost, Evaporator	17,751	17,735	$
Cost, CC Condenser	166,003	166,010	$
Mass, Refrigerant	15,073	15,066	kg
Cost, Pump	15,958	15,955	$
Cost, Turbo-compressor	6,569	6,570	$
Total Install Cost, TCCS	987,027	986,883	$
Payback Period, TCCS	4.87	4.86	years

Table A.18 Cost for each component in the TCCS system. Cost per kWh is based on the 818-kW cooling duty of the TCCS chiller.

Component	Cost		Cost per kW_{th}
Boiler	$	28,633.00	$35
PC Condenser	$	134,785.00	$165
Recuperator	$	20,165.00	$25
Economizer	$	26,458.00	$32
Chiller	$	17,735.00	$22
CC Condenser	$	166,010.00	$203
Piping	$	6,418.00	$8
Refrigerant	$	165,730.00	$203
Pump	$	15,955.00	$20
Heat Recovery	$	23,095.00	$28
Turbocompressor	$	6,570.00	$8
Other	$	5,250.00	$6
Total	$	616,801.88	$754
Total Install	$	986,883.00	$1,207

B. Thermodynamic State Points for Turbo-Compression Cooling Systems

The following section provides thermodynamic state points for each TCCS, DMS, and, ORC with various heat exchanger effectivenesses. TCCS and DMS heat exchanger effectiveness inputs were varied from +10% to – 50% of the original effectiveness values, and ORC effectiveness inputs were varied from +10% to –70% of the original effectiveness values. The state point numbering scheme used for the TCCS are shown in Figure A.3. The state point numbering scheme used for the DMS and ORC are shown in Figure B.1 and B.2, respectively.

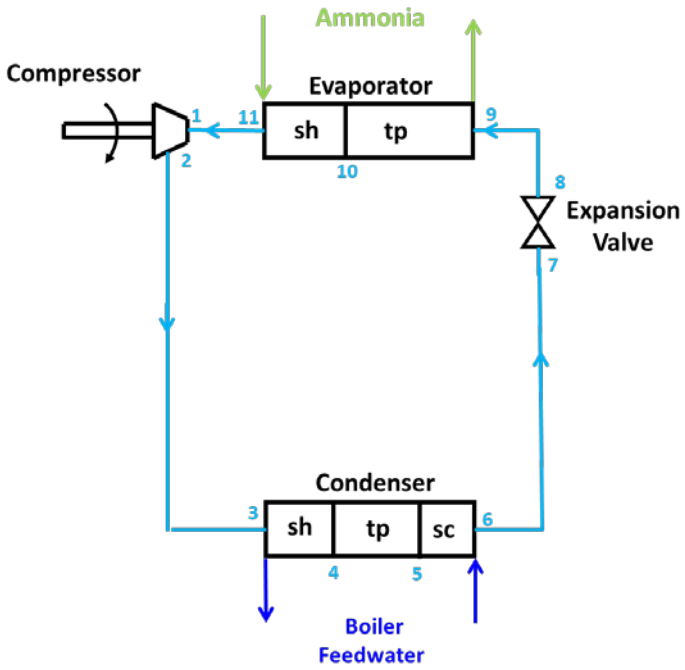

Figure B.1 Process flow diagram of the DMS with state points and external flows designated.

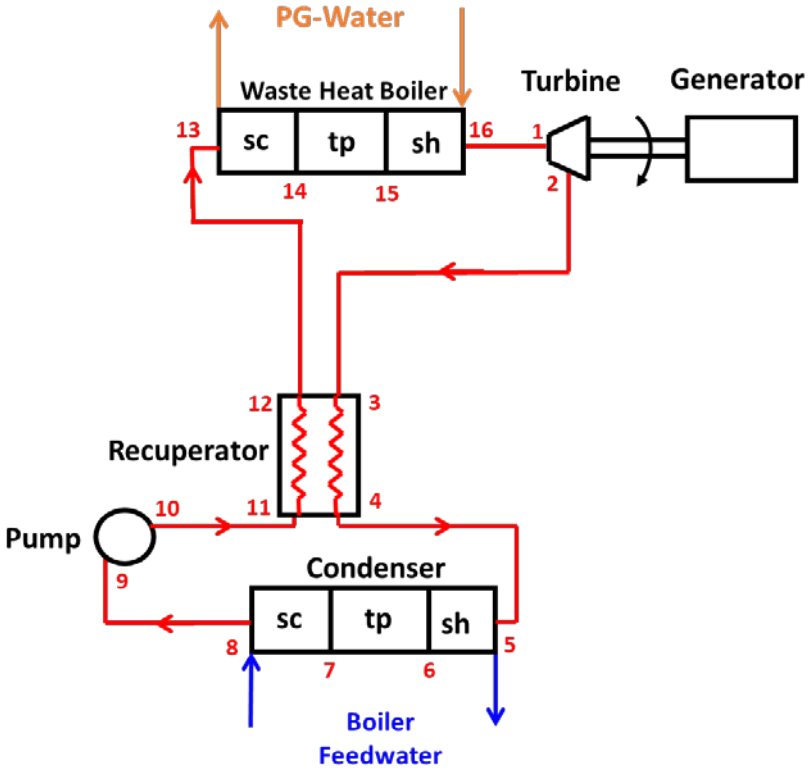

Figure B.2 Process flow diagram of the ORC with state points and external flows designated.

Table B.1 State points for the TCCS with effectiveness varied by +10%.

	Power Cycle				Cooling Cycle			
	Temperature	**Enthalpy**	**Pressure**	**Entropy**	**Temperature**	**Enthalpy**	**Pressure**	**Entropy**
R134a	**°C**	**kJ kg^{-1}**	**kPa**	**kJ kg^{-1} K^{-1}**	**°C**	**kJ kg^{-1}**	**kPa**	**kJ kg^{-1} K^{-1}**
1	96.5	306	2700	0.958	28.7	275	351	1
2	41.6	281	651	0.978	53.1	293	645	1.01
3	41.6	281	651	0.978	53.1	293	645	1.01
4	29	269	651	0.937	38.2	278	645	0.968
5	29	269	651	0.937	38.2	278	645	0.968
6	24.2	264	651	0.921	23.9	264	645	0.921
7	24.2	85.3	651	0.321	23.9	84.9	645	0.319
8	23.3	83.9	651	0.316	23	83.6	645	0.315
9	23.3	83.9	651	0.316	23	83.6	645	0.315
10	25	86.5	2700	0.319	5.05	83.6	351	0.319
11	25	86.5	2700	0.319	5.05	83.6	351	0.319
12	33.9	99.1	2700	0.361	5.05	253	351	0.929
13	33.9	99.1	2700	0.361	28.7	275	351	1
14	47.4	119	2700	0.424				
15	47.4	119	2700	0.424				
16	81.2	177	2700	0.594				
17	81.2	280	2700	0.887				
18	96.5	306	2700	0.958				

Table B.2 State points for the TCCS with original effectiveness values.

	Power Cycle				Cooling Cycle			
	Temperature	**Enthalpy**	**Pressure**	**Entropy**	**Temperature**	**Enthalpy**	**Pressure**	**Entropy**
R134a	**°C**	**kJ kg^{-1}**	**kPa**	**kJ kg^{-1} K^{-1}**	**°C**	**kJ kg^{-1}**	**kPa**	**kJ kg^{-1} K^{-1}**
1	94.6	305	2620	0.957	26.5	273	349	0.997
2	41.8	281	664	0.976	51.3	291	650	1.01
3	41.8	281	664	0.976	51.3	291	650	1.01
4	30.6	270	664	0.94	38.8	278	650	0.969
5	30.6	270	664	0.94	38.8	278	650	0.969
6	24.9	264	664	0.921	24.2	264	650	0.921
7	24.9	86.2	664	0.324	24.2	85.2	650	0.32
8	24	84.9	664	0.319	23.3	84	650	0.316
9	24	84.9	664	0.319	23.3	84	650	0.316
10	25.6	87.4	2620	0.322	4.95	84	349	0.32
11	25.6	87.4	2620	0.322	4.95	84	349	0.32
12	33.5	98.6	2620	0.359	4.95	253	349	0.929
13	33.5	98.6	2620	0.359	26.5	273	349	0.997
14	44.5	115	2620	0.411				
15	44.5	115	2620	0.411				
16	79.7	174	2620	0.586				
17	79.7	281	2620	0.89				
18	94.6	305	2620	0.957				

Table B.3 State points the TCCS with effectiveness varied by – 10%.

	Power Cycle				Cooling Cycle			
	Temperature	**Enthalpy**	**Pressure**	**Entropy**	**Temperature**	**Enthalpy**	**Pressure**	**Entropy**
R134a	**°C**	**kJ kg^{-1}**	**kPa**	**kJ kg^{-1} K^{-1}**	**°C**	**kJ kg^{-1}**	**kPa**	**kJ kg^{-1} K^{-1}**
1	92.2	304	2500	0.957	24.3	271	348	0.99
2	42.4	281	680	0.975	49.6	289	655	1
3	42.4	281	680	0.975	49.6	289	655	1
4	32.4	271	680	0.943	39.3	279	655	0.97
5	32.4	271	680	0.943	39.3	279	655	0.97
6	25.7	265	680	0.92	24.4	264	655	0.921
7	25.7	87.4	680	0.328	24.4	85.6	655	0.322
8	24.8	86.1	680	0.323	23.6	84.5	655	0.318
9	24.8	86.1	680	0.323	23.6	84.5	655	0.318
10	26.4	88.4	2500	0.326	4.85	84.5	348	0.322
11	26.4	88.4	2500	0.326	4.85	84.5	348	0.322
12	33.4	98.4	2500	0.359	4.85	253	348	0.929
13	33.4	98.4	2500	0.359	24.3	271	348	0.99
14	41.9	111	2500	0.399				
15	41.9	111	2500	0.399				
16	77.5	170	2500	0.575				
17	77.5	281	2500	0.892				
18	92.2	304	2500	0.957				

Table B.4 State points for the TCCS with effectiveness varied by – 20%.

	Power Cycle				Cooling Cycle			
	Temperature	**Enthalpy**	**Pressure**	**Entropy**	**Temperature**	**Enthalpy**	**Pressure**	**Entropy**
R134a	**°C**	**kJ kg^{-1}**	**kPa**	**kJ kg^{-1} K^{-1}**	**°C**	**kJ kg^{-1}**	**kPa**	**kJ kg^{-1} K^{-1}**
1	89.2	303	2340	0.958	22.1	269	347	0.984
2	43.4	282	702	0.975	47.7	287	659	0.995
3	43.4	282	702	0.975	47.7	287	659	0.995
4	34.5	273	702	0.946	39.8	279	659	0.97
5	34.5	273	702	0.946	39.8	279	659	0.97
6	26.8	265	702	0.92	24.7	264	659	0.921
7	26.8	89	702	0.333	24.7	85.9	659	0.323
8	25.9	87.7	702	0.329	23.9	84.9	659	0.319
9	25.9	87.7	702	0.329	23.9	84.9	659	0.319
10	27.3	89.8	2340	0.331	4.78	84.9	347	0.323
11	27.3	89.8	2340	0.331	4.78	84.9	347	0.323
12	33.6	98.7	2340	0.361	4.78	253	347	0.929
13	33.6	98.7	2340	0.361	22.1	269	347	0.984
14	39.7	108	2340	0.389				
15	39.7	108	2340	0.389				
16	74.5	164	2340	0.56				
17	74.5	281	2340	0.896				
18	89.2	303	2340	0.958				

Table B.5 State points for the TCCS with effectiveness varied by – 30%.

	Power Cycle				Cooling Cycle			
	Temperature	**Enthalpy**	**Pressure**	**Entropy**	**Temperature**	**Enthalpy**	**Pressure**	**Entropy**
R134a	**°C**	**kJ kg^{-1}**	**kPa**	**kJ kg^{-1} K^{-1}**	**°C**	**kJ kg^{-1}**	**kPa**	**kJ kg^{-1} K^{-1}**
1	85	302	2120	0.96	20	267	349	0.977
2	45.1	283	732	0.975	45.7	285	663	0.988
3	45.1	283	732	0.975	45.7	285	663	0.988
4	37	275	732	0.949	40	279	663	0.971
5	37	275	732	0.949	40	279	663	0.971
6	28.2	266	732	0.919	24.8	264	663	0.921
7	28.2	91	732	0.34	24.8	86.2	663	0.324
8	27.3	89.7	732	0.335	24.2	85.3	663	0.321
9	27.3	89.7	732	0.335	24.2	85.3	663	0.321
10	28.6	91.5	2120	0.337	4.91	85.3	349	0.325
11	28.6	91.5	2120	0.337	4.91	85.3	349	0.325
12	34.2	99.6	2120	0.364	4.91	253	349	0.929
13	34.2	99.6	2120	0.364	20	267	349	0.977
14	38.1	105	2120	0.382				
15	38.1	105	2120	0.382				
16	70.1	156	2120	0.538				
17	70.1	281	2120	0.9				
18	85	302	2120	0.96				

Table B.6 State points for the TCCS with effectiveness varied by – 40%.

	Power Cycle				Cooling Cycle			
	Temperature	**Enthalpy**	**Pressure**	**Entropy**	**Temperature**	**Enthalpy**	**Pressure**	**Entropy**
R134a	**°C**	**kJ kg^{-1}**	**kPa**	**kJ kg^{-1} K^{-1}**	**°C**	**kJ kg^{-1}**	**kPa**	**kJ kg^{-1} K^{-1}**
1	79.3	300	1850	0.963	18.2	265	357	0.969
2	47	284	771	0.975	43	282	663	0.98
3	47	284	771	0.975	43	282	663	0.98
4	40	277	771	0.953	43	282	663	0.98
5	40	277	771	0.953	43	282	663	0.98
6	30	267	771	0.919	24.8	264	663	0.921
7	30	93.6	771	0.348	24.8	86.2	663	0.324
8	29.1	92.3	771	0.344	24.3	85.4	663	0.321
9	29.1	92.3	771	0.344	24.3	85.4	663	0.321
10	30.1	93.7	1850	0.345	5.56	85.4	357	0.325
11	30.1	93.7	1850	0.345	5.56	85.4	357	0.325
12	35.1	101	1850	0.369	5.56	254	357	0.929
13	35.1	101	1850	0.369	18.2	265	357	0.969
14	35.1	101	1850	0.369				
15	35.1	101	1850	0.369				
16	64	146	1850	0.508				
17	64	279	1850	0.904				
18	79.3	300	1850	0.963				

Table B.7 State points for the TCCS with effectiveness varied by – 50%.

	Power Cycle				Cooling Cycle			
	Temperature	**Enthalpy**	**Pressure**	**Entropy**	**Temperature**	**Enthalpy**	**Pressure**	**Entropy**
R134a	**°C**	**kJ kg^{-1}**	**kPa**	**kJ kg^{-1} K^{-1}**	**°C**	**kJ kg^{-1}**	**kPa**	**kJ kg^{-1} K^{-1}**
1	68.2	296	1350	0.972	18.2	264	399	0.957
2	51.5	287	844	0.979	37.5	277	645	0.966
3	51.5	287	844	0.979	37.5	277	645	0.966
4	45	281	844	0.958	37.5	277	645	0.966
5	45	281	844	0.958	37.5	277	645	0.966
6	33.2	268	844	0.918	23.9	264	645	0.921
7	33.2	98.2	844	0.363	23.9	84.9	645	0.319
8	32.3	97	844	0.359	23.5	84.3	645	0.317
9	32.3	97	844	0.359	23.5	84.3	645	0.317
10	32.8	97.6	1350	0.36	8.87	84.3	399	0.32
11	32.8	97.6	1350	0.36	8.87	84.3	399	0.32
12	37.4	104	1350	0.381	8.87	256	399	0.927
13	37.4	104	1350	0.381	18.2	264	399	0.957
14	37.4	104	1350	0.381				
15	37.4	104	1350	0.381				
16	51	125	1350	0.447				
17	51	276	1350	0.911				
18	68.2	296	1350	0.972				

Table B.8 State points for the DMS with effectiveness varied by +10%.

	DMS			
	Temperature	**Enthalpy**	**Pressure**	**Entropy**
R134a	**°C**	**kJ kg^{-1}**	**kPa**	**kJ kg^{-1} K^{-1}**
1	28.2	275	327	1.01
2	51.3	292	585	1.02
3	51.3	292	585	1.02
4	51.3	292	585	1.02
5	51.3	292	585	1.02
6	20.7	262	585	0.922
7	20.7	80.3	585	0.304
8	20.2	79.5	585	0.301
9	20.2	79.5	585	0.301
10	3.08	79.5	327	0.305
11	3.08	79.5	327	0.305

Table B.9 State points for the DMS with original effectiveness values.

	DMS			
	Temperature	**Enthalpy**	**Pressure**	**Entropy**
R134a	**°C**	**kJ kg^{-1}**	**kPa**	**kJ kg^{-1} K^{-1}**
1	25.8	273	322	1
2	49.7	290	589	1.01
3	49.7	290	589	1.01
4	49.7	290	589	1.01
5	49.7	290	589	1.01
6	20.9	262	589	0.922
7	20.9	80.6	589	0.305
8	20.4	79.9	589	0.303
9	20.4	79.9	589	0.303
10	2.62	79.9	322	0.306
11	2.62	79.9	322	0.306

Table B.10 State points the DMS with effectiveness varied by –10%.

	DMS			
	Temperature	**Enthalpy**	**Pressure**	**Entropy**
R134a	**°C**	**kJ kg^{-1}**	**kPa**	**kJ kg^{-1} K^{-1}**
1	23.3	271	316	0.997
2	48.2	289	593	1.01
3	48.2	289	593	1.01
4	48.2	289	593	1.01
5	48.2	289	593	1.01
6	21.2	262	593	0.922
7	21.2	80.9	593	0.306
8	20.7	80.2	593	0.304
9	20.7	80.2	593	0.304
10	2.11	80.2	316	0.307
11	2.11	80.2	316	0.307

Table B.11 State points for the DMS with effectiveness varied by –20%.

	DMS			
	Temperature	**Enthalpy**	**Pressure**	**Entropy**
R134a	**°C**	**kJ kg^{-1}**	**kPa**	**kJ kg^{-1} K^{-1}**
1	20.7	269	310	0.991
2	46.6	287	597	1
3	46.6	287	597	1
4	46.6	287	597	1
5	46.6	287	597	1
6	21.4	262	597	0.922
7	21.4	81.3	597	0.307
8	20.9	80.6	597	0.305
9	20.9	80.6	597	0.305
10	1.58	80.6	310	0.309
11	1.58	80.6	310	0.309

Table B.12 State points for the DMS with effectiveness varied by –30%.

	DMS			
	Temperature	**Enthalpy**	**Pressure**	**Entropy**
R134a	**°C**	**kJ kg^{-1}**	**kPa**	**kJ kg^{-1} K^{-1}**
1	18	266	305	0.984
2	44.9	285	601	0.996
3	44.9	285	601	0.996
4	44.9	285	601	0.996
5	44.9	285	601	0.996
6	21.6	262	601	0.922
7	21.6	81.6	601	0.308
8	21.2	81	601	0.306
9	21.2	81	601	0.306
10	1.1	81	305	0.311
11	1.1	81	305	0.311

Table B.13 State points for the DMS with effectiveness varied by –40%.

	DMS			
	Temperature	**Enthalpy**	**Pressure**	**Entropy**
R134a	**°C**	**kJ kg^{-1}**	**kPa**	**kJ kg^{-1} K^{-1}**
1	15.5	264	302	0.977
2	42.8	283	605	0.99
3	42.8	283	605	0.99
4	42.8	283	605	0.99
5	42.8	283	605	0.99
6	21.8	263	605	0.922
7	21.8	81.9	605	0.309
8	21.4	81.3	605	0.307
9	21.4	81.3	605	0.307
10	0.874	81.3	302	0.312
11	0.874	81.3	302	0.312

Table B.14 State points for the DMS with effectiveness varied by –50%.

	DMS			
	Temperature	**Enthalpy**	**Pressure**	**Entropy**
R134a	**°C**	**kJ kg^{-1}**	**kPa**	**kJ kg^{-1} K^{-1}**
1	13.6	262	311	0.968
2	39.8	280	605	0.98
3	39.8	280	605	0.98
4	39.8	280	605	0.98
5	39.8	280	605	0.98
6	21.8	263	605	0.922
7	21.8	81.9	605	0.309
8	21.5	81.4	605	0.308
9	21.5	81.4	605	0.308
10	1.69	81.4	311	0.312
11	1.69	81.4	311	0.312

Table B.15 State points for the ORC with effectiveness varied by +10%.

	ORC			
	Temperature	**Enthalpy**	**Pressure**	**Entropy**
R134a	**°C**	**kJ kg^{-1}**	**kPa**	**kJ kg^{-1} K^{-1}**
1	96.9	303	2870	0.947
2	33.1	275	551	0.97
3	33.1	275	551	0.97
4	23.3	265	551	0.938
5	23.3	265	551	0.938
6	18.8	261	551	0.923
7	18.8	77.6	551	0.295
8	18.4	77.1	551	0.293
9	18.4	77.1	551	0.293
10	20.3	80	2870	0.297
11	20.3	80	2870	0.297
12	27.1	89.5	2870	0.329
13	27.1	89.5	2870	0.329
14	27.1	89.5	2870	0.329
15	27.1	89.5	2870	0.329
16	84	182	2870	0.61

Table B.16 State points for the ORC with original effectiveness values.

	ORC			
	Temperature	**Enthalpy**	**Pressure**	**Entropy**
R134a	**^{o}C**	**kJ kg^{-1}**	**kPa**	**kJ kg^{-1} K^{-1}**
1	95.2	303	2770	0.947
2	33.5	275	556	0.97
3	33.5	275	556	0.97
4	24.5	266	556	0.941
5	24.5	266	556	0.941
6	19.1	261	556	0.923
7	19.1	78	556	0.296
8	18.7	77.5	556	0.295
9	18.7	77.5	556	0.295
10	20.5	80.3	2770	0.298
11	20.5	80.3	2770	0.298
12	26.8	89.1	2770	0.327
13	26.8	89.1	2770	0.327
14	26.8	89.1	2770	0.327
15	26.8	89.1	2770	0.327
16	82.4	179	2770	0.601

Table B.17 State points the ORC with effectiveness varied by –10%.

	ORC			
	Temperature	**Enthalpy**	**Pressure**	**Entropy**
R134a	**^{o}C**	**kJ kg^{-1}**	**kPa**	**kJ kg^{-1} K^{-1}**
1	93.1	302	2650	0.949
2	34.1	276	563	0.97
3	34.1	276	563	0.97
4	25.8	268	563	0.944
5	25.8	268	563	0.944
6	19.5	261	563	0.923
7	19.5	78.6	563	0.298
8	19.1	78.1	563	0.296
9	19.1	78.1	563	0.296
10	20.8	80.7	2650	0.3
11	20.8	80.7	2650	0.3
12	26.6	88.8	2650	0.327
13	26.6	88.8	2650	0.327
14	26.6	88.8	2650	0.327
15	26.6	88.8	2650	0.327
16	80.3	175	2650	0.589

Table B.18 State points for the ORC with effectiveness varied by –20%.

	ORC			
	Temperature	**Enthalpy**	**Pressure**	**Entropy**
R134a	**°C**	**kJ kg^{-1}**	**kPa**	**kJ kg^{-1} K^{-1}**
1	90.3	302	2490	0.951
2	34.9	276	571	0.971
3	34.9	276	571	0.971
4	27.3	269	571	0.947
5	27.3	269	571	0.947
6	20	262	571	0.922
7	20	79.3	571	0.3
8	19.6	78.8	571	0.299
9	19.6	78.8	571	0.299
10	21.2	81.2	2490	0.302
11	21.2	81.2	2490	0.302
12	26.5	88.6	2490	0.327
13	26.5	88.6	2490	0.327
14	26.5	88.6	2490	0.327
15	26.5	88.6	2490	0.327
16	77.3	169	2490	0.574

Table B.19 State points for the ORC with effectiveness varied by –30%.

	ORC			
	Temperature	**Enthalpy**	**Pressure**	**Entropy**
R134a	**°C**	**kJ kg^{-1}**	**kPa**	**kJ kg^{-1} K^{-1}**
1	86.5	301	2270	0.954
2	36.1	277	583	0.973
3	36.1	277	583	0.973
4	29.1	270	583	0.95
5	29.1	270	583	0.95
6	20.6	262	583	0.922
7	20.6	80.2	583	0.303
8	20.2	79.7	583	0.302
9	20.2	79.7	583	0.302
10	21.6	81.8	2270	0.304
11	21.6	81.8	2270	0.304
12	26.5	88.7	2270	0.327
13	26.5	88.7	2270	0.327
14	26.5	88.7	2270	0.327
15	26.5	88.7	2270	0.327
16	73.2	162	2270	0.553

Table B.20 State points for the ORC with effectiveness varied by –40%.

	ORC			
	Temperature	**Enthalpy**	**Pressure**	**Entropy**
R134a	**°C**	**kJ kg^{-1}**	**kPa**	**kJ kg^{-1} K^{-1}**
1	80.9	299	1970	0.958
2	37.8	278	598	0.975
3	37.8	278	598	0.975
4	31.3	272	598	0.954
5	31.3	272	598	0.954
6	21.5	262	598	0.922
7	21.5	81.4	598	0.308
8	21.1	80.9	598	0.306
9	21.1	80.9	598	0.306
10	22.3	82.6	1970	0.308
11	22.3	82.6	1970	0.308
12	26.8	88.9	1970	0.329
13	26.8	88.9	1970	0.329
14	26.8	88.9	1970	0.329
15	26.8	88.9	1970	0.329
16	66.8	151	1970	0.522

Table B.21 State points for the ORC with effectiveness varied by –50%.

	ORC			
	Temperature	**Enthalpy**	**Pressure**	**Entropy**
R134a	**°C**	**kJ kg^{-1}**	**kPa**	**kJ kg^{-1} K^{-1}**
1	71.6	296	1540	0.965
2	40.1	280	622	0.978
3	40.1	280	622	0.978
4	34.2	274	622	0.959
5	34.2	274	622	0.959
6	22.7	263	622	0.921
7	22.7	83.2	622	0.314
8	22.4	82.6	622	0.312
9	22.4	82.6	622	0.312
10	23.1	83.8	1540	0.313
11	23.1	83.8	1540	0.313
12	27.2	89.6	1540	0.333
13	27.2	89.6	1540	0.333
14	27.2	89.6	1540	0.333
15	27.2	89.6	1540	0.333
16	56.3	133	1540	0.472

Table B.22 State points for the ORC with effectiveness varied by –60%.

	ORC			
	Temperature	**Enthalpy**	**Pressure**	**Entropy**
R134a	**°C**	**kJ kg^{-1}**	**kPa**	**kJ kg^{-1} K^{-1}**
1	53.1	288	889	0.977
2	43.6	283	663	0.982
3	43.6	283	663	0.982
4	38.3	278	663	0.965
5	38.3	278	663	0.965
6	24.8	264	663	0.921
7	24.8	86.2	663	0.324
8	24.5	85.6	663	0.322
9	24.5	85.6	663	0.322
10	24.7	85.9	889	0.322
11	24.7	85.9	889	0.322
12	28.3	91.1	889	0.34
13	28.3	91.1	889	0.34
14	28.3	91.1	889	0.34
15	28.3	91.1	889	0.34
16	35.1	101	889	0.372

Table B.23 State points for the ORC with effectiveness varied by –70%.

	ORC			
	Temperature	**Enthalpy**	**Pressure**	**Entropy**
R134a	**°C**	**kJ kg^{-1}**	**kPa**	**kJ kg^{-1} K^{-1}**
1	43.2	281	734	0.969
2	43	281	730	0.969
3	43	281	730	0.969
4	43	281	730	0.969
5	43	281	730	0.969
6	28.1	266	730	0.919
7	28.1	90.9	730	0.339
8	27.7	90.3	730	0.337
9	27.7	90.3	730	0.337
10	27.8	90.3	734	0.337
11	27.8	90.3	734	0.337
12	27.8	90.3	734	0.337
13	27.8	90.3	734	0.337
14	27.8	90.3	734	0.337
15	27.8	90.3	734	0.337
16	28.3	91.2	734	0.34

LIST OF ABBREVIATIONS

Abbreviation	Name
TCCS	turbo-compression cooling system
PRS	primary refrigeration system
DMS	dedicated mechanical subcooler
ORVC	Organic Rankine vapor compression cycle
ORC	organic Rankine cycle
FWE	feedwater economizer
VCRC	vapor compression refrigeration cycle
COP	coefficient of performance
SLHX	suction line heat exchanger
IMS	integrated mechanical subcooler
TMY3	typical meteorological year (1991-2005)
NG	natural gas
pg	propylene glycol - water mixture
PBP	Payback period
NPV	Net Present Value